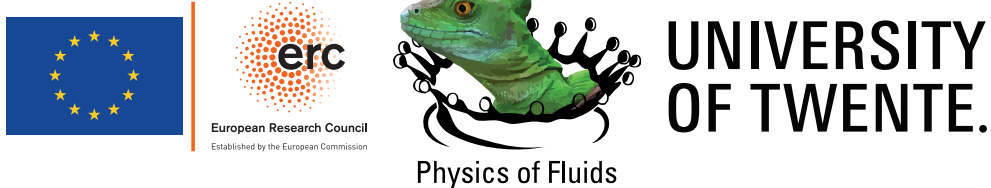


Viscous Free-Surface Flows

Vatsal Sanjay

Graduation committee members:

Prof. Dr. Jennifer L. Herek (chairperson)	University of Twente
Prof. Dr. rer. nat. Dr. h. c. Detlef Lohse (promotor)	University of Twente
Prof. Dr. David Quéré	ESPCI & Ladhyyx
Prof. Dr. Ir. E. Harald van Brummelen Eindhoven	University of Technology
Prof. Dr. Ir. Wilko Rohlfs	University of Twente
Prof. Dr. Marjolein van der Linden	University of Twente
Assist. Prof. Dr. Maziyar Jalaal	University of Amsterdam



The work in this thesis was carried out at the Physics of Fluids group of the Faculty of Science and Technology of the University of Twente. This thesis was financially supported by the ERC Advanced Grant No. 740479-DDD.

Dutch title:

Viskeuze Stromingen bij Vrije-Oppervlakken

Publisher:

Vatsal Sanjay, Physics of Fluids, University of Twente,
P.O. Box 217, 7500 AE Enschede, The Netherlands

<https://www.vatsalsanjay.com>

Printed by: Gildeprint

Copyright © 2022 Vatsal Sanjay. All rights reserved.

No part of this work may be reproduced or transmitted for commercial purposes, in any form or by any means, electronic or mechanical, including photocopying and recording, or by any information storage or retrieval system, except as expressly permitted by the author.

ISBN: 978-90-365-5407-7

DOI: 10.3990/1.9789036554077

VISCOUS FREE-SURFACE FLOWS

DISSERTATION

to obtain
the degree of doctor at the Universiteit Twente,
on the authority of the rector magnificus,
prof. dr. ir. A. Veldkamp,
on account of the decision of the Doctorate Board,
to be publicly defended
on Friday the 15th of July 2022 at 12:45

by

Vatsal Sanjay
Born on the 5th of February 1996
in RS Tank Laheriasarai, Bihar, India

This dissertation has been approved by the promotor:

Prof. Dr. rer. nat. Dr. h. c. Detlef Lohse

To Anjali,
the one constant of my life.



Scan me for a soft copy of
this Ph.D. thesis

Contents

Introduction	1
I Drop Impact	15
1 Impact forces of water drops falling on superhydrophobic surfaces	17
1.1 Introduction	18
1.2 Setup	19
1.3 Formation of a second peak in the force	21
1.4 Weber number dependence of the characteristics times	23
1.5 Influence of Weber number on the first peak	23
1.6 Influence of Weber number on the second peak	25
1.7 Conclusions and outlook	27
Appendices	29
1.A Experimental method	29
1.B Numerical method	31
1.C Superhydrophobic vs. hydrophilic surfaces	36
1.D Some notes on the different regimes of drop impact	38
1.E Calculation of the jet and retraction characteristics	46
1.F Code availability	52
1.G Supplemental movies	52
2 When does a drop stop bouncing?	55
2.1 Introduction	56
2.2 Governing equations	57
2.3 Bouncing inhibition	59

2.4 Limiting cases	64
2.5 Conclusions and outlook	74
Appendices	77
2.A Measuring the restitution coefficient	77
2.B Influence of Weber number	77
2.C Code availability	79
2.D Supplemental movies	80
3 Drop impact on viscous liquid films	81
3.1 Introduction	82
3.2 Methods	84
3.3 Phenomenology	87
3.4 Phenomenological model	92
3.5 Influence of drop and film parameters	95
3.6 Bouncing inhibition on low Ohnesorge number films	100
3.7 Conclusions and outlook	104
Appendices	109
3.A Air layer rupture	109
3.B Substrate independent bouncing	109
3.C Influence of the impact Weber number on bouncing drops	114
3.D Measuring film thickness	114
3.E Measuring the restitution coefficient	115
3.F Code availability	115
3.G Supplemental movies	115
4 Lifting a sessile oil drop with an impacting one	117
4.1 Introduction	118
4.2 Method	120
4.3 Experimental observations	122
4.4 Direct numerical simulations	126
4.5 Conclusions and outlook	133
Appendices	135
4.A Contact angle measurements	135
4.B Water-on-water drop impact	135
4.C Simulation methodology	137
4.D Energy budget calculations	139

4.E	Code availability	140
4.F	Supplemental movies	140
II	Retraction & Bursting	143
5	Taylor-Culick retractions and the influence of the surroundings	145
5.1	Introduction	146
5.2	Film bursting at an air-liquid interface	150
5.3	Numerical framework	158
5.4	Taylor-Culick retractions: numerics	163
5.5	Taylor-Culick retractions: a force perspective	170
5.6	Demonstration of the scaling relationships	173
5.7	Taylor-Culick retractions: an energetics perspective	176
5.8	Conclusions and outlook	184
Appendices		187
5.A	Classical Taylor-Culick retractions	187
5.B	Energy calculations	191
5.C	Code availability	194
5.D	Supplemental movies	194
6	Bursting bubbles in a viscoplastic medium	197
6.1	Introduction	198
6.2	Numerical framework & problem description	200
6.3	Effects of yield stress on the bursting bubble	203
6.4	What happens to the initial surface energy?	209
6.5	Final crater shapes	211
6.6	Regime map	214
6.7	Conclusions and outlook	216
Appendices		219
6.A	Governing equations	219
6.B	The Newtonian limit	220
6.C	The effect of the Ohnesorge number, Oh	222
6.D	Energy budget calculations	224
6.E	Code availability & choosing numerical parameters	226
6.F	Supplemental movies	231

Conclusion and outlook	233
References	243
Summary	275
Samenvatting	279
Acknowledgments	283
About the author	289

Introduction

Liquids rule our lives in more ways than usually perceived. In one of his popular-science books, Miodownik [1] delineates the fickle nature of the life-sustaining, delightful, and yet at times, potentially dangerous fluid flow processes. To cite a few examples, the blood flow in our body sustains life, whereas nitroglycerin-based explosives hold the inherent amplitude to cause severe damage. Nonetheless, aesthetically pleasing waterfalls are a relief to sore eyes for everyone. What is even more intriguing is how many of the examples discussed in Miodownik [1] and our everyday encounter with liquids for cooking, drinking, and cleaning involve flows at the interface between two fluids, one of which offers negligible tangential shear stress. Such flows are categorized as free-surface flows [2] and are the subject of this thesis.

From the atomization chamber that fuels an aircraft to the Moka pot that fueled the author while finishing this thesis, all involve intricate free-surface flows. Such processes often span over multi-scales, for example, from slamming of ocean waves onto ships and sloshing of liquid cargo to that of coffee or tea in a cup [3], and can involve multi-physics from self-propelled drops on a superheated surface (the so-called Leidenfrost drops, [4–6]) to disintegration of liquids in strong electric fields (for example, electrospray from Taylor cones, [7, 8]). Yet another example of free-surface flows involves a glass of wine where a liquid film climbs along the wall, evaporates, and drips tiny droplets (known as “tears” of wine owing to the Marangoni stresses, [9, 10]). It is, therefore, safe to claim that free-surface flows are omnipresent.

This thesis elucidates two classes of the above-mentioned free-surface phenomena, namely, the impact of liquid drops on non-wetting substrates (part I) and capillary driven retraction and bursting of films and free-surface bubbles, respectively (part II). In all the cases, we pay special attention to viscous stresses and how they dictate the fate of such free-surface flows.

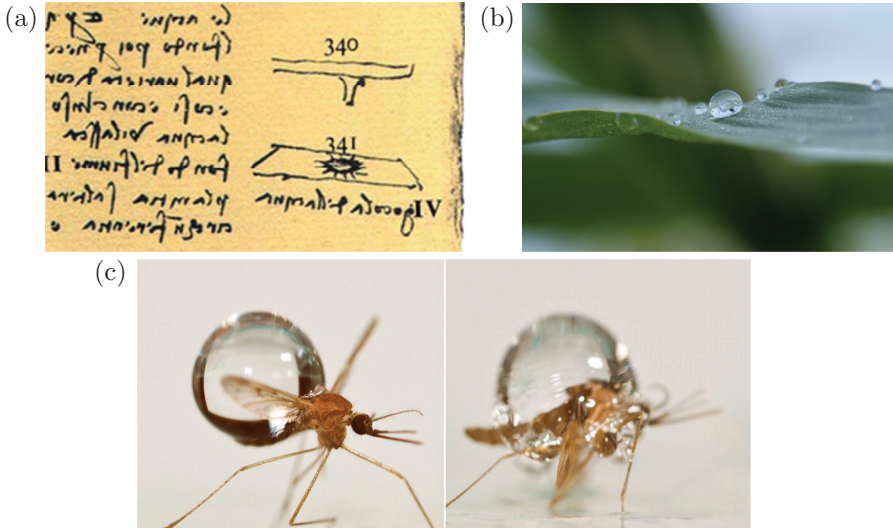


Figure 1: (a) Sketch of a water drop falling on a rigid immobile substrate by da Vinci [13]. (b) A drop of dew sitting on a non-wetting leaf, nature’s way of keeping flora dry (adapted with permission from Seyfert [23]). (c) A water drop impacting a mosquito [24].

Part I: Drop Impact

It is fascinating to watch raindrops hitting a solid surface [11, 12]. This phenomenon has piqued the interest of scientists for over five centuries, ever since Leonardo da Vinci sketched a water drop impacting a rigid immobile substrate (see figure 1a, reproduced from the margin of folio 33r in Codex Hammer/Leicester (1506 – 1510), [13]), who also noted the axisymmetry of drop impact and rebound. However, it was only in 1876-77 (still over one-and-a-half century ago) when Arthur Mason Worthington [14, 15] published the first photographs of the drop impact process, stimulating artists, scientists, and engineers alike ever since. Indeed, drop impact processes are not only interesting from a point of view of fundamental research but also find relevance in inkjet printing [16], cooling applications [17–19], pesticides application [20, 21], and criminal forensics [22].

Upon impact [25], the liquid first spreads [26, 27] until it reaches its maximal extent [28–31]. For a perfectly wetting substrate, for example, glass or paper [16], the drop sticks to it. However, for a non-wetting substrate, for example, plant leaves (see figure 1b, [23, 32, 33]), the drops can ricochet

off following rich dynamics: from the maximum spreading extent, it recoils, following a capillary-driven Taylor-Culick type retraction parallel to the substrate to minimize its surface energy [34–39], and ultimately bounces off in an elongated shape perpendicular to the substrate [40–42]. Following the first observations by Worthington [14, 15], these elongated shapes are called Worthington jets, and are formed by the flow-focusing due to capillary waves [43, 44] and drop retraction [36].

Such drop impact and bouncing behavior abound in nature as non-wetting surfaces provide plants and animals with a natural way to keep dry [24, 32, 33]. Such rebound behaviors are also important in various industrial processes [45] such as self-cleaning [46], keeping clothes dry [47], and anti-fogging surfaces [48]. However, the repellent behavior of these non-wetting substrates is volatile and can fail due to external disturbances such as pressure [49–52], evaporation [53–55], mechanical vibration [56], or the impact forces of prior droplets [57]. Hence, for most of these applications, the drop impact forces can lead to severe unwanted consequences, such as soil erosion [58] or the damage to engineered surfaces [59–61]. A thorough understanding of the drop impact forces is thus needed to develop countermeasures against these damages [62]. Consequently, it is natural to ask how much force the substrate (plant leaves or insects) experiences during such impact and takeoff events (see figure 1c, [3, 24] and chapter 1).

In most of the applications mentioned above, such as self-cleaning [46] and anti-fogging [48], it is pertinent that the drops bounce off the surface. On the other hand, bouncing must be suppressed for various other applications, such as inkjet printing [16] or pesticide deposition [20, 21, 63]. Therefore, one often wonders when will a drop stop bouncing? We will answer this question in chapter 2 by studying the role of viscosity and gravity on bouncing inhibition of impacting drops. Furthermore, in chapter 3, we extend this work to cases where the substrate is coated with a viscous oil film and an air layer is trapped between it and the impacting drop, delaying their contact.

In fact, in 1881, Reynolds [64] noticed a delay in coalescence between an impacting drop and a pool of the same liquid, owing to an air layer between them. Interfacial processes such as Marangoni flow [65], Leidenfrost effect [4–6, 66–69], inverse Leidenfrost effect [70–72], or electromagnetic forces [73, 74] can further stabilize the sandwiched air/vapor layer to facilitate levitation. Moreover, even drops impacting on rigid substrates encounter such air layers that can delay coalescence [75]. In 2012, van der Veen et al. [76] used direct interferometry measurements to quantify these air-layers [also see 77–79].

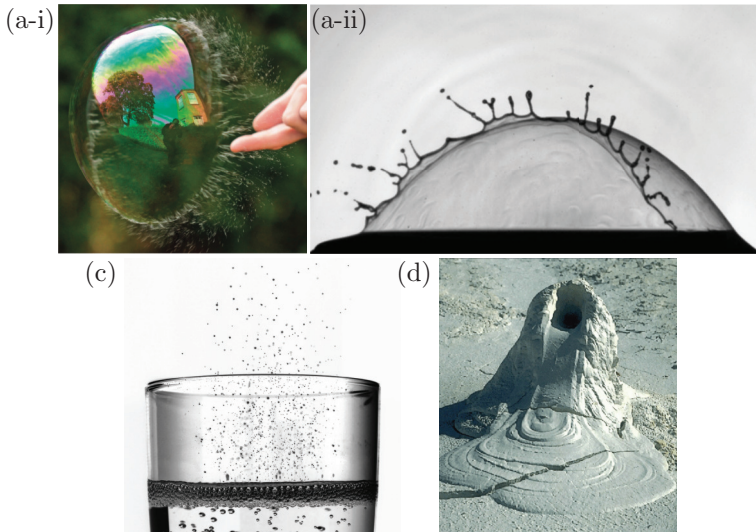


Figure 2: (a-i) Playing with soap bubbles (reprinted with permission from Guyon et al. [83]) as a pierced soap bubble shrinks (and vanishes) to minimize its surface area and (a-ii) a controlled experiment of the same process [84]. (b) Bubbles bursting at the free-surface of champagne [85]. (c) A mud volcano (reprinted with permission from Balmforth et al. [86]).

Furthermore, they also facilitate superamphiphobic-like bouncing [80]. We also address such behaviors in chapter 3. A further extension of bouncing off viscous liquid films is the collision between an impacting drop and a sessile one sitting on a non-wetting substrate. A better understanding of such impacts is crucial in the emerging field of additive manufacturing. For example, in 3D printing, which is one of the widely used additive manufacturing techniques, the relative precision of the drop deposition and its shape evolution may decide the success or failure of a printed device. Although it has been shown that the collision of two freely flying droplets offers much richer dynamics than the impact of a single drop [81, 82], the collision between an impacting drop and a sessile one is still not well explored. So, in chapter 4, we demystify such collision scenarios.

Part II: Retraction & Bursting

Ever since the seminal works of Savart [87, 88, 89], fluid dynamicists have been intrigued by liquid films, sheets, and soap bubbles for over two centuries. It is

particularly bewitching to watch these sheets shrink and vanish to minimize their surface area once a hole nucleates on them (see figure 2a; also notice the liquid filaments that rapidly break up to generate a myriad of tiny droplets.). Consequently, such bursting of liquid (e.g., soap) films in the air is perhaps the most widely studied example of sheet destabilization and retraction – an area of active research since the pioneering works of Dupré [90, 91], Rayleigh [92], Taylor [34], Culick [35], McEntee and Mysels [93] in the late nineteenth and mid-twentieth century to the more recent investigations of Deka and Pierson [38], Lhuissier and Villermaux [84], Bremond and Villermaux [94], Müller et al. [95], Munro et al. [96].

Such retraction processes involve the release of excess surface energy as the interfacial area of the film decreases. Indeed, Dupré [90, 91] wrongly assumed that the ‘entire’ surface energy released during such retractions manifests as the kinetic energy of the film [92] and calculated a retraction velocity that was off by a factor of $\sqrt{2}$ when compared to the experiments, leading to the famous Dupré-Rayleigh paradox [97]. Taylor [34] circumvented this paradox by using force/momentum balance to calculate the retraction velocity, which agreed with experiments. However, it was only when Culick [35] realized that the missing link was viscous dissipation that the paradox was solved [98]. The correct energy balance requires that the rate of surface energy released should be distributed equally into an increase in kinetic energy of the rim and the viscous dissipation inside the film. Consequently, such retractions are now referred to as Taylor-Culick retractions. More recently, Pierson et al. [37], Deka and Pierson [38], Savva and Bush [99] have further enhanced the understanding of the role of internal viscous stresses in such retraction processes. In chapter 5, we focus on the role of external viscous stresses on the retraction of liquid films.

Common realizations of Taylor-Culick retractions include bursting of bubbles at a liquid-gas free-surface (figure 2a-ii, [84]). Once the liquid film separating the gas bubble from the gaseous surrounding disappears, an open cavity is formed [100] whose collapse leads to a series of rich dynamical processes that involve flow-focusing owing to capillary waves [101, 102] and may lead to the formation of a Worthington jet [103]. Perfect flow-focusing can also result in an ultra-thin and fast singular jet. Such free-surface bubble bursting is seen in a glass of champagne or other sparkling wine (figure 3c) and is often credited for enhancing the mouthfeel of the taster [85, 104–106].

For Newtonian liquids like champagne (figure 2b), Duchemin et al. [102], Gordillo and Rodríguez-Rodríguez [103], Gañán-Calvo [107], Deike et al. [108] have extensively studied the bursting bubble process, resulting in a profound

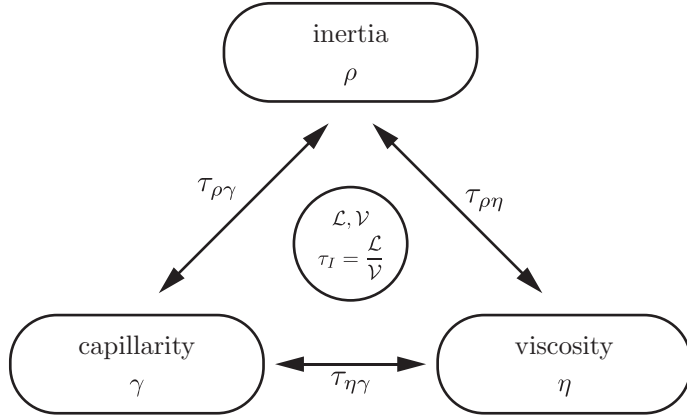


Figure 3: Important scales for viscous free-surface flows. Here, \mathcal{V} and \mathcal{L} are the relevant velocity and length scales associated with the flow, whereas ρ , γ , and η are the material properties of the fluid, namely, density, surface tension coefficient, and viscosity, respectively. τ_{ij} denote several timescales, which are used throughout this thesis: the inertial timescale, $\tau_I = \mathcal{L}/\mathcal{V}$, inertio-capillary timescale, $\tau_{\rho\gamma} = \sqrt{\rho\mathcal{L}^3/\gamma}$, inertio-viscous timescale, $\tau_{\rho\eta} = \rho\mathcal{L}^2/\eta$, and the visco-capillary time scale, $\tau_{\eta\gamma} = \eta\mathcal{L}/\gamma$.

understanding of the physics of bubble bursting in Newtonian fluids. Surprisingly, very little is known about some other common realizations of bursting bubbles: in geophysics, for example, bubbles bursting at the free surface of mud volcanoes (figure 2c) and in the food industry, where the rheological properties of the medium influence the collapse of bubble cavities. These materials behave more like an elastic solid below critical stress (yield stress); however, they flow above this critical stress. Readers can find detailed reviews on yield stress fluids in Balmforth et al. [86], Bird et al. [109], Coussot [110], Bonn et al. [111]. In such cases, the viscous stresses are enhanced by this non-zero yield stress enabling the free surface to sustain finite deformations. In chapter 6, we elucidate the physics of a bursting bubble in a viscoplastic medium by analyzing the role of yield stress on the free-surface phenomenon of the collapse of a bubble cavity driven by capillarity to approach minimum surface area configuration.

Relevant timescales and dimensionless numbers

Ever since the pioneering ideas of Buckingham [112, 113], fluid dynamicists highly value dimensionless numbers as they give a convenient way to express

the control and output parameters of a process. It is common to express these numbers as ratios of different force, time, or length scales [16]. Figure 3 illustrates the relevant forces (inertia, capillarity, and viscosity) that we will discuss throughout this thesis and the associated timescales: visco-capillary ($\tau_{\eta\gamma}$), inertio-capillary ($\tau_{\rho\gamma}$), inertio-viscous ($\tau_{\rho\eta}$), and inertial (τ_I), defined as

$$\tau_{\eta\gamma} = \frac{\eta\mathcal{L}}{\gamma}, \quad \tau_{\rho\gamma} = \sqrt{\frac{\rho\mathcal{L}^3}{\gamma}}, \quad \tau_{\rho\eta} = \frac{\rho\mathcal{L}^2}{\eta}, \quad \tau_I = \frac{\mathcal{L}}{V}. \quad (1)$$

Here, V and \mathcal{L} are the relevant velocity and length scales associated with the flow, whereas ρ , γ , and η are the material properties of the fluid, namely, density, surface tension coefficient, and viscosity, respectively. The visco-capillary timescale ($\tau_{\eta\gamma}$) is associated with capillary driving and viscous resistance, for example, thinning of a viscous liquid thread [114]. The inertio-capillary timescale ($\tau_{\rho\gamma}$) measures the duration of processes driven by capillary and resisted by inertia, for example, it is the Rayleigh timescale for the breakup of an inviscid fluid jet or that of capillary oscillations of a freely suspended liquid drop [115]. Furthermore, the inertio-viscous timescale ($\tau_{\rho\eta}$) estimates the duration of processes involving inertia and viscous stresses, for example, the development of boundary layers during drop impact [116]. Lastly, the inertial timescale (τ_I) is associated with flows involving only inertia, for example, inertial shock that follows the impact of an inviscid drop [62].

Using the above-mentioned timescales, we define several dimensionless numbers and use them throughout this thesis. The square of the ratio of the inertio-capillary to inertial timescales gives the Weber number (chapters 1–5),

$$We = \left(\frac{\tau_{\rho\gamma}}{\tau_I} \right)^2 = \frac{\rho V^2 \mathcal{L}}{\gamma}, \quad (2)$$

that compares the inertia and capillary stresses. Furthermore, the ratio of inertio-viscous to inertial timescale defines the Reynolds number,

$$Re = \frac{\tau_{\rho\eta}}{\tau_I} = \frac{\rho V \mathcal{L}}{\eta}, \quad (3)$$

that compares the inertial and viscous stresses. Moreover, taking the ratio of visco-capillary and inertial timescales gives the capillary number (chapter 5),

$$Ca = \frac{\tau_{\eta\gamma}}{\tau_I} = \frac{\eta V}{\gamma}. \quad (4)$$

Next, we can also take the ratios of the compound timescales (inertio-capillary to inertio-viscous or visco-capillary to inertio-capillary) to define the Ohnesorge number (used in all chapters),

$$Oh = \frac{\tau_{\rho\gamma}}{\tau_{\rho\eta}} = \frac{\tau_{\eta\gamma}}{\tau_{\rho\gamma}} = \frac{\eta}{\sqrt{\rho\gamma\mathcal{L}}}, \quad (5)$$

named after the German fluid dynamicist, Wolfgang von Ohnesorge. We refer the readers to McKinley and Renardy [117] to learn more about this less-known “numberman” of fluid dynamics. The Ohnesorge number requires special mention because it entails a convenient way of involving all the three relevant forces (inertia, capillary, and viscous) in any free-surface fluid dynamics problem (see figure 3). Furthermore, we use it as a proxy to estimate the importance of viscous dissipation throughout this thesis. Indeed, in all the capillary-driven processes (drop oscillation, retraction, and take-off in chapters 1–4, and rupture and bursting in chapters 5–6), a large Ohnesorge number ($Oh \gg 1$) implies dominance of viscous stresses.

It is also common to use the Laplace number, La , defined as

$$La = \frac{\rho\gamma\mathcal{L}}{\eta^2} = \frac{1}{Oh^2} \quad (6)$$

which is conceptually similar to the Ohnesorge number [117].

Of course, introducing forces other than the ones mentioned in figure 3 will add more dimensionless numbers to the list mentioned above. For example, the Bond number (chapter 2), given by,

$$Bo = \frac{\rho g \mathcal{L}^2}{\gamma} \quad (7)$$

compares gravity to the capillary forces, where g is the acceleration due to gravity. Furthermore, yield stress (σ_y) of viscoplastic fluids is often characterized using the plastocapillary number (chapter 6), defined as,

$$\mathcal{J} = \frac{\sigma_y \mathcal{L}}{\gamma} \quad (8)$$

that compares the yield and capillary stresses.

Lastly, geometric features and constraints can also enrich the number of dimensionless numbers. For example, for the case of binary drop impact [81, 82], the offset d between the two droplets can be non-dimensionalized using the relevant length scale (for example, drop's radius), giving the dimensionless offset parameter as (chapter 4)

$$\chi = \frac{d}{\mathcal{L}}. \quad (9)$$

Another example can be found for the case of drop impact on liquid films (chapter 3 and Tang et al. [118]) where the dimensionless film thickness can be given as

$$\Gamma = \frac{h_f}{\mathcal{L}}, \quad (10)$$

where h_f is the thickness of the film.

We can use the dimensionless numbers described above to illustrate the region of interest in different fluid dynamics processes. Figure 4 exemplifies one such operating parameter space for drop-on-demand inkjet printing in terms of the Ohnesorge number Oh (that involves only material properties, equation (5)) and Reynolds number Re (that involves both flow and material properties, equation (3)). Readers are referred to Lohse [16] for a detailed review and the state-of-the-art of inkjet printing process.

A guide through the thesis

In this thesis, we will investigate the role of viscous stresses on several free-surface processes. Here, we provide a guide through the thesis and the key questions that we ask in each chapter.

In **chapter 1**, we study the normal force profile of water drops (fixed Ohnesorge number Oh) impacting superhydrophobic surfaces. We vary We

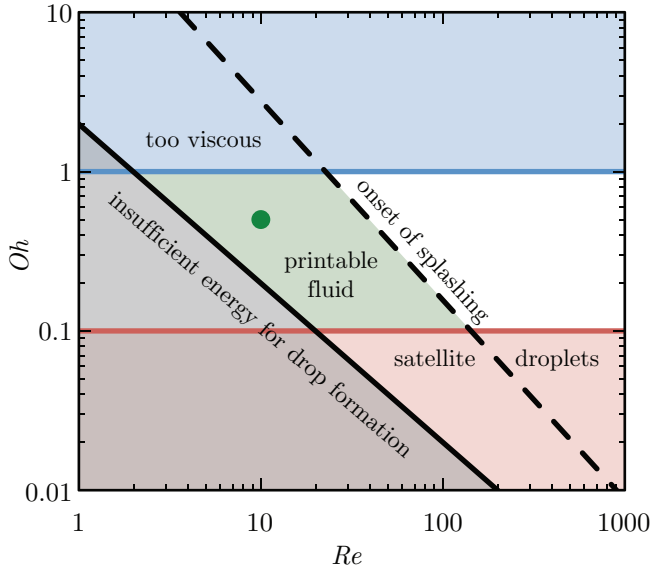


Figure 4: Parameter space in terms of Ohnesorge number Oh and Reynolds number Re showing the operating regime for stable drop-on-demand inkjet printing (green shaded area). The green dot corresponds to the material properties of a typical ink under standard operating conditions. The drop needs sufficient kinetic energy to eject out of the nozzle requiring that $We > 4$ or $Re \geq 2/Oh$ [119]. In terms of the material properties of the ink, printing will fail if the ink is too viscous ($Oh \geq 10$) or if satellite drops form ($Oh \leq 1/10$) [120–122]. Lastly, the criterion for the onset of splashing is given by $OhRe^{5/4} \geq 50$ following the work of Derby [123, also see chapter 1] and further restricts the printable region for inkjet printers. Similar parameter space for inkjet printing is also available in Lohse [16], McKinley and Renardy [117], Derby [123], von Ohnesorge [124]. This figure is reproduced from Lohse [16] with permission from the author.

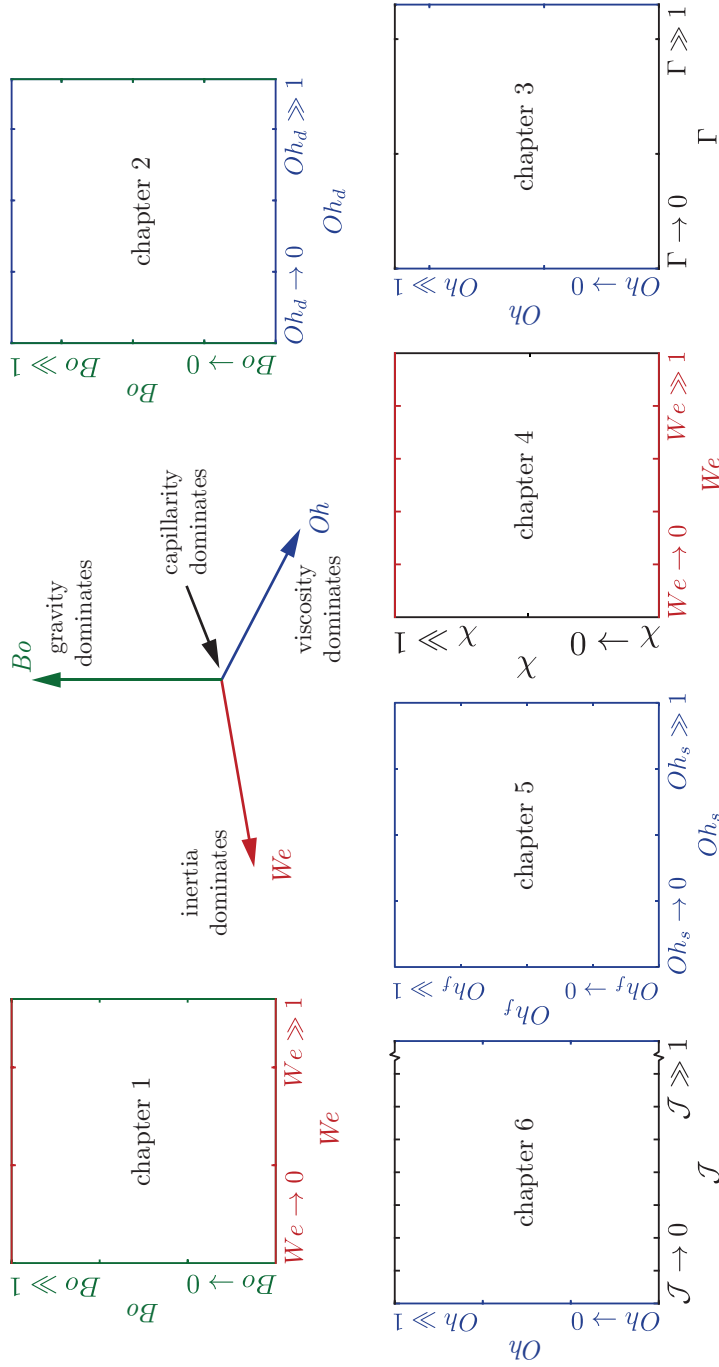


Figure 5: Dimensionless numbers used in the present thesis. The Weber number We (equation (2)), the Bond number Bo (equation (7)), and the Ohnesorge number Oh (equation (5)) are the three central dimensionless numbers that respectively compare inertial, gravity, and viscous and inertial to capillary stresses. In the subsequent chapters, we will keep at least one of these numbers as a control parameter. We also stress that we use the Oh as a proxy for viscous dissipation throughout the thesis. Additionally, we use the dimensionless film thickness Γ (equation (10)) in chapter 3, dimensionless offset χ (equation (9)) between the two drops in chapter 4, and the plasto-capillary number \mathcal{J} (equation (8)) in chapter 6. In conclusion to this thesis (figure C1), we redraw this figure with the filled-in regime maps for each chapter.

(equation (2)) and Bo (equation (7)), see figure 5, to answer the following questions:

Chapter 1

1. What sets the magnitude of the normal reaction force between the impacting drop and the non-wetting substrate?
2. What sets the timescales associated with the normal reaction force?

In **chapter 2**, we investigate how viscous stresses and gravity conspire against capillarity to inhibit drop bouncing off non-wetting substrates by varying Oh (equation (5)) and Bo (equation (7)), see figure 5. We ask the following questions:

Chapter 2

1. When does a drop stop bouncing?
2. How does a viscous drop stop bouncing?
3. How does a heavy drop stop bouncing?

In this chapter, we also vary the We (equation (2)) to study its effect on the bouncing to non-bouncing transition in the Bo - Oh parameter space.

In **chapter 3**, we investigate drops bouncing off viscous liquid films that mimic atomically smooth substrates. The repellent behavior of such substrates requires the presence of an air layer trapped between it and an impacting drop. This work varies the Oh (equation (5)) of both the drop and the film and Γ (equation (10)) to answer the following questions (figure 5):

Chapter 3

1. What happens when a liquid drop bounces off an atomically smooth deformable substrate?
2. How does the presence of a viscous film affect the bouncing inhibition discussed in chapter 2?

In **chapter 4**, we probe how to lift a sessile oil drop with an impacting one. This chapter is a natural extension to chapter 3 where we studied drop impact on flat (zero curvature) films. In this chapter, we study similar impacts on a finite curvature sessile drop at different We (equation (2)). We

also vary the offset χ (equation (9)) between the impacting and sessile drops to comprehensively study the drop-on-drop impact process and focus on the following key questions (figure 5):

Chapter 4

1. What is the energy transfer between the two drops when an impacting drop hits a sessile one?
2. Can a moving-impact drop lift a lazy sessile drop sitting on a non-wetting substrate?

In **chapter 5**, we elucidate the influence of the surroundings on Taylor-Culick retractions by exploring three canonical configurations: the classical Taylor-Culick retractions and the generalized ones, namely those fully submerged in an oil bath, and those occurring at an oil-air interface. We vary the Oh (equation (5)) associated with both the film and the surroundings (figure 5) and seek answers to the following questions:

Chapter 5

1. Does the inertia of the surrounding medium matter during capillary driven retraction of liquid films?
2. How does viscous dissipation influence film retraction?
3. Where does the bulk of viscous dissipation occur during the Taylor-Culick retraction of films?

In **chapter 6**, we study how viscoplasticity controls the fate of a bubble bursting at a free surface by varying Oh (equation (5)) and \mathcal{J} (equation (8)), see figure 5. The chapter answers the following questions:

Chapter 6

1. How do viscosity and viscoplasticity influence the capillary-driven bursting of the bubble at a liquid-gas free-surface?
2. Can a liquid-gas free surface sustain non-zero surface energies in the presence of yield stress?

The thesis ends with a conclusion and outlook section where we redraw figure 5 with the filled-in regime maps for each chapter and summarize the answers to all the questions posed above.

Part I

Drop Impact

Chapter 1

Impact forces of water drops falling on superhydrophobic surfaces^o

A falling liquid drop, after impact on a rigid substrate, deforms and spreads, owing to the normal reaction force. Subsequently, if the substrate is non-wetting, the drop retracts and then jumps off. As we show here, not only is the impact itself associated with a distinct peak in the temporal evolution of the normal force, but also the jump-off, which was hitherto unknown. We characterize both peaks and elucidate how they relate to the different stages of the drop impact process. The time at which the second peak appears coincides with the formation of a Worthington jet, emerging through flow-focusing. Even low-velocity impacts can lead to a surprisingly high second peak in the normal force, even larger than the first one, namely when the Worthington jet becomes singular due to the collapse of an air cavity in the drop.

^oSubmitted as: Bin Zhang, **Vatsal Sanjay**, Songlin Shi, Yinggang Zhao, Cunjing Lv, Xi-Qiao Feng, and Detlef Lohse, *Impact forces of water drops falling on superhydrophobic surfaces*, Phys. Rev. Let. (2022). Experiments are done by Zhang and Lv; simulations by Sanjay; analysis and writing by Zhang, Sanjay, Lv, and Lohse; and supervision by Lv and Lohse. Proofread by everyone.

1.1 Introduction

In 1876–77, Arthur Mason Worthington [14, 15] published the first photographs of the drop impact process, stimulating artists and researchers alike for an almost one-and-a-half century. Such drop impacts on solid surfaces are highly relevant from an application point of view, namely in inkjet printing [16], spray coating [17], criminal forensics [22], and many other industrial and natural processes [41, 42, 45]. For most of these applications, the drop impact forces, which are the subject of this chapter, can lead to serious unwanted consequences, such as soil erosion [58] or the damage of engineered surfaces [59–61]. A thorough understanding of the drop impact forces is thus needed to develop countermeasures against these damages [62]. Consequently, recent studies have analyzed the temporal evolution of these forces [26, 27, 125–129].

These studies were, however, up to now limited to wetting scenarios. Then, not surprisingly, the moment of the drop touch-down [25, 26] manifests itself in a pronounced peak in the temporal evolution of the drop impact force, whereas this force is much smaller during droplet spreading [30, 41]. For the non-wetting case, i.e., for superhydrophobic surfaces, the drop impact dynamics is much richer: then, after reaching its maximal diameter, the drop recoils [130] and can generate an upward, so-called Worthington jet [14, 44]. Ultimately, the drop can even ricochet off the superhydrophobic surface [131]. Such spectacular water repellency can occur in nature [49, 50, 132], and has various technological applications [133–137], including on moving substrates [138], where the droplet dynamics is even richer. This feature of superhydrophobicity however is volatile and can fail due to external disturbance such as pressure [49–52], evaporation [53–55], mechanical vibration [56], or the impact forces of prior droplets [57].

This chapter extends the studies on drop impact forces to the impact on superhydrophobic surfaces. Our key result is that then, next to the first above-mentioned peak in the drop impact force at drop touch-down, a *second peak* in the drop impact force occurs, which under certain conditions can be even more pronounced than the first peak. The physical origin of the second peak lies in momentum conservation: when at the final phase of droplet recoil, the above-mentioned upward Worthington jet forms, momentum conservation also leads to a downward jet inside the drop [139–142]. It manifests itself in the second peak in the temporal evolution of the force on the substrate. Using both experiments and direct numerical simulations (DNS) with the volume-of-fluid method [143], we will elucidate the physics of this very rich dynamical

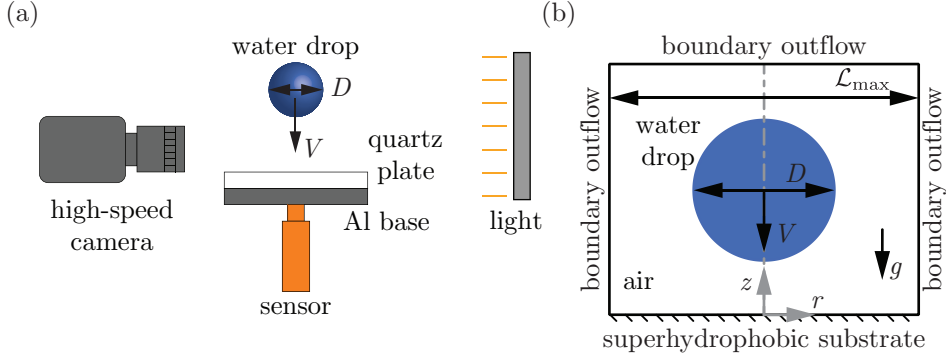


Figure 1.1: (a) Experimental setup: a water drop of diameter D impacts a superhydrophobic quartz plate at velocity V . (b) Axi-symmetric simulation domain with the appropriate boundary conditions and relevant material and flow properties. The boundaries are kept far away from the drop to avoid feedback ($\mathcal{L}_{\max} \gg D$).

process and study its dependence on the control parameters.

This chapter is organized as follow: § 1.2 briefly describes the experimental and numerical setups followed by § 1.3 that correlates the temporal variation of the normal reaction with different stages of the drop impact process. We then elucidate the dependence of Weber number on the characteristic times (§ 1.4) and the two peaks in the transient normal reaction force (§ 1.5 and 1.6). The chapter culminates in conclusions and an outlook in § 1.7.

1.2 Setup

The experimental setup is sketched in figure 1.1(a). A water drop impacts a quartz plate whose upper surface is coated with silanized silica nanobeads with diameter of 20 nm (Glaco Mirror Coat Zero; Soft99) [52, 144] to attain superhydrophobicity. We directly measure the impact force $F(t)$ by synchronizing high-speed photography with fast force sensing (also see § 1.A for details of the experimental setup).

In DNS (figure 1.1b), ideal superhydrophobicity is maintained by assuming that a thin air layer is present between the drop and the substrate [145, also see chapters 2, and 4], and forces are calculated by integrating the pressure field (p) at the substrate,

$$\mathbf{F}(t) = F(t)\hat{\mathbf{z}} = \left(\int_{\mathcal{A}} (p - p_0) d\mathcal{A} \right) \hat{\mathbf{z}}, \quad (1.1)$$

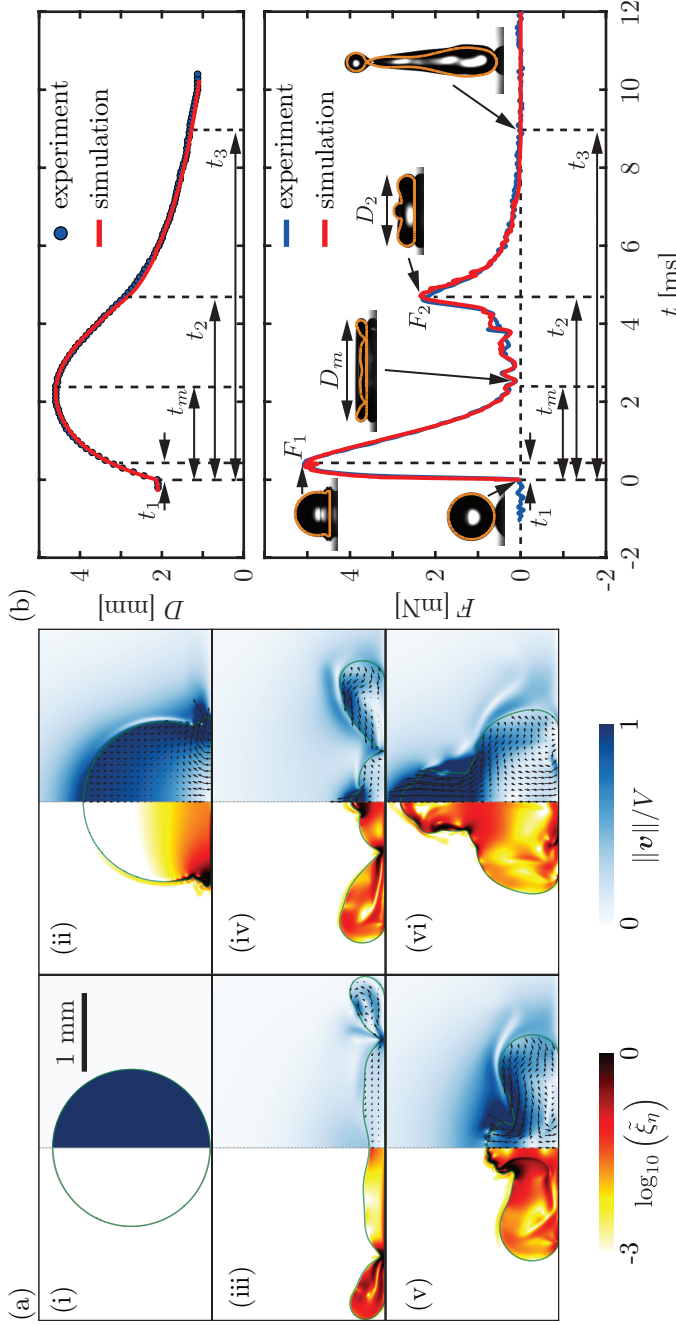


Figure 1.2: (a) Numerical results for a drop impact dynamics for a $D = 2.05$ mm diameter water drop falling at a speed of $V = 1.20$ m/s: $t =$ (i) 0 ms (touch-down), (ii) 0.37 ms, (iii) 2.5 ms, (iv) 3.93 ms, (v) 4.63 ms, and (vi) 5.25 ms. The left part of each numerical snapshot shows the dimensionless viscous dissipation function, ξ on a \log_{10} scale and the right part the velocity field magnitude normalized with the impact velocity. The black velocity vectors are plotted in the center of mass reference frame of the drop to elucidate the internal flow. (b) Spreading diameter $D(t)$ and impact force $F(t)$ on the substrate as function of time: comparison between experiments and simulations ($W\epsilon = 40$). The insets show representative snapshots at specific time instants overlaid with the drop boundaries from simulations in orange, revealing good agreement. $F_1 \approx 5.1$ mN and $F_2 \approx 2.3$ mN are the two peaks of the normal force $F(t)$ at $t_1 \approx 0.37$ ms and $t_2 \approx 4.63$ ms, respectively. t_m is the moment corresponding to the maximum spreading of the drop and t_3 represents the end of contact ($F = 0$). D_m and D_2 are the spreading diameters of the drop at t_m and t_2 , respectively. Also see supplemental movie 1.

where p_0 is the ambient pressure. Furthermore, \mathcal{A} and $\hat{\mathbf{z}}$ are the area of the superhydrophobic substrate and a unit vector perpendicular to it, respectively (also see appendix 1.B for details of the simulation setups).

The initial drop diameter D ($2.05 \text{ mm} \leq D \leq 2.76 \text{ mm}$)[○] and the impact velocity V ($0.38 \text{ m/s} \leq V \leq 2.96 \text{ m/s}$) are independently controlled. The drop material properties are kept constant (density $\rho_d = 998 \text{ kg/m}^3$, surface tension coefficient $\gamma = 73 \text{ mN/m}$, and dynamic viscosity $\eta_d = 1.0 \text{ mPas}$). All experiments were carried out at ambient air pressure and temperature. The Weber number (ratio of drop inertia to capillary pressure) $We \equiv \rho_d V^2 D / \gamma$ ranges between 1 – 400 and the Reynolds number (ratio of inertial to viscous stresses) $Re \equiv \rho_d V D / \eta_d \approx 800$ to 10^5 . Note that for our simulations, we keep the drop Ohnesorge number (ratio of inertio-capillary to inertio-viscous timescales) $Oh \equiv \eta_d / (\rho_d \gamma D)^{1/2}$ constant at 0.0025 to mimic 2 mm diameter water drops.

1.3 Formation of a second peak in the force

In this section, we elucidate the temporal variation of the normal reaction force and the corresponding drop impact dynamics. Figure 1.2(a) illustrates the different stages of the drop impact process for $We = 40$, and figure 1.2(b) quantifies the spreading diameter $D(t)$ (maximum width of the drop at time t) and the normal force $F(t)$ (also see supplemental movie 1). Note the remarkable quantitative agreement between the experimental and the numerical data for both $D(t)$ and $F(t)$, giving credibility to both. As the drop touches the surface (figure 1.2a-i), the normal force $F(t)$ increases sharply to reach the first peak with amplitude $F_1 \approx 5.1 \text{ mN}$ in a very short time $t_1 \approx 0.37 \text{ ms}$ (figure 1.2a-ii). At this instant, the spreading diameter $D(t)$ is equal to the initial drop diameter D , $D(t_1) \approx D$ [26, 27, 127–129]. Subsequently, the normal force reduces at a relatively slow rate to a minimum ($\approx 0 \text{ mN}$) at $t_m \approx 2.5 \text{ ms}$. Meanwhile the drop reaches a maximum spreading diameter $D(t_m) = D_m$ (figure 1.2a-iii). The force profile $F(t)$, until this instant, is very close to that on a hydrophilic surface (see § 1.C). However, contrary to the wetting scenario, on superhydrophobic substrates, the drop starts to retract, creating high local viscous dissipation in the neck region connecting the drop with its rim (figure 1.2a-iii,iv). Through this phase of retraction, the normal reaction

[○]Note that we use diameter of the drop as the length scale in this chapter contrary to its radius that we use throughout this thesis. We do so for ease of comparison with the earlier work of Gordillo et al. [27], see figures 1.3 and 1.4.

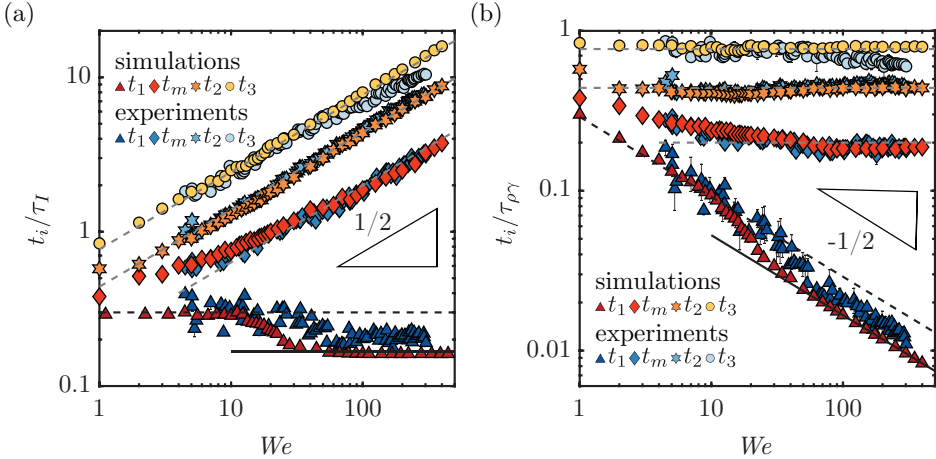


Figure 1.3: Characteristic times as functions of the Weber number We . The times t_1 , t_m , t_2 , and t_3 are normalized by the inertial timescale $\tau_I = D/V$ in panel (a), or by the inertia-capillary timescale $\tau_{\rho\gamma} = (\rho_d D^3 / \gamma)^{1/2}$ in panel (b). The black dashed and solid lines represent $t_1 \sim \tau_I$. The black dashed and solid lines represent $t_1 \approx 0.3\tau_I$ and $t_1 \approx 1/6\tau_I$, respectively. The gray dashed lines show the best straight line fits to the experimental data, $t_m \approx 0.20\tau_{\rho\gamma}$, $t_2 \approx 0.44\tau_{\rho\gamma}$, and $t_3 \approx 0.78\tau_{\rho\gamma}$.

force is small, but shows several oscillations owing to traveling capillary waves for $2.5 \text{ ms} < t < 3.8 \text{ ms}$ (figure 1.2b). The drop retraction and the traveling capillary waves lead to flow focusing at the axis of symmetry, creating the Worthington jet (figure 1.2a-iv,v) and hence also the opposite momentum jet that results in an increase in the normal force $F(t)$. Consequently, the hitherto unknown second peak appears, here with an amplitude $F_2 \approx 2.3 \text{ mN}$ and at time $t_2 \approx 4.63 \text{ ms}$. Lastly, the normal force $F(t)$ decays slowly (figure 1.2a-v,vi) to zero, finally vanishing at $t_3 \approx 8.84 \text{ ms}$. This time instant t_3 is a much better estimate for the drop contact time as compared to the one observed at complete detachment from side view images which is about 2 ms longer in this case [131, 146]. Therefore, in summary, here we have identified the mechanism for the formation of the second peak in the normal force and four different characteristic times, t_1 , t_m , t_2 , and t_3 (figure 1.2b).

1.4 Weber number dependence of the characteristics times

Next, we look into the dependence of the four different characteristic times on the impact Weber number We . The instant t_1 of the first peak of the force

$F(t)$ scales with the inertial timescale (figure 1.3a), i.e., $t_1 \sim \tau_I = D/V$ with different We -dependent prefactors (≈ 0.3 at low and ≈ 0.167 at high We , respectively). The solid black line in figure 1.3(a) is the theoretical inertial prediction by Gordillo et al. [27], $t_1/\tau_I = 1/6$, and matches our experimental and in particular numerical data. As seen from figure 1.3, the other three characteristic times scale differently with We than t_1 . Specifically, t_2 and t_3 become independent of We when rescaled with the inertio-capillary time $\tau_\gamma = (\rho_d D_0^3 / \gamma)^{1/2}$ while t_m has a weak We -dependence at low We , and becomes We -independent only for $We \gtrsim 10$, see figure 1.3(b). The reason for this We -independent behavior is that the impact process is analogous to one complete drop oscillation [131] which is determined by the inertio-capillary time $\tau_{\rho\gamma}$ [115]. Maximum spreading (t_m) occurs at almost one-quarter of a full oscillation (consistent with our result $t_m \approx 0.20\tau_{\rho\gamma}$) whereas the complete contact time t_3 takes about one full oscillation (consistent with our result $t_3 \approx 0.78\tau_{\rho\gamma}$). Finally, the time instant $t_2 \approx 0.44\tau_{\rho\gamma}$ of the second peak in the impact force coincides with the time when the drop's motion changes from being predominantly radial to being vertical, as this moment is associated with the formation of the Worthington jet [147, p. 18-20]. Note that here for the impact on the superhydrophobic substrate, the duration of non-zero forces (e.g., for $We = 40$ we find $t_3/\tau_I \approx 5.2$, figure 1.2c) is much longer than that for the impact on a hydrophilic surfaces Gordillo et al. [27], Mitchell et al. [128], where for the same $We = 40$ one has $t_3/\tau_I \approx 2.0$ (also see § 1.C).

1.5 Influence of Weber number on the first peak

As the drop falls on a substrate, momentum conservation implies $F_1 \sim V(dm/dt)$, where the mass flux dm/dt can be calculated as $dm/dt \sim \rho_d V D^2$ [126]. As a result, $F_1 \sim \rho_d V^2 D^2$, as shown in figure 1.4(a) for high Weber numbers ($We > 30$, $F_1 \approx 0.81\rho_d V^2 D^2$). This asymptote also matches the experimental and theoretical results of similar studies conducted on hydrophilic substrates [27, 127]. Indeed, the first peak force originates from an inertial shock following the impact of drops onto an immobile substrate and is independent of the wettability. Further, the minimum Reynolds number for the current work is 800, which is well above the criterion ($Re > 200$) for viscosity-independent results [27, 127]. One would expect $\tilde{F}_1 \equiv F_1/\rho_d V^2 D^2$ to be constant throughout the range of our parameter space. Nonetheless, when $We < 30$, the data deviates from the inertial asymptote. Such deviations have been reported previously on hydrophilic surfaces as well [126]. Here, inertia is not the sole governing

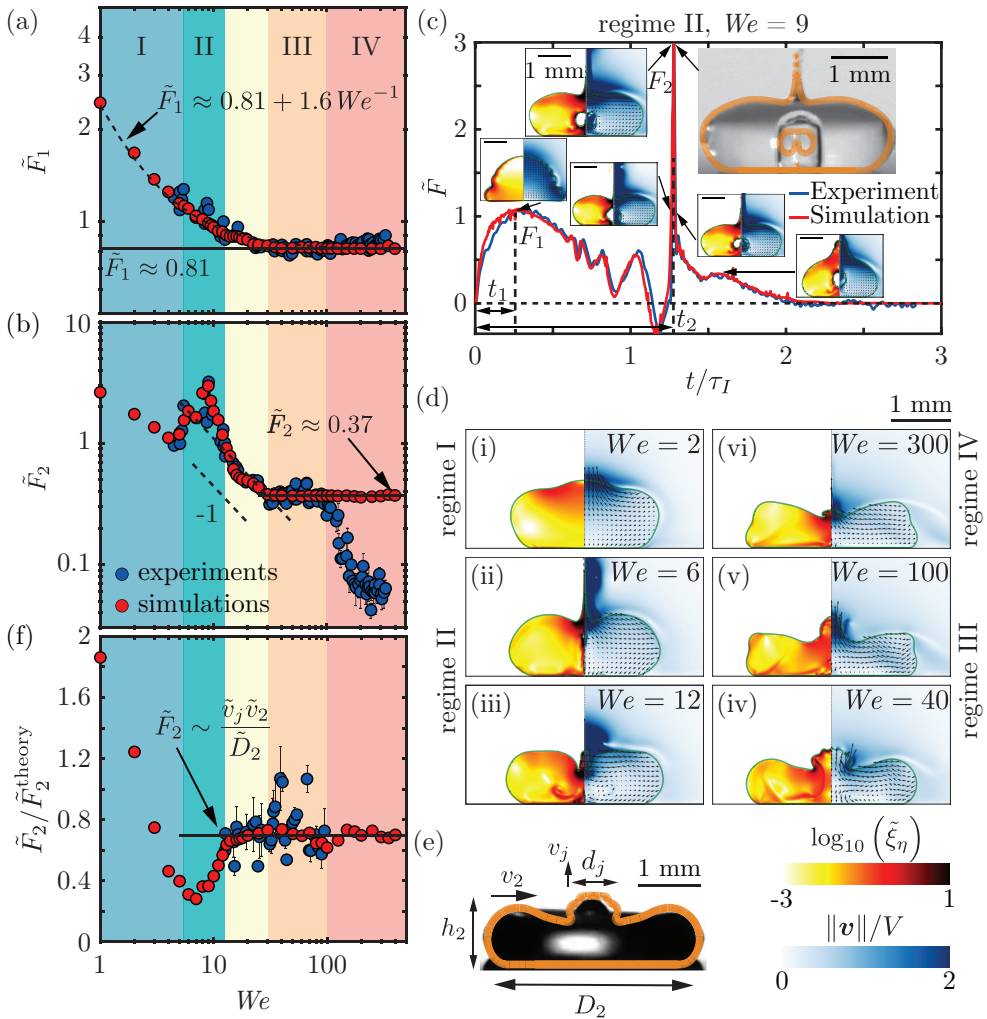


Figure 1.4: Dimensionless peak forces $\tilde{F}_i \equiv F_i / (\rho_d V^2 D^2)$, (a) \tilde{F}_1 , (b) \tilde{F}_2 as functions of We . For \tilde{F}_1 , the black dashed and solid lines represent $\tilde{F}_1 \approx 0.81 + 1.6We^{-1}$ and $\tilde{F}_1 \approx 0.81$, respectively. Using \tilde{F}_2 , we identify four regimes, I. Capillary ($We < 5.3$), II. Singular jet ($5.3 < We < 12.6$), III. Inertial ($30 < We < 100$), and IV. Splashing ($We > 100$). The black dotted and solid lines represent $\tilde{F}_2 \sim We^{-1}$ and $\tilde{F}_2 \sim We^0$, respectively. (c) Evolution of the normal force $F(t)$ of an impacting drop for the case with highest \tilde{F}_2 ($We = 9$). Note again the outstanding agreement between the experimental and the numerical results, including the various wiggles in the curve, which originate from capillary oscillations. Insets show drop morphology at specific time instants. (d) Snapshots at the instants of the second peak force (t_2) for $We =$ (i) 6, (ii) 12, (iii) 40, (iv) 100, and (v) 300. (e) Drop geometry at t_2 for $We = 40$ (along with the orange drop contour from numerics) to mark its spreading diameter D_2 , height h_2 , retraction velocity v_2 , jet diameter d_j and jet velocity v_j . (f) Comparison of the second peak force \tilde{F}_2 with its theoretical prediction $\tilde{F}_2^{\text{theory}} = \tilde{v}_j \tilde{v}_2 / \tilde{D}_2$ (equation. (1.3)).

force, and it competes with surface tension. We propose a generalization of the first peak of the impact force to $F_1 = \alpha_1 \rho_d V^2 D^2 + \alpha_2 (\gamma/D) D^2$, based on dimensional analysis, with α_1 and α_2 as free parameters. From the best fit to all the experimental and numerical data, we obtain $\tilde{F}_1 \approx 0.81 + 1.6 We^{-1}$, which well describes the data, see figure 1.4(a).

1.6 Influence of Weber number on the second peak

We now focus on the second peak F_2 of the impact force $F(t)$. In figure 1.4(b), we show the We -dependence of the non-dimensional version thereof, $\tilde{F}_2 \equiv F_2/(\rho_d V^2 D^2)$. We identify four main regimes, namely I. Capillary ($We < 5.3$), II. Singular jet ($5.3 < We < 12.6$), III. Inertial ($30 < We < 100$), and IV. Splashing ($We > 100$). The range $12.6 < We < 30$ marks the transition from the singular jet to the inertial regime.

In regime I ($We < 4.5$), the amplitude F_2 of the second peak is smaller than the resolution (0.5 mN) of our force transducer, so we cannot distinguish it in experiments. Capillary oscillations dominate the flow in this regime [40], leading to more than two peak forces, remarkably perfectly identical to what is observed in our simulations (see figure 1.4d-i and supplemental movie 2).

In regime II, with increasing We , there is a sharp increase in the amplitude \tilde{F}_2 of the second peak. A striking feature of this regime is that the magnitude of the second peak force exceeds that of the first one, $\tilde{F}_2 > \tilde{F}_1$, see figure 1.4(c) which illustrates the case with the highest second peak force ($\tilde{F}_2 = 2.98$, occurring for $We = 9$, supplemental movie 3). The large force amplitude in this regime correlates to the formation of an ultra-thin and high-velocity singular Worthington jet [44]. Here, the Worthington jet is most pronounced as it results from the collapse of an air-cavity as well as the converging capillary waves (see insets of figures 1.4c and 1.4d-ii, iii). It is reminiscent of the hydrodynamic singularity that accompanies the bursting of bubbles at liquid-gas interfaces [see § chap:BurstingBubbleVP and 148, 149]. Outside regime II such bubbles do not form, see figure 1.4(d-iii – d-v). Consistent with this view, the case with maximum peak force ($We = 9$, figure 1.4b) entrains the largest bubble. Another characteristic feature of this converging flow is that, despite having a small Ohnesorge number (= 0.0025) that is often associated with inviscid potential flow inside the drop [150], it still shows high rates of local viscous dissipation near the axis of symmetry (figures 1.4c insets and 1.4(d-i – d-iii)), due to the singular character of the flow (also see supplemental movie 4).

When We is further increased, we (locally) find $\tilde{F}_2 \sim We^{-1}$ in the tran-

sition regime ($12.6 < We < 30$), followed by $\tilde{F}_2 \sim We^0$ in the inertial regime III ($30 < We < 100$). Specifically, by employing best fits, we obtain

$$\tilde{F}_2 = \frac{F_2}{\rho_d V^2 D^2} \approx \begin{cases} 11 We^{-1} & (12.6 < We < 30), \\ 0.37 & (30 < We < 100). \end{cases} \quad (1.2)$$

We will now rationalize this experimentally and numerically observed scaling behavior of the amplitude F_2 of the second peak using scaling arguments. As already mentioned, figure 1.4(d) shows that the second peak in the force at t_2 coincides with an upwards jet, which has typical velocity v_j (see § 1.E for calculation details) and typical diameter d_j , figure 1.4(e). Figure 1.4(d) also illustrates strong radially symmetric flow focusing due to the retracting drop in regimes II and III. We define the recoiling velocity of the drop at time t_2 as v_2 , the droplet height at that moment as h_2 , and the droplet diameter at that moment as $D_2 = D(t_2)$, see again figure 1.4(e). Note that regime II also includes stronger converging capillary waves and the collapsing air cavity (figure 1.4c insets and Fig. 1.4d-i,ii). The presence of the substrate breaks the symmetry in vertical direction, directing the flow into the Worthington jet. Using continuity and balancing the volume flux at this instant t_2 , we obtain $v_2 D_2 h_2 \sim v_j d_j^2$. Of course, D_2 and h_2 are also related by volume conservation. Assuming a pancake-type shape at t_2 , we obtain $D_2^2 h_2 \sim D^3$ [30] and therefore, $v_j d_j^2 \sim v_2 D^3 / D_2$. As the drop retracts, the velocity of the flow field far away from the jet is parallel to the base (figure 1.4d). So, the occurrence and strength of the second peak F_2 is mainly a result of the flow opposite to the vertical Worthington jet (figure 1.4c-iii – c-v), which naturally leads to $F_2 \sim \rho_d v_j^2 d_j^2$ (momentum flux balance in the vertical direction). Combining the above arguments, we get $F_2 \sim \rho_d v_j v_2 D^3 / D_2$ which can be non-dimensionalized with the inertial pressure force $\rho_d V^2 D^2$ to obtain

$$\tilde{F}_2 = \frac{F_2}{\rho_d V^2 D^2} \sim \frac{\tilde{v}_j \tilde{v}_2}{\tilde{D}_2}, \quad (1.3)$$

where, $\tilde{v}_j = v_j/V$, $\tilde{v}_2 = v_2/V$, and $\tilde{D}_2 = D_2/D$ are the dimensionless jet velocity, drop retraction velocity, and spreading diameter, respectively, all at t_2 .

Figure 1.4(f) compares the amplitude of the second peak as obtained from the experiments and simulations with the theoretical prediction of equation (1.3) (also see § 1.E). Indeed, this scaling relation reasonably well describes the transitional regime II-III and regime III data. Obviously, in regime I, the theoretical prediction is invalid because the hypothesis of flow focusing

breaks down, and capillary oscillations dominate the flow, with no Worthington jet occurring. Further, equation (1.3) over-predicts the forces in regime II because efficient capillary waves focusing and air cavity collapse lead to extremely high-velocity singular jets. The entrained air bubble also shields momentum transfer from the singular Worthington jet to the substrate (insets of figure 1.4c).

We finally come to the very large impact velocities of regime IV. Then, when $We \gtrsim 100$, in the experiments splashing occurs [42], see supplemental movie 5. At such high We , the surrounding gas atmosphere destabilizes the rim [116, 151]. Therefore, in regime IV, kinetic and surface energies are lost due to the formation of satellite droplets, resulting in diminishing \tilde{F}_2 in the experiments (figure 1.4b). In contrast, for our axisymmetric (by definition) simulations, the above-mentioned azimuthal instability is absent [116] and the plateau $\tilde{F}_2 \approx 0.37$ continues in this regime. Consequently, equation (1.3) holds only for the simulations in regime IV (figure 1.4f), and not for the experiments. Further analysis of the experimentally observed fragmentation scenario is beyond the scope of the present work. For future work, we suggest that one could also experimentally probe F_2 in this regime by suppressing the azimuthal instability (for instance, by reducing the atmospheric pressure [152]).

1.7 Conclusions and outlook

In this chapter, we have experimentally obtained the normal force profile of water drops impacting superhydrophobic surfaces. To elucidate the physics and study the internal flow, we used direct numerical simulations, which perfectly match the experimental results without any fitting parameter. In the force profile, we identified two prominent peaks. The first peak arises from an inertial shock following the impact of the impacting drop onto the immobile substrate. The hitherto unknown second peak occurs before the drop rebounds. The variation of the amplitude of this peak with Weber number results in four distinct regimes, namely the capillary, singular jet, inertial, and splashing regime. This peak in the force occurs due to the momentum balance when the Worthington jet is created by flow focusing, owing either to capillary waves (singular jet regime) or drop retraction (inertial regime). Surprisingly, even a low Weber number impact (singular jet regime) can lead to a highly enhanced peak in the force profile, triggered by the collapse of an air cavity. Lastly, we have derived scaling relations for these peak forces. Our

results thus give a fundamental understanding of the drop impact dynamics on a non-wetting surface and the forces associated with it. Such insight is crucial to develop countermeasures to the failure of superhydrophobicity in technological applications (for e.g., by avoiding the regime $5.3 < We < 12.6$ or reducing the spacing of the textures [49]). Interesting and relevant extensions of our work include the study of impact forces of viscous drops, which will show quite different scaling behavior [153], and of Leidenfrost drops [6].

Acknowledgments

We thank Marie-Jean Thoraval, Uddalok Sen, and Pierre Chantelot for stimulating discussions.

Appendix

1.A Experimental method

Figure 1.A.1a illustrates the experimental setup that consists of four main units: a drop generation unit, a superhydrophobic substrate, a force measurement unit and a high-speed photography unit (also see figure 1.1a).

1.A.1 Drop generation unit

The drop generation unit is used to create drops of different sizes and impact velocities independently (initial drop diameter D ($2.05\text{ mm} \leq D \leq 2.76\text{ mm}$) and the impact velocity V ($0.38\text{ m/s} \leq V \leq 2.96\text{ m/s}$)). Deionized water drops are created by employing suspended needles that are connected to a syringe pump. To suppress disturbances, the drop is created at a very smooth flow rate, i.e., 0.5 mL/min . The drop diameter is varied by employing needles of different sizes, and the impact velocity is controlled by changing the distance between the needle and the sample by employing a vertical translation stage.

1.A.2 Superhydrophobic substrate

A water drop impacts a quartz plate whose upper surface is coated with silanized silica nanobeads with diameter of 20 nm (Glaco Mirror Coat Zero; Soft99) [52, 144] to attain superhydrophobicity (figure 1.A.1b). The advancing and receding contact angles of water drops are $167^\circ \pm 2^\circ$ and $154^\circ \pm 2^\circ$, respectively.

1.A.3 Force measurement unit

The core apparatuses of the force measurement unit include a sample, a high-precision transducer, a charge amplifier and a data acquisition system. The

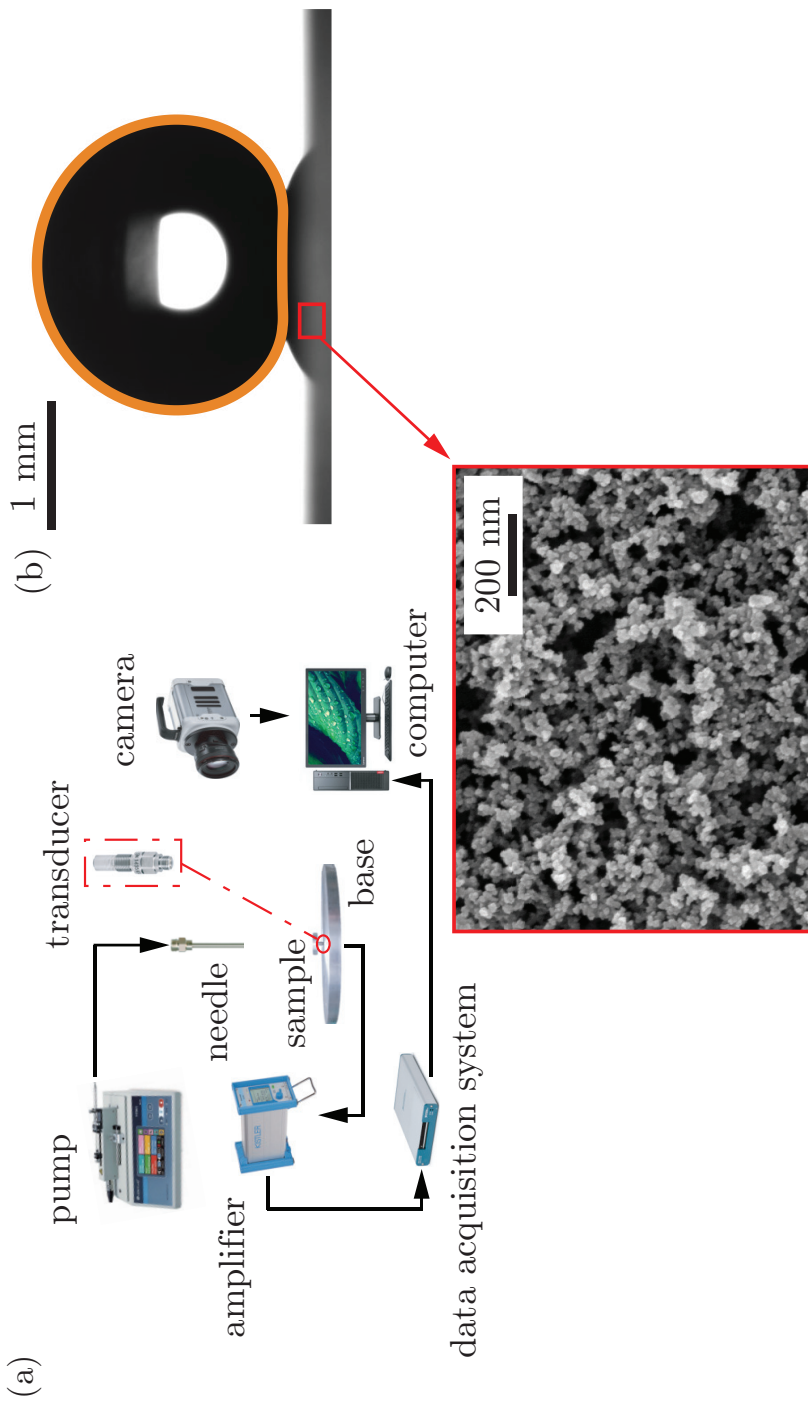


Figure 1.A.1: (a) Experimental setup, consisting of four main units: a drop generation unit, a superhydrophobic substrate, a force measurement unit, and a high-speed photography unit. Relevant appurtenant devices are shown. Also see figure 1.1(a). (b) Snapshot of a water drop sitting on a superhydrophobic substrate with overlaid orange boundary from simulation. The inset shows the scanning electron microscopy (SEM) image of the superhydrophobic surface covered by hydrophobic nanoparticles.

lower surface of the quartz plate is glued to an aluminum base, which is screwed vertically into a high-precision piezoelectric force transducer (Kistler 9215A) with a resolution of 0.5 mN. The impact force between the drop and the sample is measured by the collection of the charge generated by the transducer, and the charge is immediately converted into a voltage by employing an amplifier (Kistler 5018A). Comparing to the weak charge signal that is sensitive to the environment noise (such as triboelectricity due to the movement of the cable, or magnetic fields in the environment, etc.), the amplified voltage signal is more robust for transmitting and processing. After that, the amplified analog signals are converted into the digital signals by employing a data acquisition system (NI USB-6361 driven by Labview) at a sampling rate of 100 kHz. Finally, the unit of the measured signal is changed from Voltage (V) to Newton (N) via the calibration coefficient of the force transducer.

In our experiment, high-frequency vibrations of the experimental setup are inevitably induced by the drop impact, and they will superimpose on the temporal evolution of the impact force. Based on a well-designed method [125], the influences resulting from these high-frequency vibrations have been successfully removed by employing a low pass filter (with a cut-off frequency of 5 kHz).

1.A.4 High-speed photography

Lastly, the fast force sensing technique described above is synchronized with the high-speed photography unit containing a high-speed camera (Photron Fastcam Nova S12) and a micro Nikkor 105 mm f/2.8 imaging lens. To realize a synchronization of the evolution of the drop morphology and the transient force, the high-speed camera is triggered by the data acquisition system when the impact force is larger than 1 mN. A LED light (CLL-1600TDX) of adjustable output power is used to illuminate the scene of the impingement. We efficiently record the drop impact phenomenon at 10,000 fps with a shutter speed 1/20,000 s.

1.B Numerical method

This section elucidates the direct numerical simulation framework used to study the drop impact process (figure 1.1b) using the free software program, Basilisk C [143].

1.B.1 Governing equations

For an incompressible flow, the mass conservation requires the velocity field to be divergence-free ($\nabla \cdot \mathbf{v} = 0$). Furthermore, the momentum conservation reads

$$\frac{\partial(\rho\mathbf{v})}{\partial t} + \nabla \cdot (\rho\mathbf{v}\mathbf{v}) = -\nabla p' - [\rho](\mathbf{g} \cdot \mathbf{z}) \hat{\mathbf{n}}\delta_s + \nabla \cdot (2\eta\mathcal{D}) + \mathbf{f}_\gamma. \quad (1.4)$$

Here, the terms on the left hand side represent momentum advection. On the right hand side, the deformation tensor, \mathcal{D} is the symmetric part of the velocity gradient tensor ($\mathcal{D} = (\nabla\mathbf{v} + (\nabla\mathbf{v})^T)/2$). Further, p' denotes reduced pressure field, $p' = p - \rho\mathbf{g} \cdot \mathbf{z}$, where, p and $\rho\mathbf{g} \cdot \mathbf{z}$ represent the mechanical and the hydrostatic pressures, respectively, with \mathbf{g} and $\mathbf{z} = z\hat{\mathbf{z}}$ representing the gravitational acceleration and the vertical coordinate vectors, respectively (z is the distance away from the superhydrophobic substrate and $\hat{\mathbf{z}}$ is a unit vector, see figure 1.1b). Using this reduced pressure approach ensures an exact hydrostatic balance as described in Popinet [154], Popinet and collaborators [155]. We also use this reduced pressure approach in chapter 2. Note that this formulation requires an additional singular body force ($[\rho](\mathbf{g} \cdot \mathbf{z}) \hat{\mathbf{n}}\delta_s$) at the interface. Here, $[\rho]$ is the density jump across the interface, $\hat{\mathbf{n}}$ is the interfacial normal vector, $\hat{\mathbf{n}} = \nabla H/\|\nabla H\|$, and δ_s is the *Dirac-delta function*, $\delta_s = \|\nabla H\|$, where H is the Heaviside function. Consequently, δ_s is non-zero only at the liquid-air interface and has units of 1/length Tryggvason et al. [for detailed derivation, see appendix B of 2]. Furthermore, we employ one-fluid approximation [2, 156] to solve these equations employing volume of fluid (VoF) method for interface tracking, whereby the Heaviside function can be approximated by the VoF marker function Ψ ($\Psi = 1$ inside the liquid drop, and $\Psi = 0$ in the air). Subsequently, the material properties (such as density ρ and viscosity η) change depending on which fluid is present at a given spatial location,

$$\rho = \Psi\rho_d + (1 - \Psi)\rho_a, \quad (1.5)$$

$$\eta = \Psi\eta_d + (1 - \Psi)\eta_a, \quad (1.6)$$

where, the subscripts d and a denote drop and air, respectively. The VoF marker function (Ψ) follows the advection equation [2, 156],

$$\left(\frac{\partial}{\partial t} + \mathbf{v} \cdot \nabla \right) \Psi = 0. \quad (1.7)$$

Lastly, a singular body force \mathbf{f}_γ is applied at the interfaces to respect the dynamic boundary condition. The approximate forms of this force follows [157]

$$\mathbf{f}_\gamma = \gamma \kappa \delta_s \hat{\mathbf{n}} \approx \gamma \kappa \nabla \Psi. \quad (1.8)$$

Here, γ is the drop-air surface tension coefficient and κ is the curvature calculated using the height-function method. During the simulations, the maximum time-step needs to be less than the oscillation period of the smallest wave-length capillary wave because the surface-tension scheme is explicit in time [158, 159].

In our simulations, ideal superhydrophobicity is maintained by assuming that a thin air layer is present between the drop and the substrate [145]. The normal force on this substrate can be calculated using [160]

$$\mathbf{F}(t) = \int_{\mathcal{A}} ((p - p_0) (\mathbf{I} \cdot \hat{\mathbf{z}}) - 2\eta_a (\mathbf{D} \cdot \hat{\mathbf{z}})) d\mathcal{A}, \quad (1.9)$$

where, p and p_0 are the dynamic pressure distribution at the substrate and the ambient pressure, respectively. Here, \mathbf{I} is the second-order identity tensor. Further, $\hat{\mathbf{z}}$ is the unit vector normal to the substrate (figure 1.1b) and \mathcal{A} represents substrate's area. Note that the contribution from the second term on the right-hand side of equation (1.9) is the normal viscous force due to the air layer between the drop and the substrate and is negligible as compared to the pressure integral. Therefore, we can calculate the normal impact force simply by integrating the pressure field at the substrate (see equation (1.1)).

Despite a low viscosity associated with the water drops, the viscous dissipation can still be significant in some cases, especially during flow focusing and capillary waves resonance (see figures 1.4c,d). To identify these regions of high viscous dissipation, we also measure the viscous dissipation function, given by [160]

$$\xi_\eta = 2\eta (\mathbf{D} : \mathbf{D}), \quad (1.10)$$

which on non-dimensionalization using the drop diameter (D), density (ρ_d), and impact velocity (V) gives

$$\tilde{\xi}_\eta \equiv \frac{\xi_\eta}{\rho_d V^3 / D} = \frac{2}{Re} \left(\Psi + \frac{\eta_a}{\eta_d} (1 - \Psi) \right) (\tilde{\mathbf{D}} : \tilde{\mathbf{D}}), \quad (1.11)$$

where, the Reynolds number ($Re = \rho_d V D / \eta_d$) is the ratio of inertial to viscous stresses, and $\tilde{\mathbf{D}} = \mathbf{D} / (V/D)$.

1.B.2 Relevant dimensionless numbers

In the experiments, the initial drop diameter D ($2.05 \text{ mm} \leq D \leq 2.76 \text{ mm}$) and the impact velocity V ($0.38 \text{ m/s} \leq V \leq 2.96 \text{ m/s}$) are independently controlled. The drop material properties are kept constant (density $\rho_d = 998 \text{ kg/m}^3$, surface tension coefficient $\gamma = 73 \text{ mN/m}$, and dynamic viscosity $\eta_d = 1.0 \text{ mPas}$). As a result, we identify the following dimensionless numbers,

$$We = \frac{\rho_d V^2 D}{\gamma} \quad (1.12)$$

$$Oh = \frac{\eta_d}{\sqrt{\rho_d \gamma D}} \quad (1.13)$$

$$Bo = \frac{\rho_d g D^2}{\gamma} \quad (1.14)$$

where, We is the impact Weber number which is a ratio of the inertial to capillary pressures. The Ohnesorge number (Oh) is the ratio between the inertia-capillary to the inertia-viscous time scales and is kept constant at 0.0025 to mimic 2 mm diameter water drops. Furthermore, the Bond number (Bo) is the ratio of the gravitational to the capillary pressure, which is also fixed at 0.5 for the same reason. To test the sensitivity of our results on Bo , we also varied its value as $0.0005 \leq Bo \leq 0.5$ with no effect on the magnitude of the forces or the four regimes reported in figure 1.4. Lastly, to minimize the influence of the surrounding medium, ρ_a/ρ_d and η_a/η_d are fixed at 10^{-3} and 3×10^{-3} , respectively.

1.B.3 Domain description

Figure 1.1(b) represents the axi-symmetric computational domain where $r = 0$ denotes the axis of symmetry. A no-slip and non-penetrable boundary condition is applied on the substrate along with zero pressure gradient. Here, we also use $\Psi = 0$ to maintain a thin air layer between the drop and the substrate. Physically, it implies that the minimum thickness of this air layer is $\Delta/2$ throughout the whole simulation duration (where Δ is the minimum grid size). Further, boundary outflow is applied at the top and side boundaries (tangential stresses, normal velocity gradient, and ambient pressure are set to zero).

Furthermore, the domain boundaries are far enough not to influence the drop impact process ($L_{\max} \gg D$). Basilisk C [143] also allows for adaptive

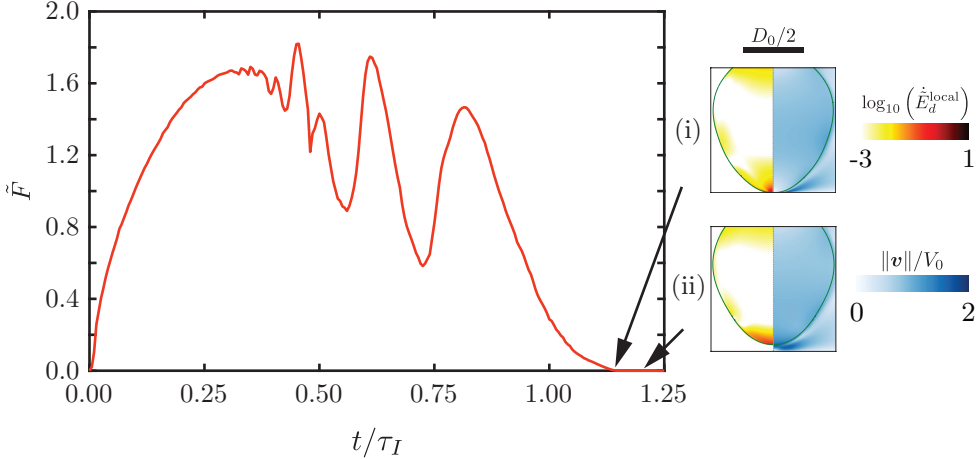


Figure 1.B.1: Temporal variation of the normal contact force for $We = 2$. The insets show two key instances: (i) time $t_3 = 1.14\tau_I$ when F vanishes which marks the contact time of the drop at the substrate and (ii) detachment time ($1.2\tau_I$) as seen from the side view image. Also see supplemental movie S2.

mesh refinement (AMR) with maximum refinement in the regions of high velocity gradients and at the drop-air interface. With such an adaptive mesh refinement, we can resolve the length scales pertinent to capture the bouncing process, i.e., the flow inside the drop and the region near the substrate. The adaption is based on minimizing the error estimated using the wavelet algorithm [161] in the volume of fluid tracers, interfacial curvatures, velocity field, vorticity field and rate of viscous dissipation with tolerances of 10^{-3} , 10^{-4} , 10^{-2} , 10^{-2} , and 10^{-3} , respectively [162]. We also undertook a mesh independence study to ensure that the results are independent of this mesh resolution. We use a minimum grid size $\Delta = D/1024$ for this study. Note that the cases in regime II (singular jet) requires a refinement of $\Delta \approx D/4098$ near the axis of symmetry. The simulation source codes, as well as the post-processing codes used in the numerical simulations, are permanently available at author's GitHub repository [162].

1.B.4 Calculating the time of contact

In the main text, we emphasize that the time instant t_3 at which the normal contact force between the drop and the substrate vanishes is a much better estimate for the drop contact time as compared to the one observed at complete

detachment from side view images. This observation is consistent with the literature [76, 79, 146, 163] and is elucidated in Fig. 1.B.1 for $We = 2$. In this case, $t_3 = 1.14\tau_I$ whereas the side view images show complete detachment at $t = 1.2\tau_I$. The effect is further enhanced for higher We , see for comparisons, supplemental movies S1 ($We = 40$) and S2 ($We = 2$).

1.C Superhydrophobic vs. hydrophilic surfaces

To differentiate between impact forces on superhydrophobic surfaces to that of hydrophilic ones [26, 27, 125–129], we carry out test impacts on hydrophilic surfaces. The hydrophilic sample is a quartz plate, cleaned by surfactant, deionized water, alcohol and deionized water in sequence before the experiment. The advancing and receding contact angles of the deionized water drops on the quartz surface are $47^\circ \pm 2^\circ$ and $13^\circ \pm 2^\circ$, respectively (figure 1.C.1a). The superhydrophobic surface is a Glaco-coated quartz plate [52, 144] as described in § 1.A.2, on which the advancing and receding contact angles are $167^\circ \pm 2^\circ$ and $154^\circ \pm 2^\circ$, respectively (figure 1.C.1b).

Figure 1.C.1c compares the impact on superhydrophobic and hydrophilic substrates for impact corresponding to $We = 40.4$ ($D = 2.05$ mm and $V = 1.20$ m/s). The comparison shows that in the spreading stage ($0 < t < 2$ ms), the transient force profiles overlap. In the time span $2\text{ ms} < t < 9\text{ ms}$, the transient force profile of the drop impact on the hydrophilic surface only has slight fluctuations around zero. In contrast to the hydrophilic one, there is an obvious peak force (i.e. F_2 , corresponding to $t \approx 4.63$ ms) in the retraction stage of the drop impact on the superhydrophobic surface.

Furthermore, the impact force F_1 on the superhydrophobic surface is equal to the maximum impact force on the hydrophilic surface. To obtain a comprehensive understanding, we extracted experimental data (the maximum impact force) from previous literature performed on hydrophilic surfaces [27, 126–129, 164]. Moreover, we carried out experiments on hydrophilic quartz surfaces with an apparent contact angle of $40 \pm 4^\circ$. Then, as shown in Fig. 1.C.1(d), we make a comparison of F_1 between previous work (on hydrophilic surfaces) and our work (on both hydrophilic and superhydrophobic surfaces). As shown in Fig. 1.C.1(d), the data on both superhydrophobic and hydrophilic surfaces in our study are consistent with each other. Furthermore, when $We > 30$, the data in the present work and previous literature are consistent with each other. Therefore, F_1 only depends on the Weber number, rather than the wettability of the surface.

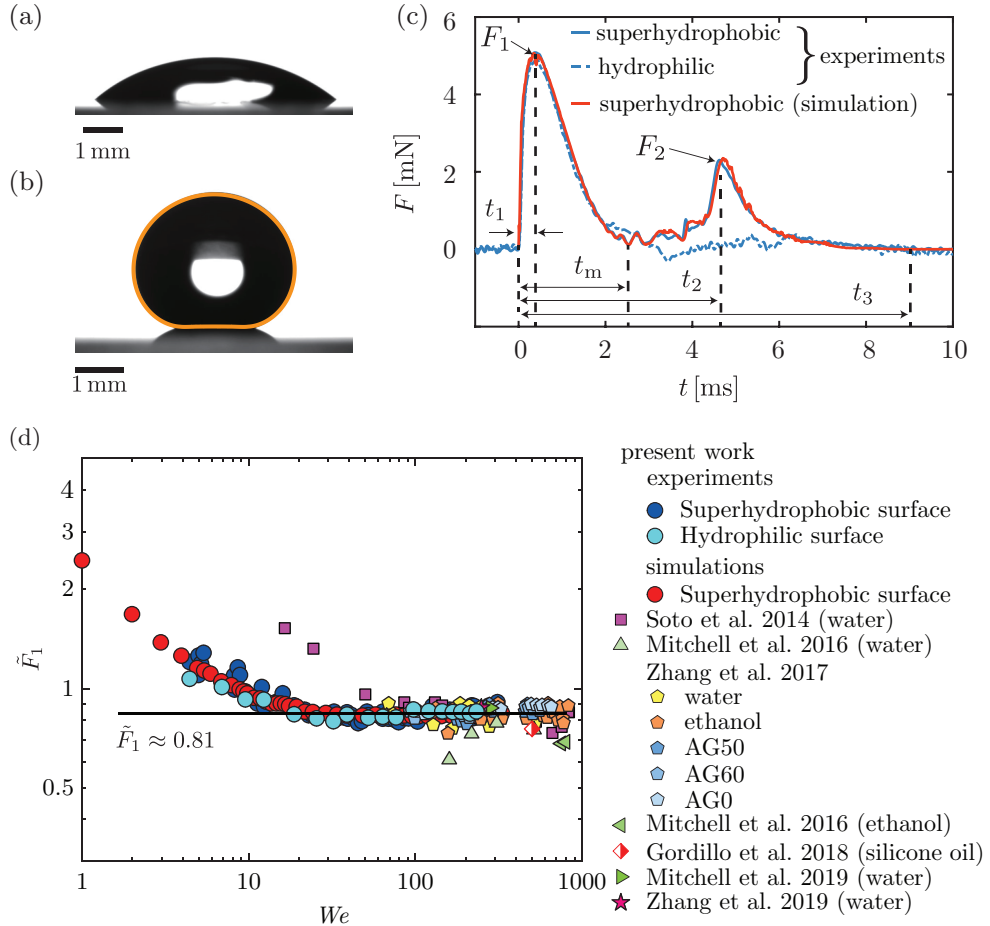


Figure 1.C.1: Wettability of the surfaces and the corresponding transient force profiles. Water drops depositing on (a) hydrophilic and (b) superhydrophobic surfaces with apparent contact angles of $40^\circ \pm 4^\circ$ and $165^\circ \pm 1^\circ$, respectively. For the superhydrophobic case, the drop boundary from simulation is overlaid in orange. (c) Transient force profiles on the hydrophilic and superhydrophobic surfaces. The initial diameter of the drops is 2.05 mm, and the impact velocity is 1.20 m/s, corresponding to $We = 40$. (d) Variation of the first dimensionless peak force \tilde{F}_1 as a function of We . Also see figures 1.2(b) and 1.4(a).

1.D Some notes on the different regimes of drop impact

1.D.1 Regime II: singular Worthington jet

In the main text, we discussed several features of regime II. In this appendix, we further elucidate this regime using the three representative cases, and look at the transient force profile (figure 1.D.1) and the anatomy of flow inside the drops (figure 1.D.2). We replot the data for $We = 9$ (figures 1.D.1a and 1.D.2a) which shows the maximum force amplitude, and choose $We = 5$ (figures 1.D.1b and 1.D.2b) and $We = 12$ (figures 1.D.1c and 1.D.2c) near the boundaries of regime II (also see supplemental movie 4). The transient force profiles show similar features for these three different Weber numbers. After the impact at $t = 0$, there is a sharp increase in the force which reaches the maximum at $t = t_1$. As the drops spread further, their morphology feature distinct pyramidal structures owing to the capillary waves [43] that manifest as oscillations in the temporal evolution of the forces. Then, the drop spreads to a maximum radial extent at $t = t_m$ followed by the retraction phase as the surface tension pulls the drop radially inwards, further enhancing the capillary waves. These traveling capillary waves interact to form an air-cavity, for instance, see $t = 0.9t_2$. The cavity collapses to create high-velocity singular Worthington jets. Subsequently, a bubble is entrained. Comparing the force profile for $We = 9$ with that of $We = 5$ and $We = 12$ reveal differences owing to the corresponding air cavities and bubble entrainment. The flow focusing is the most efficient for $We = 9$, as evidence from the sharp peak in the transient force evolution. This capillary resonance leads to a strong downward momentum jet and hence the maximum amplitude F_2 at time $t = t_2$. Bubble entrainment does not occur for either $We = 5$ or $We = 12$ (see $t_2 < t < 1.2t_2$). Consequently, the maximum force amplitude diminishes for these two cases.

Another characteristic feature of this regime is the occurrence of negative contact force between the drop and the substrate immediately before the formation of a singular Worthington jet and the second peak in normal contact force. Fig. 1.D.3 illustrates one such case for $We = 9$ where the contact force is negative for $1.1\tau_I \lesssim t \lesssim 1.2\tau_I$ implying that the drop is pulling on the substrate instead of pushing it (Fig. 1.D.3(a)). Earlier works [27, 125, 165] have attributed this negative force to the wetting properties of the substrates, particularly adhesion between the drop and the substrate [166, 167], viscoelastic effects or deformation of the substrate [27]. However, none of these effects are present in our work. To demystify the occurrence of this negative force, we monitor the pressure field inside the drop (side view, Fig. 1.D.3(b)) and on the

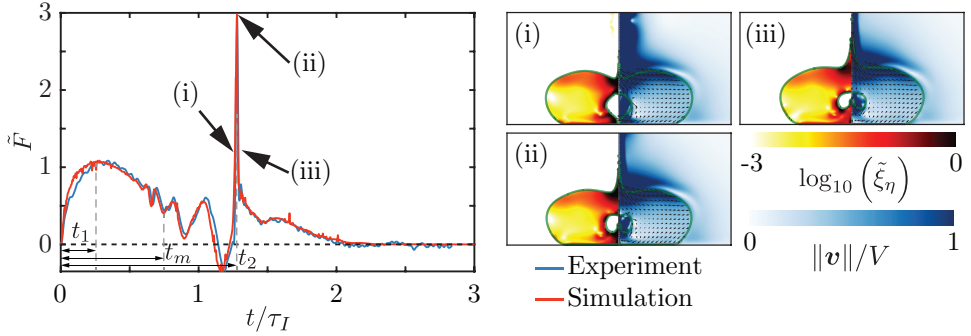
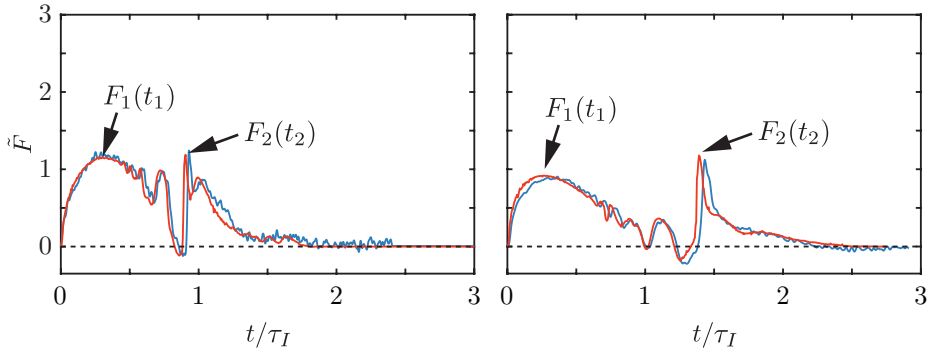
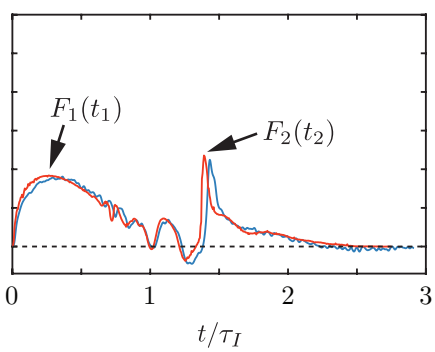
(a) $We = 9$ (b) $We = 5$ (c) $We = 12$ 

Figure 1.D.1: Evolution of the normal force $\tilde{F}(t) = F(t)/\rho_d V^2 D^2$ of a drop impacting on the superhydrophobic surface in the singular Worthington jet regime for $We =$ (a) 9, (b) 5, and (c) 12. Insets in panel (a) show the drop morphology and flow anatomy close to the capillary resonance that leads to a hydrodynamic singularity. Note the outstanding agreement between the experimental (blue line) and the numerical (red line) results, including the various wiggles in the curve, which originate from capillary oscillations for panel (a). The left part of each numerical snapshot shows the dimensionless viscous dissipation function $\tilde{\xi}_\eta$ on a \log_{10} scale and the right part shows the velocity field magnitude normalized with the impact velocity. The black velocity vectors are plotted in the center of mass reference frame of the drop to clearly elucidate the internal flow.

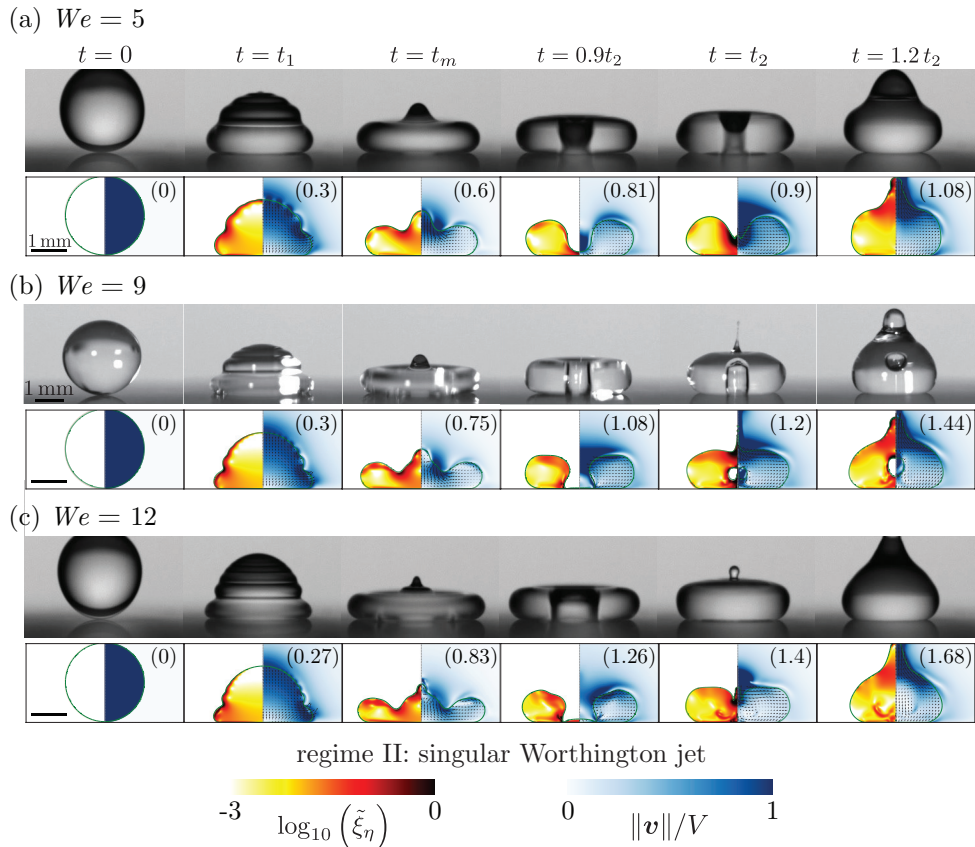


Figure 1.D.2: Drop impact on the superhydrophobic surface in the singular Worthington jet regime for $We =$ (a) 9, (ii) 5, and (iii) 12. The left part of each numerical snapshot shows the dimensionless viscous dissipation function $\tilde{\xi}_\eta$ on a \log_{10} scale and the right part shows the velocity field magnitude normalized with the impact velocity. The black velocity vectors are plotted in the center of mass reference frame of the drop to clearly elucidate the internal flow. The numbers in the top right of each numerical snapshot mentions the dimensionless time t/τ_I .

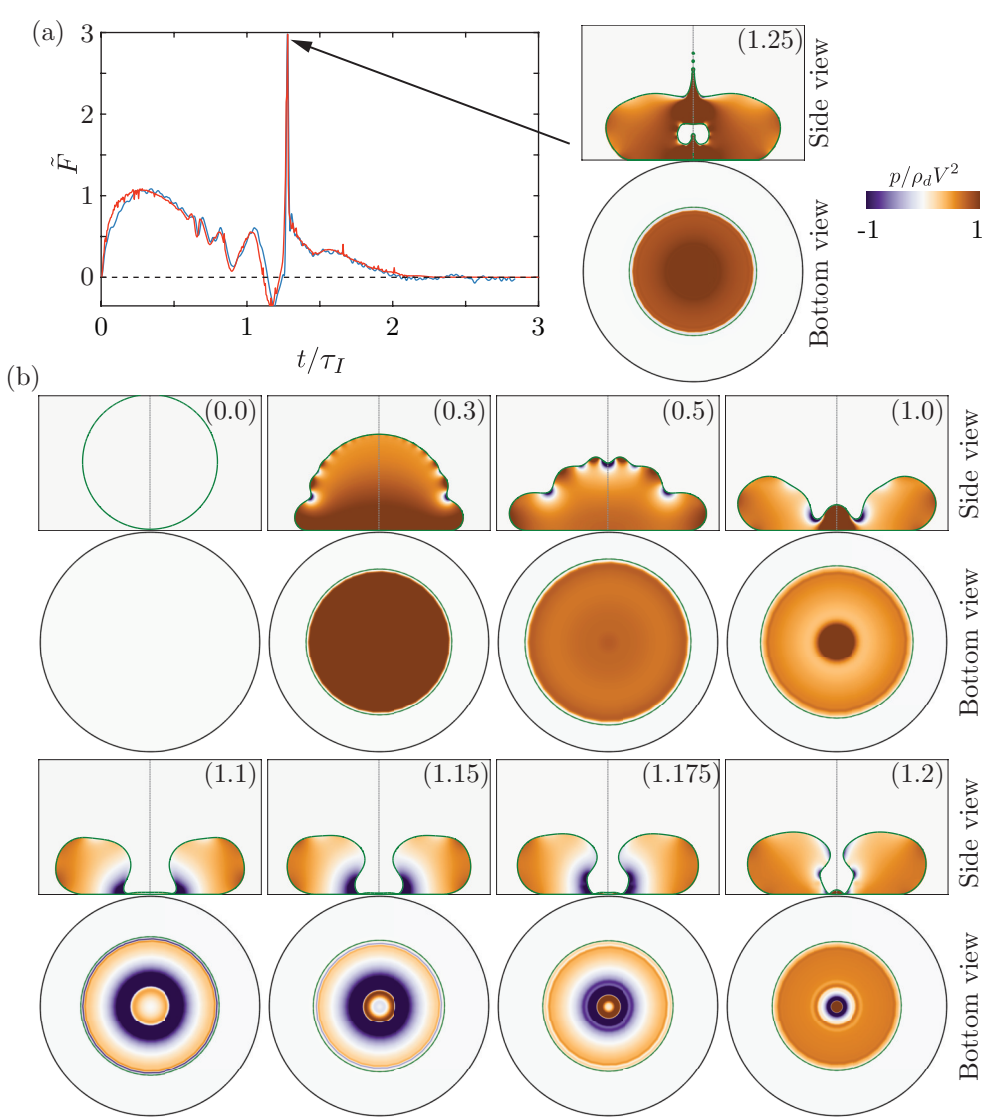


Figure 1.D.3: Contact force and pressure field during drop impact on the superhydrophobic surface in the singular Worthington jet regime, $We = 9$. (a) Temporal variation of the contact force. Notice that the contact force is negative for $1.1\tau_I \lesssim t \lesssim 1.2\tau_I$. (b) Simulation snapshots showing the pressure field p normalized by the inertial pressure $\rho_d V^2$ in the side and bottom view images. The numbers in the top right of each numerical snapshot mentions the dimensionless time t/τ_I .

substrate (bottom view, Fig. 1.D.3(b)). We observe large negative pressures (purple regions in the pressure field) on the substrate immediately prior to the formation of a singular Worthington jet and the second peak in normal contact force owing to the negative curvature on the surface of the drop as the air-cavity forms due to focusing of the capillary waves. Consequently, negative capillary pressure causes a pressure deficit inside the drop, and the drop pulls on the substrate instead of pushing it (brown regions in the pressure field).

1.D.2 Transitional regime II-III and inertial regime III

In the main text, we used the flow focusing due to drop retraction to find an expression for the amplitude F_2 (see, equation (1.3)) that entails two scaling behaviors depending on the We (see equation (1.2)). To address the crossover of these two scaling relations, (i.e., $We = 30$), we check the deformation of the drop at the moment of maximum spreading and the corresponding position of the drop apex.

To make a comparison, we exemplary choose $We = 20$ ($D = 2.05\text{ mm}$, $V = 0.83\text{ m/s}$) and $We = 80$ ($D = 2.05\text{ mm}$, $V = 1.69\text{ m/s}$), and show their impact behaviors in figures 1.D.4(a) and (b), respectively. By simulations, the anatomy of the inner flow field of the drop are discernible (see the right panels). For the case $We = 20$, the solid-liquid contact region is close to the initial drop diameter when F_1 is attained at $t_1 = 0.6\text{ ms}$. Meanwhile, the excited capillary wave propagates along the drop surface and then deforms the drop into a pyramidal shape at 1.5 ms . Then, the drop reaches its maximum spreading diameter D_m at $t_m = 2.3\text{ ms}$. Notice that at this moment, the drop apex is higher than the height of the rim and is still moving downwards. After that, the drop starts to recoil, and the drop apex descends to its lowest level after t_m . During the recoil, the retreating drop deforms into a pancake shape with air in the center, as shown at 4.0 ms . As time progresses, the retracting flow fills the cavity and creates an upward jet at $t_2 = 4.5\text{ ms}$, which results in F_2 .

On the other hand, for the case with $We = 80$, a thin liquid film appears, and the solid-liquid contact area is close to the initial drop diameter when F_1 is attained, similar to the case with $We = 20$. However, unlike the previous case, $t_1 = 0.2\text{ ms}$ (see § 1.4). Moreover, there is no obvious capillary wave propagating on the drop surface, as shown at 1.0 ms . Then, the drop apex continuously moves downwards, and its height reaches the height of the rim, and this moment happens before the drop reaches its maximum spreading diameter D_m at $t_m = 2.0\text{ ms}$. Shortly after t_m , the drop recoils, while the film

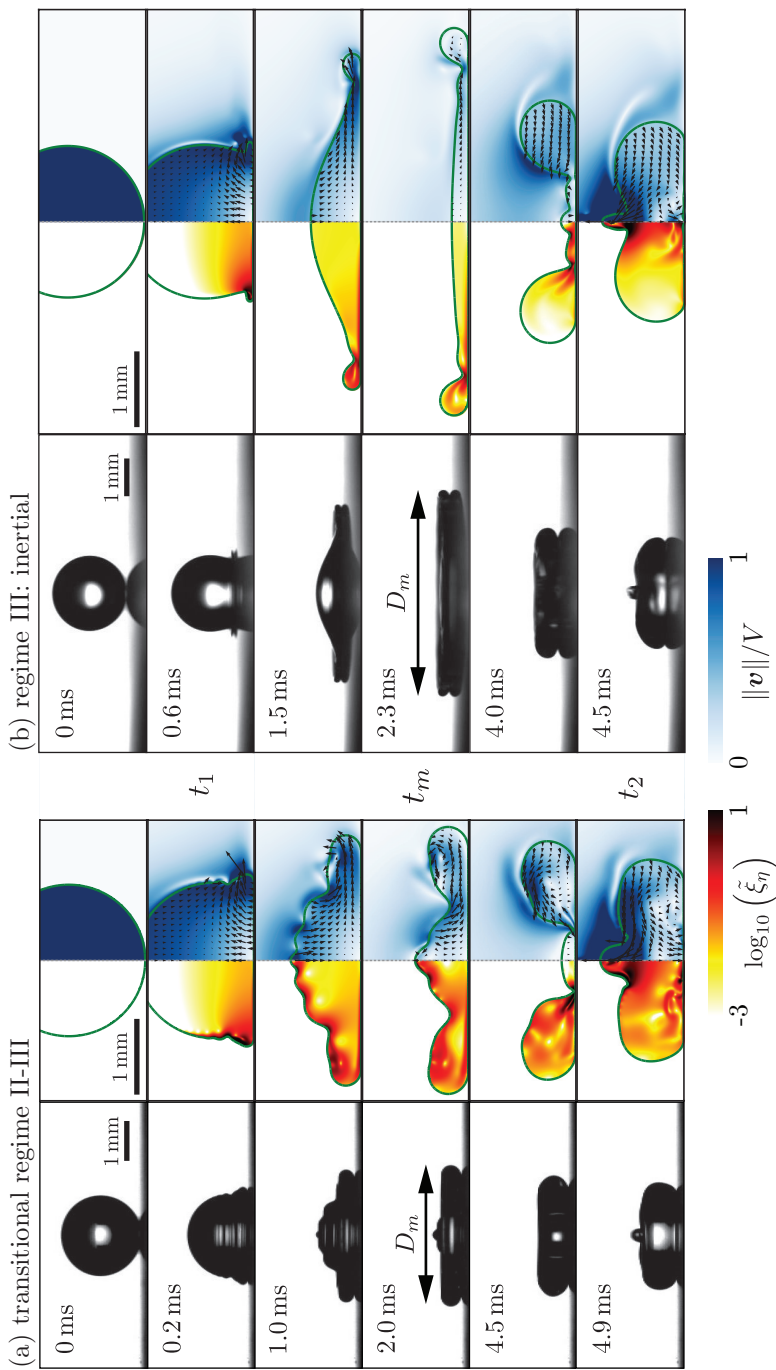


Figure 1.D.4: Snapshots of drop shape with time at different Weber numbers, $We = (a) 20 (b) 80$.

thickness in the central region remains the same (see 4.5 ms, [116]). Then, the thickening retracting flow converges and collides at the film center to form an upward jet to result in F_2 , as shown at 4.9 ms.

Based on the above results, we gain the following insight. For small We (figure 1.D.4a, $We = 20$), the drop attains D_m (at time t_m) before its apex descends to its lowest level (at time $\sim D/V$), leading to a puddle-shaped drop [30]. This observation indicates that at t_2 , a competition exists between two flows in the central region of the drop, respectively, coming from the rim and the drop apex. However, for large We (figure 1.D.4b, $We = 80$), the drop apex attains its lowest level before t_m , so the drop has a pizza shape [30, 116]. Equating the two timescales together, one obtains a crossover Weber number $We^* = 25$, which is close to the value 30 observed in our work. Alternatively, equating the two scaling relations in equation (1.2) gives a more accurate estimate of the crossover Weber number as $We^* = 29.7$.

1.D.3 Regime IV: drop splashing

The main text reported differences between the experimental and numerical observations in regime IV. Here, we further delve into this discrepancy to identify the reasons behind it (figure 1.D.5). At high impact velocities ($We = 225$ in figure 1.D.5), splashing occurs in the experiments [42]. At such high We , the surrounding gas atmosphere destabilizes the rim, breaking it [116, 151]. The limit for splashing observed in this work ($We \geq 100$, see figure 1.4) is in agreement with the predictions in previously predicted works of Lohse [16], Derby [123], Riboux and Gordillo [151] (see figure 4).

In regime IV, a part of kinetic and surface energies are lost due to the formation of satellite drops (figure 1.D.5b), resulting in diminishing \tilde{F}_2 in the experiments (Fig 1.D.5(a)). Obviously, such azimuthal instability is absent in the simulations (axisymmetric by definition), which leads to a better flow-focusing at the center. Indeed, Eggers et al. [116] were able to simulate cases with We as high as 1000 without breakup. Consequently, equation (1.3) holds only for the simulations in regime IV and not for the experiments. Notice that the experimental and numerical $F(t)$ magnitudes only disagree near $t = t_2$. Further, the time at which the second peak is reached is still at $t_2 \approx 0.44\tau_{p\gamma}$, as explained in the main text. For future work, we suggest that one could also experimentally probe F_2 in this regime by suppressing the azimuthal instability (for instance, by reducing the atmospheric pressure [152]).

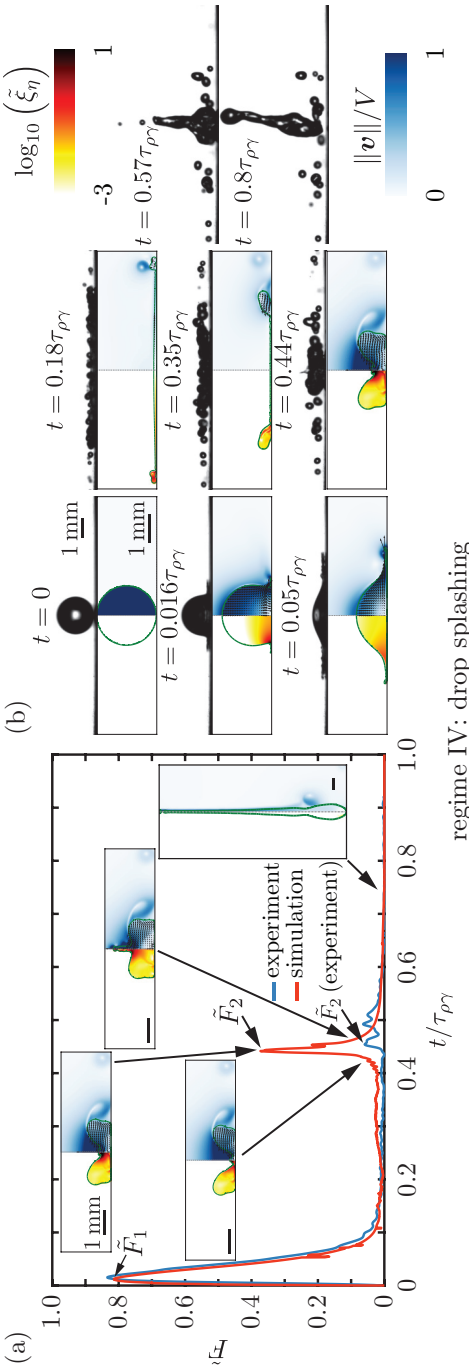


Figure 1.D.5: Drop impact on the superhydrophobic surface at a high Weber number, $We = 225$. (a) Evolution of the transient impact force. (b) Snapshots of the corresponding drop geometry in the spreading and recoiling stages. Notice that the experimental and numerical $F(t)$ magnitudes only disagree near $t = t_2$. Further, the time at which the second peak is reached is still at $t_2 \approx 0.44\tau_{\rho\gamma}$, as explained in the main text. The left part of each numerical snapshot shows the dimensionless viscous dissipation function, $\tilde{\xi}_\eta$ on a \log_{10} scale and the right part shows the velocity field magnitude normalized with the impact velocity, $\|\mathbf{v}\|/V$. The black velocity vectors are plotted in the center of mass reference frame of the drop to clearly elucidate the internal flow.

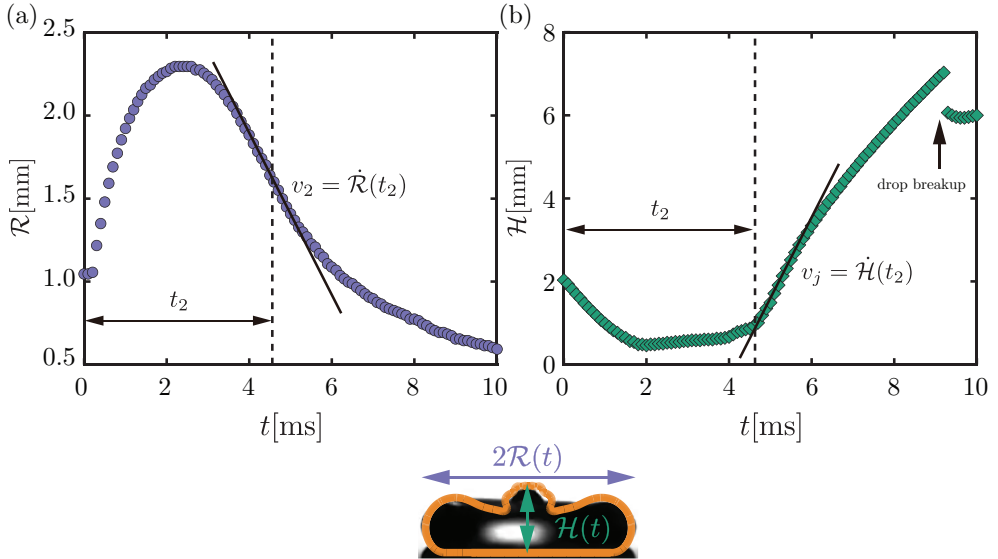


Figure 1.E.1: Experimental time evolution of (a) spread radius $\mathcal{R}(t)$ and (b) the drop height $\mathcal{H}(t)$. Inset illustrates the drop geometry. The retraction velocity $v_2 = \dot{\mathcal{R}}(t_2)$ and the jet velocity $v_j = \dot{\mathcal{H}}(t_2)$ are represented by the slopes of the solid lines at t_2 in (a) and (b), respectively. Here, $We = 40$.

1.E Calculation of the jet and retraction characteristics

1.E.1 Experiments

In this section, we illustrate how to extract v_2 and v_j from the experiments. As an example, we choose $We = 40$. As shown in figure 1.E.1, we first track the instantaneous values of the width $2\mathcal{R}(t)$ (figure 1.E.1a) and the height $\mathcal{H}(t)$ (figure 1.E.1b) of the drop. We observe that just after the impingement, the drop height decreases with a constant velocity [27, 116] until the inertial shock propagates throughout the drop. As time progresses, $\mathcal{R}(t)$ and $\mathcal{H}(t)$ respectively reach their maximum and minimum values simultaneously (at $t_m \approx 2.5$ ms). Moving forward in time, $\mathcal{R}(t)$ decreases, whereas $\mathcal{H}(t)$ increases linearly until t_2 . After this moment, we observed a sharp increase of $\mathcal{H}(t)$ until the drop breaks into the base drop and a small droplet (see the insets in figure 1.2a of the main text). We define the recoiling velocity v_2 of the drop and the jet velocity v_j as:

$$v_2 = \dot{\mathcal{R}}(t_2) = \left. \frac{d\mathcal{R}(t)}{dt} \right|_{t_2}, \quad (1.15)$$

$$v_j = \dot{\mathcal{H}}(t_2) = \left. \frac{d\mathcal{H}(t)}{dt} \right|_{t_2}. \quad (1.16)$$

As shown in figure 1.E.1(a), $v_2 = \dot{\mathcal{R}}(t_2)$ is obtained by a linear fitting (black line) to the experimental data around $(t_2, \mathcal{R}(t_2))$. Similarly, as shown in figure 1.E.1(b), $v_j = \dot{\mathcal{H}}(t_2)$ is obtained by a linear fitting (black line) to the experimental data around $(t_2, \mathcal{H}(t_2))$. Note that in the experiments, we can only measure the maximum height of the drop. Consequently, when the rim thickness exceeds the drop's height, \mathcal{H} identifies the height of the rim (particularly for $t < t_m$). So, we use the datapoints after $t = t_2$ to calculate the jet velocity. Nonetheless, the jet velocity v_j extracted at $t = t_2^+$ from the experiments are consistent very well with our simulation (where we can precisely calculate the jet velocity, see § 1.E.2), as well as the results obtained by Bartolo et al. [44], as discussed in § 1.E.3.

1.E.2 Simulations

To characterize the jet, we track the interfacial location (or height of the drop, $\mathcal{H}(t)$) at the axis of symmetry ($r = 0$). Similarly, to characterize retraction, we track the radial extent of the drop ($2\mathcal{R}(t)$). Further, $\dot{\mathcal{H}} = d\mathcal{H}/dt$ measures the velocity of this jet, and $\dot{\mathcal{R}} = d\mathcal{R}/dt$ accounts for the retraction velocity. Figure 1.E.2 shows the temporal variation of $\dot{\mathcal{H}}$ (panel i) and $\dot{\mathcal{R}}$ (panel ii) for two representative Weber numbers, $We = 9$ (panel a) and 100 (panel b). As the drop impacts, the top of the drop keeps moving with a constant velocity ($\dot{\mathcal{H}} \approx V$) [27, 116], consistent with our experiments. However, during this period, the radial velocity magnitude increases to a maximum and then decreases to zero at the instant of maximum spreading.

For low to moderate Weber number impacts ($We = 9$ in figure 1.E.2a), the pyramidal morphology result in capillary oscillations aiding the flow focusing in the retraction phase. Consequently, both the normal force (F) and the jet velocity ($\dot{\mathcal{H}}$, figure 1.E.2a-i) reach the maxima simultaneously at $t = t_2$. Further, the retraction velocity (figure 1.E.2a-ii) show oscillations due to capillary waves.

On the other hand, for high Weber number impacts ($We = 100$ in figure 1.E.2b), the jet velocity is minimum at the instant of maximum spreading.

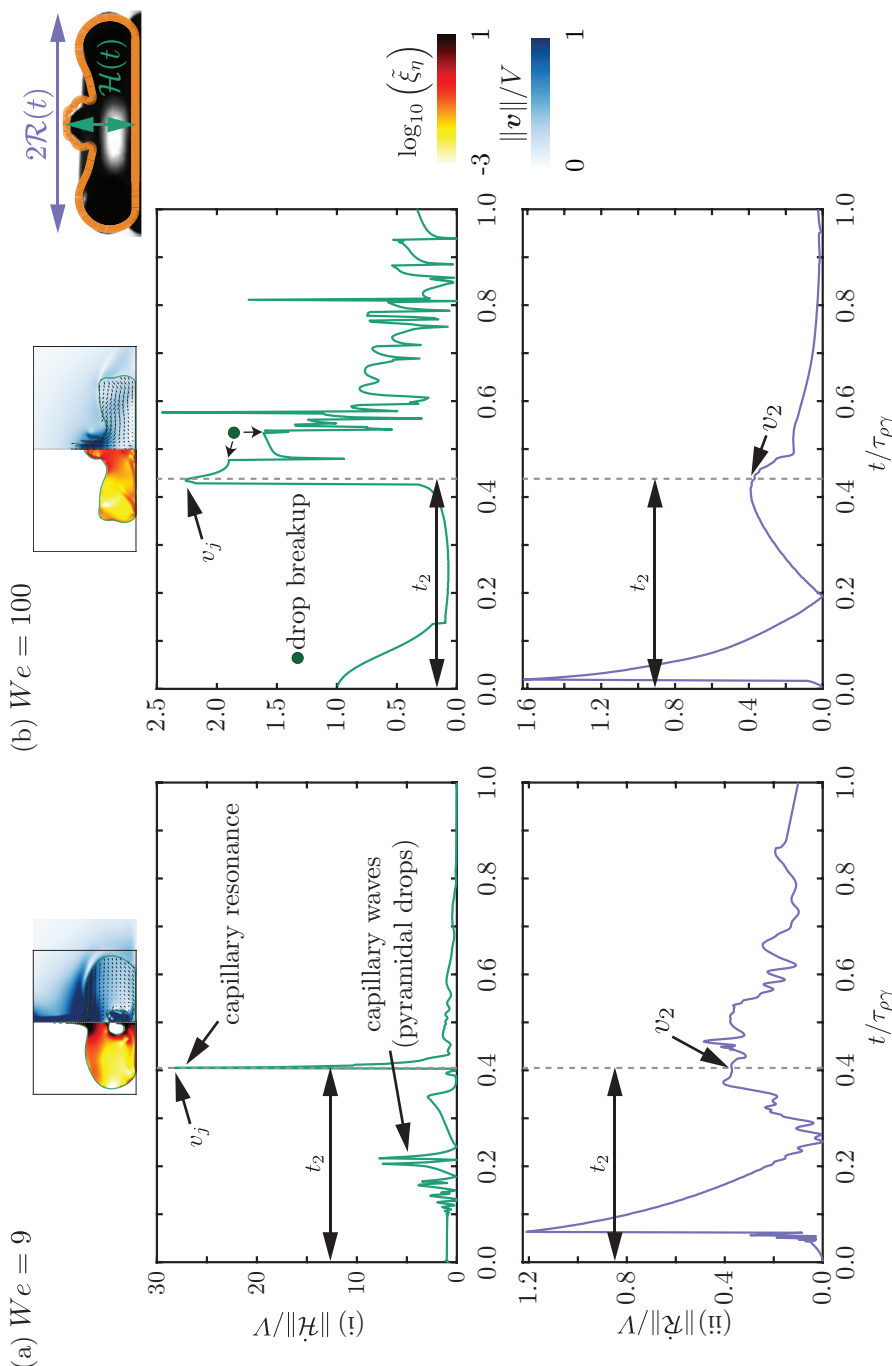


Figure 1.E.2: Calculation of the (i) jet velocity (v_j) and (ii) retraction velocity (v_2) for Eq. (2) of the main manuscript for two representative cases: $We = (a) 9$ and (b) 100. Inset illustrates the drop geometry where \mathcal{H} is the height of the drop at the axis of symmetry and $2\mathcal{R}$ is its radial extent. The jet velocity is $v_j = \dot{\mathcal{H}}(t_2)$ and the retraction velocity is $v_2 = \dot{\mathcal{R}}(t_2)$. Notice that the time at which second peak is reached still scales with the inertia-capillary timescale $t_2 \sim \tau_{\rho\gamma}$, as described in the main text, irrespective of the We ($t_2 = 0.405\tau_{\rho\gamma}$ for $We = 9$, and $t_2 = 0.437\tau_{\rho\gamma}$ for $We = 100$).

Then, Taylor-Culick type retraction occurs increasing the retraction velocity to a maximum which then decreases due to finite size of the drop [36–38, 116]. During this retraction phase, flow focusing and asymmetry provided by the substrate lead to a sudden increase in the jet velocity (figure 1.E.2b-i) that is immediately followed by occurrence of the second peak in the transient force profile (at t_2). The retraction velocity at this instant is very close to its maximum temporal value (figure 1.E.2b-ii).

For both cases, notice that the time at which second peak is reached still scales with the inertio-capillary timescale $t_2 \sim \tau_{\rho\gamma}$, as described in the main text, irrespective of the We ($t_2 = 0.405\tau_{\rho\gamma}$ for $We = 9$, and $t_2 = 0.437\tau_{\rho\gamma}$ for $We = 100$).

In summary,

$$v_j = \dot{\mathcal{H}}(t_2) \quad (1.17)$$

$$v_2 = \dot{\mathcal{R}}(t_2). \quad (1.18)$$

Lastly, we can also characterize the maximum lateral extent D_2 of the drop at the instant t_2 of second peak in the normal reaction force F_2 as

$$D_2 = 2\mathcal{R}(t_2), \quad (1.19)$$

in both experiments as well as simulations.

1.E.3 Results

We will devote the rest of this appendix to relate the different flow properties in equation (1.3) (also see figure 1.E.3a) to the control parameter, i.e., the impact Weber number We . For the transitional regime II-III ($12.6 < We < 30$), at the moment of second peak, the dimensionless diameter (\tilde{D}_2) and the dimensionless drop retraction velocity (\tilde{v}_2) are independent of the impact Weber number We (figures 1.E.3b, c). Further, the jet velocity decreases with increasing Weber number following $\tilde{v}_j = v_j/V \sim 1/We$ (figure 1.E.3d). This decrease is consistent with the data extracted from Bartolo et al. [44]. Substituting these in equation (1.3), one obtains $\tilde{F}_2 \sim 1/We$. However, the prefactor that best fits the experimental and numerical data in equation (1.2) is much larger than order 1, which may be caused by the enhanced flow and momentum focusing due to both capillary waves and drop retraction.

For regime III ($30 < We < 100$), there is a slight increase in \tilde{D}_2 (figure 1.E.3b) but it is still best represented by a plateau. Furthermore, with

1

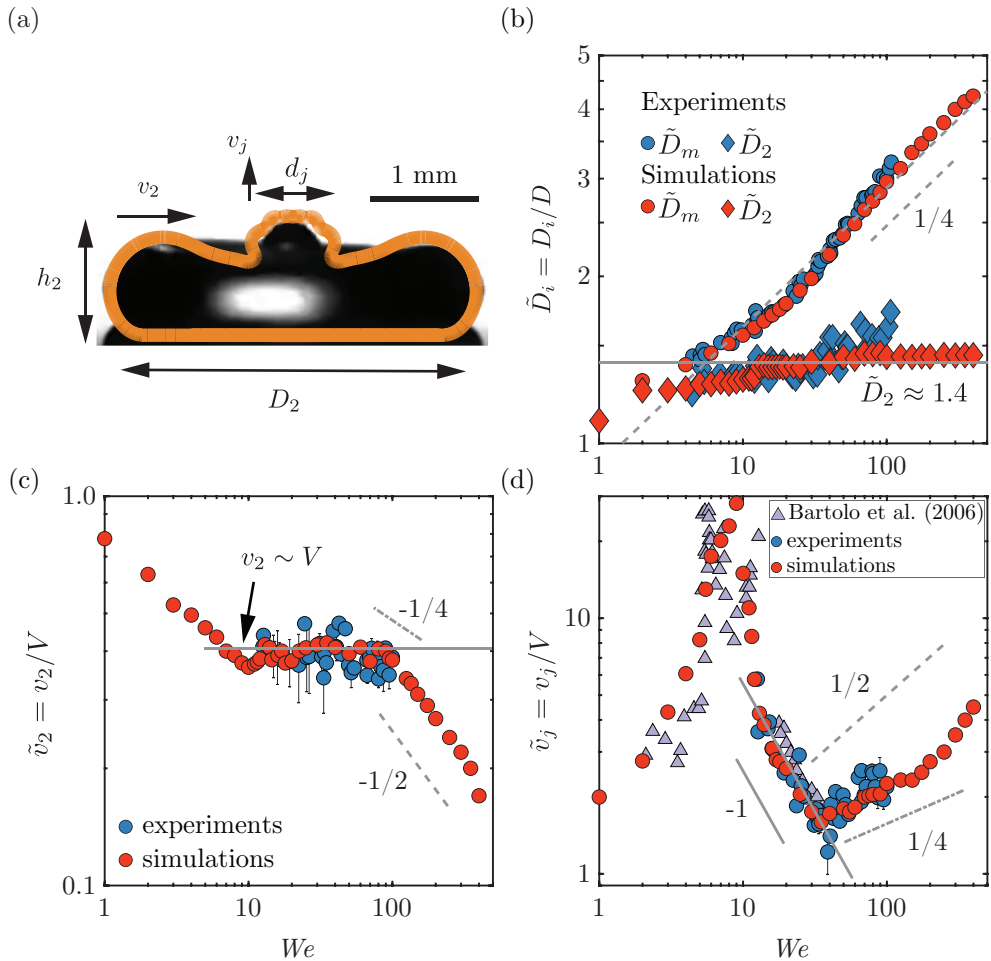


Figure 1.E.3: (a) Drop geometry at t_2 for $We = 40$ (along with the drop contour from numerics in orange) to illustrate the drop spreading diameter D_2 , drop height h_2 , retraction velocity v_2 , jet diameter d_j and jet velocity v_j . (b) Variation of the dimensionless spreading diameter at t_m and t_2 (given by $\tilde{D}_{max} = \tilde{D}(t_m)$ and $\tilde{D}_2 = \tilde{D}(t_2)$, respectively). The gray dotted and solid lines represent $\tilde{D}_{max} \sim We^{1/4}$ and $\tilde{D}_2 \approx 1.4$, respectively. (c) Variation of drop retraction velocity \tilde{v}_2 at t_2 with We . The gray solid line represents $v_2 \sim V$. The gray dotted and dashed-dotted lines correspond to $We^{-1/2}$ and $We^{-1/4}$, respectively, and are meant only as guides to the eye. (d) Variation of the (non-dimensionalized) jet velocity $\tilde{v}_j = v_j/V$ with We . The data from Bartolo et al. [44] are also shown in the same panel. The gray solid line represents $\tilde{v}_j \sim We^{-1}$. The gray dotted and dashed-dotted lines correspond to $We^{1/2}$ and $We^{1/4}$, respectively, and are meant only as guides for the eye.

increasing We , \tilde{v}_2 decreases whereas \tilde{v}_j increases (figures 1.E.3c,d). We have shown gray lines as guides to the eye to represent these trends. However, due to limited range of We , we refrain from claiming any scaling relations here. Coincidentally, these changes in \tilde{D}_2 , \tilde{v}_2 , and \tilde{v}_j compensate each other such that equation (1.3) still holds. Consequently, the second peak force scales with the inertial pressure force $F_2 \sim \rho_d V^2 D^2$ (equation (1.2)).

Alternatively, we can use the expressions for the amplitude of the second peak of force between the drop and the substrate to predict the velocity of the Worthington jet. For $We \gg 1$, the drop forms a thin sheet at the instant of maximum spreading ($t = t_m$, see figures 1.D.4b and 1.D.5). This sheet retracts following Taylor-Culick type retraction at low Ohnesorge numbers ($Oh \ll 1$). As a result, the retraction velocity scale can be given as [36, 116]:

$$v_2 \sim \sqrt{\frac{\gamma}{\rho_d h_2}}, \quad (1.20)$$

where, γ and ρ_d are the surface tension coefficient and density of the liquid drop, respectively. Further, v_2 is the retraction velocity at $t = t_2$ and h_2 is the height of the drop at that instant which is related to the spreading diameter following volume conservation as $h_2 \sim D^3/D_2^2$. Substituting this expression in equation (1.20) and normalizing with V , we get

$$\tilde{v}_2 \sim D_2 \sqrt{\frac{\gamma}{\rho_d V^2 D^3}} = \frac{\tilde{D}_2}{\sqrt{We}}. \quad (1.21)$$

The finite size of the retracting drop may account for the deviations from equation (1.21) in figures 1.E.3(b,c) [37, 38]. Further, using $\tilde{F}_2 \sim \tilde{v}_2 \tilde{v}_j / \tilde{D}_2 \sim \mathcal{O}(1)$ for $We \gg 1$, we obtain

$$\tilde{v}_j \sim \sqrt{We}. \quad (1.22)$$

Unfortunately, we cannot confirm the validity of this scaling behavior in figure 1.E.3(d) due to a limited range of We as mentioned above. For completeness, in figure 1.E.3(b), we also show the maximum spreading diameter from our experiments and simulations are in a remarkable agreement. We refer the readers to [28, 29, 116] for further discussions on the influence of We on the maximum spreading diameter.

1.E.4 Outlook on the scaling relations

In this section and figure 1.E.3, we probe several scaling behaviors in an attempt to relate the internal flow characteristics, i.e., the jet and retraction velocities, to the impact Weber number. However, verifying the predicted scaling behaviors requires a larger range of Weber numbers that we do not study due to experimental and numerical limitations. For example, at very high-velocity impacts, the drop splashes and breaks into many satellite droplets in the experiments [151]. For future work, we suggest that one could experimentally probe this regime by suppressing the azimuthal instability (for instance, by reducing the atmospheric pressure [152]). However, even in such a scenario, at very high impact velocities ($We \gg 1$), the substrate roughness may play a role in both drop spreading and retraction [168]. In numerical simulations, one can probe this regime by using drops that are slightly more viscous than water, as done by Eggers et al. [116]. However, such a study is numerically costly for water drops impacting at very large We due to the separation of length scales between the initial diameter of the drop and the very thin lamella during spreading. Furthermore, the interfacial undulations (traveling capillary waves) further restrict both the spatial and temporal resolutions.

1.F Code availability

All codes used in this chapter are permanently available at Sanjay [162].

1.G Supplemental movies

These supplemental movies are available at Sanjay [[external YouTube link](#), 169].

SM1: The evolution of the transient force of a water drop impacting on the superhydrophobic surface at a moderate Weber number $We = 40$ (corresponding to $D = 2.05$ mm and $V = 1.20$ m/s), with simultaneous drop geometry recorded experimentally at 10,000 fps with the exposure time of 1/20,000 s. The left part of the numerical video shows the dimensionless viscous dissipation function on a \log_{10} scale and the right part shows the velocity field magnitude normalized with the impact velocity.

SM2: The evolution of the transient force of a water drop impacting on the superhydrophobic surface at a low Weber number $We = 2$ (Regime I:

capillary), with simultaneous drop geometry evolution. The left part of the numerical video shows the dimensionless viscous dissipation function on a \log_{10} scale and the right part shows the velocity field magnitude normalized with the impact velocity.

- SM3: The evolution of the transient force of a water drop impacting on the superhydrophobic surface at Weber number $We = 9$ (corresponding to $D = 2.76$ mm and $V = 0.49$ m/s), with simultaneous drop geometry recorded experimentally at 10,000 fps with the exposure time of 1/50,000 s. The ultra-thin and fast singular jet is reminiscent of the hydrodynamic singularity. The left part of the numerical video shows the dimensionless viscous dissipation function on a \log_{10} scale and the right part shows the velocity field magnitude normalized with the impact velocity.
- SM4: Boundaries of the singular jet regime: the evolution of the transient force of a water drop impacting on the superhydrophobic surface at three representative Weber numbers in regime II, $We = 5$, $We = 9$, and $We = 12$, with simultaneous drop geometry evolution. The left part of the numerical video shows the dimensionless viscous dissipation function on a \log_{10} scale and the right part shows the velocity field magnitude normalized with the impact velocity.
- SM5: Contact force and pressure field during drop impact on the superhydrophobic surface in the singular Worthington jet regime, $We = 9$. Simulation shows the pressure field p normalized by the inertial pressure $\rho_d V^2$ on the left and the magnitude of velocity field $\|\mathbf{v}\|$ normalized by the impact velocity V on the right in the side view images and pressure field in the bottom view images.
- SM6: The evolution of the transient force of a water drop impacting on the superhydrophobic surface at a high Weber number $We = 225$ (drop splashing regime, corresponding to $D = 2.05$ mm and $V = 2.83$ m/s), with simultaneous drop geometry recorded experimentally at 10,000 fps with the exposure time of 1/20,000 s. The left part of the numerical video shows the dimensionless viscous dissipation function on a \log_{10} scale and the right part shows the velocity field magnitude normalized with the impact velocity.
- Bonus: Conference (Physics@Veldhoven 2022) talk titled “How much force is required to play ping-pong with water droplets?” presenting the results from this chapter.

chapter 1: impact forces of water drops falling
on superhydrophobic surfaces



source code



supplemental movies

Chapter 2

When does a drop stop bouncing?^o

As a liquid drop impacts a non-wetting substrate in presence of a gravitational field, it spreads while converting the initial kinetic energy into surface energy to reach a maximum extent which only weakly depends on the initial impact velocity. At this stage, the drop stops and then recoils following a capillary-driven Taylor-Culick type retraction, gaining kinetic energy as its surface area decreases. This drop recoil creates a radially symmetric flow inside the drop. The presence of the substrate creates an asymmetry and directs this flow in the upward direction against gravity. Throughout these stages, viscous dissipation enervate the internal momentum of the flow. Eventually, at the end of the retraction stage, if the upward flow is strong enough to overcome gravity, the drop bounces off the non-wetting substrate. In this article, we investigate how viscous stresses and gravity conspire against capillarity to inhibit the drop to bounce off non-wetting substrates. Drawing an analogy with the case of coalescence-induced jumping of two identical drops, we propose the criterion $Oh_{d,c} + Bo_c = 1$ (i.e., sum of the critical drop Ohnesorge and Bond numbers being one), for this bouncing to non-bouncing transition and check its validity by employing axially symmetric direct numerical simulations. We also delve into the two asymptotes ($Oh_{d,c} = 1$ for $Bo \ll 1$, and $Bo_c = 1$ for $Oh_d \ll 1$) to demystify the mechanisms associated to this transition and analyze the salient characteristics of the drop impact process, including the contact time, coefficient of restitution, and energy budgets.

^oIn preparation as: **Vatsal Sanjay**, Pierre Chantelot, and Detlef Lohse, *When does a drop stop bouncing?*, J. Fluid Mech. Simulations are done by Sanjay; analysis and writing by Sanjay and Chantelot; and supervision by Lohse. Proofread by everyone.

2.1 Introduction

Drop impacts have intrigued scientists ever since Leonardo da Vinci sketched a water drop splashing onto a sheet of paper in the margin of folio 33r in Codex Hammer/Leicester (1506 – 1510) [13]. In particular, the striking patterns created by drop fragmentation, at high impact velocity, have attracted attention [11, 41, 170, 171]. Lower velocity impacts, although they do not cause drops to shatter, also give rise to a rich variety of phenomena [14, 15, 41, 42, 66, 172]. The rebound of drops on non-wetting substrates may be one of the most fascinating of such interactions [40, 131, 173].

Upon impact, the liquid first spreads [26, 27] until it reaches its maximal extent [28–31]. It then recoils, following a Taylor-Culick type retraction parallel to the substrate [34–39], and ultimately bounces off in an elongated shape perpendicular to the substrate [40–42]. Furthermore, throughout these stages, viscous dissipation enervate the internal momentum of the flow and can even suppress bouncing [30, 145, 153].

Such rebounds abound in nature, as non-wetting surfaces provide plants and animals a natural way to keep dry [32, 33], and are relevant in many industrial processes [45], such as inkjet printing [16], cooling applications [17–19], pesticides application [20, 21], and criminal forensics [22]. In some applications, it is pertinent that drops ricochet off the surface, such as self-cleaning [46], keeping clothes dry [47], and anti-fogging surfaces [48]. However, in most applications, bouncing must be suppressed, for example in inkjet printing [16], cooling applications [17–19], pesticides application [20], and criminal forensics [22].

Therefore, it is natural to wonder when does a drop stop bouncing? On one hand, Biance et al. [174] found that heavy drops, i.e., drops larger than their gravito-capillary length $l_c = \sqrt{\gamma/\rho_d g}$, where γ is the drop-air surface tension coefficient, ρ_d is the density of the drop and g is the acceleration due to gravity, cannot bounce. On the other hand, Jha et al. [153] showed that there exists a critical viscosity, two orders of magnitude higher than that of water, beyond which aqueous drops do not bounce either, irrespective of their impact velocity. I.e., both gravity and viscosity counteract the bouncing. In this chapter, we investigate and quantify how exactly gravity and viscous stresses conspire against capillarity to prevent drops from bouncing off non-wetting substrates, using direct numerical simulations. We focus on evidencing the mechanisms of bouncing inhibition, and exhibit a simple criterion delineating the bouncing to non-bouncing transition through an analogy with coalescence-induced drop

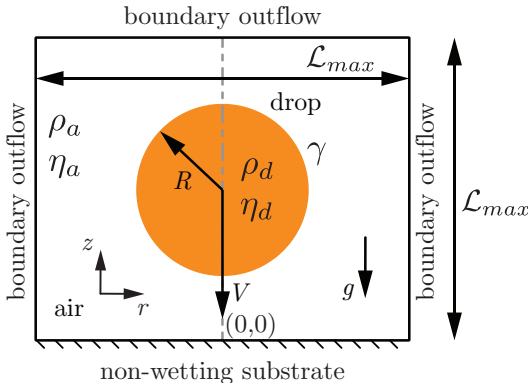


Figure 2.2.1: Axi-symmetric computational domain used to study impact of a drop with radius R and velocity V on an ideal non-wetting substrate. The subscripts d and a denote the drop and air, respectively, to distinguish their material properties, namely, density ρ and viscosity η . The drop-air surface tension coefficient is γ and g denotes the acceleration due to gravity. The gray dashed-dotted line represents the axis of symmetry, $r = 0$. Boundary outflow is applied at the top and side boundaries (tangential stresses, normal velocity gradient, and ambient pressure are set to zero). The domain boundaries are far enough not to influence the drop impact process ($\mathcal{L}_{max} \gg R$).

jumping [175–177].

The chapter is organized as follows: § 2.2 discusses the governing equations employed in this work. § 2.3 explores the bouncing to non-bouncing transition and formulates a criterion for the inhibition of bouncing based on first principles followed by § 2.4 which delves into the limiting cases of this criterion. The paper ends with conclusions and an outlook on future work in § 2.5.

2.2 Governing equations

We employ direct numerical simulations to study the drop impact process (figure 2.2.1), using the free software program Basilisk C [143] that employs the geometric volume of fluid (VoF) method for interface reconstruction [158]. For an incompressible flow, the mass conservation requires the velocity field to be divergence-free (tildes denote dimensionless quantities throughout this manuscript),

$$\tilde{\nabla} \cdot \tilde{\mathbf{v}} = 0, \quad (2.1)$$

where we non-dimensionalize the velocity field with the inertio-capillary velocity $V_{\rho\gamma} = \sqrt{\gamma/\rho_d R}$, where γ , ρ_d and R are the surface tension coefficient between the drop and air, density of the drop, and its radius, respectively, see figure 2.2.1). We can further non-dimensionalize all lengths with the radius of the drop R , time with the inertio-capillary timescale $\tau_{\rho\gamma} = R/V_{\rho\gamma} = \sqrt{\rho_d R^3/\gamma}$, and pressure with the capillary pressure, $p_\gamma = \gamma/R$, to write the momentum equation as

$$\frac{\partial(\tilde{\rho}\tilde{\mathbf{v}})}{\partial\tilde{t}} + \nabla(\tilde{\rho}\tilde{\mathbf{v}}\tilde{\mathbf{v}}) = -\tilde{\nabla}\tilde{p}' + \tilde{\nabla}\cdot(2Oh\tilde{\mathcal{D}}) + \tilde{\mathbf{f}}, \quad (2.2)$$

where the deformation tensor, \mathcal{D} is the symmetric part of the velocity gradient tensor ($= (\nabla\mathbf{v} + (\nabla\mathbf{v})^T)/2$). Note that axial symmetry is assumed throughout this chapter. The Ohnesorge number Oh (ratio of inertio-capillary to inertio-viscous time scales) and the dimensionless density $\tilde{\rho}$ are written using the one-fluid approximation [2, 156] as

$$Oh = \Psi Oh_d + (1 - \Psi) Oh_a, \quad (2.3)$$

$$\tilde{\rho} = \Psi + (1 - \Psi) \frac{\rho_a}{\rho_d}, \quad (2.4)$$

where Ψ is the VoF tracer ($= 1$ for drop and 0 otherwise), and ρ_a/ρ_d is the air–drop density ratio. Here,

$$Oh_d = \frac{\eta_d}{\sqrt{\rho_d\gamma R}} \quad \text{and} \quad Oh_a = \frac{\eta_a}{\sqrt{\rho_d\gamma R}} \quad (2.5)$$

are the Ohnesorge numbers based on the viscosities of the liquid drop and of air, respectively.

To minimize the influence of the surrounding medium, we keep ρ_a/ρ_d and Oh_a fixed at 10^{-3} and 10^{-5} , respectively. Lastly, \tilde{p}' denotes the reduced pressure field, $\tilde{p}' = \tilde{p} + Bo\tilde{z}$, where, \tilde{p} and $Bo\tilde{z}$ represent the mechanical and the hydrostatic pressures, respectively. Here, the Bond number Bo compares gravity to the surface tension force and is given by

$$Bo = \frac{\rho_d g R^2}{\gamma}, \quad (2.6)$$

and \tilde{z} is the distance away from the non-wetting substrate (see figure 2.2.1). Using this reduced pressure approach ensures an exact hydrostatic balance as described in Popinet [154], Popinet and collaborators [155]. This formulation requires an additional singular body force at the interface such that $\tilde{\mathbf{f}}$ takes the form [157],

$$\tilde{\mathbf{f}} \approx \left(\tilde{\kappa} + Bo \left(1 - \frac{\rho_a}{\rho_d} \right) \tilde{z} \right) \tilde{\nabla} \Psi \quad (2.7)$$

where the first and second terms on the right-hand side are the local capillary and hydrostatic pressure jumps across the interface, respectively with $\tilde{\kappa}$ the interfacial curvature calculated using the height-function approach [158].

Figure 2.2.1 shows the axi-symmetric computational domain where we solve the equations discussed above. Initially, we assume that the drop is spherical and that it impacts with a dimensionless velocity, $\tilde{V} = V/V_{\rho\gamma} = \sqrt{We}$, where the impact Weber number

$$We = \frac{\rho_d R V^2}{\gamma} \quad (2.8)$$

is the ratio of the inertial pressure during impact to the capillary pressure. We refer the readers to § 1.B, and Popinet and collaborators [143], Popinet [158, 161], Zhang et al. [178], Sanjay [179] for details of the computational method employed in this work.

2.3 Bouncing inhibition

We investigate the behavior of drops impacting on non-wetting substrates by exploring the influence of the following dimensionless parameters: the Weber number $We = \rho R V^2 / \gamma$, the Bond number $Bo = \rho_d g R^2 / \gamma$, and the Ohnesorge number $Oh_d = \eta_d / \sqrt{\rho_d \gamma R}$. In Figure 2.3.1, we evidence the bouncing to non-bouncing transition in the parameter space spanned by the Ohnesorge and Bond numbers for several fixed Weber numbers. We extract several key pieces of information from this regime map.

- (i) The Weber number has a small influence on the transition between the bouncing and non-bouncing regime in the range probed in this study, $We = 1 - 50$, consistent with Jha et al. [153] for the bouncing inhibition of viscous drops (also see appendix 2.B).

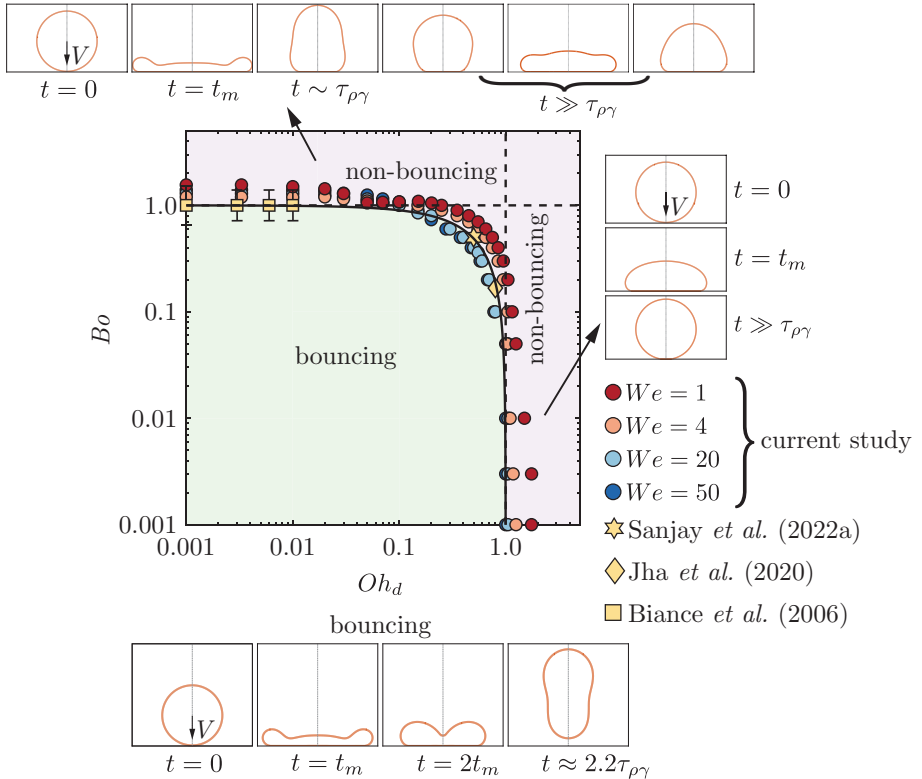


Figure 2.3.1: Regime map in terms of the Bond number $Bo = \rho_d g R^2 / \gamma$ and the drop Ohnesorge number $Oh_d = \eta_d / \sqrt{\rho_d \gamma R}$, marking the bouncing and non-bouncing regimes identified in this work. The data points represent the transition between bouncing and non-bouncing regimes at different Weber numbers We , and the insets illustrate typical cases in these regimes. The yellow data points are extracted from the literature for comparison. The solid black line delineates the theoretical prediction of this transition (equation (2.14)). Lastly, the black dotted vertical and horizontal lines mark the limiting cases, $Oh_{d,c} = 1$ and $Bo_c = 1$, respectively. See also supplementary movie 1.

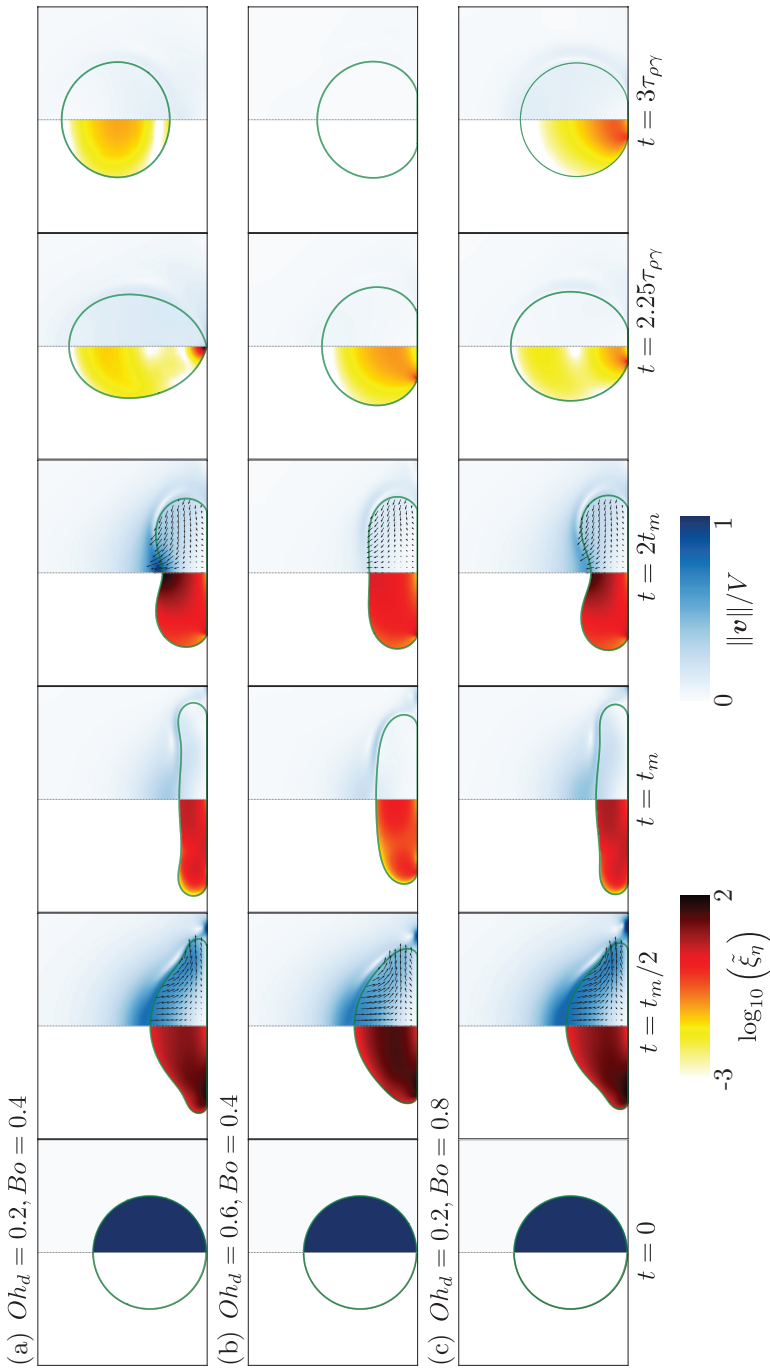


Figure 2.3.2: Three representative cases away from the two asymptotes: direct numerical simulations snapshots illustrating the drop impact dynamics for $(Oh_d, Bo) = (0.2, 0.4)$ (a), $= (0.6, 0.4)$ (b), and $= (0.2, 0.8)$ (c). The left hand side of each numerical snapshot shows the dimensionless viscous dissipation function $\tilde{\xi}_\eta = 2 Oh \left(\tilde{\mathcal{D}} : \tilde{\mathcal{D}} \right)$ on a \log_{10} scale to identify regions of maximum dissipation (black). The right hand side shows the magnitude of the velocity field normalized by the initial impact velocity, V . The black velocity vectors are plotted in the center of mass reference frame of the drop to clearly show the internal flow. For all the cases shown here, the impact Weber number is $We = 20$. See also supplementary movie SM2.

- (ii) We recover the two limiting cases of non–bouncing (see insets of figure 2.3.1): drops smaller than their visco-capillary length, (i.e., $R < \eta_d^2/\rho_d\gamma$) stop bouncing due to viscous dissipation [153], while those larger than their gravito-capillary length, (i.e., $R > \sqrt{\gamma/\rho_d g}$) cannot bounce due to their weight [174]. We elaborate on the mechanisms of rebound inhibition in these two non–bouncing regimes in § 2.4.
- (iii) Experiments performed with millimeter–sized drops of water or silicone oil do not lie on either asymptote, suggesting that both the effect of viscosity and gravity need to be taken into account to predict the bouncing to non–bouncing transition.

In this section, we focus on situations where bouncing is prevented by both viscous and gravitational effects (i.e., $Bo < 1$ and $Oh_d < 1$). Figure 2.3.2 shows snapshots illustrating three representative cases lying in this region of the parameter space for $We = 20$. Each snapshot displays three pieces of information: (i) the position of the liquid–air interface, (ii) the dimensionless rate of viscous dissipation per unit volume (i.e., the viscous dissipation function, left panel), and (iii) the magnitude of the velocity field normalized by the impact velocity (right panel). For $Oh_d = 0.2$ and $Bo = 0.4$ (figure 2.3.2a), the drop undergoes typical rebound dynamics. The liquid first spreads radially up to $t = t_m$, when the maximum extent is reached [28–30, 116]. This stage is followed by liquid retraction [36], parallel to the substrate, until the drop contracts ($t = 2t_m$) and the motion becomes vertical [147, 178]. Finally, the drop leaves the substrate at $t = 2.25\tau_{\rho\gamma}$ [40, 131].

Surprisingly, increasing Oh_d to 0.6, below the critical value reported by Jha et al. [153], while keeping $Bo = 0.4$ (figure 2.3.2b) prevents the rebound. The motion is damped before the drop can bounce off the substrate. Similarly, increasing Bo to 0.8, below the critical value reported by Biance et al. [174], while fixing $Oh_d = 0.2$ (figure 2.3.2c), also inhibits bouncing. Yet, the deposited liquid undergoes multiple oscillation cycles on the substrate before coming to rest (see the last snapshot $t = 3\tau_{\rho\gamma}$).

In all three cases, the impact dynamics and flow in the drop are qualitatively similar until the maximum extent is reached at $t = t_m$. At this instant, the absence of internal flow suggests that the initial kinetic energy has either been converted into surface energy or lost to viscous dissipation, which occurs throughout the drop volume owing to $Oh_d \sim \mathcal{O}(0.1)$ [116]. Close to the bouncing to non–bouncing transition, the rebound can thus be understood as a process which converts an initial surface energy into kinetic energy, disen-

tangling the later stages of the rebound from the initial impact dynamics.

This observation prompts us to introduce an analogy with coalescence-induced jumping, in which an excess surface energy, gained during coalescence, is converted into upward motion of the liquid [175]. The spread drop, at rest at $t = t_m$, reduces its surface area through a Taylor-Culick type retraction [36], converting excess surface energy into kinetic energy. The capillary force driving this radially inwards flow is

$$F_\gamma \sim \gamma R. \quad (2.9)$$

Similarly as in coalescence-induced jumping of two identical drops, a dissipative force $F_\eta \sim \Omega \eta_d \nabla^2 v$, where Ω is the volume of the drop and v is a typical radial flow velocity, opposes the capillarity driven flow [176, 177]. Taking v as $V_{\rho\gamma}$ at leading order, the resistive viscous force scales as

$$F_\eta \sim \eta V_{\rho\gamma} R, \quad (2.10)$$

and the effective momentum converging in the radial direction reads

$$P_r \sim \int (F_\gamma - F_\eta) dt. \quad (2.11)$$

The asymmetry stemming from the presence of the substrate enables the conversion of the radially inward momentum to the upwards direction (figure 2.3.2, $t = 2t_m$). Following Mouterde et al. [176], Lecointre et al. [177], we assume that the vertical momentum scales with the radial one such that $P_v \sim P_r$, allowing us to determine a criterion for the bouncing transition by balancing the rate of change of vertical momentum with the drop's weight F_g

$$\frac{dP_v}{dt} = F_g \sim \rho_d R^3 g. \quad (2.12)$$

Using equations (2.9) – (2.11), we obtain

$$\gamma R - \eta V_{\rho\gamma} R \sim \rho_d R^3 g. \quad (2.13)$$

Lastly, substituting $V_{\rho\gamma} = \sqrt{\gamma/\rho_d R}$, and rearranging, we arrive at a criterion to determine the bouncing to non-bouncing transition as

$$Oh_{d,c} + Bo_c = 1, \quad (2.14)$$

which is independent of the impact Weber number We . In equation (2.14) and throughout the manuscript, the subscript c stands for ‘critical’. Equation (2.14) is the main equation of this chapter. In principle, the derivation of this equation only suggests ~ 1 on the right hand side of equation (2.14) and not $= 1$, but as we will see from the limiting cases treated in § 2.4, the equality sign is justified.

We test the criterion in equation (2.14) for the bouncing and non-bouncing transition against data extracted from our direct numerical simulations and experiments from Jha et al. [153], Biance et al. [174], Sanjay et al. [180]. In figure 2.3.1, the solid black line representing equation (2.14) is in excellent quantitative agreement with the data when viscous and gravitational effects conspire to inhibit bouncing, as well as in the two limiting regimes, $Oh_{d,c} = 1$ for $Bo \ll 1$ [153], and $Bo = 1$ for $Oh_d \ll 1$ [174] (black dotted lines). In the next section, we focus on evidencing the physical mechanisms leading to bouncing suppression in each of the two limiting case.

2.4 Limiting cases

2.4.1 How does a viscous drop stop bouncing?

We first investigate how viscous dissipation prevents drops much smaller than their gravito-capillary length (*i.e.* with $Bo \ll 1$) from bouncing. In this regime, the transition criterion, equation (2.14), reduces to

$$Oh_{d,c} = 1. \quad (2.15)$$

We sweep across this asymptote by setting $Bo = 0$ and systematically varying the drop Ohnesorge number, Oh_d . We characterize the rebound behavior by measuring the apparent contact time between the drop and the substrate t_c and the coefficient of restitution ε , that we define as $\varepsilon = v_{cm}(t_c)/V$, where $v_{cm}(t_c)$ is the center of mass velocity at take-off. The determination of t_c and ε from the DNS is detailed in appendix 2.A. In figure 2.4.1, we plot the coefficient of restitution ε and the normalized contact time $t_c/\tau_{\rho\gamma}$ as a function of Oh_d for Weber numbers ranging from 1 to 50. The effect of Oh_d on t_c and ε is markedly different.

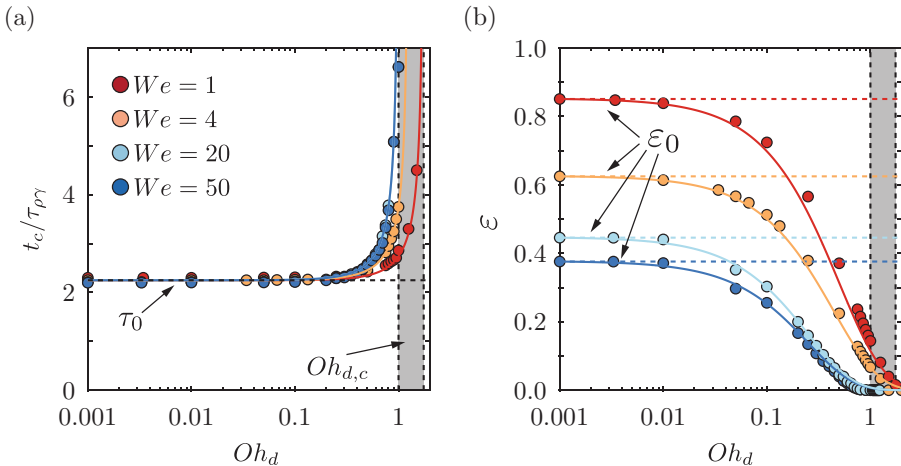


Figure 2.4.1: Light drop asymptote, $Bo = 0$: variation of the (a) contact time t_c normalized by the inertio-capillary timescale $\tau_{\rho\gamma} = \sqrt{\rho_d R^3 / \gamma}$, and (b) restitution coefficient ε with the drop Ohnesorge number Oh_d at different Weber numbers We . In both panels, the solid lines represent the theoretical predictions using a spring-mass-damper system [contact time, equation (2.20) and restitution coefficient, equation (2.21), 153]. The horizontal dotted lines represent the contact time and restitution coefficient values in the limit of inviscid drops ($Oh_d \ll 1$). The limiting value of contact time $\tau_0 = 2.25$ is independent of We while that of restitution coefficient ε_0 depends on We . Lastly, the dotted black vertical lines and the gray shaded regions mark the critical Ohnesorge number $Oh_{d,c} \sim \mathcal{O}(1)$ beyond which drops do not bounce.

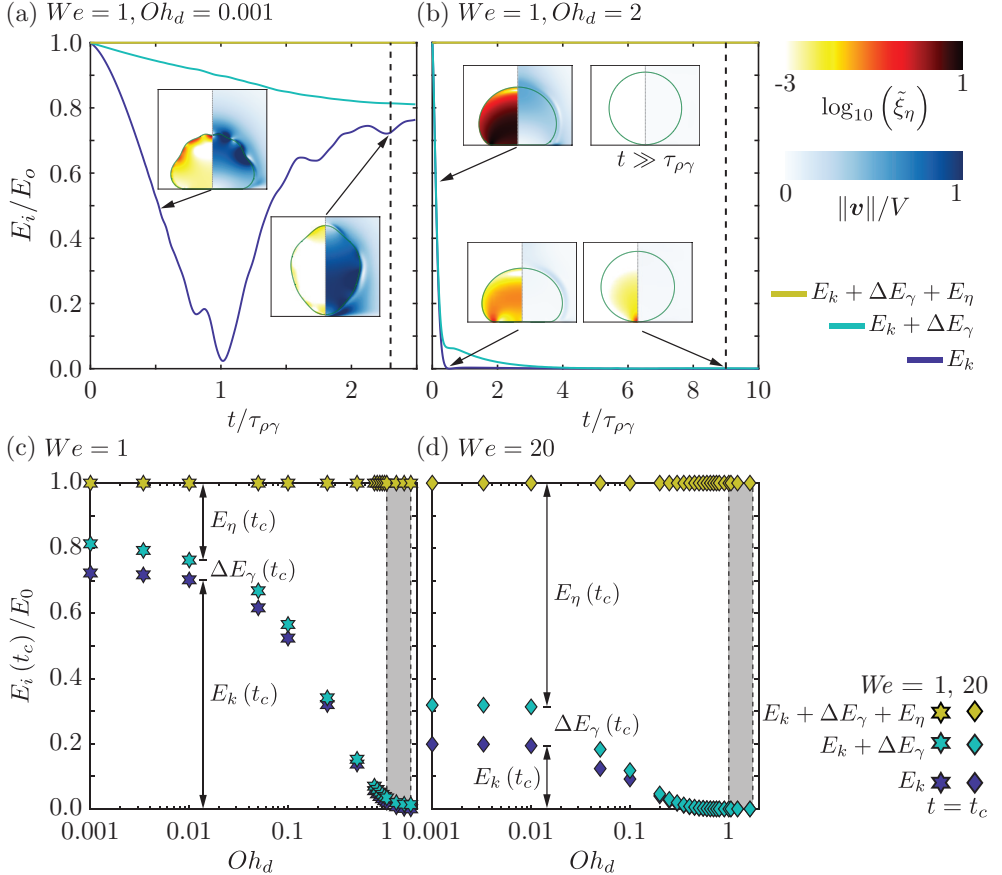


Figure 2.4.2: Details of the light drop asymptote, $Bo = 0$: energy budgets for typical drop impacts at $We = 1$ for $Oh_d = 0.001$ (a) and $Oh_d = 2$ (b). E_k and E_η represent the kinetic energy and viscous dissipation, respectively. ΔE_s denote the change in surface energy with its zero set at $t = 0$. The numerical snapshots in the insets illustrate the drop morphologies and the anatomy of flow inside them. Left hand side of each snapshot shows the dimensionless viscous dissipation function $\tilde{\xi}_\eta = 2Oh(\tilde{\mathcal{D}} : \tilde{\mathcal{D}})$ on a \log_{10} scale to identify regions of maximum dissipation (black). The right hand side shows the magnitude of the velocity field normalized by the initial impact velocity, V . The black dotted lines in panels (a) and (b) mark the instant when the drop takes off and when the normal contact force between the drop and the substrate is minimum, respectively ($t = t_c$). Energy distributions at t_c for $We = 1$ (c) and $We = 20$ (d) as a function of Oh_d . The black vertical lines and the gray shaded regions mark the critical Ohnesorge number $Oh_{d,c} \sim \mathcal{O}(1)$ beyond which drops do not bounce. See also supplementary movie 3.

On the one hand, the coefficient of restitution monotonically decreases from its inviscid, Weber dependent value ε_0 with increasing Oh_d , until a critical Ohnesorge number $Oh_{d,c}$, of order one, marking bouncing inhibition is reached. On the other hand, even increasing Oh_d by over two orders of magnitude hardly affects t_c which keeps its inviscid, Weber independent value $t_c = \tau_0 = 2.25\tau$, expected from the inertia-capillary scaling [131, 181], until t_c diverges as $Oh_{d,c}$ is reached. The value is also in good agreement with the fundamental mode of drop oscillation $\pi/\sqrt{2}$ [115]. Therefore, even as Oh_d is increased, the drop impact and bouncing behavior are still analogous to one complete drop oscillation cycle [153].

To further investigate these behaviors, we seek to understand the different energy transfers by looking at the overall energy budgets in figure 2.4.2. The energy balance reads

$$\tilde{E}_0 = \tilde{E}_k(\tilde{t}) + \Delta\tilde{E}_\gamma(\tilde{t}) + \tilde{E}_\eta(\tilde{t}), \quad (2.16)$$

where the energies are normalized using the capillary energy scale (γR^2), and E_0 is the initial kinetic energy of the drop, ($\tilde{E}_0 = E_0/(\gamma R^2) = (2\pi/3)We$). At any time t , $E_k(t)$ and $E_\gamma(t)$ are the kinetic and surface energy of the drop, with $\Delta E_\gamma(t) = E_\gamma(t) - E_\gamma(t=0)$. Finally, $E_\eta(t)$ is the viscous dissipation until time t . Readers are referred to Wildeman et al. [30], Sanjay et al. [39], Ramírez-Soto et al. [145], Landau and Lifshitz [160] for details of energy budget calculations.

The initial kinetic energy is transferred into surface energy during the impact and spreading phases and back during the retraction and take-off stages. Throughout the process, viscous stresses dissipate energy, hampering the recovery of drop's kinetic energy. For low We and Oh_d , the drop recovers a large proportion of initial kinetic energy, $E_k(t_c) \approx 0.75E_0$ (figure 2.4.2a and $Oh_d \ll 1$ in figure 2.4.2c). It is noteworthy that despite having a small Oh_d , almost 20% of the initial kinetic energy still goes into viscous dissipation, which is restricted to the boundary layer at the drop-air interface and happens primarily due to the high-frequency capillary waves on the surface of the drop [see the insets of figure 2.4.2a and 43, 178]. On the contrary, at high Oh_d , the viscous boundary layer is as large as the drop itself [116] and consequently, dissipation happens throughout the drop (see figure 2.4.2b and its insets). Beyond the critical Ohnesorge number $Oh_{d,c}$, the drop impact process becomes over-damped as the drop loses all its energy by the time it reaches maximum compression, after which it slowly relaxes back to a spherical shape and stays on the substrate (figure 2.4.2b and $Oh_d \sim \mathcal{O}(1)$ in figure 2.4.2c). We can

predict this $Oh_{d,c}$ by balancing the initial kinetic energy $E_0 = (2\pi/3)\rho_d R^3 V^2$ with the viscous dissipation during drop impact given by,

$$E_\eta(t) = \int_0^t \int_\Omega \xi_\eta d\Omega dt = 2\eta_d \int_0^t \int_\Omega (\mathcal{D} : \mathcal{D}) d\Omega dt, \quad (2.17)$$

where ξ_η is the viscous dissipation function and $d\Omega$ is the differential volume of the drop. Guided by our observation that dissipation occurs throughout the drop, we assume that $\|\mathcal{D}\| \sim V/R$, $\Omega \sim R^3$, and we know that even as Oh_d approaches $Oh_{d,c}$, we can still approximate the contact time with the inertio-capillary timescale. Therefore, we get

$$E_\eta(\tau_{\rho\gamma}) \sim \eta_d \left(\frac{V}{R}\right)^2 R^3 \tau_{\rho\gamma}. \quad (2.18)$$

Balancing $E_\eta(\tau_{\rho\gamma})$ with the initial kinetic energy $E_0 \sim \rho_d R^3 V^2$ gives,

$$\rho_d R^3 V^2 \sim \eta_d \left(\frac{V}{R}\right)^2 R^3 \tau_{\rho\gamma}, \quad (2.19)$$

which on rearranging gives $Oh_{d,c} \sim \mathcal{O}(1)$, consistent with the $Bo \rightarrow 0$ limit of equation (2.14), and agreeing well with the gray shaded regions in figure 2.4.1 and 2.4.2. Furthermore, at such high values of Oh_d , the drops become less deformable [182], diminishing the fraction of energy that goes to surface energy at take off (figures 2.4.2c,d).

To further rationalize these observations and predict the dependence of the rebound time and restitution coefficient on Oh_d , we compare our simulation results to the spring-mass-damper system that has been shown to capture these variations successfully [153, 180]. In such a model, the time of apparent contact is given by

$$t_c = \tau_0 \left(\frac{1}{\sqrt{1 - (Oh_d/Oh_{d,c})^2}} \right), \quad (2.20)$$

and matches well with the simulation data (figure 2.4.1a). Here, the critical Ohnesorge number $Oh_{d,c}$ at which bouncing stops is taken from simulations.

By evaluating the drop's take-off velocity at this instant, Jha et al. [153] predicted the coefficient of restitution, written in our notations, as

$$\varepsilon = \varepsilon_0 \exp \left(\frac{-\beta Oh_d / Oh_{d,c}}{\sqrt{1 - (Oh_d / Oh_{d,c})^2}} \right), \quad (2.21)$$

where ε_0 is the We -dependent coefficient of restitution in the inviscid drop limit (see appendix 2.B) and $\beta = 4 \pm 0.25$ is a fitting parameter that best fits our data (notice the remarkable agreement in figure 2.4.1b). Note that Jha et al. [153] further reduced equation (2.21) to $\varepsilon \approx \varepsilon_0 \exp(-\alpha Oh_d)$ for $Oh_d \ll Oh_{d,c}$, where $\alpha = \beta / Oh_{d,c} = 2.5 \pm 0.5$ best fits all their experimental datapoints, independent of the impact Weber number. The equivalent fitting parameter for our case is $\alpha' = \beta' / Oh_{d,c} = 3 \pm 1$, which is very close to Jha et al. [153], despite a difference in Bo [0 here vs. 0.167 for 153, also see § 2.4.2, and appendix 2.B].

Lastly, figure 2.4.1 also highlights that $Oh_{d,c}$ varies weakly with We , $Oh_{d,c} = 1.75, 1.5, 1, 1$ at $We = 1, 4, 20, 50$, respectively, as evidenced by the narrow grey shaded region, and in agreement with the limit predicted from equation (2.14). We stress that the variation of the coefficient of restitution in the shaded region, where $\varepsilon < 0.1$, is weak and would not be noticed in typical side view experiments. Indeed, $\varepsilon = 0.1$ corresponds to a center of mass rebound height of 0.01 times the initial impact height that sets We . For $We = 1$, this gives a rebound height of 10 μm which is too small to be experimentally measurable.

The primary influence of We is to decrease the inviscid limit restitution ε_0 . To understand this behavior, we also plot the energy distribution at take-off for $We = 20$ in figure 2.4.2(d). We clearly observe that irrespective of the drop Ohnesorge number, the viscous dissipation is higher for $We = 20$ as compared to that of $We = 1$ (figure 2.4.2c). Even more strikingly, the fraction of energy lost to viscous dissipation amounts to almost 70% of the initial energy, even in the inviscid drop limit for $We = 20$. This increase in dissipation can be attributed to more deformable drops at higher We and flow enhancement during retraction owing to a strong radially inward flow field (see the inertial regime of chapter 1). The dissipation is not only restricted to the boundary layers at the drop-air free-surface but also at the axis of drop when the retraction phase ends (see figure 1.2 which has the same We based on the radius of the drop). Consequently, ε decreases with increasing We . We further elaborate on this variation in appendix 2.B.

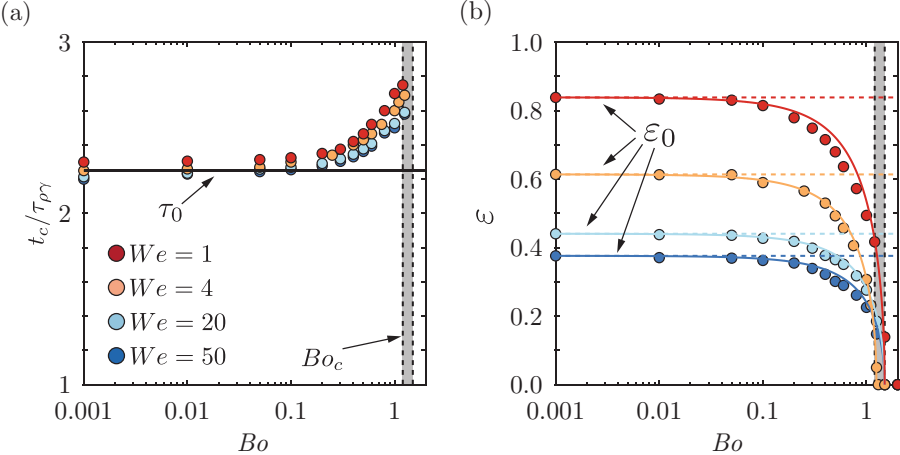


Figure 2.4.3: Inviscid drop asymptote ($Oh_d = 0.01 \ll 1$): variation of the (a) contact time t_c normalized by the inertia-capillary timescale $\tau_{\rho\gamma} = \sqrt{\rho_d R^3 / \gamma}$, and (b) restitution coefficient ε with the Bond number Bo at different Weber numbers We . In both panels, the solid lines represent the theoretical predictions from a spring-mass analogy [equation 2.24, 174]. The horizontal dotted line in panel (b) represents the restitution coefficient values in the limit of zero Bond number ($Bo \rightarrow 0$). This limiting value of restitution coefficient ε_0 depends on We . Notice that although the restitution coefficients match with the predictions from the model, the contact time show slight deviations from the prediction of a constant contact time, $\tau_0 = 2.25$, when Bo_c is approached. Lastly, the dotted black vertical lines and the gray shaded regions mark the critical Bond number $Bo_c \sim \mathcal{O}(1)$ beyond which drops do not bounce.

2.4.2 How does a heavy drop stop bouncing?

For drops much larger than their visco-capillary lengths (drop Ohnesorge number $Oh_d \ll 1$), the criterion for bouncing inhibition (equation (2.14)) reduces to

$$Bo_c = 1. \quad (2.22)$$

In this section, we sweep across this asymptote by setting $Oh_d = 0.01 \ll 1$ and systematically varying the Bond number, Bo . The choice of Oh_d stems from the constancy of ε and viscous dissipation as shown in figures 2.4.1 and 2.4.2 for $Oh_d \lesssim 0.01$, and discussed later in this section.

At this asymptote, increase in Bo hardly influences the drop contact time. This behavior is similar to the $Oh_d = 0$ asymptote (§ 2.4.1). However, in contrast to that asymptote, even as we approach Bo_c , beyond

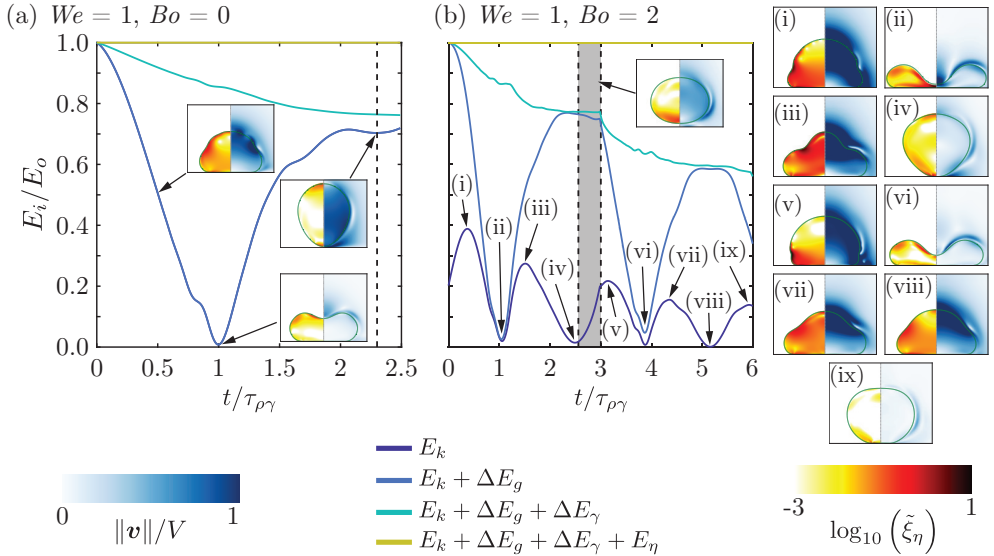


Figure 2.4.4: Details of the inviscid drop asymptote ($Oh_d = 0.01 \ll 1$): energy budgets for typical drop impacts at $We = 1$ for $Bo = 0$ (a) and $Bo = 2$ (b) in the limit of inviscid drops. E_k and E_η represent the kinetic energy and viscous dissipation, respectively. ΔE_g and ΔE_s denote the change in gravitational potential energy and surface energy, respectively with their zeroes set at the instant of maximum spreading of the impacting drop, and at $t = 0$, respectively. The numerical snapshots in the insets illustrate the drop morphologies and the anatomy of flow inside them. Left hand side of each snapshot shows the dimensionless viscous dissipation function $\tilde{\xi}_\eta = 2Oh(\tilde{\mathcal{D}} : \tilde{\mathcal{D}})$ on a \log_{10} scale to identify regions of maximum dissipation (black). The right hand side shows the magnitude of the velocity field normalized by the initial impact velocity V . The black dotted line in panel (a) marks the instant when the drop takes off, setting $t_c = 2.3\tau_{\rho\gamma}$. In panel (b), the black vertical lines and the gray shaded regions bound the time interval when the normal contact force between the drop and the substrate is zero. See also supplementary movie 4.

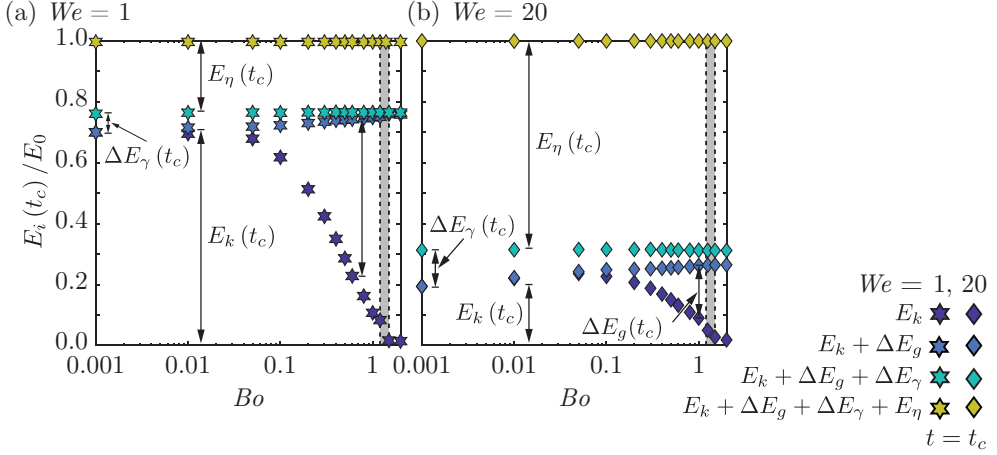


Figure 2.4.5: Details of the inviscid drop asymptote ($Oh_d = 0.01 \ll 1$): energy distributions at t_c for $We = 1$ (a) and $We = 20$ (b) as a function of Bo . For non-bouncing cases, t_c represents the end of first drop oscillation cycle, for example $t_c = 2.5\tau_{\rho\gamma}$ in figure 2.4.4(b). The black vertical lines and the gray shaded regions in each panel mark the critical Bond number $Bo_c \sim \mathcal{O}(1)$ beyond which drops do not bounce.

which the drop cannot leave the substrate, the contact time is only marginally higher than τ_0 (its value at $Bo = 0$, figure 2.4.3a). Of course, for $Bo > Bo_c$, the contact time t_c is undefined. Similarly, as $Bo = Bo_c$ is reached, the restitution coefficient decreases sharply to zero. However, in the intermediate range, $0 < Bo < Bo_c$, the restitution coefficient deviates only slowly from ε_0 , its We -dependent value at zero Bond number (figure 2.4.3b). Finally, yet another similarity to the previous asymptote is the influence of increasing the impact Weber number, We which does not change the contact time but decreases the restitution coefficient monotonically (figure 2.4.3b). Moreover, We only weakly influences the critical Bond number Bo_c (gray shaded region in figure 2.4.3).

To further investigate these behaviors, we seek to understand the different energy transfers by looking at the overall energy budgets in figure 2.4.4. The energy balance (equation (2.16)) now has an additional contribution due to gravitational potential energy, ΔE_g , whose zero is set at the instant of maximum drop compression. The modified energy balance reads

$$\tilde{E}_0 = \tilde{E}_k(\tilde{t}) + \Delta \tilde{E}_g + \Delta \tilde{E}_\gamma(\tilde{t}) + \tilde{E}_\eta(\tilde{t}), \quad (2.23)$$

where the initial energy also includes gravity, $\tilde{E}_0 = (4\pi/3)(We/2 + Bo(1 - \mathcal{H}))$, where \mathcal{H} is the center of mass height of the drop at maximum compression.

Figure 2.4.4(a) illustrates the energy budget for $(We, Oh, Bo) = (1, 0.01, 0)$. Comparing it with the case shown in figure 2.4.2(a) (where $Oh = 0.001$), surprisingly, we encounter many similarities. They follow similar temporal dynamics, and the fraction of kinetic energy recovered at take-off and the viscous dissipation until this instant are the same, even though Oh differs by an order of magnitude. Although a higher Oh_d increases the viscous boundary layer and the dissipation is spread throughout the drop, it attenuates most of the high-frequency capillary waves, decreasing the local viscous dissipation function (*c.f.*, insets of figures 2.4.2a and 2.4.4a). Consequently, the total dissipation is the same and explains the constancy of ε .

We now look at a case where $Bo > Bo_c$, see figure 2.4.4(b). Just before impact, the drop has a higher initial energy owing to the contribution from gravitational potential. As a result, upon impact with the substrate, the drop accelerates until the inertial shock propagates throughout the drop [see figure 2.4.4b-i and 27, 62], after which the kinetic energy decreases as the drop then reaches maximum compression (figure 2.4.4b-ii). The maximum spreading time ($t_m \approx \tau_{\rho\gamma}$) is same for both cases even though the drop undergoes more deformation at a higher Bo . This higher deformation coupled with an accelerated flow owing to gravity, enhances the absolute viscous dissipation but, coincidentally, the ratio of this dissipation to the initial energy is still similar to the case of $Bo = 0$. During the retraction stage, the kinetic energy of the drop increases (figure 2.4.4b-ii to 2.4.4b-iii) until the motion goes from being dominantly in the radial direction to being dominantly in the axial direction [figure 2.4.4b-iii, $t \approx 1.5\tau_{\rho\gamma}$, see 147, 178]. Beyond this instant, gravity opposes the upward motion of the drop as its kinetic energy decreases and eventually at $t \approx 2.5\tau_{\rho\gamma}$ (figure 2.4.4b-iv) the center of mass of the drop starts moving in the downward direction. By this time, only $\approx 20\%$ of drop's initial energy goes to viscous dissipation, identical to the case of $Bo = 0$. Interestingly, the drop can still detach from the substrate owing to capillary oscillations (see the gray shaded region in figure 2.4.4b and the corresponding inset), but the center of mass velocity is always in the downward direction and we categorize this case as non-bouncing. Subsequently, the drop undergoes several capillary oscillations at the substrate with a time period of $\approx 2.5\tau_{\rho\gamma}$ (figure 2.4.4b-v to 2.4.4b-ix) until all its energy is lost to viscous dissipation [174].

In summary, as Bo increases, the fraction of initial energy that goes into viscous dissipation is constant. However, the gravitational potential energy

increases, leading to a decrease in both the surface and kinetic energy of the drop at take-off, which eventually stops bouncing at Bo_c (figure 2.4.5a,b). To further rationalize these observations and predict the dependence of ε on Bo , guided by our simulation results, we used the simplest non-dissipative spring-mass model that incorporates gravity, developed by Biance et al. [174], written in our notation as

$$\varepsilon = \varepsilon_0 \sqrt{\left(1 - \frac{Bo}{Bo_c}\right) \left(1 + \frac{1}{3} \frac{Bo}{Bo_c}\right)}. \quad (2.24)$$

This expression perfectly reproduces the variation of ε across the entire range of Bo (figure 2.4.3b). Here, we extract Bo_c from our simulation data.

2.5 Conclusions and outlook

Drops smaller than their visco-capillary length, i.e., $Oh_d > 1$ stop bouncing due to viscous dissipation, while those larger than their gravito-capillary length, i.e., $Bo > 1$ cannot bounce due to their weight. In this contribution, we have addressed the bouncing inhibition for drops of intermediate sizes (i.e., $\eta_d^2/\rho_d\gamma < R < \sqrt{\gamma/\rho_d g}$). Particularly, we investigated how viscous stresses and gravity conspire against capillarity to inhibit drop bouncing off non-wetting substrates. Drawing an analogy with the case of coalescence-induced jumping of two identical drops [175–177], we proposed the criterion, $Oh_{d,c} + Bo = 1$, for this bouncing to non-bouncing transition. Through a series of direct numerical simulations, we showed the validity of this criterion over a wide range of We in the Bo – Oh_d phase space. We also studied the two limiting cases and elucidated how the drops stop bouncing by exploring the drop morphology and flow anatomy. These two asymptotes show several distinguishing features.

For drops much smaller than their gravito-capillary lengths ($Bo \ll 1$), as the Oh_d increases, the drop impact and bouncing behavior are still analogous to one complete drop oscillation cycle. The time of contact hardly changes from its inviscid limit even when Oh_d is increased over two orders of magnitude until a critical Ohnesorge number $Oh_{d,c} \sim \mathcal{O}(1)$ is reached at which the contact time diverges. On the other hand, the restitution coefficient decays exponentially with increasing Oh_d , owing to increased viscous dissipation. These observations are consistent with previous studies and the spring-mass-damper theoretical model developed by Jha et al. [153]. Beyond the critical

Ohnesorge number, the process becomes over-damped as the drop loses all its energy by the time it reaches maximum compression, after which it slowly relaxes back to a spherical shape and stays on the substrate.

For drops much larger than their visco-capillary lengths ($Oh_d \ll 1$), similar to the above asymptote, an increase in Bo hardly influences the drop contact time. Even as we approach the critical Bond number $Bo_c \sim \mathcal{O}(1)$, beyond which the drop cannot leave the substrate, the contact time is only marginally higher than its value at $Bo \rightarrow 0$. Moreover, the restitution coefficient deviates slowly from ε_0 , its We -dependent value at zero Bond number, until Bo_c is reached, decreasing sharply to zero. We used the simplest non-dissipative spring-mass model that incorporates gravity, developed by Biance et al. [174], to study this behavior which matches perfectly with our simulation results in the inviscid drop limit. Indeed, an increase in Bo does not change the fraction of the initial energy of the drop that goes into viscous dissipation during the drop impact and retraction process. Beyond Bo_c , the drop stops bouncing because the flow generated during the retraction phase is insufficient to lift the drop owing to its weight. Lastly, contrary to the viscous limit, even when the drop cannot leave the substrate, it has sufficient surface and kinetic energies to undergo several oscillation cycles at the substrate.

We further emphasize that both the bouncing inhibition and drop contact time are reasonably insensitive to an increase in impact Weber number (We), which only manifests as a decrease in the restitution coefficient owing to higher viscous dissipation provided, of course, that We is not too small ($We \ll 1$) or not too large ($We \gtrsim 100$), so that axial symmetry would be broken.

We emphasize here that this work deciphers the theoretical upper bound of the bouncing to non-bouncing transition on an ideal non-wetting substrate. Indeed, the water drops can cease bouncing due to substrate pinning on non-ideal superhydrophobic substrates [183]. We further make idealization regarding the surrounding medium by keeping its Ohnesorge number small ($Oh_a = 10^{-5}$) so that it does not influence the impact process, and the dissipation is primarily inside the drop. The surrounding medium might play a role in the impact of microdroplets if Oh_a is comparable to Oh_d [80, 184]. Lastly, we solely focus on drops impacting with velocities exceeding or equal to their inertio-capillary velocity ($We \geq 1$). It will be interesting to extend this work for $We \ll 1$ where the drops only deform weakly, and the velocity field inside them is still significant at the instant of maximum spreading. One can either use a quasi-static model of bouncing drops [150] or an analogy with non-linear springs [185] to probe that regime. Another extension would be to the case of very large We

so that the axial symmetry is lost and full three-dimensional simulations must be calculated, but this regime is beyond the scope of the present work.

Acknowledgments

We thank Aditya Jha for sharing data. We also thank Uddalok Sen, Maziyar Jalaal, Andrea Prosperetti, David Quéré, and Jacco Snoeijer for stimulating discussions. We acknowledge Srinath Lakshman for preliminary experiments that made us numerically and theoretically explore the effect of gravity in viscous drop bouncing.

Appendix

2.A Measuring the restitution coefficient

Throughout this chapter, we have used the time of contact and restitution coefficient to study the drop impact dynamics. In this appendix, we describe how to consistently measure this restitution coefficient which is the ratio of take-off velocity $v_{\text{cm}}(t_c)$ to the impact velocity V ,

$$\varepsilon = \frac{v_{\text{cm}}(t_c)}{V}, \quad (2.25)$$

where t_c denotes the contact time when the drop leaves the substrate. Note that for our simulations, we assume an ideal non-wetting substrate by ensuring that a thin air layer (with a minimum thickness of $\Delta = R/1024$, where Δ is the minimum grid size employed in the simulations), is always present between the drop and the substrate [also see 145]. Inspired by chapter 1, we define the end of contact as the instant when the normal reaction force $F(t)$ between the substrate and the drop is zero [for calculation details, see equation (1.1) and 178], as shown in figure 2.A.1(a). Subsequently, we read out the center of mass velocity (figure 2.A.1b) at this instant. If this center of mass velocity is not in the upward direction (i.e., it is zero or negative), we categorize the case as non-bouncing. For the representative case in figure 2.A.1, $\varepsilon = 0.47$.

2.B Influence of Weber number

This work shows that the bouncing inhibition and drop contact time are fairly insensitive to an increase in the impact Weber number (in the range $1 \leq We \leq 50$) while the restitution coefficient decreases monotonically due to higher viscous dissipation. To further investigate this dependence, figure 2.B.1

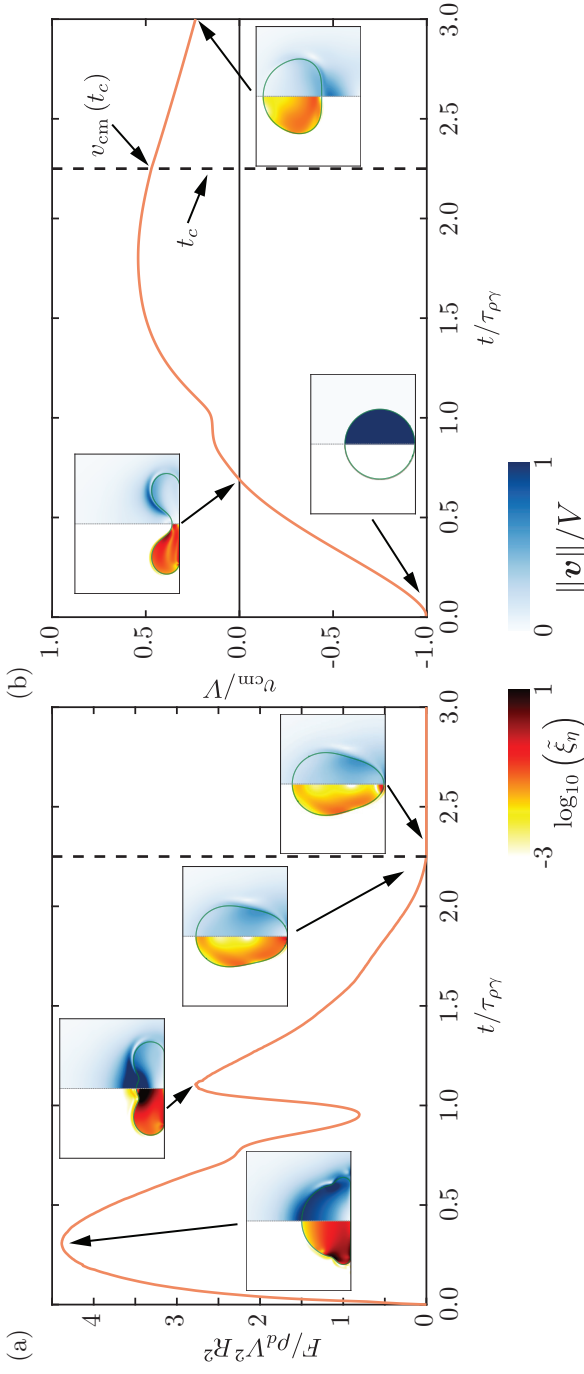


Figure 2.A.1: A representative temporal variation of (a) the normal reaction force F on the drop and (b) its center of mass velocity v_{cm} . Time is normalized using the inertia-capillary timescale $\tau_{\rho\gamma}$. Insets illustrate the different stages of drop impact process. The background shows the magnitude of the rate of viscous dissipation per unit volume ($\tilde{\xi}_\eta = 2O\!h(\tilde{\mathcal{D}} : \tilde{\mathcal{D}})$) on the left and the magnitude of velocity field normalized by the impact velocity on the right. The vertical dashed black line represents the contact time calculated using the criterion, $F = 0$ marking the end of contact between the drop and the substrate. Here, $(W_e, O\!h_d, Bo) = (4, 0.034, 0.5)$, the contact time $t_c = 2.25\tau_{\rho\gamma}$, and the coefficient of restitution $\varepsilon = 0.47$.

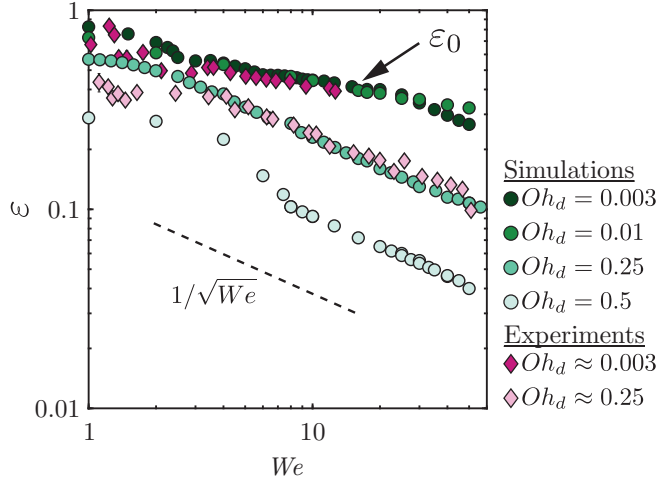


Figure 2.B.1: Variation of restitution coefficient with the impact Weber number (We) at different drop Ohnesorge number (Oh_d). The simulations (circle data points) match perfectly with the experimental results (diamond data points) of Jha et al. [153] without any fitting parameters. ε_0 is the restitution coefficient in the inviscid drop limit. The black dotted line represents $1/\sqrt{We}$. Here, the Bond number $Bo = 0.167$.

illustrates this variation of restitution coefficient with We . In the inviscid drop limit ($Oh_d \lesssim 0.1$), ε_0 marks the restitution coefficient which we use to scale the theoretical models used in § 2.4 [also see 153, 174]. For this range of impact Weber number $1 \leq We \leq 50$, ε_0 does not follow the $1/\sqrt{We}$ scaling relation developed by Biance et al. [174]. Interestingly, the restitution coefficient for viscous drop impacts ($Oh_d \gtrsim 0.1$) seems to follow this scaling relation, implying that the take-off velocity scales with the Taylor-Culick velocity ($v_{cm}(t_c) \sim \sqrt{\gamma/\rho_d R}$), and is independent of the impact velocity V , consistent with our assumption that the retraction and take-off stages are independent of the Weber number and disentangled from the initial impact dynamics. We caution here that the range of We is too small to claim these scaling relations convincingly. Lastly, notice the remarkable agreement between our simulations and the experimental data points from Jha et al. [153] for two different drop Ohnesorge numbers, which differ by over two orders of magnitude.

2.C Code availability

The codes used in the present article are permanently available at Sanjay [179].

2.D Supplemental movies

These supplemental movies are available at Sanjay [[external YouTube link, 186](#)].

In all these videos, the left hand side of each snapshot shows the dimensionless viscous dissipation function $\tilde{\xi}_\eta = 2Oh(\tilde{\mathcal{D}} : \tilde{\mathcal{D}})$ on a \log_{10} scale to identify regions of maximum dissipation (black). The right hand side shows the magnitude of the velocity field normalized by the initial impact velocity, V .

- 2**
- SM1: Typical bouncing (left) and non-bouncing drop cases that we study in this work. Also see figure 2.3.1.
 - SM2: Three representative cases away from the two asymptotes: direct numerical simulations snapshots illustrating the drop impact dynamics. Also see figure 2.3.2.
 - SM3: To study the details of the light drop asymptote, $Bo = 0$, here we show two typical cases to show inhibition of bouncing owing to enervation of internal momentum by viscous dissipation.
 - SM4: To study the details of the inviscid drop asymptote, $Oh_d = 0.01 \ll 1$, here we show two typical cases to show how gravity ceases the bouncing of a drop by pulling it down. Note that even though the case with $Bo = 2$ manages to leave the substrate, its center of mass velocity vector points downwards throughout the duration when it is levitating over the substrate.

chapter 2: when does a drop stop bouncing?



source code



supplemental movies

Chapter 3

Drop impact on viscous liquid films^o

3

When a liquid drop falls on a solid substrate, an air layer is trapped between them, delaying the occurrence of liquid–solid contact. For impacts on smooth substrates, such an air film can prevent wetting, allowing the drop to bounce off with dynamics identical to that observed for impacts on superamphiphobic materials. In this chapter, we investigate similar bouncing phenomena, occurring on viscous liquid films, that mimic atomically smooth substrates, with the goal to probe their repellent properties. In the case of highly viscous or very thin films, the impact dynamics are not affected by the presence of the viscous film. Within this substrate–independent limit, repellency is suppressed once the drop viscosity exceeds a critical value as on superamphiphobic substrates. For thicker or less viscous films, both the drop and film properties influence the rebound dynamics and conspire to inhibit bouncing above a critical film thickness. This substrate–dependent regime also admits a limit, for low viscosity drops, in which the film properties alone determine the limits of repellency. We elucidate the mechanisms associated to the bouncing to floating transition using experiments, simulations, and a minimal model that predicts the main characteristics of drop impact, the contact time and coefficient of restitution.

^oSubmitted as: **Vatsal Sanjay**, Srinath Lakshman, Pierre Chantelot, Jacco H. Snoeijer, and Detlef Lohse, *Drop impact on viscous liquid films*, J. Fluid Mech. Simulations are done by Sanjay; experiments by Lakshman; writing and analysis by Sanjay, Lakshman, and Chantelot; and supervision by Snoeijer and Lohse. Proofread by everyone.

3.1 Introduction

Liquid drop impact on solids and liquids abound in nature [45] and are essential for several industrial applications, such as inkjet printing [16] and criminal forensics [22]. Consequently, drop impact has garnered extensive attention [41, 42, 170, 172, 187] ever since the seminal work of Worthington [14, 188]. Impacts can result in either contact or levitation (bouncing/floating) outcomes, depending on whether the air layer trapped between the drop and the substrate drains completely during impact.

For low impact velocities, the buildup of the lubrication pressure in the draining air layer prevents the drop from contacting with the underlying surface, leading to drop bouncing/floating on this layer [76, 189–192]. Drops that bounce/float in such a scenario are realized in several configurations, for example on solid surfaces [80, 193], liquid films [118, 194–196], stationary [197–199] or vibrating liquid pools [200, 201], or even soap films [202]. Interfacial processes such as Marangoni flow [65] or the generation of vapor below a drop deposited on a superheated substrate [the Leidenfrost effect where the liquid levitates on a cushion of its own vapor, 4–6, 69] can further stabilize the sandwiched air/vapor layer to facilitate levitation, even for the dynamic case of drop impact [66–68]. Drops can also defy gravity and levitate thanks to the so-called inverse Leidenfrost effect [70–72], or electromagnetic forces [73, 74].

At higher impact velocities, the air layer ruptures, leading to contact. The rupture occurs due to a strong van der Waals attractive force between the droplet and the substrate, which comes into play as the thickness of the gas layer reduces below a thickness of the order of $10 - 100$ nm [see appendix 3.A, and 203–205]. Additionally, surface asperities that are of the order of the minimum gas layer thickness can also cause rupture, binding the drop to the surface [80, 206, 207].

In this work, we perform experiments and direct numerical simulations (DNS) to investigate drop rebound on viscous liquid films. In the limit of thin enough viscous coatings, the substrate mimics an atomically smooth solid and displays a superamphiphobic-like repellent behavior [195, 208]. This substrate-independent bouncing [208–211] can be compared with that observed on superhydrophobic substrates whereby the apparent contact time is given by the oscillation time of a drop [115], owing to the drop impact-oscillation analogy [131]. However, unlike ideal Rayleigh oscillations, the collisions are partially inelastic due to viscous dissipation [212]. The elasticity of such impacts can be increased by reducing the viscosity of the drop

[40, 131]. As a result, such an impacting drop can be modeled using quasi-ideal spring with stiffness given by the surface tension coefficient [213]. In addition, when the drop viscosity increases and viscous dissipation becomes significant, this spring couples with a linear damper whose strength is proportional to the drop’s viscosity [see appendix 3.B, and 153]. The adoption of such a spring-mass-damper system has led to several successful predictions of the drop impact dynamics in a variety of configurations such as viscous bouncing [150, 153], spontaneous levitation [214], fast bouncing [215], and walking drops [216].

In the opposing limit of thick liquid films (pools), drops can also bounce/float [64, 217]. However, unlike solids and very thin films, these pools deform on impact and can absorb a part of the impact kinetic energy in the form of (i) interfacial deformation, (ii) internal kinetic energy, and (iii) viscous dissipation [182]. Consequently, the impact outcomes also include a substrate-dependent regime which culminates in the transition from bouncing to floating, where the drop cannot take off from the liquid surface which loses its repellent property. Hao et al. [195] studied the transition from the substrate-independent to substrate-dependent bouncing for water drops and reported that the critical film thickness marking this transition depends on the film viscosity and the impact velocity of the drops.

Here, we aim to understand how the thickness and viscosity of liquid coatings influence the rebound characteristics, culminating in the loss of repellency, that is the transition from bouncing to floating. We seek to disentangle how the initial kinetic energy of an impacting drop can be absorbed through dissipation and energy transfers in the drop and the liquid film.

The chapter is organized as follows: § 3.2 describes the experimental and numerical methods followed by § 3.3, where we discuss the phenomenology of the drop impact dynamics on viscous liquid films. Guided by our experimental and numerical observations, we develop a phenomenological model in § 3.4, extending on the spring-mass-damper analogy by considering the coating as an additional source of dissipation. In § 3.5, we test the validity and applicability of this model by comparing the predicted values of the coefficient of restitution with our observations when varying both the drop and film properties. We also delineate the various regimes observed in this work by measuring the critical film thicknesses at which the substrate-independent to substrate-dependent and bouncing to floating transitions occur and compare their observed values with the model predictions. Further, § 3.6 delves into the cases where our phenomenological model fails to predict the observed dynamics. The chapter

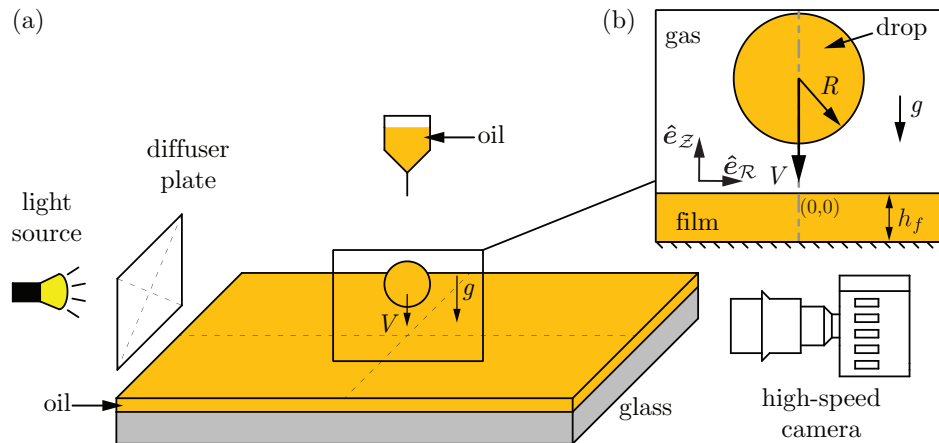


Figure 3.1.1: (a) Schematic (not to scale) of the experimental setup. (b) Side view visualization of the drop impact process as viewed using the high-speed camera. This inset also shows the axi-symmetric domain used in the direct numerical simulations.

ends with a conclusion and outlook in § 3.7.

3.2 Methods

3.2.1 Experimental details

Our experiments, outlined in figure 3.1.1, consist of silicone oil droplets, with radius R , density ρ_d , and viscosity η_d , impacting on silicone oil films with thickness h_f , density ρ_f , and viscosity η_f . We choose silicone oil as a working fluid as its viscosity can be varied over a wide range, here from 0.8 mPa.s to 96 mPa.s, while keeping its density and surface tension coefficient (γ) nearly constant, as evidenced in table 3.2.1. Droplets with radius $R = 1.0 \pm 0.1$ mm are released from a calibrated needle tip whose height can be varied to adjust the impact velocity V from 0.1 m/s to 0.5 m/s. The rupture of the air layer, mediating the interaction between the drop and the film, determines the upper bound of the bouncing regime and sets the maximal impact velocity, here Weber number (i.e., ratio of inertial to capillary stresses) $We \equiv \rho_d RV^2/\gamma \lesssim \mathcal{O}(10)$ [see appendix 3.A and 204, 218]. We further fix the impact velocity at $V = 0.3 \pm 0.03$ m/s, corresponding to $We = 4$, and focus on the influence of the material properties of the drop and the film on the impact process (see § 3.2.2). Indeed, this process is fairly independent of We in the narrow range

Silicone oil	ρ (kg/m ³)	η (mPa.s)	γ (mN/m)
SE 1	818	0.8	17
AK 5	920	4.6	19
AK 10	930	9.3	20
AK 20	950	19	21
AK 35	960	34	21
AK 50	960	48	21
AK 100	960	96	21

Table 3.2.1: Properties of liquids used in the experiments. γ is the liquid-air surface tension coefficient. The silicone oil manufacturers are Shin Etsu (SE) and Wacker Chemie AG (AK).

of We in which bouncing occurs without air layer rupture (see appendices 3.A and 3.C).

Films of controlled thickness, varying from 0.01 mm to 1 mm, are prepared by spincoating the liquid for $h_f < 0.03$ mm, or by depositing a known volume of silicone oil on a glass slide and allowing it to spread when $h_f > 0.03$ mm. We measure the thickness of spincoated films using reflectometry [219], with an uncertainty of ± 0.1 μ m, while the thicker films obtained from the deposition method are characterized from side-view imaging, using a procedure detailed in appendix 3.D, with an uncertainty of ± 30 μ m. We record the impact dynamics using a high-speed side-view imaging at 10,000 frames per second (Photron UX100).

3.2.2 Governing equations & Numerical framework

This section elucidates the direct numerical simulation (DNS) framework used to study the drop impact process with the free software program, Basilisk C [143], using the volume of fluid (VoF, equation (3.1) for tracking the interface, Tryggvason et al. 2, Prosperetti and Tryggvason 156). In this work, we have three fluids, namely, the drop, film, and air, denoted by (d), (f), and (a), respectively (figure 3.1.1). In order to track the three fluids and employ the non-coalescence between the drop and the film, we use two VoF tracer fields, Ψ_1, Ψ_2 [145]

$$\left(\frac{\partial}{\partial t} + \mathbf{v} \cdot \nabla \right) \{ \Psi_1, \Psi_2 \} = 0, \quad (3.1)$$

where \mathbf{v} is the velocity field. The use of two VoF fields, followed by interface reconstruction and implicit tagging of the air medium ($= 1 - \Psi_1 - \Psi_2$), ensures that the two tracers never overlap [145, 220]. As a result, there is always a thin air layer between the two liquids. Our continuum-based simulations are thus not sufficient to predict the coalescence or non-coalescence of interfaces [204]. We take this information from experiments (see appendix 3.A for details).

The adaptive mesh refinement (AMR) allows us to resolve all the length scales pertinent to the flow. The adaption is based on minimizing the error estimated using the wavelet algorithm [161] in the volume of fluid tracers, interfacial curvatures, velocity field, vorticity field and rate of viscous dissipation with tolerances of 10^{-3} , 10^{-4} , 10^{-2} , 10^{-2} , and 10^{-3} [221]. We ensure that at least 15–20 grid cells are present across the minimum liquid film thickness ($\Gamma = h_f/R = 0.01$) studied in this work to resolve the velocity gradients in the film [222, 223]. The minimum thickness of the air layer is of the order of the minimum grid size $\Delta = R/2048$. Further note that this thickness can be greater than this minimum owing to flow characteristics. For example, the shear stress balance across the interface with high viscosity ratios delays the drainage of air layer [224].

For an incompressible flow, the mass conservation requires the velocity field to be divergence-free. Furthermore, the momentum conservation reads (tildes denote dimensionless quantities)

$$\left(\frac{\partial}{\partial \tilde{t}} + \tilde{\mathbf{v}} \cdot \tilde{\nabla} \right) \tilde{\mathbf{v}} = \frac{1}{\tilde{\rho}} \left(-\tilde{\nabla} p + \tilde{\nabla} \cdot (2Oh\tilde{\mathcal{D}}) \right) - Bo \hat{\mathbf{e}}_{\mathcal{Z}} + \tilde{\mathbf{f}}_{\gamma}, \quad (3.2)$$

where the coordinate dimensions, velocity field \mathbf{v} , and pressure p are normalized using the drop radius R , inertia-capillary velocity scale $V_{\rho\gamma} = \sqrt{\gamma/\rho_d R}$ and capillary pressure $P_{\gamma} = \gamma/R$, respectively. The bracketed term on the left hand side of equation (3.2) is the material derivative. On the right hand side, $\hat{\mathbf{e}}_{\mathcal{Z}}$ is a unit vector in the vertically upward direction (see figure 3.1.1b) and the deformation tensor, $\tilde{\mathcal{D}}$ is the symmetric part of the velocity gradient tensor $\left(\tilde{\mathcal{D}} = \left(\tilde{\nabla} \tilde{\mathbf{v}} + (\tilde{\nabla} \tilde{\mathbf{v}})^T \right) / 2 \right)$. Further, we employ one-fluid approximation [2, 156] to solve these equations whereby the material properties (such as dimensionless density $\tilde{\rho} = \rho/\rho_d$ and dimensionless viscosity Oh) change depend-

ing on which fluid is present at a given spatial location (equations (3.3)–(3.4)).

$$\tilde{\rho} = \Psi_1 + \Psi_2 \frac{\rho_f}{\rho_d} + (1 - \Psi_1 - \Psi_2) \frac{\rho_a}{\rho_d} \quad (3.3)$$

$$Oh = \Psi_1 Oh_d + \Psi_2 Oh_f + (1 - \Psi_1 - \Psi_2) Oh_a \quad (3.4)$$

where, the Ohnesorge number Oh is the ratio between the inertio-capillary to the visco-capillary time scales. It is defined for all the three phases: drop Ohnesorge number ($Oh_d = \eta_d/\sqrt{\rho_d\gamma R}$), film Ohnesorge number ($Oh_f = \eta_f/\sqrt{\rho_d\gamma R}$), and air Ohnesorge number ($Oh_a = \eta_a/\sqrt{\rho_d\gamma R}$). Furthermore, ρ_f/ρ_d and ρ_a/ρ_d are the film-drop and air-drop density ratios. For simplification, we use $\rho_f/\rho_d = 1$ (also see table 3.2.1). In order to keep the surrounding medium as air, ρ_a/ρ_d and Oh_a are fixed at 10^{-3} and 10^{-5} , respectively. The Bond number, $Bo = \rho_d g R^2/\gamma = 0.5$ is the ratio of the gravitational to the capillary pressure which is also kept fixed during this study. The initial condition (figure 3.1.1b), is given by the normalized impact velocity, $\tilde{V} = \sqrt{We}$.

Lastly, a singular body force $\tilde{\mathbf{f}}_\gamma$ is applied at the interfaces to respect the dynamic boundary condition across them. The approximate forms of these forces follow from Brackbill et al. [157] as

$$\tilde{\mathbf{f}}_\gamma \approx \tilde{\kappa}_1 \tilde{\nabla} \Psi_1 + \tilde{\kappa}_2 \tilde{\nabla} \Psi_2. \quad (3.5)$$

Here, κ_1 and κ_2 are the curvatures associated with Ψ_1 and Ψ_2 , respectively, calculated using the height-function method. During the simulations, the maximum time-step needs to be less than the oscillation period of the smallest wave-length capillary wave because the surface-tension scheme is explicit in time [158, 159].

3.2.3 Domain description

Figure 3.1.1(b) represents the axi-symmetric computational domain. A tangential stress-free and non-penetrable boundary condition is applied on each of the domain boundaries. The pressure gradient is also set to zero at these boundaries. In the cases where a Worthington jet formed post-impact breaks into small droplets, boundary outflow is applied at the top boundary so that these drops do not interfere with the drop rebound process. Furthermore, the domain boundaries are far enough so that they do not influence the process. The cases with low Oh_f need extra care with the train of capillary waves formed post-impact as these waves can reflect back from the walls.

3.3 Phenomenology

In figure 3.3.1, we compare the behaviour of a typical silicone oil drop ($R = 1.0\text{ mm}$, $V = 0.35\text{ m/s}$ and $\eta_d = 4.6\text{ mPa.s}$) impacting on films with a fixed viscosity $\eta_f = 96\text{ mPa.s}$ but with contrasting thicknesses $h_f = 0.01, 0.35$, and 0.85 mm . We show a one-to-one comparison between experimental and DNS snapshots and display three pieces of information: the position of the liquid-air interfaces (green lines) that can be directly compared with experiments, the rate of viscous dissipation per unit volume (left panel of each snapshot), and the magnitude of the velocity field (right panel of each snapshot).

For the thinnest film ($h_f = 0.01\text{ mm}$, figure 3.3.1a) and supplementary video SM1), the drop deforms as it comes in apparent contact with the film mediated by the air layer, an instant that we choose as the origin of time $t = 0$. The drop spreads until it reaches its maximal lateral extent, recoils and rebounds in an elongated shape after a time $t_c = 15.6 \pm 0.1\text{ ms}$, called the contact time. Throughout the impact process, viscous stresses inside the drop dissipates energy (see $t = 1.5$ and 7.5 ms). Consequently, after take off, the drop reaches a maximal center of mass height of $H = 2.0 \pm 0.1\text{ mm}$ relative to the undisturbed film surface, from which we deduce the restitution coefficient defined as $\varepsilon = \sqrt{2g(H - R)}/V$, here $\varepsilon = 0.48$. In the simulations, we measure the same value of the restitution coefficient using the method described in appendix 3.E. This behavior is in quantitative agreement with that reported for the impact of a viscous drop on a superhydrophobic surface by Jha et al. [153], suggesting that the presence of both the air and liquid film have a negligible influence on the macroscopic dynamics of the rebound, and that viscous dissipation in the drop determines the rebound height.

For $h_f = 0.35\text{ mm}$ (figure 3.3.1b) and supplementary video SM2), despite the noticeable deformation of the liquid film, the qualitative features of the bounce are similar. We further observe that as the drop takes off, the film free surface has not yet recovered its undisturbed position. We measure an increase of the contact time to $t_c = 17 \pm 0.1\text{ ms}$ and a decrease in the rebound elasticity, with $H = 1.6 \pm 0.1\text{ mm}$ leading to $\varepsilon = 0.37$. The DNS snapshots show that in this case, viscous dissipation occurs both in the drop and the underlying liquid. Qualitatively, the instantaneous rate of viscous dissipation in the drop is similar for $h_f = 0.01\text{ mm}$ and $h_f = 0.30\text{ mm}$, suggesting that the decrease in rebound elasticity is primarily linked to the increased film dissipation.

Finally, for $h_f = 0.85\text{ mm}$ (figure 3.3.1c and supplementary video SM3), the film deformation increases and the substrate loses its repellent ability.

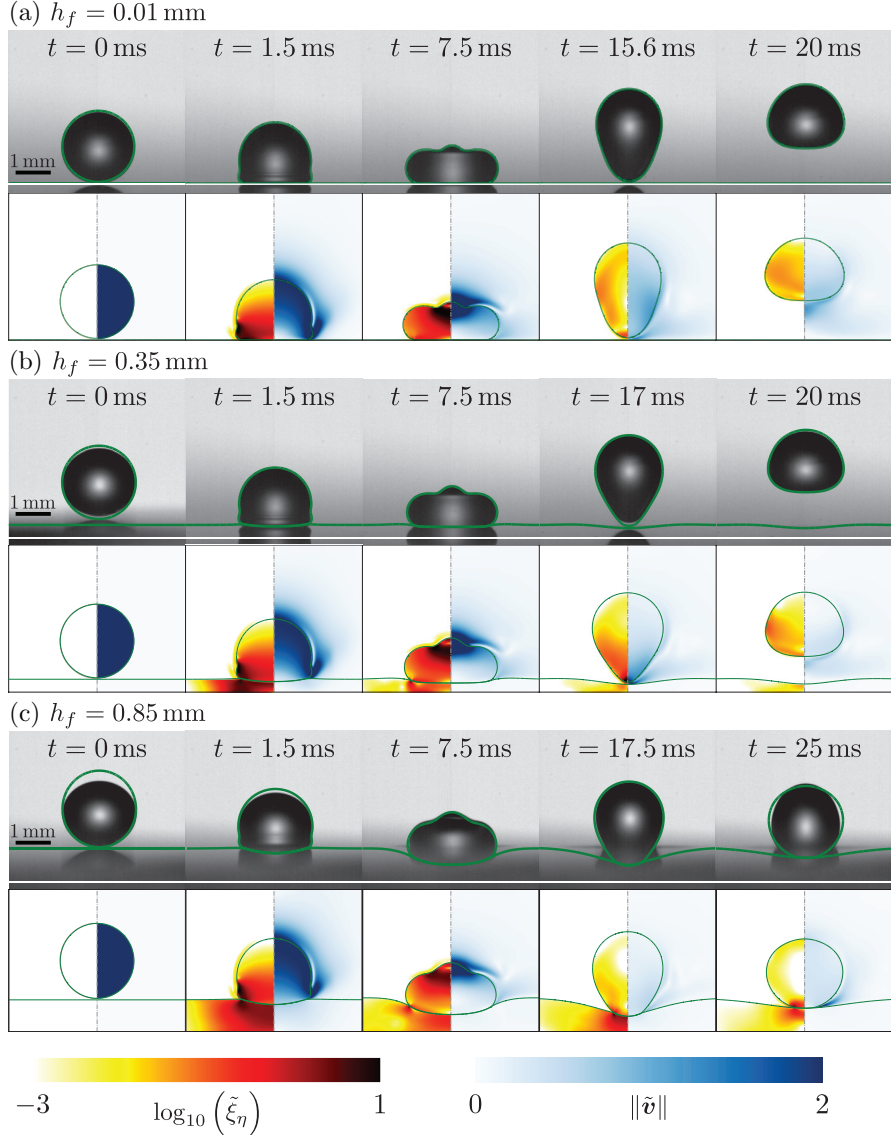


Figure 3.3.1: Effect of film thickness on the drop impact process: comparison of the experimental and DNS snapshots of the impact process on films with h_f = (a) 0.01 mm, (b) 0.35 mm, and (c) 0.85 mm. In each panel, the top row contains the experimental images with (green) interface outline from DNS, and the bottom row contains numerical snapshots showing the dimensionless rate of viscous dissipation per unit volume ($\tilde{\xi}_\eta = 2O_h(\tilde{\mathcal{D}} : \tilde{\mathcal{D}})$) on the left and the magnitude of dimensionless velocity field (\tilde{v}) on the right. We show $\tilde{\xi}_\eta$ on a \log_{10} scale to identify regions of maximum dissipation (marked with black for $\tilde{\xi}_\eta \geq 10$). For all the cases in this figure, $R = 1 \text{ mm}$, $V = 0.3 \text{ m/s}$, $\eta_d = 4.6 \text{ mPa.s}$ and $\eta_f = 96 \text{ mPa.s}$, giving $(We, Oh_d, Oh_f) = (4, 0.034, 0.67)$. Also see supplementary videos SM1–SM3.

The drop center of mass does not take off above $H = R$, the drop floats on top of the liquid film, a situation that corresponds to the inhibition of bouncing for which $\varepsilon \approx 0$ and the contact time diverges. In this case, we notice that the experimental and numerical interface profiles differ at $t = 0$ ms. This initial discrepancy, caused by drop oscillations upon detachment from the needle, does not affect the subsequent impact dynamics and the impact outcome, as evidenced by the good agreement of the interface profiles at later instants.

We now systematically vary the film thickness h_f keeping the drop and film viscosity constant ($\eta_d = 4.6$ mPa.s and $\eta_f = 96$ mPa.s) and plot, in figure 3.3.2(a) and (b), the contact time t_c and the coefficient of restitution ε extracted from experiments (circles) and DNS (hexagrams). Experiments and simulations are in excellent agreement when varying the film thickness by two orders of magnitude, $h_f = 0.01$ mm – 1 mm. The existence of two regimes is readily apparent. Firstly, for $h_f \lesssim 0.1$ mm, both t_c and ε are independent of h_f . The value of the contact time in this regime, $t_c = 15.6 \pm 0.5$ ms, corresponds to that expected from the inertio-capillary scaling [131, 181]. The contact time is proportional to $\tau_{\rho\gamma} = \sqrt{\rho_d R^3 / \gamma}$ with a prefactor 2.2 ± 0.1 , in good agreement with that calculated by Rayleigh [115] for the fundamental mode of drop oscillation $\pi/\sqrt{2}$. Similarly, the plateau value of the coefficient of restitution $\varepsilon = 0.47 \pm 0.04$ is in reasonable agreement with that reported for the impact of water drops on superhydrophobic substrates for similar drop Ohnesorge number Oh_d and impact Weber number We [153]. We therefore refer to this regime as substrate-independent rebound (see also appendix 3.B).

Secondly, for $h_f \gtrsim 0.1$ mm, the contact time and coefficient of restitution are influenced by the film thickness. We observe that t_c increases (figure 3.3.2a) and ε decreases (figure 3.3.2b,c) with increasing h_f until t_c diverges and bouncing ceases ($\varepsilon = 0$) for $h_f \approx 0.75$ mm. This critical thickness marks the threshold of the rebound behavior and the transition to the floating regime. Here, the rebound characteristics vary significantly with h_f and we therefore refer to this regime as substrate-dependent.

Finally, we characterize the transition from the substrate-independent to the substrate-dependent regime by introducing the thickness $h_{f,1}$, in dimensionless form $\Gamma_1 = h_{f,1}/R$, which marks the decrease of ε to 0.9 times its plateau value ε^* . Similarly, we define the critical thickness $h_{f,2}$, respectively $\Gamma_2 = h_{f,2}/R$, associated to the transition from the substrate-dependent to the floating regime as the smallest film thickness which results in $\varepsilon = 0$. The impact dynamics can be categorized into three distinct regimes: a substrate-independent regime for $\Gamma = h_f/R \leq \Gamma_1$, a substrate-dependent regime for

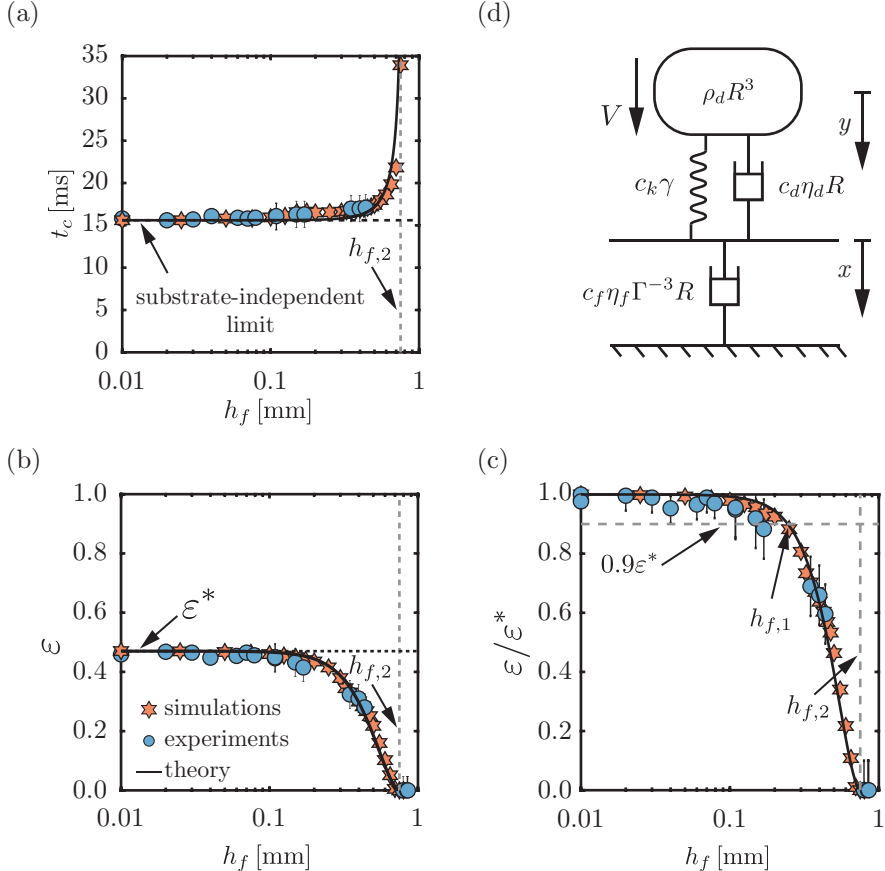


Figure 3.3.2: Effect of the film thickness on the rebound characteristics for $R = 1$ mm, $V = 0.3$ m/s, $\eta_d = 4.6$ mPa.s and $\eta_f = 96$ mPa.s, i.e., $(We, Oh_d, Oh_f) = (4, 0.034, 0.67)$: (a) contact time t_c , (b) restitution coefficient ε , and (c) restitution coefficient normalized by its substrate independent value as a function of film thickness h_f . Circles and hexagrams represent experiments and DNS, respectively. In panels (a) and (b), the horizontal black dashed lines represent the substrate-independent limits of contact time and restitution coefficient, respectively, while the solid black line is from the phenomenological model with $c_k, c_d = 2, 5.6$ (see § 3.4 and appendix 3.B). The least square fit performed on the data with equations (3.17)-(3.18) gives $c_f = 0.46 \pm 0.1$. Different critical thicknesses are also marked, $h_{f,1}$ marks the substrate-independent to substrate-dependent transition ($\varepsilon/\varepsilon^*(h_f = h_{f,1}) = 0.9$) and $h_{f,2}$ marks the transition from bouncing to floating regimes. (d) Schematic diagram of the phenomenological model that describes the droplet impact process on a liquid film. The parameters: ρR^3 , $\eta_d R$, and γ are associated to the drop properties and $\eta_f \Gamma^{-3} R$ is associated with the film properties. The drop and the film displacements are denoted by y and x , respectively.

$\Gamma_1 < \Gamma < \Gamma_2$, and a floating regime for $\Gamma \geq \Gamma_2$.

3.4 Phenomenological model

We now seek to rationalize the dependence of the rebound time and elasticity with the substrate and drop properties by constructing a minimal model, guided by our experimental and numerical observations. We build on the classical description of a drop as a liquid spring which reflects the balance of inertia and capillarity during a rebound [131, 213]. Here, we consider viscous drops and further add a damping term to the liquid spring, an approach which has been shown to successfully capture the variation of contact time and coefficient of restitution with over two orders of magnitude variation in liquid viscosities [153]. Similarly, we interpret the film behavior through the liquid spring analogy. The film motion contrasts with that of the drop, while the latter displays a full cycle of oscillation during a rebound, the former never returns to its undisturbed position (see figure 3.3.1). This observation leads us to consider that the damping component dominates the behavior of the liquid film, and neglect the contributions of inertia and surface tension. We further discuss this assumption and its validity in § 3.6.

In figure 3.3.2(d), we present a sketch of the model, where we assume that the droplet and the film are connected in series during apparent contact, and show the scaling forms of the drop and film components. The scaling relations for the drop mass, stiffness and damping are taken from the work of Jha et al. [153] as proportional to ρR^3 , γ , and $\eta_d R$, respectively, with corresponding prefactors of 1, c_k , and c_d . We determine the values of c_k and c_d from results in the substrate-independent bouncing regime (see appendix 3.B). The scaling form of the film damping term is chosen as proportional to $\eta_f \Gamma^{-3} R$, where $\Gamma = h_f/R$, with corresponding prefactor of c_f (figure 3.3.2d). This is built on two key assumptions. First, we assume that the lubrication approximation holds in the film as, for sufficiently high film Ohnesorge numbers ($Oh_f \gtrsim 0.1$), the slopes associated to the film deformations are small ($\Gamma \ll 1$, $Oh_f \sim \mathcal{O}(1)$, see § 3.6 for limitations). And second, we choose to consider the drop as an impacting disk rather than a sphere [225] owing to the rapid drop spreading upon impact [30, 116], which results in a damping term proportional to Γ^{-3} instead of Γ^{-1} [225]. Lastly, we fit the prefactor c_f to our experiments and simulations, and discuss it throughout the chapter.

The equations of motion for the model system read

$$\rho R^3 \ddot{y} = -c_k \gamma (y - x) - c_d \eta_d R (\dot{y} - \dot{x}), \quad (3.6)$$

$$0 = +c_k \gamma (y - x) + c_d \eta_d R (\dot{y} - \dot{x}) - c_f \eta_f \Gamma^{-3} R \dot{x}, \quad (3.7)$$

where y and x are the displacements of the drop and the film relative to their initial position in the reference frame of the laboratory, and the dots denote time derivatives. We point out that by setting $\dot{x} = x = 0$, we recover the model proposed by Jha et al. [153], which extends the analogy between the drop impact process and a spring-mass system [174, 213] by adding a damper to account for viscous dissipation in the drop. Here, we additionally consider viscous dissipation in the liquid coating and model the film as a damper without inertia.

Similarly as for the governing equations in DNS, we make equations (3.6) and (3.7) dimensionless using the length scale R and the time scale $\tau_{\rho\gamma}$ and use tildes to identify dimensionless variables. Next, we obtain an equation of motion for the drop deformation $\tilde{z} = \tilde{y} - \tilde{x}$, namely

$$\left(1 + \frac{c_d Oh_d}{c_f Oh_f \Gamma^{-3}}\right) \ddot{\tilde{z}} + c_d Oh_d \left(1 + \frac{c_k}{c_d Oh_d \cdot c_f Oh_f \Gamma^{-3}}\right) \dot{\tilde{z}} + c_k \tilde{z} = 0, \quad (3.8)$$

which admits oscillatory solutions, that is drop rebound, under the condition

$$\omega^2 = 4c_k - \left(c_d Oh_d - \frac{c_k}{c_f Oh_f \Gamma^{-3}}\right)^2 > 0, \quad (3.9)$$

We note that ω^2 decreases with increasing Γ for fixed Oh_d and Oh_f , in qualitative agreement with the existence of a critical film height above which bouncing stops (figure 3.3.2b). Equation (3.9) allows us to determine the bounds of the bouncing regime in terms of a critical drop Ohnesorge number $Oh_{d,c}$ and film thickness Γ_2 . Discarding the two roots of the equation $\omega^2 = 0$ that yield unphysical negative values of $Oh_{d,c}$ and Γ_2 , we obtain

$$Oh_{d,c} = \frac{1}{c_d} \left(2\sqrt{c_k} + \frac{c_k}{c_f} \left(\Gamma_2/Oh_f^{1/3}\right)^3\right), \text{ and} \quad (3.10)$$

$$\Gamma_2/Oh_f^{1/3} = \left(\frac{c_f}{c_k} (c_d Oh_d + 2\sqrt{c_k})\right)^{1/3}. \quad (3.11)$$

Equations (3.9)–(3.11) evidence that the role of the film viscosity and height are intertwined as we find the combination $\Gamma/Oh_f^{1/3}$. Furthermore, the substrate-independent bouncing threshold is recovered when the film mobility, $\Gamma/Oh_f^{1/3}$, tends to 0, that is for very thin and/or very viscous films. Indeed, equations (3.10)–(3.11) become

$$Oh_{d,c} = \frac{2\sqrt{c_k}}{c_d}, \text{ and} \quad (3.12)$$

$$\Gamma_2/Oh_f^{1/3} = \left(2 \frac{c_f}{\sqrt{c_k}}\right)^{1/3}, \quad (3.13)$$

for the limiting cases of substrate-independent ($\Gamma/Oh_f^{1/3} \rightarrow 0$), and inviscid drop ($Oh_d \rightarrow 0$) asymptotes, respectively.

To go further, we solve equation (3.8) with the initial conditions $\tilde{z} = 0$ and $\dot{\tilde{z}} = \sqrt{We}$ at $\tilde{t} = 0$, yielding

$$\tilde{z}(\tilde{t}) = \frac{2\sqrt{We}}{\Omega} \exp\left(-\frac{\phi\tilde{t}}{2}\right) \sin\left(\frac{\Omega\tilde{t}}{2}\right), \quad (3.14)$$

$$\text{where } \phi = \frac{c_k + c_d Oh_d c_f Oh_f \Gamma^{-3}}{c_d Oh_d + c_f Oh_f \Gamma^{-3}} \quad (3.15)$$

$$\text{and } \Omega = \omega \left(1 + \frac{c_d Oh_d}{c_f Oh_f \Gamma^{-3}}\right)^{-1} \quad (3.16)$$

can be interpreted as an effective damper and angular frequency, respectively, by comparing the above expression to the one obtained by Jha et al. [153] for $\Gamma/Oh_f^{1/3} \rightarrow 0$. We can deduce the expressions for both the contact time and the coefficient of restitution using these pieces of information. The contact time is taken as the instant at which the drop deformation \tilde{z} comes back to zero, which occurs at $\Omega\tilde{t} = 2\pi$, giving

$$\frac{t_c}{\tau_{\rho\gamma}} = \frac{2\pi}{\omega} \left(\frac{c_d Oh_d}{c_f Oh_f \Gamma^{-3}} + 1 \right). \quad (3.17)$$

Equation (3.17) is then used to compute the coefficient of restitution ε as the ratio of rebound velocity, $\dot{\tilde{z}}(t_c)$, to the impact velocity, \sqrt{We} . We immediately notice that this definition yields an expression for ε that does not depend on

We, in contrast with the experimentally observed decrease of ε with We . Similarly as in Jha et al. [153], we resolve this discrepancy by scaling the coefficient of restitution by ε_0 , its We -dependent value in the substrate-independent limit for inviscid drops

$$\varepsilon = \varepsilon_0 \exp \left(-\frac{\pi}{\omega} \left(c_d Oh_d + \frac{c_k}{c_f Oh_f \Gamma^{-3}} \right) \right), \quad (3.18)$$

where the prefactor ε_0 is obtained by fitting the substrate-independent experiments. We also recover the expressions for t_c and ε for viscous drop impact on non-wetting substrates [153], allowing us to determine c_k and c_d (see appendix 3.B).

We test the model predictions for the contact time and rebound elasticity in the substrate-dependent regime by comparing the data (symbols) presented in figures 3.3.2(a,b,c) to least-square fits of equations (3.17) and (3.18) with c_f as a free parameter (solid lines) and taking $\varepsilon_0 = 0.58$ (see appendix 3.B). We find that the model accurately predicts the variation of t_c and ε with Γ for $c_f = 0.46 \pm 0.1$.

We now assess the predictive ability and the limits of this minimal model by experimentally and numerically varying the drop and film Ohnesorge numbers. We give particular attention to the value of the coefficient c_f necessary to fit the model to this data, and to the two asymptotes predicted by the model that bound the region of bouncing drops (equations (3.12)-(3.13)).

3.5 Influence of drop and film parameters

3.5.1 Influence of the film Ohnesorge number

We first vary the film Ohnesorge number Oh_f while keeping the drop and impact properties constant. In figure 3.5.1(a), we show the evolution of the coefficient of restitution ε for drops with $Oh_d = 0.034$ as a function of the dimensionless film thickness Γ while exploring two decades in film viscosity, $Oh_f = 0.01 - 2.0$. On the one hand, as expected, the coefficient of restitution value is not affected in the substrate-independent limit. On the other hand, the substrate-dependent behavior shows the influence of Oh_f and we identify two regimes. For $Oh_f \lesssim 0.1$, the evolution of ε with Γ does not depend on Oh_f , as illustrated by the data collapse in figure 3.5.1(a). However, for $Oh_f \gtrsim 0.1$, increasing the film viscosity leads to a larger extent of the

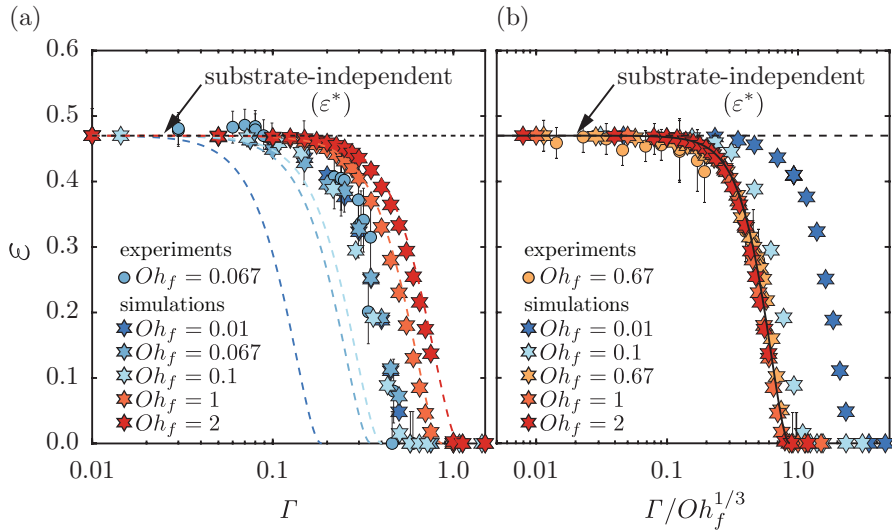


Figure 3.5.1: Influence of the film parameters on the impact characteristics: variation of the coefficient of restitution ω as a function of (a) the film thickness Γ and (b) the effective film mobility $\Gamma/Oh_f^{1/3}$. In panels (a) and (b), the circles and hexagrams correspond to the results from experiments and simulations, respectively. The colored dashed lines in panel (a) and the solid black line in panel (b) illustrate the results from the phenomenological model (equation (3.18)) with parameters $c_k = 2$, $c_d = 5.6$ and $c_f = 0.46$. Black dashed lines in panels (a) and (b) mark the substrate-independent limit of restitution coefficient ε^* . For all cases in this figure, $Oh_d = 0.034$ and $We = 4$.

substrate-independent plateau and to an increase of the critical film thickness at which bouncing stops. This change in the Oh_f dependence can be tracked by monitoring the two dimensionless critical film thicknesses $\Gamma_1 = h_{f,1}/R$, and $\Gamma_2 = h_{f,2}/R$, which increase from 0.17 to 0.33 and 0.58 to 1.1, respectively, when Oh_f is increased from 0.1 to 2.0. We interpret the two behaviors observed in the substrate-dependent regime in the light of our minimal model, which predicts that the effective film mobility, $\Gamma/Oh_f^{1/3}$, controls dissipation in the substrate. In figure 3.5.1(b), we plot the coefficient of restitution data presented in (a) after rescaling the horizontal axis by $Oh_f^{-1/3}$. The data now collapse for $Oh_f \gtrsim 0.1$, indicating that the proposed approximations capture the large viscosity limit but breaks down for lower film Ohnesorge numbers. We further evidence the validity and failure of the minimal model by plotting the prediction of equation (3.18) with $c_f = 0.46$ (solid black line).

3.5.2 Influence of the drop Ohnesorge number

In this section, we focus on the influence of the drop Ohnesorge number on the rebound elasticity. In figure 3.5.2(a), we plot the coefficient of restitution as a function of the dimensionless film thickness for a fixed $Oh_f = 0.667$ and for varying Oh_d spanning the range 0.01–0.133. Increasing Oh_d affects ε across all film thicknesses. In the substrate-independent region, the coefficient of restitution decreases with increasing drop Ohnesorge number. In appendix 3.B, we show that the plateau values reported in figure 3.5.2(a) decay exponentially with increasing Oh_d as predicted by Jha et al. [153]. To better illustrate the influence of Oh_d in substrate-dependent regime, we normalize the coefficient of restitution ε by its substrate-independent value ε^* (figure 3.5.2b). The data collapse only for small Γ indicating that the drop and film characteristics both conspire to determine the substrate-dependent behavior. We monitor the Oh_d dependence through the evolution of Γ_1 and Γ_2 , that both decrease with increasing Ohnesorge number.

3.5.3 Influence of Oh_f and Oh_d on the critical film thicknesses

We now characterize the influence of the drop and film Ohnesorge number by quantitatively reporting their effect on the critical thicknesses for substrate-independent to substrate-dependent (Γ_1) and bouncing to floating (Γ_2) transitions. Indeed, we have shown above that these two critical thicknesses are good proxies to characterize the continuous transition from substrate-independent bouncing to rebound inhibition. In figures 3.5.3(a,b), we show Γ_1 and Γ_2 as

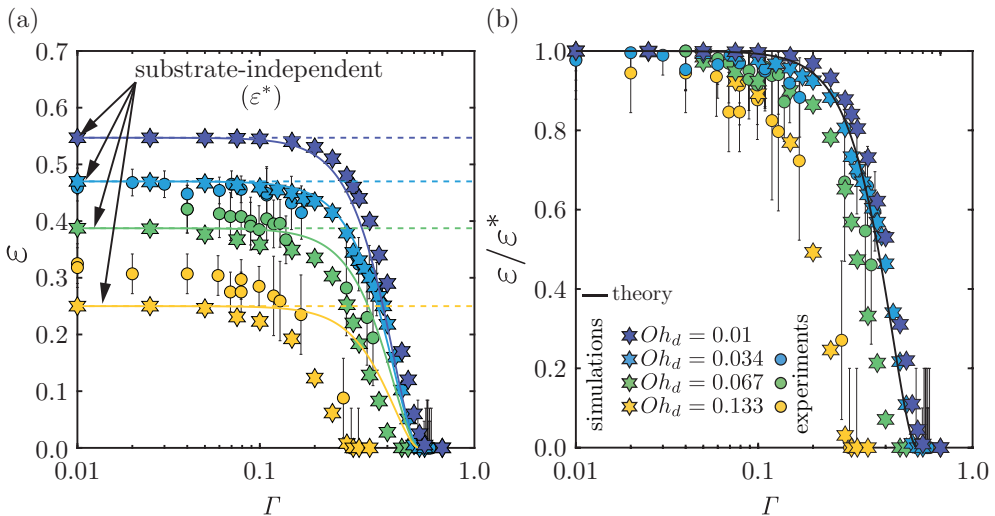


Figure 3.5.2: Influence of the drop parameters on the rebound elasticity: variation of (a) the coefficient of restitution ε and (b) the coefficient of restitution normalized with its substrate-independent value $\varepsilon/\varepsilon^*$ as a function of film thickness Γ . The circles and hexagrams correspond to the results from the experiments and simulations, respectively. In panel (a), the dashed lines denote the plateau values of the restitution coefficient ε^* which depend on Oh_d . In panels (a) and (b), the solid lines represent the results from the phenomenological model (equation (3.18)) with parameters $c_k = 2$, $c_d = 5.6$ and $c_f = 0.46$. For all cases in this figure, $Oh_f = 0.667$ and $We = 4$.

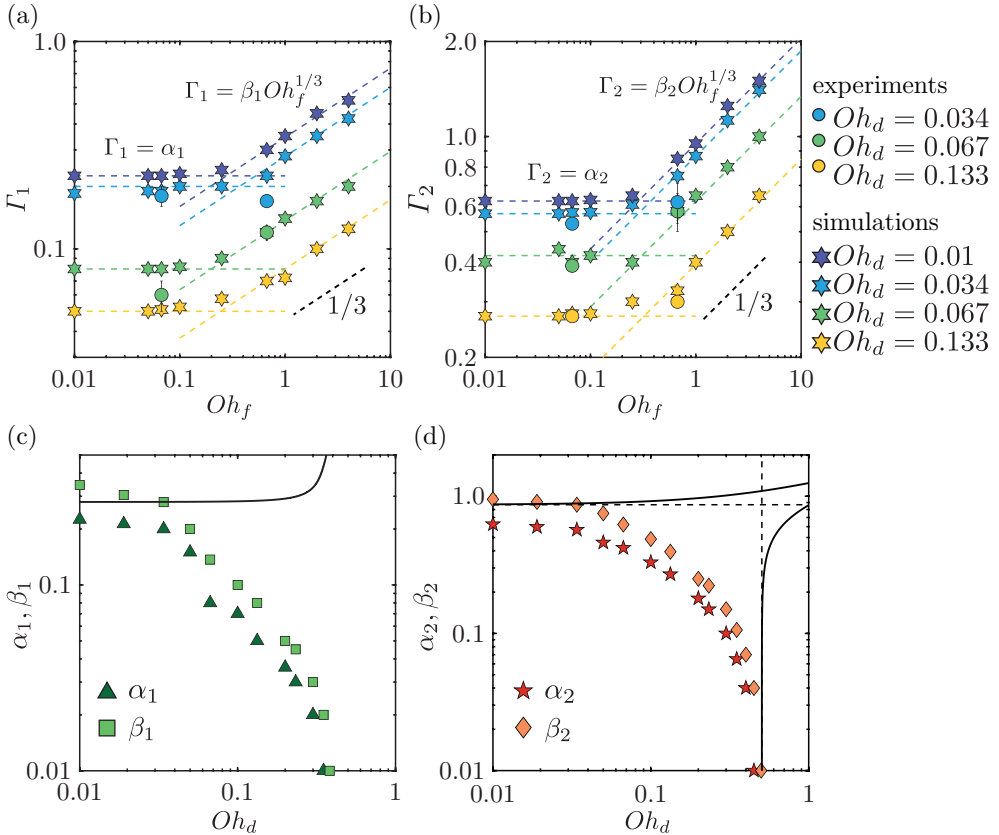


Figure 3.5.3: Critical film thickness marking the transition from (a) substrate-independent to substrate-dependent bouncing Γ_1 and (b) bouncing to floating Γ_2 as a function of Oh_f at different Oh_d . Prefactors (c) α_1 and β_1 , and (d) α_2 and β_2 as a function of Oh_d . The solid black line in panel (c) represents the model prediction for β_1 , equation (3.19). The solid black lines in panel (d) represent the model predictions for β_2 using equations (3.10)-(3.11), and the black dashed lines show the two asymptotes, equations (3.12)-(3.13).

a function of the film Ohnesorge number for Oh_d in the range $0.01 - 0.133$. This representation reflects the existence of the two distinct regimes reported in figure 3.5.1.

First, when $Oh_f \lesssim 0.1$, Γ_1 and Γ_2 are independent of Oh_f and we write $\Gamma_1 = \alpha_1(Oh_d)$ and $\Gamma_2 = \alpha_2(Oh_d)$. This observation is in contradiction with the expectations from our minimal model which predicts that Oh_f influences the values of Γ_1 and Γ_2 . Surprisingly, this Oh_f -independence of the critical thicknesses and the collapse observed in figure 3.5.1(a) suggest that the energy transfer to the film (in the form of kinetic and surface energies) and the film viscous dissipation are independent of film viscosity for $Oh_f \lesssim 0.1$. We will further elaborate on this regime in § 3.6.

Second, for larger film Ohnesorge numbers, the dissipation in the film is captured by the lubrication approximation ansatz. As a result, both critical thicknesses follow the relations $\Gamma_1 = \beta_1(Oh_d)Oh_f^{1/3}$ and $\Gamma_2 = \beta_2(Oh_d)Oh_f^{1/3}$, as predicted by the model. Beyond this scaling relation, the accuracy of the minimal model is tied to its ability to predict the prefactors β_1 and β_2 when $Oh_f \gtrsim 0.1$. In figures 3.5.3(c,d), we plot β_1 and β_2 as a function of the drop Ohnesorge number. Both prefactors show a plateau for $Oh_d \lesssim 0.03$ before decreasing monotonically with the drop Ohnesorge number. We compare the measured prefactors to the model predictions which we plot as a solid lines in figures 3.5.3(c,d). β_1 is obtained by solving $\varepsilon = 0.9\varepsilon^*$, yielding

$$\beta_1 = c_f^{1/3} \left[\frac{-c_d Oh_d (1 - r^2) + 2r \sqrt{c_k(1 + r^2) - c_d^2 Oh_d^2}}{c_k(1 + r^2)} \right]^{1/3}, \quad (3.19)$$

$$\text{where, } r = \frac{c_d Oh_d}{\sqrt{4c_k - c_d^2 Oh_d^2}} - \frac{\ln(0.9)}{\pi}, \quad (3.20)$$

and β_2 is given by equation (3.11). The model fails to capture both the decrease of β_1 and β_2 with Oh_d . Yet, we can interpret the evolution of these two prefactors along the inviscid and viscous drop limiting cases. Indeed, for inviscid drops (i.e., small Oh_d), the model predictions for β_1 and β_2 show a plateau whose value is in good agreement with that reported in experiments. Conversely, for viscous drops (i.e., large Oh_d), β_2 decreases with Oh_d to match the asymptote associated to the substrate-independent bouncing inhibition occurring at $Oh_{d,c} \approx 0.5$ (equation (3.10) and dotted line in figure 3.5.3d).

We stress that the model predictions shown in figures 3.5.3(c,d) consider a unique value of $c_f = 0.46 \pm 0.1$, determined from least-square fit in § 3.4.

We attribute the failure of the model to predict the dependence on Oh_d away from the two asymptotes to its simplified representation of the drop–film interactions. While these minimal oscillator based models remarkably predict the global outcome of a rebound, that is, for example, the contact time, coefficient of restitution, and the bounds of bouncing, they fail at accurately representing the interaction, such as the drop or film deformations (equation (3.14)), and their dynamics. For example, the force associated to drop impact is maximal at early times when the drop shape is spherical, while the force exerted by a spring is proportional to deformation. More intriguingly, the minimal model also breaks down for $Oh_f \lesssim 0.1$, where we observe that the coefficient of restitution does not depend on the film Ohnesorge number. We demystify this behavior in the next section.

3.6 Bouncing inhibition on low Ohnesorge number films

We now investigate the independence of the rebound elasticity with the film Ohnesorge number, illustrated by the data collapse of figure 3.5.1(a), for low values of Oh_f , $Oh_f \lesssim 0.1$. Figure 3.6.1(a) shows two typical impact scenarios in this regime, with $Oh_f = 0.01$ (figure 3.6.1(a - i)) and 0.1 (figure 3.6.1(a - ii)), where bouncing is inhibited by the presence of the liquid film. Although these two representative cases differ by an order of magnitude in Oh_f , qualitatively, the drop shape and flow anatomy remain similar (figure 3.6.1a, $t/\tau_{\rho\gamma} = 0.2, 1$), suggesting an equal loading on the film. Nonetheless, the film response varies. We observe capillary waves on the film-air interface for $Oh_f = 0.01$, which vanish for $Oh_f = 0.1$ owing to increases viscous attenuation (figure 3.6.1a, $t/\tau_{\rho\gamma} = 0.2, 2.65$).

To further elucidate the drop–film interaction, we compute the energy budgets associated to the two representative cases with $Oh_f = 0.01$ (figure 3.6.1(b - i)) and 0.1 (figure 3.6.1(b - ii)). The overall energy budget reads

$$E_0 = \left(E_k^d + \Delta E_\gamma^d + \Delta E_g^d \right) + E_\eta^d + \left(E_k^f + \Delta E_\gamma^f + \Delta E_g^f \right) + E_\eta^f + E_t^a, \quad (3.21)$$

where E_0 is the energy at impact (*i.e.* the sum of the drop’s kinetic and gravitational potential energies). The subscripts g, k, γ , and η denote gravitational potential, kinetic, surface, and viscous dissipation energies, respectively. Moreover, the superscripts d, f , and a represent drop, film and air, respectively. Lastly, reference values to calculate ΔE_g and ΔE_γ are at minimum E_g and

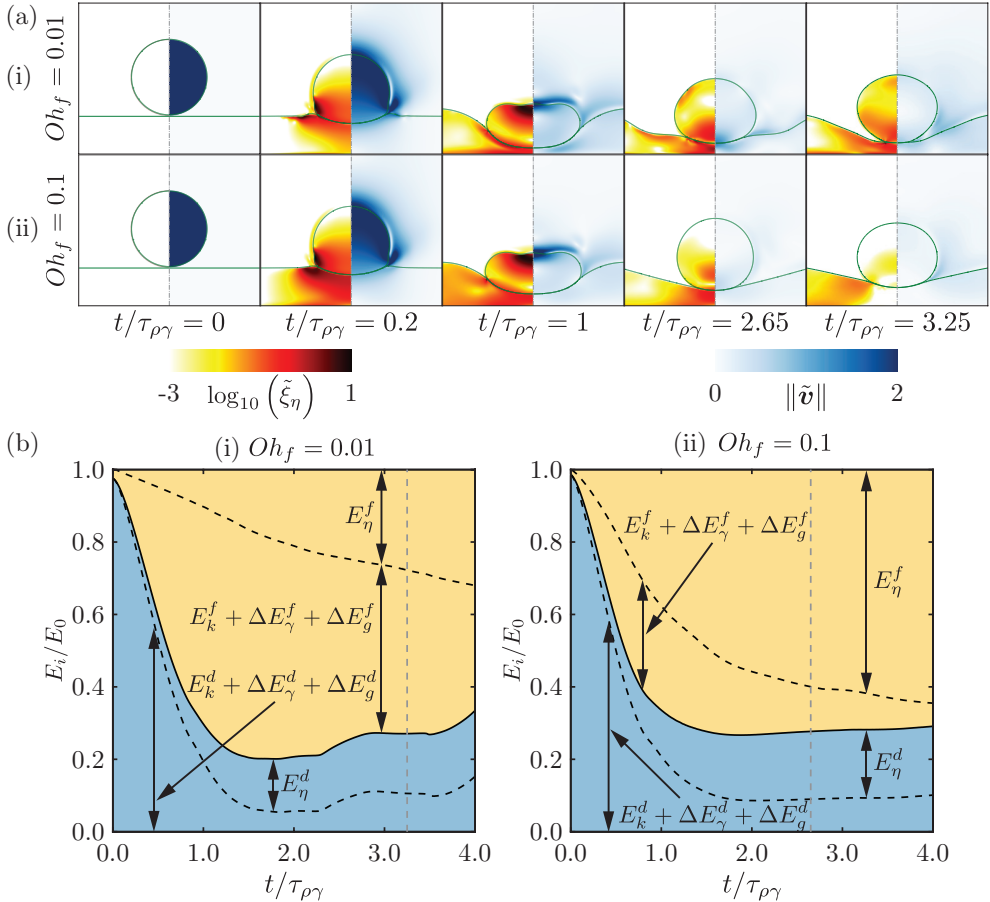


Figure 3.6.1: Oh_f independent inhibition of bouncing: (a) typical drop impact dynamics on low viscosity films. The snapshots show the dimensionless rate of viscous dissipation per unit volume ($\tilde{\xi}_\eta = 2Oh(\tilde{\mathcal{D}} : \tilde{\mathcal{D}})$) on the left and the magnitude of dimensionless velocity field ($\tilde{\mathbf{v}}$) on the right. We show $\tilde{\xi}_\eta$ on a \log_{10} scale to identify regions of maximum dissipation (marked with black for $\tilde{\xi}_\eta \geq 10$). and (b) Energy budgets for the two representative cases shown in panel (a), normalized by the available energy at the instant of impact. Here, the subscripts g , k , γ , and η denote gravitational potential, kinetic, surface, and viscous dissipation energies, respectively. The superscripts d , f , and a represent drop, film and air, respectively. The grey dashed dotted line in each panel marks the instant when the normal reaction force between the drop and the film is minimum and represents the last time instant when the drop could have bounced off the film. In each panel, $Oh_f =$ (i) 0.01 and (ii) 0.1. For all the cases, $We, Oh_d, \Gamma = 4, 0.034, 1$.

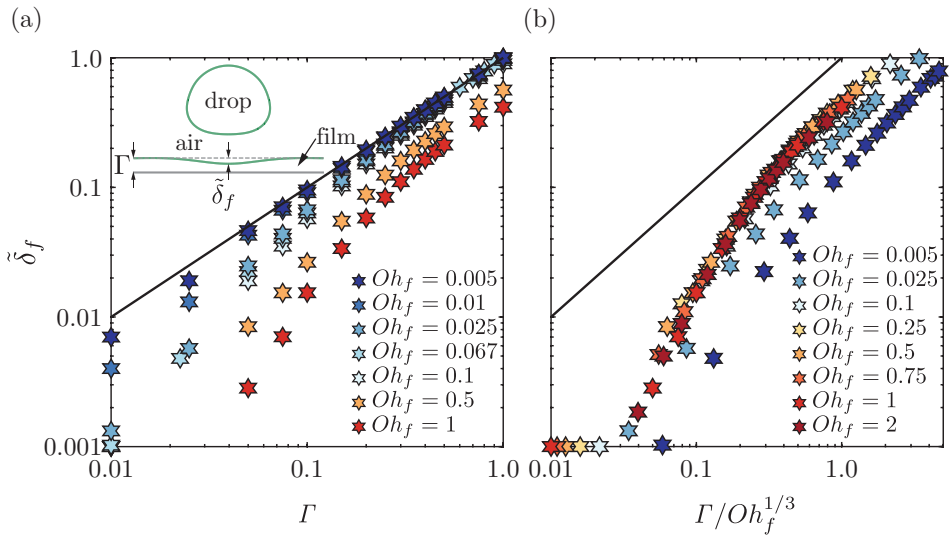


Figure 3.6.2: Variation of the maximum dimensionless film deflection $\tilde{\delta}_f = \delta_f/R$ measured from the initial film free-surface as a function of (a) the film thickness Γ and (b) the effective film mobility $\Gamma/Oh_f^{1/3}$ in the direct numerical simulations. The solid black line represents $\delta_f/R = \Gamma$ and $\delta_f/R = \Gamma/Oh_f^{1/3}$ in panels (a) and (b), respectively. The inset in panel (a) depicts the schematic representation of this film deflection δ_f .

E_γ at $t = 0$, respectively. Note that the contribution of the total energy associated with air ($E_t^a = E_k^a + E_\eta^a$) is negligible as compared to other energies ($E_t^a(t/\tau_{\rho\gamma} = 4) \approx 0.01E_0$). Readers are referred to Wildeman et al. [30], Sanjay et al. [39], Ramírez-Soto et al. [145], Landau and Lifshitz [160] for details of energy budget calculations.

In both cases, the magnitude of the drop energy (the sum of the drop's kinetic, gravitational and surface energies) at the end of the rebound cycle, that is for $t = 3.25\tau_{\rho\gamma}$ when $Oh_f = 0.01$ and $t = 2.65\tau_{\rho\gamma}$ when $Oh_f = 0.1$ (vertical grey dashed lines), is similar in the two representative cases of figure 3.6.1(b), as expected from the independence of ε with Oh_f . Note that the end of the cycle has been determined from the instant at which the reaction force between the drop and the film is minimum [see appendix 3.E and 178]. Moreover, the energy budget evidences that the viscous dissipation in the drop during the rebound is similar, indicating that the magnitude of the energy transferred from the impacting drop to the film (the sum of the film's kinetic, gravitational and surface energies, and viscous dissipation) is not affected by the one order of magnitude change in Oh_f . Yet, the distribution of the film energy is dramatically different in the two cases we consider. For $Oh_f = 0.1$, the energy transferred to the film is mostly lost to viscous dissipation, while for $Oh_f = 0.01$ the energy stored in the film's kinetic, surface and potential components dominates. We stress here that the Oh_f -independent behavior does not imply that dissipation is negligible. Indeed, the viscous dissipation in the film accounts for approximately 40% and 85% of the total energy transferred to the film for $Oh_f = 0.01$ and 0.1, respectively. This difference in the film energy distribution hints at the failure of our assumptions to neglect the film's inertia and surface tension. The minimal model is relevant only when the energy transferred to the liquid film is predominantly lost to viscous dissipation.

Guided by the energy budget analysis in the above two extreme cases, we now evidence the minimal model failure through the break up of the effective film mobility analogy, $\Gamma/Oh_f^{1/3}$, which is intimately tied to the assumption of dominant viscous dissipation in the film. The maximum film deflection δ_f controls its surface energy and velocity field (and hence the viscous dissipation). In figure 3.6.2, we report the normalized maximum film deflection $\tilde{\delta}_f = \delta_f/R$ as a function of Γ (figure 3.6.2a) for Oh_f in the range 0.01 – 2 while keeping Oh_d constant. For $Oh_f > 0.1$, the deflection decreases with increasing Oh_f , and the data collapses once the horizontal axis is rescaled by $Oh_f^{-1/3}$ (figure 3.6.2b), confirming the relevance of the proposed effective thickness.

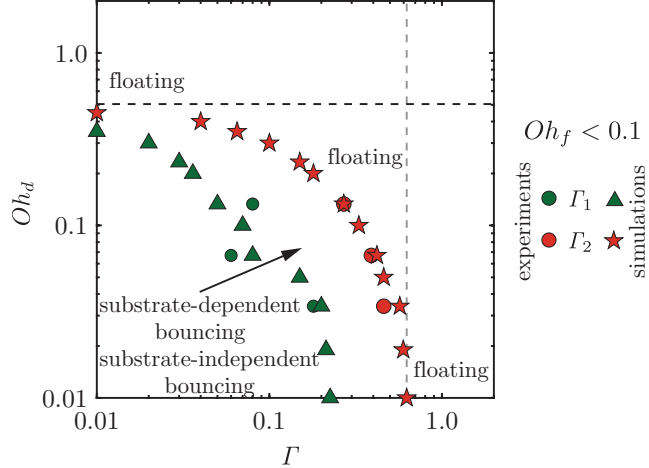


Figure 3.7.1: Regime map in terms of the drop Ohnesorge number Oh_d and dimensionless film thickness Γ for $Oh_f < 0.1$, showing the transitions between different regimes identified in this work. Γ_1 marks the transition from substrate-independent bouncing to substrate-dependent bouncing whereas Γ_2 marks the transition from bouncing to floating regimes. The black dotted line represents the substrate-independent asymptote for bouncing to floating transition (equation (3.12)), and the gray dotted line is drawn as a guide to the eye by using the numerical data and shows the inviscid drop asymptote for bouncing to floating transition.

However, for lower film Ohnesorge numbers, $\tilde{\delta}_f$ scales with Γ independent of Oh_f illustrating the limits of our hypotheses. Here, one might be tempted to replace the film damper in our model ($c_f \eta_f \Gamma^{-3}$) with $c_f \Gamma$ in this regime. However, such a replacement still fails to appropriately account for the kinetic and surface energies of the film. Indeed, low Oh_f films are associated to capillary waves, and the maximum deflection δ_f might not be the correct length scale to mimic their behavior in a simplified model. As future work, it would be interesting to couple a linearized quasi-potential fluid model [182, 226] for the liquid pool/film with a spring-mass-damper system for the liquid drop to further investigate this regime.

3.7 Conclusions and outlook

In this work, we perform experiments and direct numerical simulations of the rebound of an oil drop impacting on a deformable oil film. We elucidate the role of the drop and film properties, the Ohnesorge numbers of the drop Oh_d

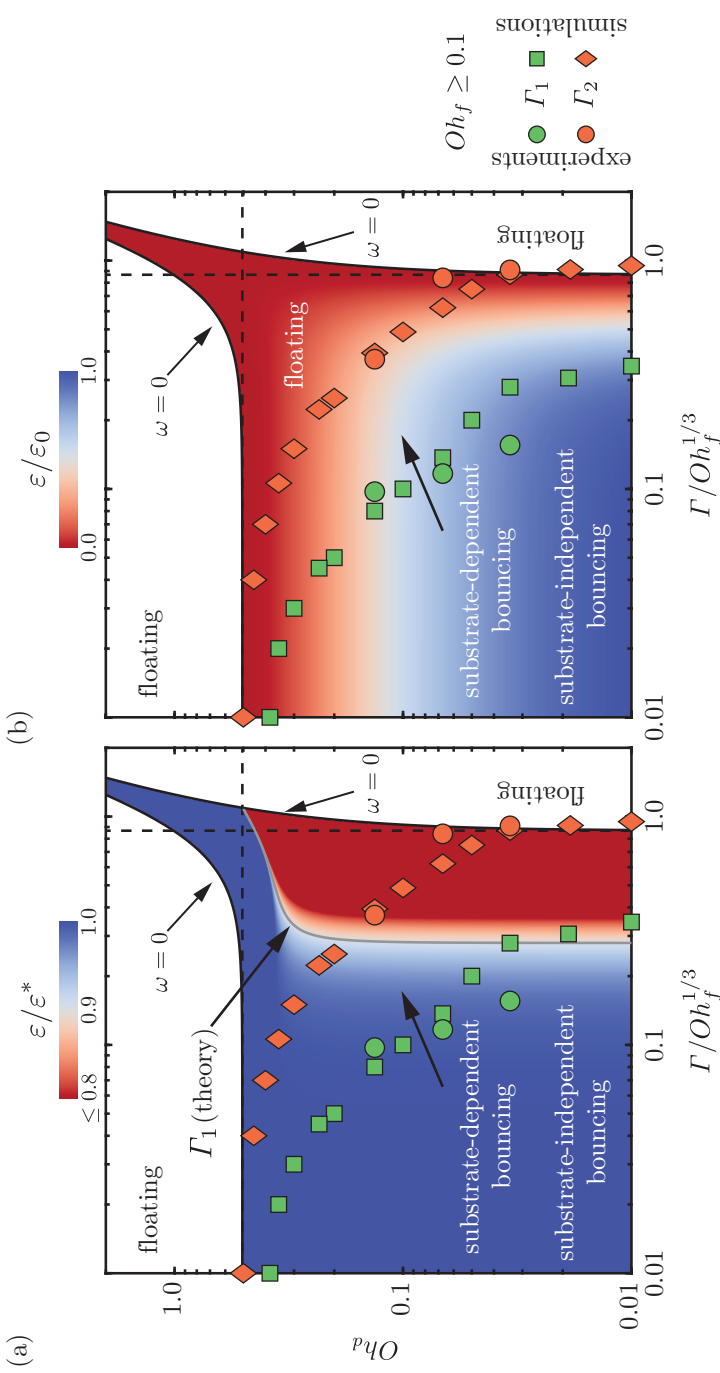


Figure 3.7.2: Regime map in terms of the drop Ohnesorge number Oh_d and modified dimensionless film thickness $\Gamma/Oh_f^{1/3}$ for $Oh_f \geq 0.1$ showing the transitions between different regimes identified in this work. Γ_1 marks the transition from substrate-independent bouncing to substrate-dependent bouncing whereas Γ_2 marks the transition from bouncing to floating regimes. The background contour illustrates the theoretical values of the coefficient of restitution ε (equation (3.18)) normalized with its (a) substrate-independent limit $\varepsilon^* = \varepsilon\left(\Gamma/Oh_f^{1/3} \rightarrow 0\right)$, equation (3.23) and (b) inviscid drop and substrate-independent limit $\varepsilon_0 = \varepsilon^*(Oh_d \rightarrow 0)$. The black solid lines shows the predicted bouncing to floating transition using the minimal phenomenological model ($\omega = 0$, equations (3.10)-(3.11)), and the black dashed lines show the two asymptotes (equations (3.12)-(3.13)) of bouncing to floating regimes. Lastly, the gray solid line shows the theoretical prediction of Γ_1 .

and the film Oh_f and the film thickness Γ , on the impact process.

For films with a low Ohnesorge number (i.e., $Oh_f < 0.1$), figure 3.7.1 summarizes the different regimes identified in this work. For small film thicknesses, we recover the substrate-independent limit where bouncing is inhibited by the high viscous dissipation in the drop [$Oh_{d,c} \sim \mathcal{O}(1)$, 153]. Increasing the film thickness reduces the drop Ohnesorge number marking the bouncing to floating transition as additional energy is transferred to the film, and similarly influences the substrate-independent to substrate-dependent transition. In the inviscid drop limit, bouncing stops once a critical film thickness ($\Gamma_2 \sim \mathcal{O}(1)$) is reached, independent of Oh_f . Here, the invariance of the energy transfer from the drop to the film with Oh_f remains to be explained and deserves further study.

For high Ohnesorge number films (i.e., $Oh_f > 0.1$), figure 3.7.2 summarizes the different regimes identified in this work. Similar to the low Oh_f case, increasing Oh_d and Γ inhibits bouncing. In contrast with the previous case, in the inviscid drop limit, the bouncing to floating transition occurs at critical film thicknesses that depend on the Ohnesorge number of the film as $\Gamma_2 \sim Oh_f^{1/3}$. We propose a minimal phenomenological model describing the key aspects of this process. The background colors in figures 3.7.2(a) and 3.7.2(b) illustrate the predicted values of the restitution coefficient ε (equation (3.18)) normalized with its substrate-independent $\varepsilon^* = \varepsilon(\Gamma/Oh_f^{1/3} \rightarrow 0)$, equation (3.23), and inviscid drop and substrate-independent $\varepsilon_0 = \varepsilon^*(Oh_d \rightarrow 0)$ values, respectively. The model accurately predicts the substrate-independent and inviscid drop asymptotes corresponding to the bouncing to floating transition i.e., Γ_2). In the latter limit, the model also captures the substrate-independent to substrate-dependent transition (i.e., Γ_1). Away from these asymptotes, the minimal model fails to predict Γ_1 and Γ_2 . We attribute this shortcoming to the simplified representation of the drop-film interactions in the model. Nonetheless, notice that the predicted values of the restitution coefficient are very close to zero beyond the bouncing to floating transition observed in the simulations. We hypothesize that the model breakdown might be caused by the neglect of gravity which is known to inhibit bouncing [174] and may prevent the take off of drops with small upward velocities. We refer the reader to Sanjay et al. [227] for a detailed study of the role of gravity in inhibiting the bouncing of viscous drops.

Finally, we stress that this study does not present an exhaustive exploration of all bouncing regimes. For example, Galeano-Rios et al. [182] have shown that spherical hydrophobic solid spheres can bounce off deep low vis-

cosity pools. Consequently, we hypothesize that the bouncing regime could resurrect at high Oh_d , Γ , and low Oh_f , evidencing non-monotonic energy transfer. It will be interesting to probe such a regime in future work.

Appendix

3.A Air layer rupture

We observe three distinct types of air layer collapse and describe their phenomenology in figure 3.A.1. Figure 3.A.1(a) illustrates the air layer break up at large Weber numbers. The air film fails during drop spreading as the intervening air layer drains below a critical thickness on the order of $10 - 100$ nm, characteristic of the range of van der Waals forces [203–205].

Figure 3.A.1(b) evidences the influence of the drop Ohnesorge number Oh_d on the coalescence transition. Drops with low Oh_d show distinct pyramidal structures owing to the capillary waves after impact [43]. The convergence of these capillary waves at the drop apex, during the retraction phase, can create an upward Worthington jet and an associated downward jet due to momentum conservation [44, 141, 178]. This downward jet can puncture the air film and lead to coalescence during the drop retraction.

Lastly, the air layer can also break due to capillary waves propagating at the surface of the film owing to low Oh_f (see figure 3.A.1c).

In summary, figure 3.A.1 shows that the critical Weber number beyond which the air layer between the drop and the film ruptures is sensitive to the Ohnesorge numbers of both the drop as well as the film [196, 228]. Subsequently, the bouncing-coalescence transition can arrest the superamphiphobic-type rebounds discussed in this work. The analysis of this transition is beyond the scope of the present study and we refer the reader to Lohse and Villermaux [12], Chubynsky et al. [204] for further discussion and review on this topic.

3.B Substrate independent bouncing

As the film thickness decreases or the film viscosity increases, the impact process becomes independent of the film properties. In this limit, $\Gamma/Oh_f^{1/3} \rightarrow 0$,

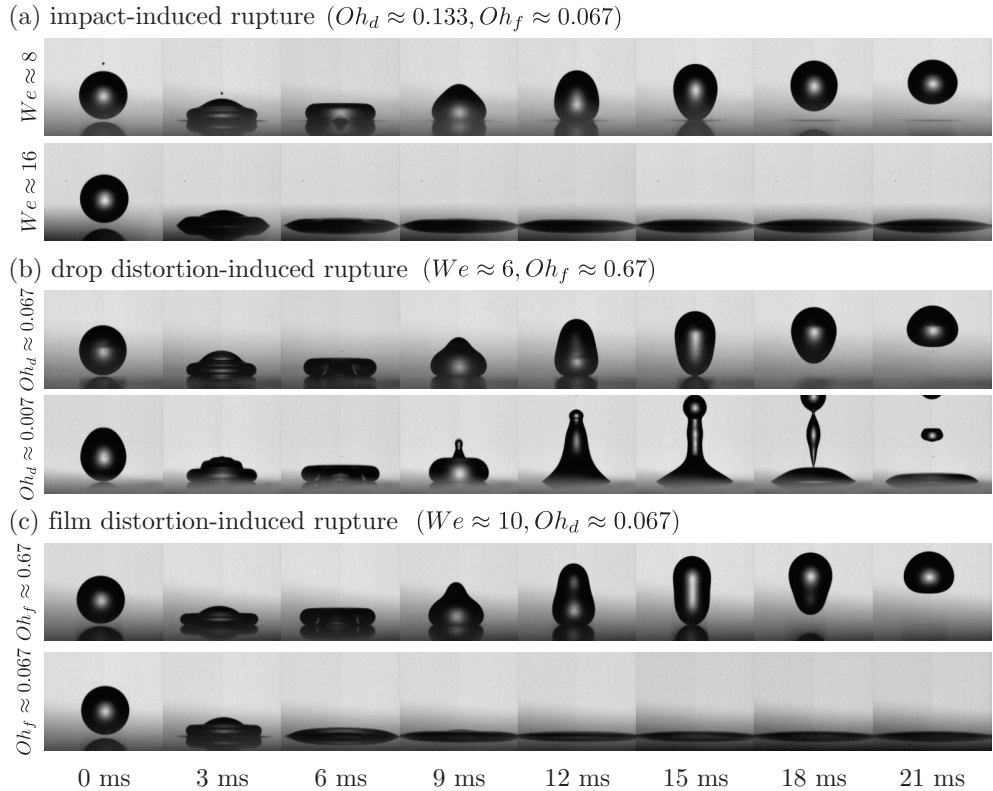


Figure 3.A.1: Rupture of the air layer and subsequent coalescence of impacting drop with the liquid coating. This rupture can occur due to: (a) impact as We increases, (b) pyramidal drop distortion and subsequent downward momentum jet as Oh_d decreases, and (c) film distortions due to capillary waves as Oh_f decreases. For panels (a) and (c), $\Gamma = 0.03$, and for panel (b) $\Gamma = 0.01$ (dry-substrate limit). For all the cases, $Bo \approx 0.5$.

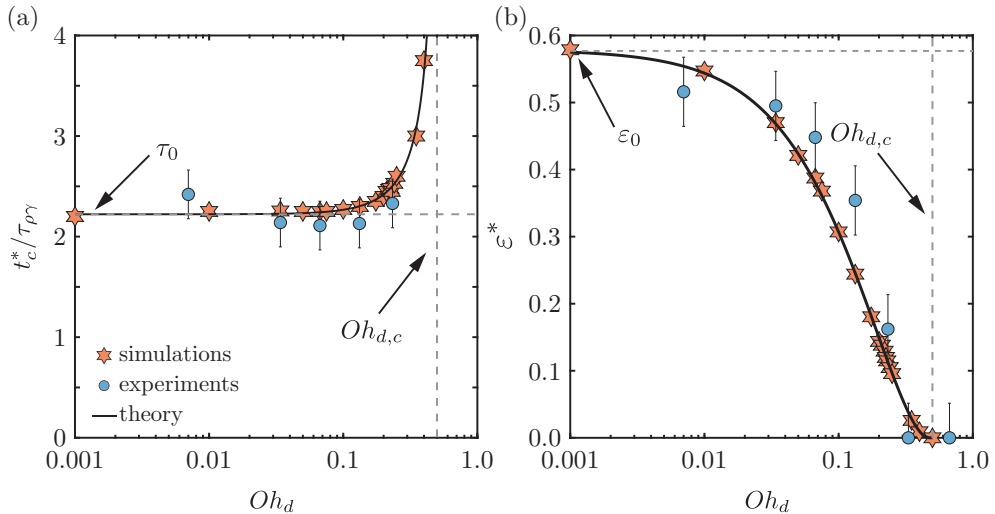


Figure 3.B.1: Substrate independent bouncing: (a) variation of contact time t_c^* normalized with inertia-capillary timescale $\tau_{\rho\gamma}$, and (b) coefficient of restitution ε^* with the drop Ohnesorge number Oh_d . The solid black lines represents the theoretical solutions, equations (3.22)-(3.23), in the substrate-independent limit which predicts an increase in contact time and an exponential decay in ε^* with Oh_d , and existence of a critical drop Ohnesorge number $Oh_{d,c}$ (dashed vertical gray line). These predictions are consistent with Jha et al. [153], and set the prefactors c_k and c_d to 2.0 ± 0.1 and 5.6 ± 0.1 , respectively. Here, $We = 4$ and $Bo = 0.5$.

the phenomenological model predictions for the contact time and restitution coefficient, equations (3.17) and (3.18), become

$$t_c^* = \tau_{\rho\gamma} \left(\frac{2\pi}{\sqrt{4c_k - c_d^2 Oh_d^2}} \right), \quad (3.22)$$

$$\varepsilon^* = \varepsilon_0 \exp \left(\frac{-\pi c_d Oh_d}{\sqrt{4c_k - c_d^2 Oh_d^2}} \right), \quad (3.23)$$

which is identical to the model developed by Jha et al. [153]. Indeed, in the substrate independent limit, bouncing off an air layer is an idealization of bouncing off dry-superamphiphobic substrates [80, 145, 178].

Reducing equation (3.22) to the case of low viscosity drops ($Oh_d \rightarrow 0$), we get $t_0/\tau_{\rho\gamma} = \pi/\sqrt{c_k}$, as expected from the water-spring analogy [131, 213]. We thus determine the prefactor c_k by fitting the inviscid limit of our data ($t_0 = 2.2\tau_{\rho\gamma}$, figure 3.B.1a) yielding

$$c_k = \left(\frac{\pi}{t_0/\tau_{\rho\gamma}} \right)^2 \approx 2, \quad (3.24)$$

which is also consistent with the values of contact time reported earlier in the literature [75] and agrees with the Rayleigh time period of drop oscillation [115].

Furthermore, applying a least square fit to our experimental and numerical data for the coefficient of restitution, which decays exponentially with increasing Oh_d (figure 3.B.1b), allows us to fix $c_d = 5.6 \pm 0.1$. Lastly, the model predicts the existence of a critical Ohnesorge number $Oh_{d,c} = 2\sqrt{c_k}/c_d \approx 0.5$ above which the drops do not bounce. This asymptote is in quantitative agreement with our data (see the dashed gray lines in figure 3.B.1).

Finally, we compare the above value of c_d to that obtained by Jha et al. [153]. To do so, we note that Jha et al. [153] further reduced equation (3.23) to $\varepsilon^* \approx \varepsilon_0 \exp(-\alpha Oh_d)$, where $\alpha = 2.5 \pm 0.5$ fit all their experimental datapoints, independent of the impact Weber number. The equivalent fitting parameter in our case is $\alpha = (\pi/2)c_d/\sqrt{c_k} \approx 6$. This discrepancy can be attributed to the different values of the critical Ohnesorge number $Oh_{d,c}$ which could stem from the Bond number variation between the two cases: $(Oh_{d,c}, Bo) \approx (0.8, 0.2)$, in Jha et al. [153], and $(0.5, 0.5)$ in this work. Exploring the influence of Bo

is beyond the scope of this chapter and we refer the reader to chapter 2 for detailed discussions.

3.C Influence of the impact Weber number on bouncing drops

Figure 3.B.2 summarizes the influence of the Weber number We on the drop impact process for a representative case with Oh_d and Oh_f as 0.034 and 0.67, respectively. Notice that both the time of contact (figure 3.B.2a) as well as the coefficient of restitution (figure 3.B.2b) are fairly independent of We for $We \geq 4$. Surprisingly, small We shows a higher value of restitution coefficient, particularly in the substrate independent regime (see again figure 3.B.2b) owing to high capillary stresses that helps drops retain the spherical shape at take-off, increasing the efficiency of the bounce. Contrary to this scenario, more elongated shapes are observed for higher We (see figure 3.3.1a,b at take-off). Furthermore, normalizing ε with the We -dependent (at fixed Oh_d) values in the dry substrate limit ε^* , we observe a collapse, similar to Jha et al. [153], insinuating that We only affects bouncing through this shape effect. Readers are referred to Sanjay et al. [227] for further discussions. Notice the discrepancy in determining Γ_2 from experiments for higher We that we cannot explain at this point as the DNS do not match with experimentally obtained We -independent Γ_2 in this regime.

3.D Measuring film thickness

Silicone oil films with thicknesses $h_f < 30\text{ }\mu\text{m}$, are prepared using spin coating and measured using reflectometry [219]. Thicker films ($h_f > 30\text{ }\mu\text{m}$) are prepared by depositing a controlled volume of silicone oil on a glass slide. The film thickness is then measured using side view imaging by locating the vertical position of the glass slide wall (green line in figure 3.D.1) and of the film free surface (red line in figure 3.D.1). The uncertainty in the film thickness measurement using this method is about $\pm 30\text{ }\mu\text{m}$, which corresponds to an uncertainty of about 3 pixels.

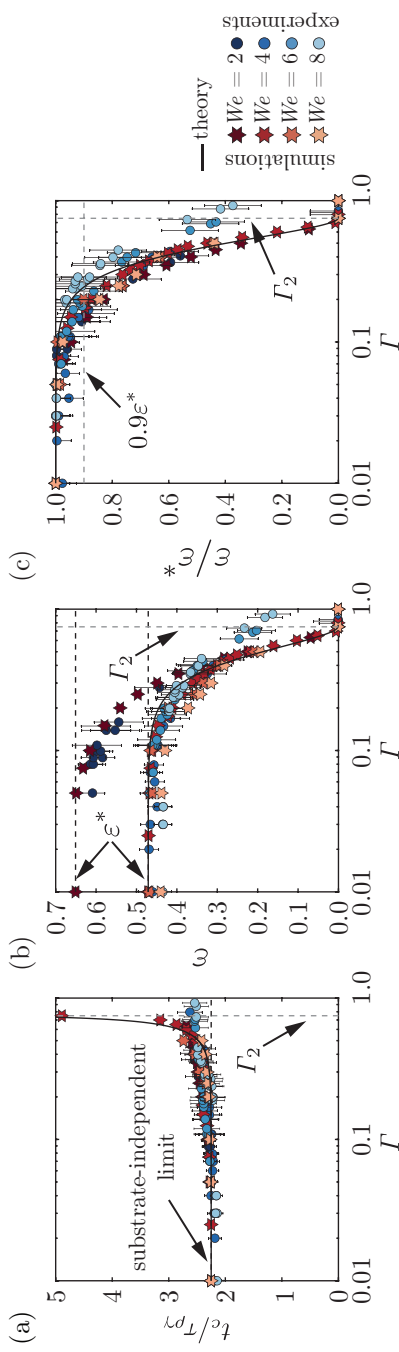


Figure 3.B.2: Influence of the impact Weber number on bouncing drops: variation of (a) time of contact t_c normalized with the inertio-capillary time scale $\tau_{\rho\gamma}$, (b) restitution coefficient, and (c) restitution coefficient normalized with its dry substrate value as a function of the dimensionless film thickness Γ . Here, $(Oh_d, Oh_f) = (0.034, 0.67)$. In each panel, solid black line represent the theoretical solution for $(c_k, c_d, c_f) = (2, 5.6, 0.46)$ and the vertical dashed gray line indicate Γ_2 above which drops do not bounce. In panels (a) and (b), black dashed lines show the dry substrate limit. Lastly, in panel (c), the horizontal dashed gray line denotes the $0.9\epsilon^*$ criterion used to determine the substrate-independent to substrate-dependent transition for bouncing drops.

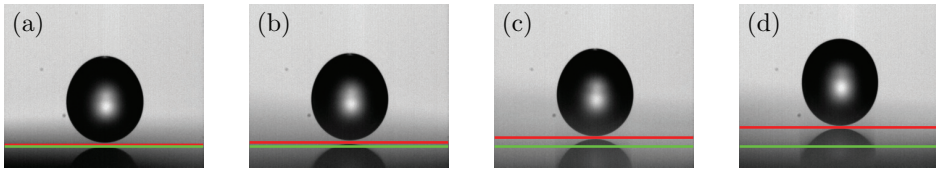


Figure 3.D.1: Side view snapshots of experiments at the instant of impact, $t = 0$. The images show the wall location denoted by a green horizontal line and the free-film interface denoted by a red horizontal line. The film thickness in each image is estimated from the vertical difference between the two lines which results in dimensionless film thickness of $\Gamma = h_f/R =$ (a) 0.05 (b) 0.11 (c) 0.23, and (d) 0.48.

3.E Measuring the restitution coefficient

Throughout this chapter, we have used the coefficient of restitution to study the drop impact on thin films. In this appendix, we describe the procedure used to determine the restitution coefficient. In experiments, we measure the drop's maximum center of mass height relative to the undisturbed film surface to get the restitution coefficient as $\varepsilon = \sqrt{2g(H - R)}/V$, where V is the impact velocity. In simulations, we measure the coefficient of restitution as the ratio of the take-off velocity $v_{\text{cm}}(t_c)$ to the impact velocity V ,

$$\varepsilon = \frac{v_{\text{cm}}(t_c)}{V} \quad (3.25)$$

where t_c denotes the contact time when the drop leaves the substrate film. The latter definition requires to precisely evaluate the contact time t_c . This is difficult as a thin film of air is always present between the drop and the film surface, we assume ideal non-coalescence between the drop and the film. In simulations, we automatize the detection of the end of apparent contact by taking t_c as the instant when the normal reaction force $F(t)$ between the film and the drop is zero [for details on the force calculation, see chapter 1 and 178]. Subsequently, we read out the center of mass velocity at this instant. If this center of mass velocity $v_{\text{cm}}(t_c)$ is not in the upward direction (i.e., it is zero or negative), we categorize the case as non-bouncing.

3.F Code availability

The codes used in the present chapter are permanently available at Sanjay [221].

chapter 3: drop impact on viscous liquid films



source code



supplemental movies

3.G Supplemental movies

These supplemental movies are available at Sanjay [external YouTube link, 229].

In all these videos, the left part of the numerical video shows the dimensionless local viscous dissipation rates on a \log_{10} scale, and the right part shows the velocity field magnitude normalized with the impact velocity. Also see figure 3.3.1.

- SM1: Comparison of the experimental and DNS snapshots of the impact process on films with $h_f = 0.01$ mm. In the experiment, $R = 1$ mm, $V = 0.3$ m/s, $\eta_d = 4.6$ mPa.s and $\eta_f = 96$ mPa.s, giving $(We, Oh_d, Oh_f) = (4, 0.034, 0.67)$.
- SM2: Comparison of the experimental and DNS snapshots of the impact process on films with $h_f = 0.35$ mm. In the experiment, $R = 1$ mm, $V = 0.3$ m/s, $\eta_d = 4.6$ mPa.s and $\eta_f = 96$ mPa.s, giving $(We, Oh_d, Oh_f) = (4, 0.034, 0.67)$.
- SM3: Comparison of the experimental and DNS snapshots of the impact process on films with $h_f = 0.85$ mm. In the experiment, $R = 1$ mm, $V = 0.3$ m/s, $\eta_d = 4.6$ mPa.s and $\eta_f = 96$ mPa.s, giving $(We, Oh_d, Oh_f) = (4, 0.034, 0.67)$.

Chapter 4

Lifting a sessile oil drop with an impacting one^o

Colliding drops are widely encountered in everyday technologies and natural processes, from combustion engines and commercial sprays to raindrops and cloud formation. The outcome of a collision depends on many factors, including the impact velocity and the degree of head-on alignment, in addition to intrinsic properties like surface tension. Yet little is known about the dynamics of an oil drop impacting an identical sessile drop sitting on a low-wetting surface. We experimentally and numerically investigate such a binary impact dynamics of low surface tension oil drops on a superamphiphobic substrate. We observe five rebound scenarios, four of which do not involve coalescence. We describe two previously unexplored cases for sessile oil drop lift-off, resulting from a drop-on-drop impact event. The simulations quantitatively reproduce all rebound scenarios and enable quantification of the velocity profiles, the energy transfers, and the viscous dissipation. Our results illustrate how varying the offset from head-on alignment and the impact velocity results in controllable rebound dynamics for low surface tension drop collisions on superamphiphobic surfaces.

^oPublished as: Olinka Ramírez-Soto, **Vatsal Sanjay**, Detlef Lohse, Jonathan T. Pham, and Doris Vollmer. *Lifting a sessile oil drop with an impacting one*, Sci. Adv. **6**, eaba4330 (2020). Experiments are done by Ramírez-Soto; simulations by Sanjay; analysis by both; and supervision by Lohse, Pham, and Vollmer. Writing and proofread by everyone.

4.1 Introduction

When a liquid drop impacts a sessile one of an identical liquid, it is intuitively expected that both drops coalesce. This process is commonly observed in day-to-day examples, such as rain or drops from a leaky faucet. However, coalescence can be obstructed by a thin layer of air between the two drops [230–232]. Insufficient thinning of this air layer during impact even enables water drops to bounce from perfectly hydrophilic surfaces, which they would otherwise wet [80, 193, 233]. In the late 1800s, Reynolds [64] noticed that water drops can glide over a pool because of this air layer. Analogously, a vapor layer also governs the Leidenfrost effect [4–6, 67, 234, 235], where a drop hovers over a superheated surface. As a result, drop bouncing, coalescence, and spreading can all be observed depending on the intrinsic properties of the liquid, as well as external parameters, such as the background pressure, collision velocity, and the impact parameter describing whether the collision is head-on or off-centered [81, 82, 236, 237]. Despite this progress in the experimental characterization of the impact dynamics, a quantitative modelling of the velocity fields and energy transfer is lacking, especially for non-aqueous liquids.

Drop impact on surfaces, and the outcome of the collision, is of practical importance for many situations. For example, in agriculture, it is essential to ensure that pesticides and other chemicals sprayed on wet leaves do not roll off and contaminate the surroundings [238]. Surfactants are often added to lower or tune interfacial tensions. Impact of low interfacial tension drops are encountered in spray coating, inkjet printing, and additive manufacturing of low surface tension liquids [239, 240]. On the other hand, removal of drops is desirable for car windows [241] and self-cleaning of surfaces. On superhydrophobic surfaces, a water drop impacting another one can lead to drop removal after coalescence if sufficient energy is exchanged between them during impact without viscous dissipation [242, 243]. Alternatively, even without an impact, the coalescence of droplets can lead to jumping if the excess surface energy released is efficiently transferred to the kinetic energy [175–177, 244].

While several reports exist on understanding how a water drop impacts a sessile water drop on a surface [237, 242, 243, 245, 246], the dynamics of a low surface tension oil drop impacting an oil drop on a non-wetting surface remains unexplored. A better understanding is, for example, desired in the emerging field of additive manufacturing. For example, in 3D printing, which is one of the widely used additive manufacturing techniques, the relative precision of

the drop deposition and its shape evolution may decide the success or failure of a printed device. It has been shown that the collisional dynamics of free-flying oil drops offer more diverse outcomes than those of water drops [81, 82]. Consequently, a number of questions arise. Do these collisions show rich dynamics also in the presence of a low-wetting surface? What are the outcomes of the drop-on-drop impact of oil on a superamphiphobic surface? How is energy transferred between the drops? Intuitively, the rebound of oil drops from a surface by impact with another oil drop seems more difficult than water for the following reasons. (i) The surface tension of most hydrocarbon oils ($\approx 25 \text{ mN/m}$) is significantly lower than that of water (72 mN/m) which reduces the transfer of surface energy to kinetic energy during the coalescence. This transfer inefficiency implies that the drops have less energy to rebound. (ii) Sessile oil drops typically have a large contact size. On a flat surface, the receding contact angle is typically below 60° and often close to zero [247]. Consequently, receding oil drops easily rupture before coming off the surface. (iii) On a superamphiphobic surface, oil drops display large apparent contact angles [133, 248]. However, the true liquid-solid contact angle is still small, leaving oil drops in a metastable state; that is, they can percolate into the surface [249]. Moreover, pressure as low as a few hundred pascals is sufficient to transition the drop from the metastable Cassie state to a state where the drop wets the surface thoroughly [133, 250]. The energy threshold needed for this transition is related to the so-called impalement pressure that depends on details of the coating and the liquid under investigation [249]. (iv) The low surface tension of oil means that the drop is easily deformable, which may give rise to enhanced viscous dissipation and energy loss upon impact. The drop can also locally impale the surface during impact [251, 252]

In this chapter, we experimentally and numerically investigate the dynamics of a low surface tension oil drop impacting a sessile drop of the same liquid, resting on a superamphiphobic surface (figure 4.2.1a). Indeed, we find that the impacting oil drop can lift the resting drop off the surface, without ever coalescing. Notably, we find four rebound scenarios without coalescence: (i) both drops rebound, (ii) two scenarios where the impacting drop rebounds while the sessile drop remains on the substrate, and (iii) the sessile drop rebounds while the impacting drop remains on the surface. We illustrate how these impact outcomes are governed by the Weber number (We , ratio of inertial to capillary stresses) and the extent of dimensionless offset from a head-on collision ($\chi = d/(2R)$, where R is the radius of each drop, and d is the distance between their centers of masses, see figure 4.2.1b). Direct numerical

simulations provide a quantitative description of (i) the velocity of both drops and of the surrounding vapor phase, (ii) how energy is transferred between the two drops during impact, and (iii) the viscous dissipation during impact and rebound. This allows for a quantitative comparison of experimental and numerical data of the rebound dynamics.

This chapter is organized as follows: § 4.2 briefly describes the experimental and numerical methods. We then explore the drop-on-drop impact by elucidating the experimental observations in § 4.3, followed by direct numerical simulations in § 4.4 where we reproduce the experimentally observed regimes and delve into the process dynamics using internal flow inside the two drops and the energy transfers between them. Lastly, the chapter ends with conclusion and outlook in § 4.5.

4.2 Method

In our experiments, a sessile oil drop is gently positioned on a superamphiphobic surface and then impacted with an identical second oil drop (figure 4.2.1a). The superamphiphobic surface is composed of a $\sim 20\text{ }\mu\text{m}$ thick layer of templated candle-soot [235, 253]. Candle soot consists of a porous network of $50 \pm 20\text{ nm}$ sized carbon nanobeads. Making use of chemical vapor deposition (CVD) of tetraethyl orthosilicate (TEOS) catalyzed by ammonia, a 25 nm thick layer of silica is deposited over the porous nanostructures to increase the mechanical stability of the fragile network (figure 4.2.1a). The soot-templated silica network is fluorinated with trichloroperfluorooctylsilane to lower the surface energy, producing a superamphiphobic surface which repels water and most oils. As a model oil, we use hexadecane for its low surface tension, low volatility, homogeneous properties and Newtonian behavior. A drop of hexadecane (figure 4.2.1a-ii) exhibits an apparent contact static angle of $\Theta^{\text{app}} = 164^\circ \pm 1^\circ$. For further details of the drop-substrate contact angle, see appendix 4.A.

For our drop impact studies, a sessile drop of hexadecane is gently placed on this superamphiphobic surface with a needle connected to a syringe pump (dosing rate: 2 mL/h). When gravity exceeds the drop-needle adhesion, the drop releases from the needle; this results in a drop volume of $V \approx 3\text{ }\mu\text{L}$ (figure 4.2.1a). This volume corresponds to a Bond number of 0.3 ($Bo = \rho_l g R^2 / \gamma$, ratio of gravitational to capillary stresses, where ρ_l is the density of the liquid, g is the gravitational acceleration, and R is the radius of a spherical droplet of identical volume). Note that a low Bond number implies that a

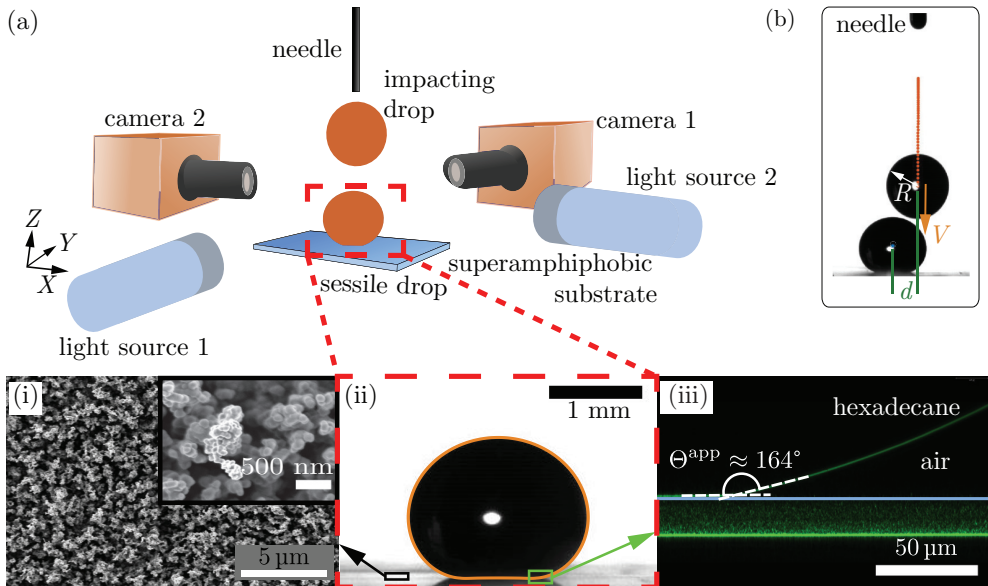


Figure 4.2.1: Experimental approach and the sessile drop: (a) Sketch of the experimental setup for binary drop impact on superamphiphobic surfaces. The needle is fixed to set the impacting height in the Z direction, and the relative distance between the sessile and impacting drops. The sessile drop is first centered along the YZ plane. Then the impacting drop is dispensed from the needle while the impact event is monitored with camera 2. Camera 1 is used to determine the relative positions of the drops in the X direction. The cameras and the light sources are aligned to observe the impact both in the XZ and YZ planes. Insets: (i) scanning electron micrograph (SEM) image of a soot-templated surface at two magnifications. (ii) hexadecane drop ($V \approx 3 \mu\text{L}$) resting on the superamphiphobic surface. The orange contour is the solution of the Young-Laplace equation [10] for a corresponding Bond number $Bo = 0.3$. (iii) confocal microscopy image showing a drop of hexadecane on the superamphiphobic surface (the blue line marks its approximate position). The image illustrates the apparent contact angle of the drop with the surface ($\Theta^{\text{app}} \approx 164^\circ$). The image is taken in reflection mode, i.e., no dye was added to the hexadecane. Reflection of light results from the differences between the refractive indices of hexadecane (1.43), air (1.0), glass and silica (≈ 1.46). The superamphiphobic layer consists mostly of air, and thus its refractive index is close to 1. Therefore, the horizontal glass-superamphiphobic layer and the hexadecane-superamphiphobic layer interfaces are clearly visible. The superamphiphobic layer itself is visible as a diffuse pattern, resulting from the reflection of light from the silica nanoparticles. (b) Image showing an off-center collision. The impact parameter is $\chi = d/(2R)$.

spherical cap can describe the drop. However, it does not provide insight on whether the drop passes the Cassie-to-Wenzel transition. Nonetheless, the shape of the drop is important as it forms the initial condition for the numerical simulation. To calculate and confirm this shape numerically, we solve the Young – Laplace equation [10]. The shape matches well with the experiments (see the orange contour in figure 4.2.1a-ii). The substrate is then translated laterally to position the sessile drop in the X and Y directions.

At an identical dosing rate, a second drop is released with an identical volume, $\mathcal{V} \approx 3 \mu\text{L}$, which impacts the sessile drop. The control parameters of the drop collision, determining the outcome, are the Weber number (We), which is related to the impact velocity (V), and the impact parameter (χ), which describes the offset from head-on alignment of the two colliding drops. The impact velocity V is controlled by varying the height of the dispensing needle from the substrate (figure 4.2.1a). The corresponding Weber number $We = \rho_l V^2 R^2 / \gamma$ compares fluid inertia and surface tension, where $\rho_l = 770 \text{ kg/m}^3$ is the density of the hexadecane and $\gamma = 27.5 \text{ mN/m}$ is its surface tension coefficient. In our experiments, the Weber number ranges from 0.02 to 9. Two synchronized high-speed cameras are perpendicularly positioned to capture the dynamics of the drops in the X , Y , and Z directions. The impact parameter of the two drops is given by the ratio $\chi = d / (2R)$, where d is the horizontal offset of the center of masses of the impacting drop and the sessile drop (figure 4.2.1b). Although we cannot exactly predict the impact parameter beforehand, the two camera system allows us to precisely measure the offset from head-on alignment by image analysis. $\chi = 0$ describes a perfect head-on collision whereas $\chi = 1$ corresponds to the situation when the two drops merely brush each-other ($d = 2R$).

4.3 Experimental observations

When varying the offset from head-on alignment χ and the Weber number We independently, six outcomes for the impact dynamics are observed, termed Cases I-VI (figure 4.3.1). The column A of images is taken just as the collision starts ($t = 0 \text{ ms}$) and is used to quantify the impact parameter, χ . Column B is at the point of maximum sessile drop compression, and column C demonstrates the shape of both drop just before they separate or coalesce. Column D illustrates the overall outcome of the collision event. We first consider the outcomes at $We \approx 1.5$ while varying χ . For a near zero χ , Case I is observed, which is a head-on collision (figure 4.3.1-I, supplemental movies 1–3). During

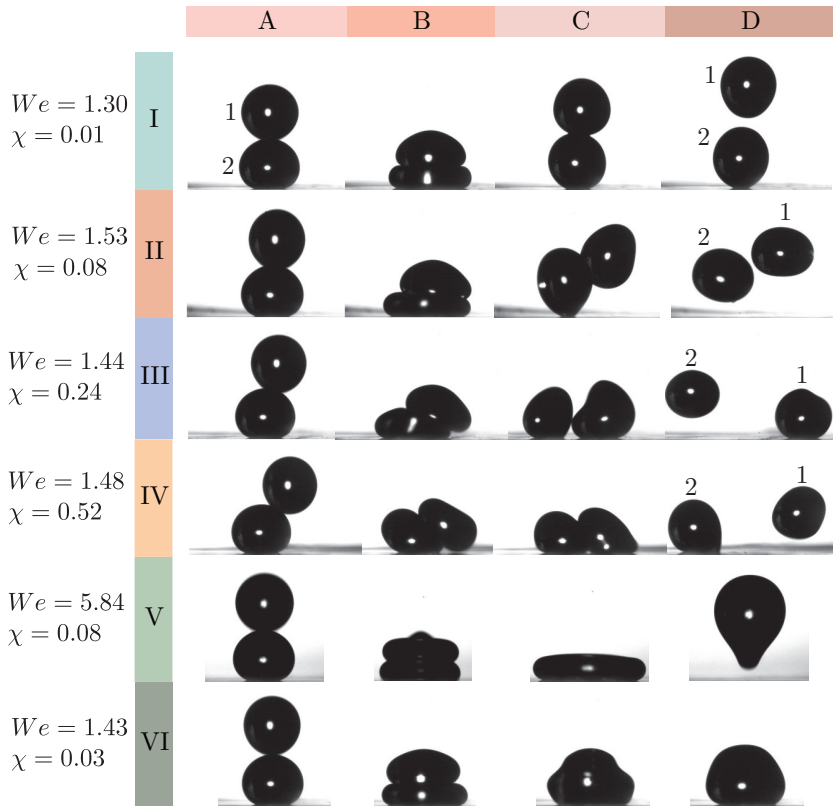


Figure 4.3.1: Snapshots of the impact dynamics: note that the drop labels 1 and 2 are for the impacting and sessile drop, respectively. Six outcomes (Cases I – VI) are observed when varying the impact parameter χ and the Weber number We independently. The rows correspond to different impact parameter for I-VI. The columns show characteristic stages of the collision process. A: just at collision, B: sessile drop at maximum compression, C: droplet shape just before separation or coalescence. D: final outcome of the impact. Volume of both drops is 3 μL . Case I, $We = 1.30$ and $\chi = 0.01$: the time stamp for each frame is: $t_A = 0 \text{ ms}$, $t_B = 8 \text{ ms}$, $t_C = 20 \text{ ms}$, $t_D = 25 \text{ ms}$. Case II, $We = 1.53$, $\chi = 0.08$: $t_A = 0 \text{ ms}$, $t_B = 8 \text{ ms}$, $t_C = 20 \text{ ms}$, $t_D = 24 \text{ ms}$. Case III, $We = 1.44$, $\chi = 0.24$: $t_A = 0 \text{ ms}$, $t_B = 8 \text{ ms}$, $t_C = 20 \text{ ms}$, $t_D = 24 \text{ ms}$. Case IV, $We = 1.48$, $\chi = 0.52$: $t_A = 0 \text{ ms}$, $t_B = 5.5 \text{ ms}$, $t_C = 7 \text{ ms}$, $t_D = 21 \text{ ms}$. Case V, $We = 5.84$, $\chi = 0.08$: $t_A = 0 \text{ ms}$, $t_B = 3.75 \text{ ms}$, $t_C = 8.5 \text{ ms}$, $t_D = 25.5 \text{ ms}$. Case VI, $We = 1.43$, $\chi = 0.03$: $t_A = 0 \text{ ms}$, $t_B = 7.5 \text{ ms}$, $t_C = 9 \text{ ms}$, $t_D = 17 \text{ ms}$.

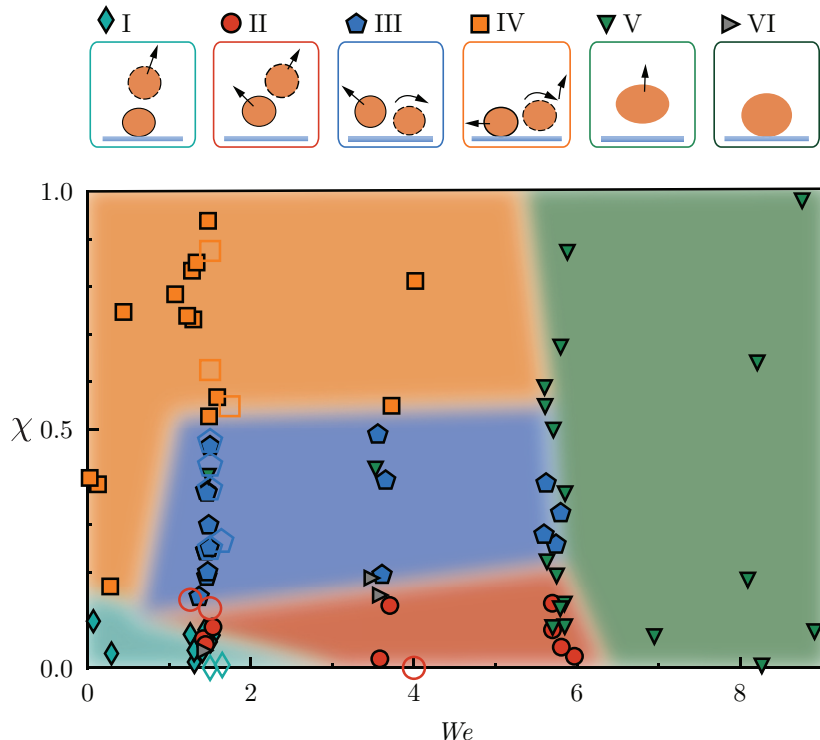


Figure 4.3.2: Regime map illustrating the observed cases as a function of the impact parameter $\chi = d/(2R)$ and Weber number We . The top sketches with the respective Roman case number are the possible outcomes after the hexadecane drop impacted on the sessile hexadecane drop. In the image strip, the sessile drop is represented with the solid outline, and the impacting drop with the dotted outline. The arrows represent the direction of motion after impact for each drop. In case III, the impacting drop has a horizontal-curved arrow that represents the rolling of the drop over the sessile drop. In case IV, the impacting drop has two associated arrows. The horizontal-curved arrow represents rolling over the sessile drop and the vertical arrow denotes bouncing after the impact event. Each possible outcome is marked by a color and symbol for identification and corresponds to the sketched cases I-VI. Closed symbols correspond to experiments and open ones to numerical simulations. The transition zones between the different scenario regions are not sharp. The colors assigned to the different cases are meant as a guide to the eye.

impact, both drops deform and spread radially, and as a result, show axial compression. The kinetic energy of the system is transferred to the surface energies of both the deformed drops. Moving forward in time, both drops start to retract. The sessile drop transfers energy back to the impacting drop in the form of kinetic energy. Upon completion of the collision, the impacting drop bounces off while the sessile drop stays on the substrate. The sessile drop also oscillates, hinting that it retains a part of the energy gained during impact. For a slightly higher offset, $\chi \lesssim 0.15$, Case II is observed (figure 4.3.1-II, supplemental movies 4–6). The initial collision is similar to Case I in that the drops collide, followed by vertical compression and lateral spreading. However, unlike Case I, the deformations are no longer symmetric, and the sessile drop also lifts off the surface. The displacement for either drop with respect to the center of mass of the initial sessile drop is in opposing lateral directions. Further increasing of the offset from head-on alignment to $\chi \lesssim 0.5$, the impacting drop glides over the sessile drop and rolls on the substrate, as illustrated by Case III (figure 4.3.1-III, $\chi = 0.24$, supplemental movies 7–9). Unlike Cases I and II, no rebound of the impacting drop is observed. Surprisingly, the sessile instead drop lifts-off the surface. As the impact parameter is increased even further ($\chi > 0.5$, Case IV), the impacting drop still rolls over the sessile drop (figure 4.3.1-IV, supplemental movies 10–12). However, during retraction, the impacting drop rebounds from the surface while the sessile drop moves along the surface.

In the above Cases I–IV, the Weber numbers were kept constant at $We \approx 1.5$ while the offset was varied. However, the outcome of the impact event also varies with the Weber number. To provide a better intuition on how both χ and We affect the observed outcomes, we plot our data as a phase diagram (figure 4.3.2). For $We \geq 6$, regardless of the impact parameter χ , we find coalescence of the two drops, as illustrated in Case V (figure 4.3.1-V, supplemental movie 13). In this regime, the air layer between the drops is unstable which results in direct contact and subsequent coalescence. The coalesced drop reaches a maximum spreading diameter during impact (column C in figure 4.3.1-V). During retraction, the drop elongates vertically and ultimately detaches from the surface. Occasionally, drops coalesce without subsequent bouncing (Case VI, figure 4.3.1-VI, supplemental movie 14). Although this outcome is rarely observed and likely caused by surface defects, we present this result for the sake of completeness to demonstrate all observed outcomes. Moreover, to consider the generality of the scenarios presented for oil-on-oil drop impact, we also tested water-on-water drop impact. Similar scenarios are

observed, as illustrated in figure 4.B.1.

4.4 Direct numerical simulations

Although the experimental observations consistently illustrate how We and χ dictate the observed impact outcomes, they lack detailed information on the velocity fields and how energy is transferred between the two drops. To access this information, we ran direct numerical simulations (DNS) and compared these results with our experimental data. For simulating non-coalescing droplets, we employ geometric Volume of Fluid (VoF) [143, 158] method with two distinct VoF tracers (see § 4.C for detailed discussions and implementation). This formulation ensures that drops cannot coalesce, reflecting the experimental situation where a finite air layer between the drops is preserved throughout the process.

We first ran four simulations choosing We and χ values within the regimes for Cases I-IV, as denoted by the open symbols in figure 4.3.2. The results are displayed in figure 4.4.1. The normalized times ($\tilde{t} = t/\tau_{\rho\gamma}$, where $\tau_{\rho\gamma} = \sqrt{(\rho_l R^3)/\gamma}$ is the inertio-capillary time scale.) correspond to the stages of the process, as described by columns A – D in figure 4.3.1. As is evident from the top rows (orange drops), the simulations reproduce the general collision outcomes consistent with the snapshots of the impact dynamics (figure 4.3.2). Moreover, the direct numerical simulations allow for quantifying the velocity vector fields for each of the cases (figure 4.4.1, bottom rows). These vector fields, combined with a calculation of the energy budget, renders it possible to quantitatively explore the dynamics of the oil drop-on-drop collision process. To account for the kinetic energy E_k , gravitational potential energy E_g , surface energy E_γ , and viscous dissipation E_η , we numerically calculated the total energy of the system as

$$E = E_m + E_\gamma + E_\eta, \quad (4.1)$$

where the energies are calculated using a method similar to the one developed by Wildeman et al. [30]. Note that E_k includes the kinetic energy of the center of mass as well as the oscillation and rotational energies obtained in the reference frame that is translating with the center of mass of the individual drops. The details of these calculations are provided in § 4.D.

While keeping the Weber number at $We = 1$, the cases appear in order from I to IV with increasing offset position from head-on alignment χ . For

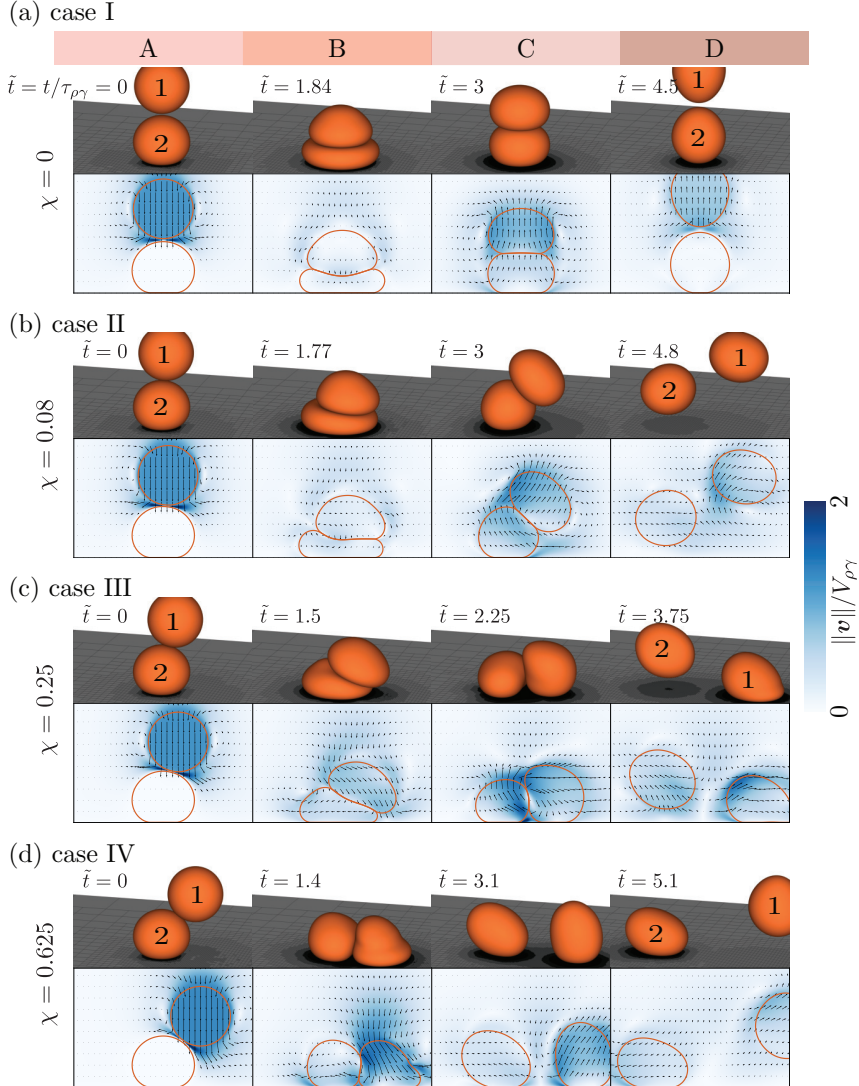


Figure 4.4.1: Snapshots from direct numerical simulations: illustration of different phases of drop-on-drop collisions and the subsequent outcomes. (a) Case I: ($\chi = 0$) impacting drop bounces back and the sessile drops stays on the substrate, (b) Case II: ($\chi = 0.08$) impacting drop bounces back and the sessile drop lifts-off from the substrate, (c) Case III: ($\chi = 0.25$) impacting drop stays on the substrate and the sessile drop lifts-off, and (d) Case IV: ($\chi = 0.625$) impacting drop bounces back and sessile drop stays on the substrate. For all these cases, $We = 1.5$. The drop labels 1 and 2 are for the impacting and sessile drops, respectively. \tilde{t} is the non-dimensionalized time used for the numerical simulations and is given by $\tilde{t} = t/\tau_{\rho\gamma}$ where $\tau_{\rho\gamma} = \sqrt{(\rho R^3)/\gamma}$ is the inertio-capillary time scale. The absolute values of the normalized velocities vary between zero (white) and twice the inertio-capillary velocity, $V_{\rho\gamma} = \sqrt{\gamma/(\rho R)}$ (dark blue).

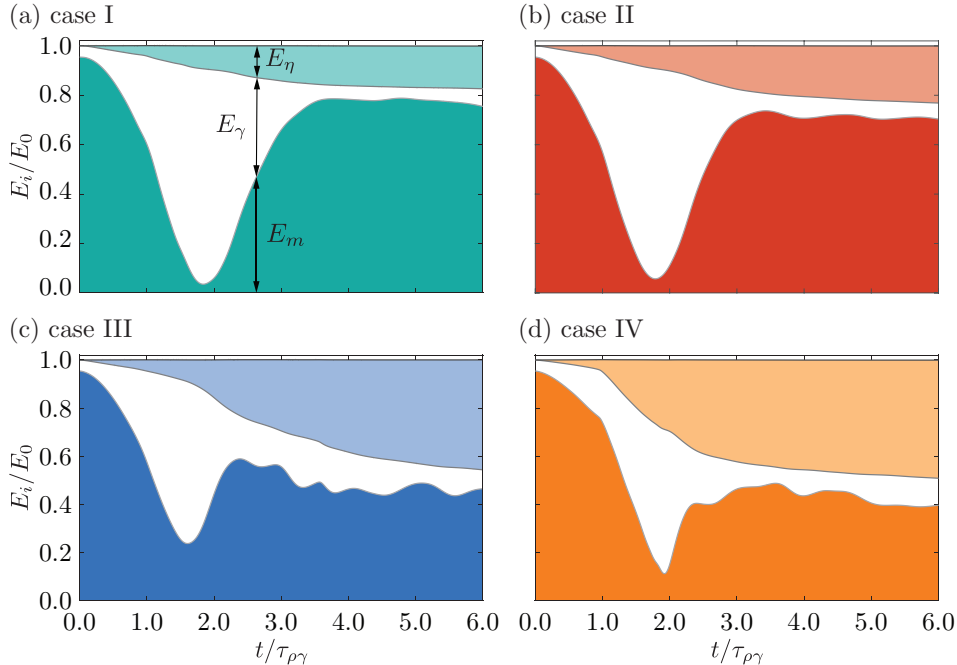


Figure 4.4.2: Energy budget: the temporal variation of energy transfer elucidates different stages of the drop-on-drop impact process at $We = 1.5$. Initially, all the energy is stored as the mechanical energy of the impacting drop and surface energy of the sessile drop (E_0). Then, the mechanical energy of the system decreases, and is transferred into the surface energy of the drops. This transfer is followed by a recovery stage where surface energy is transferred back into the mechanical energy of the system. A part of the energy is lost as viscous dissipation. This viscous dissipation takes into account the combined energy dissipated both in the liquid drops and the surrounding air. This calculation includes the air-layers between the drops, and between the drops and the superamphiphobic substrate. (a) Case I: $\chi = 0$, (b) Case II: $\chi = 0.08$, (c) Case III: $\chi = 0.25$, and (d) Case IV: $\chi = 0.625$. E_m is the total mechanical energy of the system ($E_m = E_k + E_g$), E_γ the surface energy of the two drops, and E_η the viscous dissipation in the system. Note that the total mechanical energy (E_m) includes the energy of center of mass of the drops ($E_m^{\text{CM}} = E_k^{\text{CM}} + E_g^{\text{CM}}$), where E_g^{CM} is the gravitational potential energy as well as the oscillation and rotational energies obtained in the reference frame that is translating with the center of mass of the individual drops.

all cases, the energy is initially contained in the mechanical energy of the impacting drop (i.e., its kinetic and potential energy) and the surface energy of the sessile drop. To describe the system energy of the DNS results presented in figure 4.4.1, we plot the complete energy budget for each case in figure 4.4.2. For convenience of comparison, the energies in figure 4.4.2 are normalized with the initial energy of the system.

Let us consider first a head-on collision where $\chi = 0$ (figure 4.4.1a, figure 4.4.2a, and supplementary videos 2–3, Case I), which is defined by a symmetric configuration. First, the momentum is transferred from the impacting drop to the sessile drop, as the sessile drop deforms. This transfer results in deceleration of the impacting drop. Moreover, the kinetic energy of the impacting drop transforms into the surface energy of the system. This transfer continues until $\tilde{t} = 1.84$ (Fig. 4a: Column B) when the deformation in the two drops is maximum. Even at the moment of maximal deformation of both drops, the kinetic energy remains finite because of rotational flow within the drops (figure 4.4.1a: column B, velocity field) [30]. The mechanical energy passes a minimum ($\tilde{t} = 1.84$) when the surface energy is maximal. For $\tilde{t} > 1.84$, the surface energy of the two drops is converted back into kinetic energy. Retraction of the sessile drop is hindered by the impacting one (figure 4.4.1a: column C), directly sitting on top of it. As a result, the sessile drop cannot lift-off from the substrate, but it releases any extra energy by oscillations (supplementary videos 1–2). During impact, the drops lose approximately 20% of their initial energy through viscous dissipation (figure 4.4.2a). This dissipation occurs mainly during the initial stages of the process ($\tilde{t} < 3$). It should be noted that the surface tension coefficient (γ), viscosity (η), and impact velocity (V) all affect viscous dissipation (see chapter 2). These properties are related to the Ohnesorge number ($Oh = \eta/\sqrt{\rho_l \gamma R} \approx 0.03$), which is the ratio of the inertio-capillary to inertio-viscous timescales, and the Weber number, $We = \rho_l V^2 R / \gamma \sim \mathcal{O}(1)$ (see equation (4.15) and [150, 160]). The dissipation observed in our case is lower than that reported previously for a single drop impact at comparable Oh and We on non-wetting rigid substrates (see chapter 2). In the case of a single drop impact, the velocity of the drop goes to zero quickly as it approaches a rigid substrate [28], leading to high dissipation close to the substrate. In the case of drop-on-drop impact, the sessile drop is deformable, decreasing the deceleration experienced by the impacting drop. As a result, the system retains almost 80% of its initial energy in the form of mechanical and surface energy of the drops.

For slightly off-center collisions, where $\chi = 0.08$ (figure 4.4.1b, figure 4.4.2b,

and supplementary videos 5–6, Case II), the initial collision is similar to Case I: the drops collide, followed by vertical compression and lateral spreading. However, unlike Case I, the impacting and the sessile drops lift-off from the substrate. This feature results from the loss of axial symmetry of the velocity field for $\chi > 0$. During retraction, transfer of momentum from the compressed sessile drop back to the impacting drop occurs mainly along a vector pointing normal to the apparent contact zone. Moreover, the sessile drop attempts to regain its spherical shape (minimum surface energy state). As a result, the velocity field of the sessile drop is almost parallel to the contact zone, i.e., pointing to the upper left. These opposing orientations of the velocity fields cause the impacting drop to bounce off the sessile drop, and the sessile drop to lift-off from the substrate (see the velocity vector fields in figure 4.4.1b and supplementary video 6). Viscous dissipation increases as compared to a head-on-collision, but still is maximum during the initial stages of the process owing to the dissipation in the viscous boundary layer as the impacting drop slides over the sessile one ($\tilde{t} < 3.5$, figure 4.4.2b).

As the offset is further increased to $\chi = 0.25$ (figure 4.4.1c, figure 4.4.2c, and supplementary videos 8–9, Case III), the impacting drop glides over the sessile drop (facilitated by the thin air layer), and sufficient energy is transferred to lift the sessile drop from the substrate. This can be understood from the interplay of the velocity field and the contact time (figure 4.4.1c and supplementary video 9). The relatively large offset from head-on alignment causes the averaged velocity field of the restoring impacting drop to point downwards, while the velocity field of the sessile drop is pointing upwards. The large deformations of both drops are reflected in the evolution of the surface energy (figure 4.4.2c). These large deformations also cause an increase in the viscous dissipation (E_η): at the end of the process, almost 50% of the initial energy is lost.

Finally, if the offset from head-on alignment is increased even more to $\chi = 0.625$ (figure 4.4.1d, figure 4.4.2d, and supplementary videos 11–12, Case IV), the time of contact is insufficient to transfer enough energy to the sessile drop for lift-off [254]. Moreover, the vector normal to the drop-drop contact area is farthest from vertical as compared to the normal vectors in other cases. That is, it points nearly horizontal. As a result, the sessile drop rolls along the substrate and the impacting drop instead rebounds from the surface, resembling typical drop-surface impact. In this case, most of the energy is retained by the impacting drop, as illustrated in Fig. 5d. Similar to Case III, viscous dissipation accounts for almost 50% of the initial total energy. Although in

Case I and IV the impacting drop rebounds while the sessile drop remains on the surface, we discriminate between both cases. For Case I, the vector fields are symmetric around the $X = Y = 0$ axis, whereas for Case IV the vector fields are highly asymmetric and the sessile drop rolls along the surface. Furthermore, in Case IV, the impacting drop bounces-off the substrate, as opposed to the sessile drop in Case I.

These results indicate that the DNS provide a quantitative description of the impact dynamics. At this point, we investigate whether there is a one-to-one match of the experimental data and numerical simulations; this is done by comparing the drop boundaries and experimentally-determined mechanical energies with the numerical predictions. Since we cannot exactly predict the impact parameter experimentally beforehand, we choose the control parameters for the numerical simulations by first analyzing the experimental data. Notably, we achieve a nearly quantitative agreement of the drop boundaries and experimental mechanical energies (figure 4.4.3). The different snapshots in figure 4.4.3(i-iv) refer to the following time steps: (i) at the instant of collision, (ii) sessile drop at maximum compression, (iii) droplet shape just before separation, and (iv) final outcome of the impact. We expect that slight deviations between the experimental and numerically determined drop boundaries result from marginal inaccuracies in the experimental determination of the off-set parameter. However, the agreement is remarkably good, keeping in mind that there are no fitting parameters.

In figure 4.4.3(a-v) and 4.4.3(b-v), we compare the measured experimental mechanical energies (data points) with those calculated using simulations (dotted lines). The calculated mechanical energies exceed the experimentally determined energies. To understand the origin of this discrepancy, one needs to consider that experimentally, we are only able to measure the vertical and horizontal displacements to approximate the mechanical energy of each drop. The images analysis did not offer an easy route to quantify the contribution of the rotational and oscillation energies that are included in the numerically calculated mechanical energy, E_m . Therefore, to test whether neglecting the rotational and oscillation energies in our experiments causes the discrepancy, we calculated the center of mass mechanical energies (E_m^{CM}) for the two drops numerically (figure 4.4.3a-v and 4.4.3b-v, see § 4.D for details of calculation). The zero of the potential energy ($E_g^{\text{CM}} = 0$) refers to the center of mass of the sessile drop at $t = 0$. This implies that E_g^{CM} of the sessile drop becomes negative during compression. The center of mass kinetic energy (E_k^{CM}) is added to this value to get E_m^{CM} , i.e., $E_m^{\text{CM}} = E_k^{\text{CM}} + E_g^{\text{CM}}$. As illustrated in

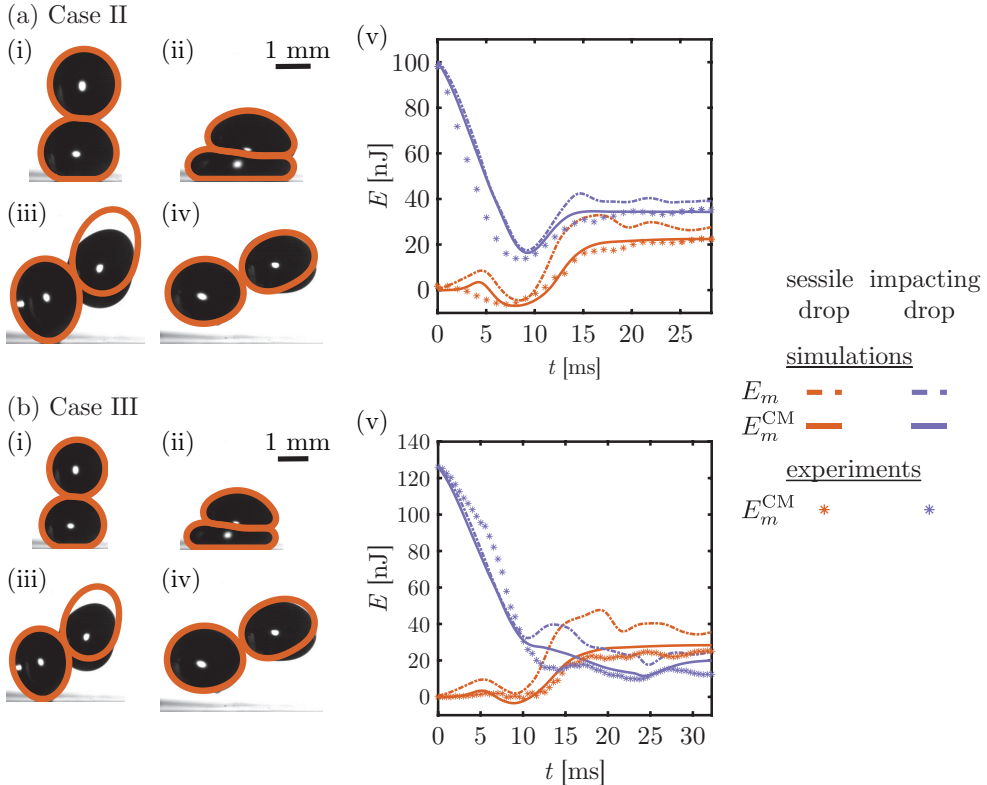


Figure 4.4.3: Validation of the numerical code: (a) Case II: both sessile and impacting drop lift-off ($We = 1, \chi \approx 0.08$) for $t =$ (i) 0 ms, (ii) 8 ms, (iii) 20 ms, (iv) 24 ms, and (b) Case III: sessile drop lifts-off and impacting drop rolls on the substrate ($We = 1, \chi \approx 0.25$) for $t =$ (i) 0 ms, (ii) 8 ms, (iii) 20 ms, (iv) 24 ms. In the subfigures (i) to (iv), overlay of experimental images and DNS results (orange contour) are shown. (v) The mechanical energy of the center of mass (E_m^{CM}) calculated from experiments and simulations match within the experimental error. Note that in experiments, we could only keep track of the motion of the center of mass whereas in numerical simulations, the entire velocity field is known. Using this information, we can calculate the overall energy budgets. Here, the total mechanical energy of the drops (E_m) is shown in solid lines for reference. Error estimated in the experimental data is approximately 20% of the total energy.

figure 4.4.3(a-v) and 4.4.3(b-v), the numerical results (solid lines) now nearly overlay the experimental results (data points). This holds for both the temporal development of the energy for the sessile drop as well as the impacting drop. Supposedly, the small discrepancies may arise from finite adhesion of the sessile drop to the substrate in the experiments (which is not accounted for in the simulations). An additional source of error may arise from the selection of time $t = 0$. We choose $t = 0$ based on the time instant when the sessile drop starts to feel the presence of the velocity field of the impacting drop, i.e., when the kinetic energy of the center of mass of the sessile drop becomes non-zero. Nevertheless, the remarkable agreement between the experimental and numerical results for the center of mass mechanical energies illustrate that the DNS are able to describe the oil drop-on-drop impact physics accurately. This allows for quantifying the contribution of the rotational and oscillatory energies. As future work, one can also estimate these contributions from experimentally obtained boundaries of the drops by employing the method described in Moláček and Bush [150].

4.5 Conclusions and outlook

By combining systematic experiments with numerical simulations, we illustrate how to predict and control the outcome of binary oil drop impacts on low adhesion surfaces. Four non-coalescing outcomes are attainable by varying the Weber number We and the offset from head-on alignment of the impacting drops χ . One-to-one comparisons between the experimentally and numerically determined drop boundaries and center of mass mechanical energies illustrate the power of the direct numerical simulations for quantitatively predicting the dynamics of drop-on-drop impact. More specifically, our numerical simulations illustrate that these general outcomes are governed by the average direction of the flow velocity vectors during the retraction phase, which are associated with We and χ . In addition, our results indicate that the ability to remove a sessile oil drop from the surface, as in Cases II and III, first requires sufficient energy transfer from the impacting drop and subsequently requires contrasting velocity vector directions of the two retracting drops. Interestingly, our results illustrate that different outcomes exist even when the total dissipative losses of the system are similar, i.e., the alignment of impact alone can be used to determine the recovered energy distribution between the two drops after impact.

Acknowledgments

We would like to thank Hans-Jürgen Butt for fruitful discussions, Andrea Prospertti for insightful discussions on numerical simulations at different stages of the project, Pierre Chantelot for discussion on energy dissipation in single drop impact phenomenon, and Uddalok Sen for proof-reading this chapter. We would also like to thank Michael Kappl for help with the estimation of forces on the substrate, and Abhishek Khadiya for support with initial measurements.

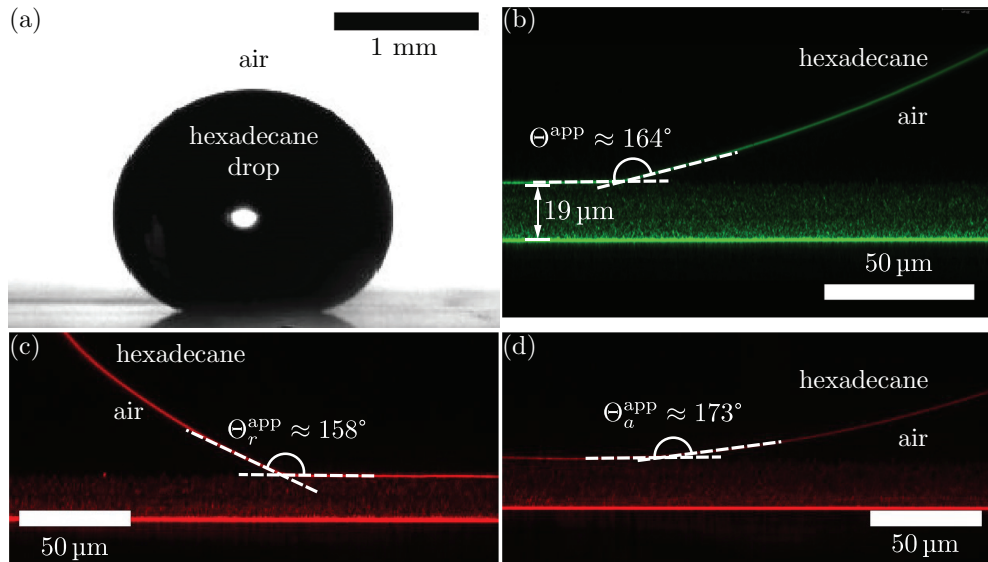
Appendix

4.A Contact angle measurements

A drop of hexadecane (figure 4.2.1a-ii) exhibits an apparent contact static angle of $\Theta^{\text{app}} = 164^\circ \pm 1^\circ$, an apparent receding contact angle of $\Theta_r^{\text{app}} = 158^\circ \pm 3^\circ$, and an apparent advancing contact angle $\Theta_a^{\text{app}} \approx 180^\circ$ [255], as determined by confocal microscopy (figure 4.2.1a-iii and 4.A.1). Low lateral adhesion of hexadecane is confirmed by measuring a low roll-off angle of $3^\circ \pm 2^\circ$ [256, 257]. Roll-off angles measurements were performed using a goniometer OCA 35 for hexadecane drops of 5 μL . The apparent contact angle was measured with a Leica TCS SP8 confocal microscope, equipped with an HCX PL APO 40x/0.85 dry objective, for a hexadecane drop of 10 μL . The advancing and receding angles were measured while moving the hexadecane drop with a needle. The needle was supported on a micrometer stage next to the confocal microscope. All angles were measured at least three times and the results are shown in figure 4.A.1.

4.B Water-on-water drop impact

For comparison, we also performed head-on and off-center collisions for water drops of a similar diameter than for oil drops. To test the generality of our experiments, we used superamphiphobic textiles instead of soot templated surfaces. Superamphiphobic textiles show slightly worse wetting properties than soot template surfaces. This is reflected in higher roll-off angles. The roll-off angle of water with the surface varied between $13^\circ - 20^\circ$ for the textile surfaces while the roll-off angles varied between $2^\circ - 5^\circ$ on the soot-templated glass. On the other hand, the Cassie-to-Wenzel transition is less likely for water drops than for oil drops. When varying the Weber number We and the impact parameter χ , the same six outcomes could be observed, same as the



4

Figure 4.A.1: Sessile oil drop on a superamphiphobic substrate: (a) shadowgraph and (b-d) confocal images of a hexadecane drop on soot-templated glass slide. The shadowgraph image shows the typical shape of a sessile hexadecane drop during the experiments. The corresponding volumetric radius is 0.9 mm. The confocal microscopy image illustrates the apparent contact angle of the drop with the surface. The image was taken in reflection mode to allow measuring the contact angle with highest possible accuracy. The measured roll-off angle of a drop of 5 μL is 3.2° (measured with a goniometer). The apparent contact angle $\Theta^{\text{app}} \approx 164^\circ$, the receding angle $\Theta_r^{\text{app}} \approx 158^\circ$, and the advancing angle $\Theta_a^{\text{app}} \approx 173^\circ$, were measured with a drop of 10 μL volume. Ideally, Θ_a^{app} should be 180° . The difference could be attributed to the limited optical contrast.

cases with hexadecane drops (figure 4.B.1)

4.C Simulation methodology

We use a finite volume method based partial differential equation solver, Basilisk C [143] for numerical simulation of incompressible Navier-Stokes equations,

$$\nabla \cdot \mathbf{v} = 0, \quad (4.2)$$

$$\frac{\partial \tilde{\mathbf{v}}}{\partial \tilde{t}} + (\tilde{\mathbf{v}} \cdot \tilde{\nabla}) \tilde{\mathbf{v}} = \frac{1}{\tilde{\rho}} \left(-\tilde{\nabla} \tilde{p} + Oh \tilde{\nabla} \cdot (2\tilde{\eta}\tilde{\mathcal{D}}) + \tilde{\kappa}\tilde{\delta}_s\hat{\mathbf{n}} \right) - Bo\hat{\mathbf{Z}}, \quad (4.3)$$

where the velocity \mathbf{v} and pressure p fields are non-dimensionalized using the inertio-capillary velocity ($V_{\rho\gamma} = \sqrt{\gamma / (\rho_l R)}$) and capillary pressure ($P_\gamma = \gamma/R$), respectively. All length scales are normalized using the radius of the impacting drop (R). In equation (4.3), \mathcal{D} is the deformation tensor (i.e., the symmetric part of the velocity gradient tensor, $\tilde{\nabla}\tilde{\mathbf{v}}$) and $\tilde{\kappa}\tilde{\delta}_s\hat{\mathbf{n}}$ represent the singular ($\delta_s = 1$ at the interfaces and 0 otherwise) surface tension force, where κ and $\hat{\mathbf{n}}$ are the interfacial curvature and normal, respectively. Since we do not vary the type of liquid during and the volume of drops in our experiments or simulations, Ohnesorge number ($Oh = \eta_l/\sqrt{\rho_l\gamma R} = 0.0216$) and Bond number ($Bo = \rho_l g R^2/\gamma = 0.308$) remain constant. Lastly, in the simulations, the impact velocity is characterized by the impact Weber number ($V = \sqrt{We}$).

We use the geometric volume of fluid (VoF) [143, 158] method for interface tracking. Consequently, one-fluid approximation [2, 156] is used in the solution of the Navier-Stokes momentum equation (equation (4.3)).

To impose the condition of non-coalescence of the drops, same as chapter 3, different VoF tracers are used for the two droplets (equation 4.4). The use of two different tracers, along with interface reconstruction, ensures that there is always a thin air layer (thickness $\sim \Delta_1$, where $\Delta_1 = R/256$ is the size of smallest grid cell in the simulation domain). Additionally, in order to model the superamphiphobic substrate, it is assumed that there is a thin air layer (thickness $\sim \Delta_2$, where $\Delta_2 = R/512$ is the smallest grid cell near the substrate) between the drops and the substrate. All other boundaries are assumed to have no flow and free slip condition. We ensure convergence by comparing the viscous dissipation of the system and have chosen Δ such that the difference between consecutive simulations is small. The properties,

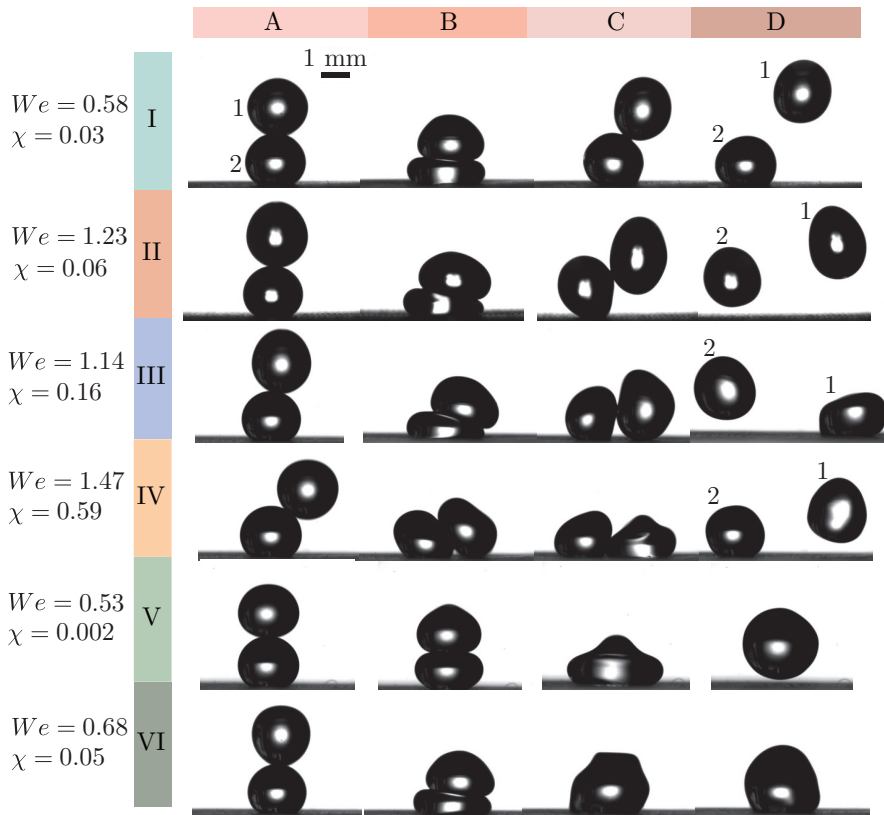


Figure 4.B.1: Snapshots of the impact dynamics of water drops: note that the drop labels 1 and 2 are for the impacting and sessile drop, respectively. Six outcomes (Cases I – VI) are observed when varying the impact parameter χ and the Weber number We independently. The rows correspond to different impact parameter for I-VI. The columns show characteristic stages of the collision process. A: just at collision, B: sessile drop at maximum compression, C: droplet shape just before separation or coalescence. D: final outcome of the impact. Volume of both drops is 8 μL . Case I, $We = 0.58$ and $\chi = 0.03$: the time stamp for each frame is: $t_A = 0 \text{ ms}$, $t_B = 10.5 \text{ ms}$, $t_C = 23 \text{ ms}$, $t_D = 36 \text{ ms}$. Case II, $We = 1.23$, $\chi = 0.06$: $t_A = 0 \text{ ms}$, $t_B = 10.5 \text{ ms}$, $t_C = 19 \text{ ms}$, $t_D = 30.5 \text{ ms}$. Case III, $We = 1.14$, $\chi = 0.16$: $t_A = 0 \text{ ms}$, $t_B = 9 \text{ ms}$, $t_C = 15 \text{ ms}$, $t_D = 30 \text{ ms}$. Case IV, $We = 1.47$, $\chi = 0.59$: $t_A = 0 \text{ ms}$, $t_B = 5.5 \text{ ms}$, $t_C = 9 \text{ ms}$, $t_D = 24 \text{ ms}$. Case V, $We = 0.53$, $\chi = 0.002$: $t_A = 0 \text{ ms}$, $t_B = 4 \text{ ms}$, $t_C = 14.5 \text{ ms}$, $t_D = 36 \text{ ms}$. Case VI, $We = 0.68$, $\chi = 0.05$: $t_A = 0 \text{ ms}$, $t_B = 10 \text{ ms}$, $t_C = 12.5 \text{ ms}$, $t_D = 21 \text{ ms}$.

such as density and viscosity are calculated using the VoF arithmetic property equations (equation 4.5, where A_{gl} is the ratio of properties of gas and liquid).

$$\left(\frac{\partial}{\partial t} + \mathbf{v} \cdot \nabla \right) \{ \Psi_1, \Psi_2 \} = 0, \quad (4.4)$$

$$\tilde{A} = A_{gl} + (1 - A_{gl}) (\Psi_1 + \Psi_2) \quad \forall A \in [\rho, \eta], \quad (4.5)$$

4.D Energy budget calculations

In this section, we discuss the different equations that we have used to calculate different energies non-dimensionalized by the capillary energy scale $\tilde{E}_i = E_i / (\gamma R^2)$. First, we discuss the calculation of energies of the center of mass of the drops (\tilde{E}_m^{CM}),

$$\tilde{E}_m^{\text{CM}} = \tilde{E}_k^{\text{CM}} + \tilde{E}_g^{\text{CM}}, \quad (4.6)$$

where \tilde{E}_k^{CM} and \tilde{E}_g^{CM} are the center of mass kinetic energy and potential energy respectively. For these calculations, we first need to find the magnitude of velocity and position of the center of mass for each drop,

$$\tilde{\mathbf{v}}^{\text{CM}} = \frac{\int_{\tilde{\Omega}} \tilde{\mathbf{v}} d\tilde{\Omega}}{\tilde{\Omega}}, \quad (4.7)$$

$$\tilde{Z}^{\text{CM}} = \frac{\int_{\tilde{\Omega}} \tilde{Z} d\tilde{\Omega}}{\tilde{\Omega}} \quad (4.8)$$

where, $d\Omega$ is the differential fluid volume. Further, E_k^{CM} and E_g^{CM} can be calculated,

$$\tilde{E}_k^{\text{CM}} = \frac{2}{3} \pi (\tilde{\mathbf{v}}^{\text{CM}} \cdot \tilde{\mathbf{v}}^{\text{CM}}), \quad (4.9)$$

$$\tilde{E}_g^{\text{CM}} = Bo \tilde{Z}^{\text{CM}}. \quad (4.10)$$

The overall energy budget consists of the total mechanical energy $\tilde{E}_m = \tilde{E}_k + \tilde{E}_g$, the surface energy \tilde{E}_γ , and the energy dissipation \tilde{E}_η , calculated as follows:

$$\tilde{E}_k = \int_{\tilde{\Omega}} \frac{1}{2} \tilde{\rho} (\tilde{\mathbf{v}} \cdot \tilde{\mathbf{v}}) d\tilde{\Omega}, \quad (4.11)$$

$$\tilde{E}_g = Bo \int_{\tilde{\Omega}} \tilde{\rho} \tilde{Z} d\tilde{\Omega}, \quad (4.12)$$

$$\tilde{E}_\gamma = \int_{\tilde{\mathcal{A}}} d\tilde{\mathcal{A}}, \quad (4.13)$$

$$\tilde{E}_\eta = \int_0^{\tilde{t}} \tilde{\xi}_\eta d\tilde{t} \quad (4.14)$$

In equations (4.11) and (4.12), energies of both the drops as well as the surrounding air medium are considered. Noticing that the density ratio of air to liquid, $\rho_{gl} = 1/770 \ll 1$ and that the domain is fixed in volume, the change in gravitational potential energy of the air medium is negligible. This implies that $E_g = E_g^{\text{CM}}$. The contributions from the surrounding air to \tilde{E}_k and \tilde{E}_η are also very small but we include them here for completeness. In equation 4.13, $d\tilde{\mathcal{A}}$ represents a differential surface. Lastly, equation 4.14 gives the total viscous dissipation in the system. In this equation, ξ_η denotes the viscous dissipation function given by

$$\tilde{E}_\eta = Oh \int_{\tilde{\Omega}} 2\tilde{\eta} (\tilde{\mathcal{D}} : \tilde{\mathcal{D}}) d\tilde{\Omega}. \quad (4.15)$$

4.E Code availability

All codes used in this chapter are permanently available at Sanjay [258].

4.F Supplemental movies

These supplemental movies are available at Sanjay [[external YouTube link](#), 259].

SM1: ($We \approx 1.30$ & $\chi \approx 0.01$) Experimental video of Case I for hexadecane drops: bouncing of impacting drop.

SM2: ($We = 1.50$ & $\chi = 0$) Simulation video of Case I for hexadecane drops: bouncing of impacting drop.

- SM3: ($We = 1.50 \& \chi = 0$) Simulation video showing velocity vectors of Case I for hexadecane drops: bouncing of impacting drop. The two-dimensional contour represents the slice $Y = 0$. Time is normalized by the capillary time scale, $\tau_{\rho\gamma} = \sqrt{(\rho_l R_0^3) / \gamma}$.
- SM4: ($We \approx 1.53 \& \chi \approx 0.08$) Experimental video of Case II for hexadecane drops: bouncing of the impacting drop followed by lift-off of the sessile drop.
- SM5: ($We = 1.50 \& \chi = 0.08$) Simulation video of Case II for hexadecane drops: bouncing of the impacting drop followed by lift-off of the sessile drop.
- SM6: ($We = 1.50 \& \chi = 0.08$) Simulation video showing velocity vectors of Case II for hexadecane drops: bouncing of the impacting drop followed by lift-off of the sessile drop. The two-dimensional contour represents the slice $Y = 0$. Time is normalized by the capillary time scale, $\tau_{\rho\gamma} = \sqrt{(\rho_l R_0^3) / \gamma}$.
- SM7: ($We = 1.50 \& \chi = 0.08$) Experimental video of Case III for hexadecane drops: sliding-off of the impacting drop on top of the sessile drop followed by lift-off of the sessile drop.
- SM8: ($We = 1.50 \& \chi = 0.25$) Simulation video of Case III for hexadecane drops: sliding-off of the impacting drop on top of the sessile drop followed by lift-off of the sessile drop.
- SM9: ($We = 1.50 \& \chi = 0.25$) Simulation video showing velocity vectors of Case III for hexadecane drops: sliding-off of the impacting drop on top of the sessile drop followed by lift-off of the sessile drop. The two-dimensional contour represents the slice $Y = 0$. Time is normalized by the capillary time scale, $V_{\rho\gamma} = \sqrt{(\rho_l R_0^3) / \gamma}$.
- SM10: ($We = 1.50 \& \chi = 0.25$) Experimental video of Case IV for hexadecane drops: sliding-off of the impacting drop on top of the sessile drop followed by its lift-off. In this case, the sessile drop stays on the substrate .
- SM11: ($We \approx 1.50 \& \chi \approx 0.625$) Simulation video of Case IV for hexadecane drops: sliding-off of the impacting drop on top of the sessile drop followed by its lift-off. In this case, the sessile drop stays on the substrate.

chapter 4: lifting a sessile oil drop with an impacting one



source code



supplemental movies

- SM12: ($We \approx 1.50$ & $\chi \approx 0.625$) Simulation video showing velocity vectors of Case IV for hexadecane drops: sliding-off of the impacting drop on top of the sessile drop followed by its lift-off. In this case, the sessile drop stays on the substrate. The two-dimensional contour represents the slice $Y = 0$. Time is normalized by the capillary time scale, $\tau_{\rho\gamma} = \sqrt{(\rho_l R_0^3) / \gamma}$.
- SM13: ($We \approx 5.84$ & $\chi \approx 0.08$) Experimental video of Case V for hexadecane drops: coalescence of drops and lift-off of coalesced drop.
- SM14: ($We \approx 1.43$ & $\chi \approx 0.03$) Experimental video of Case VI for hexadecane drops: coalescence of drops and coalesced drop remains on the substrate.

Part II

Retraction & Bursting

Chapter 5

Taylor-Culick retractions and the influence of the surroundings^o

When a freely suspended liquid film ruptures, it retracts spontaneously due to surface tension. If the film is surrounded by air, the retraction velocity approaches the constant Taylor-Culick velocity. However, when surrounded by a viscous medium, the dissipation outside dictates the magnitude of the retraction velocity. In this chapter, we study the retraction of a liquid (water) film in a viscous oil ambient (*two-phase* Taylor-Culick retractions), and that sandwiched between air and a viscous oil (*three-phase* Taylor-Culick retractions). In the latter case, the experimentally-measured retraction velocity is observed to have a weaker dependence on the viscosity of the oil phase as compared to the configuration where the water film is surrounded completely by oil. Numerical simulations indicate that this weaker dependence arises from the localization of viscous dissipation near the three-phase contact line. The speed of retraction only depends on the viscosity of the surrounding medium and not on that of the film. From the experiments and the numerical simulations, we reveal regimes for the scaling of the film Weber number We_f or the surroundings capillary number Ca_s vs. the surroundings Ohnesorge number Oh_s in the regime of highly viscous surroundings ($Oh_s \gg 1$), namely $We_f \sim Oh_s^{-2}$ and $Ca_s \sim Oh_s^0$ for the two-phase Taylor-Culick configuration, and $We_f \sim Oh_s^{-1}$ and $Ca_s \sim Oh_s^{1/2}$ for the three-phase Taylor-Culick configuration.

^oSubmitted as: **Vatsal Sanjay**, Uddalok Sen, Pallav Kant, and Detlef Lohse, *Taylor-Culick retractions and the influence of the surroundings*, J. Fluid Mech. Simulations are done by Sanjay; experiments by Sen and Kant; analysis and writing by Sanjay and Sen; and supervision by Lohse. Proofread by everyone.

5.1 Introduction

Liquid films, sheets, and shells have piqued the interest of fluid dynamicists [97, 260] for nearly two centuries ever since the seminal works of Taylor [34], Savart [87, 88, 89], Taylor [261]. A freely suspended liquid film warrants further attention among these configurations as it is inherently metastable owing to its high surface area. Indeed, if a large enough [97, 262] hole nucleates on the film, the sheet will spontaneously retract to reduce its surface area. Such interfacial destabilization leading to film rupture and bursting can also result in waterborne disease transmission [263]. The bursting of liquid films at an oil-air interface is important for various industrial applications in the chemical and petrochemical engineering sectors as well. One area of particular interest is underwater oil spills in oceans, such as the Deepwater Horizon spill in 2010 in the Gulf of Mexico [264]. For these spills, droplets (or slugs) of oil may rise to the free surface of water via buoyancy, and then rupture the free surface of water directly above it. The water film will retract upon rupture, and the oil will spread on the water surface, thus perpetuating an environmental hazard.

Perhaps the most widely studied example of sheet destabilization and retraction is during the bursting of liquid (e.g., soap) films in air – an area of active research since the pioneering works of Taylor [34], Culick [35], Dupré [90, 91], Rayleigh [92], McEntee and Mysels [93] in the late nineteenth and mid-twentieth century to the more recent investigations [38, 84, 94–96]. In these studies, the outer medium is assumed passive (inviscid and zero-inertia). The origin of the nucleation of the initial hole in the film can be manifold [12]. After film rupture, the internal viscous stresses in the film do not contribute to the momentum balance, but dictate the distribution of momentum within the film [99], as long as the Ohnesorge number of the film (ratio of its visco-capillary to inertia-capillary time scales, see § 5.3) is less than its aspect ratio (see Deka and Pierson [38]). Nonetheless, half of the surface energy released goes into internal viscous dissipation (see appendix 5.A and [35, 97, 98, 265]).

A representative schematic of the situation mentioned above is shown in figure 5.0.1a (henceforth referred to as the *classical* Taylor-Culick configuration), where the water film (f) of thickness h_0 is retracting in air (a) under the action of surface tension. The retraction velocity, v_f , in such a scenario is constant (after a period of initial transience) and approaches the Taylor-Culick velocity given by

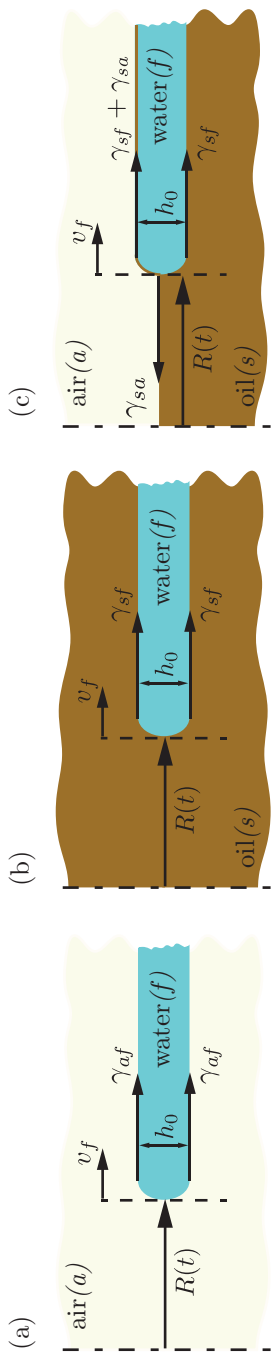


Figure 5.0.1: Schematics depicting the configurations studied in the present work: (a) retraction of a water film (f) of thickness h_0 in an air (a) environment (*classical* configuration), (b) retraction of water film (f) in an oil (s) environment (*two-phase* configuration), (c) retraction of a water film sandwiched between air and oil (*three-phase* configuration). The dot-dashed line represents the axis of rotational symmetry, and $R(t)$ is the radius of the growing hole centered at this axis. In all the schematics, the water film is retracting from left to right with velocity v_f , as indicated by the arrow, and γ_{ij} denotes the surface tension coefficient between fluids i and j .

$$v_{TC} = \sqrt{\frac{2\gamma_{af}}{\rho_f h_0}}, \quad (5.1)$$

where $2\gamma_{af}$ is the net surface tension driving the retraction (γ_{af} being the interfacial tension coefficient between the film and air) and ρ_f is the density of the liquid film (figure 5.0.1a). Furthermore, it was observed that during the retraction, the liquid collects in a thicker rim at the retracting edge of the film, particularly for low viscosity liquids [92, 266, 267, not depicted in figure 5.0.1a]. The seminal work of Keller [268] further explores the retraction of these films of non-uniform thickness.

The effect of viscosity of the film (η_f) during its retraction process has also been studied [269, 270]. Brenner and Gueyffier [271] showed that although viscosity does not have any effect on the constant retraction velocity, it can have a significant effect on the shape of the retracting edge of a planar film. They report that if the radial extent of the film is greater than its Stokes length ($= \eta_f / (\rho_f v_{TC})$), a growing rim is formed, whereas the rim is absent for the converse situation. Savva and Bush [99] extended the work by Brenner and Gueyffier [271] for highly viscous films, and also developed a lubrication model for the retraction dynamics of a circular hole. They concluded that although viscosity does not determine the magnitude of the constant retraction velocity, it does dictate the time required (post rupture) to attain that constant velocity, which increases with increasing viscosity. Recently, Pierson et al. [37], Deka and Pierson [38] revisited the viscous retraction dynamics by exploring self-similar solutions for slender filaments and sheets of finite length.

The rheological properties of the film also influence the retraction dynamics [272–275]. For instance, [276] showed that viscoelastic filaments can retract at velocities higher than the Newtonian Taylor-Culick limit owing to elastic tension. Moreover, the retraction dynamics of liquids have also been studied in the context of dewetting for a wide range of scenarios [11, 277–285]. Lastly, there has also been a recent surge in the study of liquid retraction in other configurations, such as liquid strips [286], smectic films [287], foam films [288], and emulsion films [289].

In all the aforementioned studies, the surrounding medium is assumed to play no role in the rupture dynamics. A question naturally arises: what happens when the outer medium also interacts with the retracting film? In particular, how do the viscosity and the inertia of the outer medium influence the rupture dynamics [290–293]? A representative schematic for such a sce-

nario is shown in figure 5.0.1b, where a water film is retracting in a viscous oil ambient. This geometry will henceforth be referred to as the *two-phase* configuration where the net surface tension force responsible for retraction is $2\gamma_{sf}$ (γ_{sf} being the interfacial tension coefficient between the film and the surrounding medium, see figure 5.0.1b). In such a situation, viscous dissipation is not limited only to the retracting film, but is also present in the ambient. If the ambient happens to be significantly more viscous than the film, then the dissipation in the ambient dominates. In such a situation, the retraction velocity is still a constant. However, unlike the classical case, the velocity depends on the viscosity η_s of the ambient medium [292, 294]. Common realizations of this configuration include relaxation of filaments and droplets in a viscous medium [295], or that of air-films during drop impact [293, 296]. Additionally, in this context, [297] showed that the so-called “inertially limited viscous regime” in the early-times of drop coalescence [298, 299] stems from a Taylor-Culick type retraction of the air film between the deformable drops.

In the present work, we study the influence of the surrounding medium on the retraction velocity of a ruptured liquid film using both force balance and energy conservation arguments. To accomplish this goal, along with the two canonical configurations shown in figures 5.0.1a and 5.0.1b, we also study the retraction dynamics of a liquid film sandwiched between air and a viscous oil bath. A representative schematic is shown in figure 5.0.1c. This geometry will henceforth be referred to as the *three-phase* configuration. This chapter elucidates this case experimentally by inflating an oil droplet at the air-water free-surface and letting the water film rupture. Such a configuration can also be found in the early stages of water film retraction when an air bubble approaches a water-oil interface if the oil-layer is thick enough [300, 301]. Furthermore, we also use direct numerical simulations (DNS) to demystify the retraction dynamics by using a precursor film-based three-fluid volume of fluid (VoF) method. We show that the film in this three-phase configuration still retracts with a constant velocity, and similar to the two-phase case, the retraction velocity depends on the viscosity η_s of the oil bath. However, this dependence is weaker in the three-phase configuration. Furthermore, we reveal an unprecedented scaling relationship for the retraction velocity of the film, which arises from the localization of the viscous dissipation near the three-phase contact line.

The chapter is organized as follows: § 5.2.1 describes the problem statement for the three-phase Taylor-Culick retractions along with the experimental method employed to probe this configuration. The results from these exper-

iments are discussed in § 5.2.2. § 5.3 presents the numerical framework, and § 5.4 describes the simulation results for both the two-phase and three-phase configurations. § 5.5 demonstrates the balance of forces in Taylor-Culick retractions, followed by the corresponding scaling relationships in § 5.6. Further, § 5.7 analyzes the overall energy balance, highlighting the differences in the viscous dissipation mechanisms between the two-phase and three-phase configurations. The work culminates with conclusions in § 5.8. Throughout the manuscript, we refer to Appendix 5.A for discussions on the classical Taylor-Culick retractions, and use the experimental datapoints from Reyssat and Quéré [292] for the two-phase configuration.

5.2 Film bursting at an air-liquid interface

5.2.1 Experimental method

We study the three-phase configuration experimentally by inflating an oil drop ('*s*' for 'surroundings' in figure 5.0.1c) at a water-air free interface and capturing the retraction of the water film (*f* in figure 5.0.1c). The schematic of the experimental setup is shown in figure 5.2.1a. A plastic box of dimensions 25 mm × 25 mm × 15 mm (length × width × height, Bodemschat) filled with purified water (Milli-Q) was used as the liquid bath for most of the experiments. To study the effect of the viscosity of the retracting film, the water in the bath was replaced by glycerol (Sigma-Aldrich)-water mixtures (concentrations in the range 50% – 70% by wt.) for some experiments. A dispensing needle (inner diameter = 0.41 mm, HSW Fine-Ject) was submerged within the bath such that its dispensing end was at a depth of 2.4 mm from the free surface (depth kept constant during all experiments). A silicone oil (Wacker) droplet was created at the tip of the needle by connecting it to an oil-filled plastic syringe (5 mL, Braun Injekt) via a flexible plastic PEEK tubing (Upchurch Scientific). The oil flow rate was maintained at 0.05 mL/min with the help of a syringe infusion pump (Harvard Apparatus). In the present experiments, silicone oils of different viscosities were used, and their densities (ρ_s), kinematic (ν_s), and dynamic viscosities (η_s) are listed in Table 5.2.1. It is to be noted that for only the AK 0.65 oil ($\eta_s = 4.94 \times 10^{-4}$ Pa.s), the drop is less viscous than the water film ($\eta_f = 8.9 \times 10^{-4}$ Pa.s), while for all the other oils, the film is less viscous. The oil-water interfacial tension (γ_{sf}) was considered to be 0.040 N/m [302].

The drop volume was increased by a slow infusion using the syringe pump.

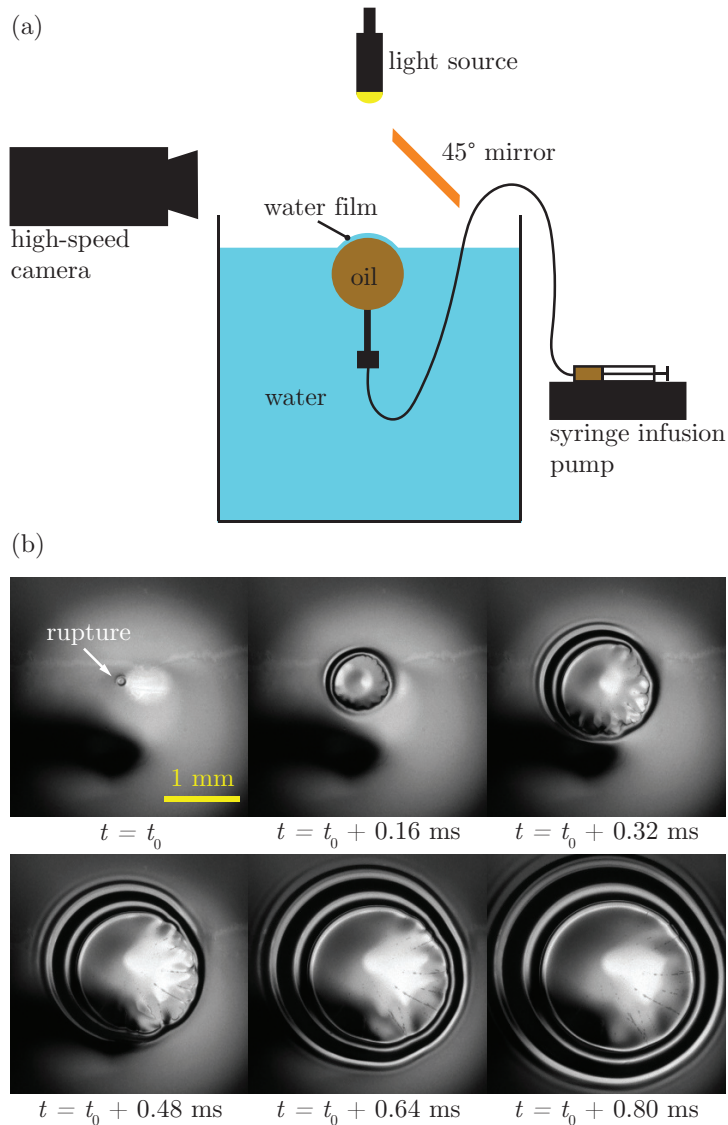


Figure 5.2.1: (a) Schematic of the experimental setup; (b) typical time-lapsed experimental snapshots of the film bursting and the subsequent retraction process ($\nu_s = 10$ cSt). The time instant $t = t_0$ denotes the first frame where bursting (indicated by the white arrow) is discernible.

The needle depth below the free surface was chosen such that the drop remained anchored to the needle during inflation. As a result, the water film right above the oil droplet progressively thins with increasing volume of the drop. Below a certain thickness, the film ruptures due to van der Waals forces [303], and subsequently retracts into the bath. This situation is analogous to the rupture and retraction of a water film sandwiched between air and a viscous oil droplet. This is also a configuration that is flipped vertically as compared to the early time scenario studied by Feng et al. [301]. Another key difference is that we ensure negligible vertical velocity at the point of rupture of the water film, making this scenario ideal for studying three-phase Taylor Culick retractions.

High-speed imaging of this rupture and retraction phenomena was performed at 50000 fps (frames-per-second) for the lower viscosity oils and at 10000 fps for the higher viscosity ones, with a $2.5\text{ }\mu\text{s}$ exposure time, by a high-speed camera (Fastcam Nova S12, Photron) connected to a macro lens (DG Macro 105 mm, Sigma) with 64 mm of lens extender (Kenko). The camera was pointed at a plane mirror (Thorlabs) inclined at 45° to the horizontal to capture the top view of the retraction phenomenon (figure 5.2.1a), while the experiments were illuminated from the top by a LED light source (KL 2500 LED, Schott). A typical bursting event is shown in figure 5.2.1b, where time $t = t_0$ indicates the instant when rupture is optically discernible. With increasing time, the size of the hole formed due to rupture increases as the film retracts. The phenomenological observations shown in figure 5.2.1b will be discussed in detail in § 5.2.2. The captured images were then further analyzed using the open-source software FIJI [304] and an in-house OpenCV-based Python script to obtain quantitative information presented in the following sections.

5.2.2 Experimental results

The rupture and retraction of a water film on the surface of an oil drop of $\eta_s = 4.94 \times 10^{-4} \text{ Pa.s}$ is shown in figure 5.2.2a (and supplemental movie 1). The timestamps indicate $(t - t_0)$, where t_0 is the time instant when rupture is optically discernible, and t is the current time. As mentioned earlier, in this particular case, the water film is more viscous than the oil. It is to be noted that in the present experiments, we could not precisely control the location of rupture as it was sensitive to experimental noise [see § 4.2 of 97]. Hence, the rupture in the present experiments did not always occur at the apex of the thinning film. Such behavior was also observed in other similar experiments of film rupture [305, 306]. The rupture location may also be determined by

Silicone oil	ρ_s (kg/m ³)	ν_s (cSt)	η_s (Pa.s)
AK 0.65	760	0.65	4.94×10^{-4}
AK 5	920	5	4.60×10^{-3}
AK 10	930	10	9.30×10^{-3}
AK 20	950	20	1.90×10^{-2}
AK 35	960	35	3.36×10^{-2}
AK 50	960	50	4.80×10^{-2}
AK 100	960	100	9.60×10^{-2}
AK 200	970	200	1.94×10^{-1}
AK 350	970	350	3.40×10^{-1}
AK 1000	970	1000	9.70×10^{-1}

Table 5.2.1: Salient properties of the silicone oils used in the present work.

a ‘prehole’ formation, also observed by Vernay et al. [289] for the bursting of emulsion-based liquid sheets. In their work, Vernay et al. [289] show that the presence of emulsion oil droplets at the air-water interface results in lowering of the local interfacial tension, leading to Marangoni flows away from that location. This flow leads to a local thinning of the film, which ultimately ruptures at that location. They also report that the prehole formation always precedes rupture in their experiments. In the present experiments, the water surface is never pristine and always contains small impurities (which are practically unavoidable). It is possible that these impurities might have reduced the local surface tension, resulting in a similar Marangoni flow leading to a prehole. For the discussion on the origin of the hole nucleation, we also refer to Lohse and Villermaux [12]. In any case, upon rupture, a circular hole is formed in the film, which grows radially in time. Therefore, the oil bounded by the periphery of the hole gets into contact with air and not with the water film. It is also noticeable that the edge of the retracting film forms a thick rim – an observation also made for the retraction of liquid films in air [265, 267, 271]. As the hole increases in size (or as the film retracts further), this rim also becomes thicker. Finally, since silicone oil prefers to spread on water [307], the retraction process ceases when the oil droplet has completely spread on water, thus creating a macroscopic film whose thickness is controlled by volume conservation and thermodynamics [10].

When the viscosity of the oil phase is increased to $\eta_s = 9.30 \times 10^{-3}$ Pa.s, the hole opening (or film retraction) dynamics (as seen in figure 5.2.2b and

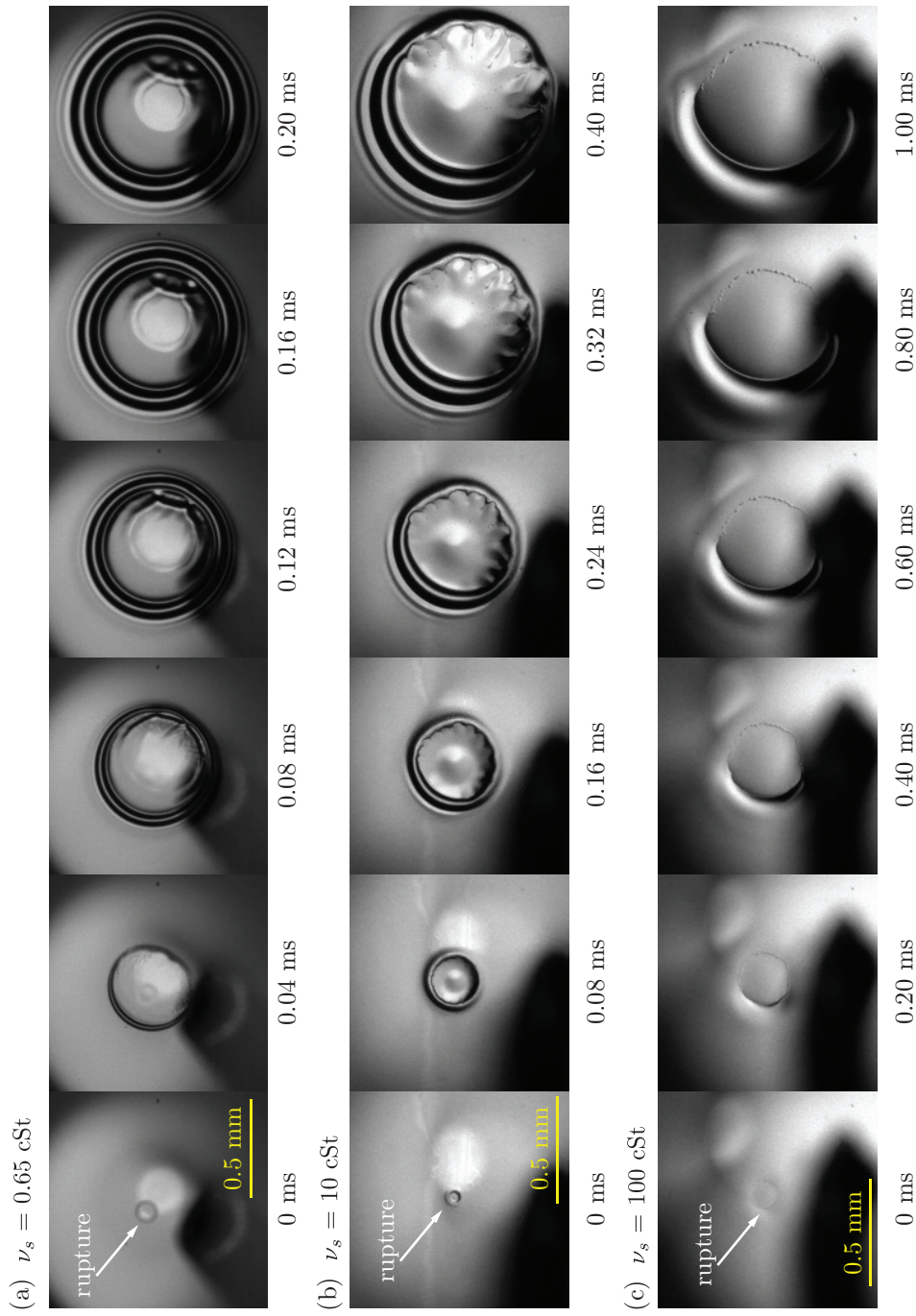


Figure 5.2.2: Time-lapsed snapshots of the post-rupture retraction of water films for different oil viscosities: (a) $\nu_s = 0.65$ cSt, (b) $\nu_s = 10$ cSt, and (c) $\nu_s = 100$ cSt. The rupture location is denoted by the white arrows, while the time stamps indicate the time since rupture is first observed (i.e., $t - t_0$). Also see supplemental movie 1.

supplemental movie 1) are qualitatively similar to that for the lower viscosity described before (figure 5.2.2a). Here also, the film forms a thick rim at its retracting edge. Nonetheless, an increase in the oil's viscosity decreases the retraction speed, as indicated by the timestamps (corresponding to $t - t_0$). This behavior is expected since the physical situation is analogous to a retracting water film shearing the free surface of viscous oil: increasing η_s increases the resistance to shearing, which in turn makes the retraction process slower.

Furthermore, the experimental snapshots show that the oil-air-water contact line exhibits corrugations during the retraction process, and fine streams of droplets are released from these corrugations. Similar observations were also made for film retraction in the two-phase configuration [292, 305] and during the rupture of the intermediate film when a drop coalesces with a pool of the same liquid in the presence of an external medium [231, 308]. The nature of the corrugations is reminiscent of the sharp tips observed during selective withdrawal [309–311] or tip streaming [312]. In a frame of reference co-moving with the rim, the film sees highly viscous oil being aspirated away from it, resulting in the formation of the sharp tips. Indeed, such a mechanism was also hinted at by Reyssat and Quéré [292] for the instabilities observed in their experiments for film retraction in the two-phase configuration. Tseng and Prosperetti [313] showed that such instabilities are formed due to the local convergence of streamlines in the neighborhood of a zero-vorticity point or line on the interface. However, a detailed and quantitative investigation of the formation and subsequent breakup of these liquid tips is beyond the scope of the present work.

For an even higher viscosity of the oil phase ($\eta_s = 9.60 \times 10^{-2}$ Pa.s, see figure 5.2.2c and supplemental movie 1), the retraction of the ruptured water film is further slowed down (as evident from the timestamps in figure 5.2.2c). Furthermore, the retracting edge also does not possess a thick rim. This observation is similar to the case of Brenner and Gueyffier [271] for the retraction of viscous films in air, where films of higher viscosity do not form a rim. Moreover, although the expanding holes for the lower η_s cases (as shown in figures 5.2.2a and 5.2.2b) are almost circular, the one for the high viscosity case shown in figure 5.2.2c is highly asymmetric. This asymmetry can be attributed to the location of the rupture not being at the film's apex. Since the rupture happens at an off-apex location, the film thickness at the location of rupture is not spatially uniform due to the curvature of the oil droplet. Hence, the retraction velocity is faster on the part of the film which has a lower thickness. Presumably, this effect is more pronounced when the overall

film retraction dynamics are slower, as is the case for the experiments shown in figure 5.2.2c. To confirm this hypothesis, one requires high-resolution measurements of the spatial variation of the film thickness, which is challenging in the present experiments (further discussed in § 5.6). The corrugations at the oil-air-water contact line are also observed in this case. However, since the retraction velocity itself is considerably smaller than for the case shown in figure 5.2.2b (see figure 5.2.3b for specific values), the tips are not as sharp, and no droplet streams are observed.

To quantify the retraction dynamics, we measure the hole opening radius from each snapshot captured using the high-speed camera. For each experimental snapshot, the area of the hole $A(t)$ is measured, and subsequently an equivalent hole opening radius $R(t)$ is calculated as $A(t) = \pi R(t)^2$. A typical measurement from the optical images is depicted in the inset of figure 5.2.3a. The temporal variation of the measured hole radius, R , is shown in figure 5.2.3a. The time instant corresponding to the first frame in which rupture is optically discernible is denoted by t_0 . Each datapoint in figure 5.2.3a denotes the mean of measurements from five independent experiments, and the error bars correspond to \pm one standard deviation. In the present work, we focus on the early moments following rupture, as indicated by the red rectangle in figure 5.2.3a. Zooming into this early time regime, as shown in figure 5.2.3b, it is observed that $R(t)$ varies linearly with time (as evident from the lines denoting linear fits in figure 5.2.3b). This variation indicates that the retraction velocity v_f ($= dR/dt$), given by the slopes of the linear fits, is constant for each viscosity. This is reminiscent of the constant rupture velocity also observed for the classical (figure 5.0.1a) and two-phase (figure 5.0.1b) Taylor-Culick configurations. Furthermore, it is also observed that with increasing η_s (or ν_s), the slope of the linear fits (hence v_f) decreases, as expected from the qualitative observations reported in figure 5.2.2.

The variation of v_f with η_s is shown in figure 5.2.3c. The typical retraction velocities are $\mathcal{O}(1 \text{ m/s})$. A decreasing v_f with increasing η_s is observed. Furthermore, for the cases where the oil is more viscous than water ($\eta_f = 8.9 \times 10^{-4} \text{ Pa.s}$), the retraction velocity varies as

$$v_f \sim \frac{1}{\eta_s^{1/2}}, \quad (5.2)$$

as evident from the line in figure 5.2.3c. This is a weaker dependence as compared to the expected $1/\eta_s$ variation observed for retraction in the two-phase configuration [294, 314]. We will attempt to explain the scalings for the

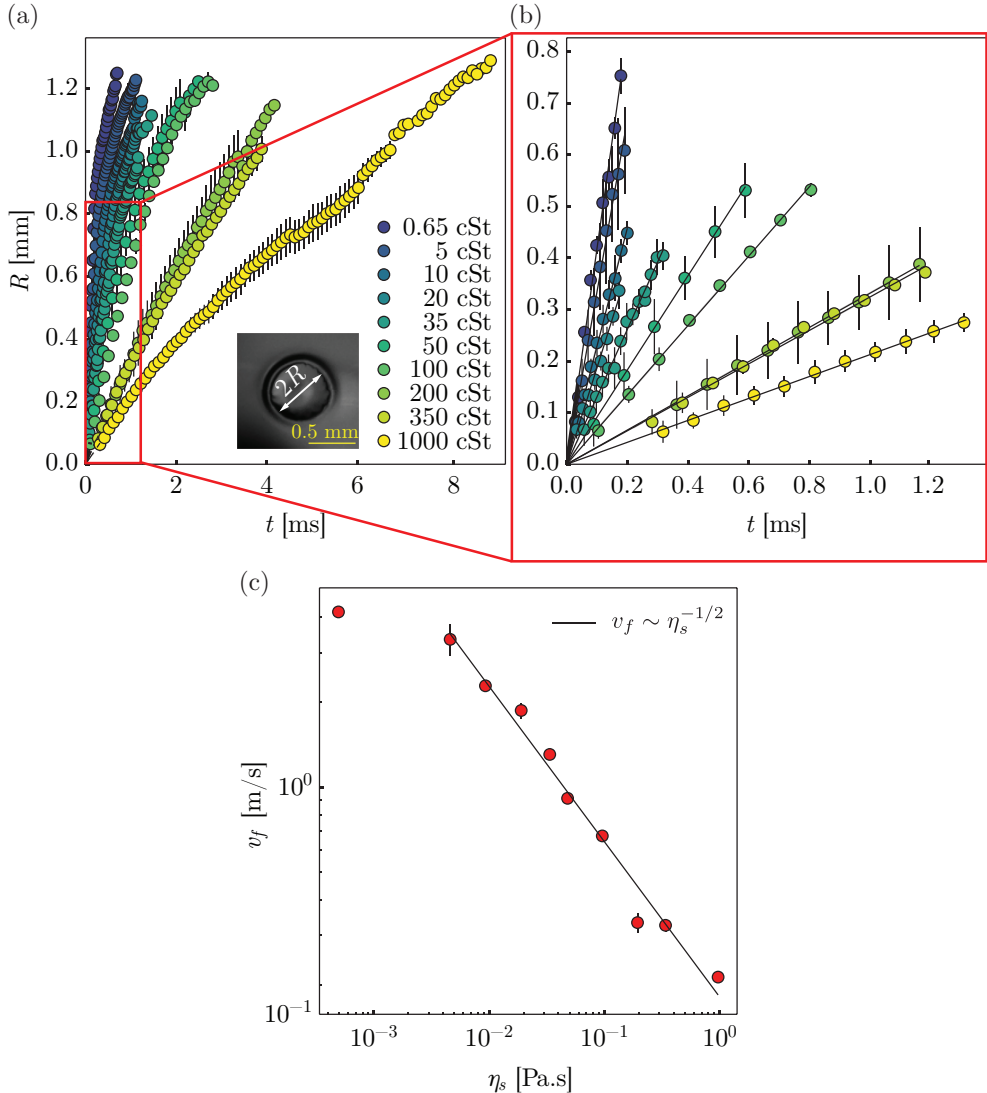


Figure 5.2.3: (a) Temporal evolution of the retraction radius (R) for oils of different kinematic viscosity (ν_s); a typical measurement is shown in the snapshot in the inset. (b) At early times (red rectangle in figure 5.2.3a), R varies linearly with time; the discrete datapoints are experimental measurements and the lines are linear fits. (c) Variation of dewetting velocity (v_f) with the dynamic viscosity of the oil phase (η_s); the discrete datapoints are experimental measurements and the line represents $v_f \sim \eta_s^{-1/2}$.

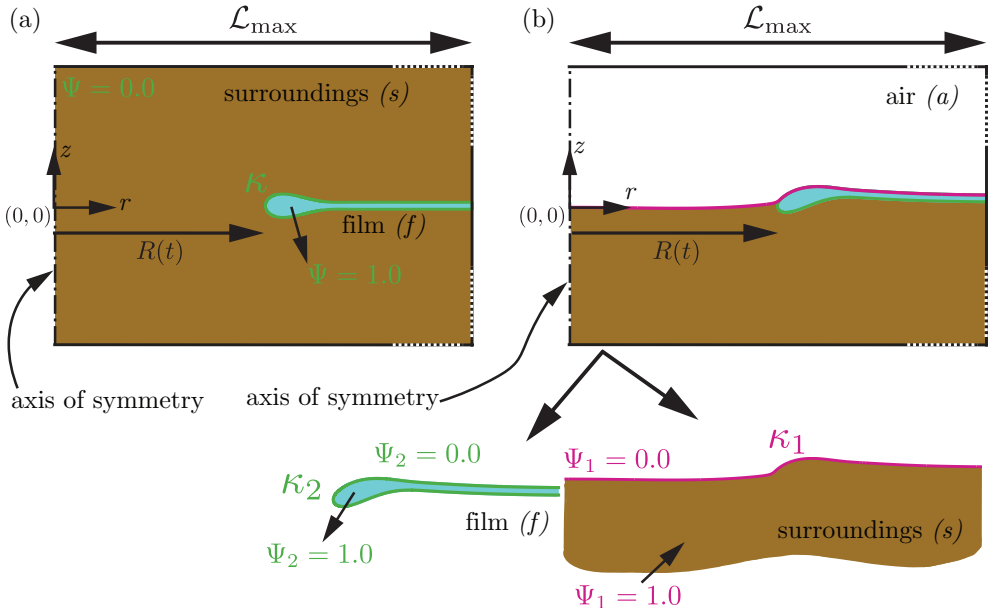


Figure 5.3.1: Computational domain for (a) two-phase and (b) three-phase Taylor-Culick retractions. For the classical case, (a) is used by replacing the surroundings (s) with air (a). The size of the domain is much larger than the hole radius ($\mathcal{L}_{\max} \gg R(t)$). Furthermore, $\mathcal{L}_{\max}/h_0 \gg \max(Oh_f, Oh_s)$.

5

two-phase and three-phase configurations in § 5.6. Furthermore, the reason for not fitting the datapoint for the case where the oil is less viscous than the water film in figure 5.2.3c will also be addressed therein.

5.3 Numerical framework

5.3.1 Governing equations

In this section, we discuss the governing equations that describe the retraction of a ruptured liquid film in the three configurations we study in this chapter, namely, the classical, two-phase, and three-phase Taylor-Culick retractions. We perform axisymmetric direct numerical simulations using the free-software volume of fluid (VoF) program, Basilisk C [143, 315], which uses the one-fluid approximation [2, 156] to solve the continuity and the Navier-Stokes equations:

$$\nabla \cdot \mathbf{v} = 0, \quad (5.3)$$

$$\frac{\partial(\rho\mathbf{v})}{\partial t} + \nabla \cdot (\rho\mathbf{v}\mathbf{v}) = -\nabla p + \nabla \cdot (2\eta\mathcal{D}) + \mathbf{f}_\gamma \quad (5.4)$$

where, \mathbf{v} and p are the velocity vector and pressure fields, respectively, η is the viscosity of the fluid, and t denotes time. Furthermore, \mathcal{D} is the symmetric part of the velocity gradient tensor ($\mathcal{D} = (\nabla\mathbf{v} + (\nabla\mathbf{v})^T)/2$), and \mathbf{f}_γ is the singular surface tension force needed in the one-fluid approximation to comply with the dynamic boundary condition at the interfaces [157].

5.3.2 Non-dimensionalization of the governing equations

We non-dimensionalize the governing equations by using the inertio-capillary velocity scale $V_{\rho\gamma}$, the thickness of the film h_0 , and the capillary pressure P_γ . These scales also define the characteristic inertio-capillary time as $\tau_{\rho\gamma}$:

$$\tau_{\rho\gamma} = \frac{h_0}{V_{\rho\gamma}} = \sqrt{\frac{\rho_f h_0^3}{2\gamma_{sf}}}, \quad V_{\rho\gamma} = \sqrt{\frac{2\gamma_{sf}}{\rho_f h_0}}, \quad P_\gamma = \frac{2\gamma_{sf}}{h_0}. \quad (5.5)$$

Here, γ_{sf} is the surface tension coefficient between the film (f) and the surrounding (s) medium, ρ_f the film density, and h_0 its thickness. The dimensionless form of the Navier-Stokes equation (5.4) is

$$\frac{\partial(\tilde{\rho}\tilde{\mathbf{v}})}{\partial\tilde{t}} + \tilde{\nabla} \cdot (\tilde{\rho}\tilde{\mathbf{v}}\tilde{\mathbf{v}}) = -\tilde{\nabla}\tilde{p} + \tilde{\nabla} \cdot (2Oh\tilde{\mathcal{D}}) + \tilde{\mathbf{f}}_\gamma, \quad (5.6)$$

where the expressions for the Ohnesorge number (Oh , ratio of visco-capillary to inertio-capillary time scales), the dimensionless density ($\tilde{\rho}$), and the singular surface tension force ($\tilde{\mathbf{f}}$) depend on the specific configurations that we discuss below.

Two-phase Taylor-Culick configuration

In this configuration, a liquid film (f) retracts in a viscous surrounding (s) medium (figure 5.3.1a). We use the volume of fluid (VoF) tracer Ψ to differentiate between the film ($\Psi = 1$) and the surroundings ($\Psi = 0$), which follows the VoF scalar advection equation,

$$\left(\frac{\partial}{\partial \tilde{t}} + \tilde{\mathbf{v}} \cdot \tilde{\nabla} \right) \Psi = 0. \quad (5.7)$$

Furthermore, the singular surface tension force is given by [157]:

$$\tilde{\mathbf{f}}_\gamma \approx (\tilde{\kappa}/2) \tilde{\nabla} \Psi, \quad (5.8)$$

where the curvature κ is calculated using the height-function approach [158]. We follow the same sign convention as Tryggvason et al. [2, see page 33]: the curvature is positive if the interface folds towards it normal $\hat{\mathbf{n}}$, i.e., $\kappa = -\nabla \cdot \mathbf{n}$. Note that the surface tension scheme in Basilisk C is explicit in time. So, we restrict the maximum time step as the characteristic inertio-capillary time based on the wavelength of the smallest capillary wave [158, 159]. Additionally, the density of the film is the same as that of the surroundings, giving $\tilde{\rho} = 1$. Lastly, the Ohnesorge number (Oh) is given by

$$Oh = \Psi Oh_f + (1 - \Psi) Oh_s, \quad (5.9)$$

where

$$Oh_f = \frac{\eta_f}{\sqrt{\rho_f (2\gamma_{sf}) h_0}} \quad \text{and} \quad Oh_s = \frac{\eta_s}{\sqrt{\rho_f (2\gamma_{sf}) h_0}} \quad (5.10)$$

are the Ohnesorge numbers based on the film and surroundings viscosities, respectively. For this configuration, we keep Oh_f constant at 0.05 [based on the experiments of 292], and vary the control parameter Oh_s in § 5.4.

Note that the computational domain in figure 5.3.1a along with equations (5.7) – (5.10) can be used to simulate classical Taylor-Culick retractions as well by replacing the surroundings (s) with air (a). We discuss the details of the classical configuration in appendix 5.A.

Three-phase Taylor-Culick configuration

In this configuration, we model the bursting of a water film at an oil drop-air interface by simulating the retraction of a fluid film (f) on an initially flat oil bath (s), while ignoring the effects of the oil drop's curvature (as the retraction length in the early time regime of figure 5.2.3b is much smaller than the oil

drop radius, see figure 5.3.1b). We extend the traditional volume of fluid (VoF) method described in § 5.3.2 to tackle three fluids by using two VoF tracers: Ψ_1 , which is tagged as 1 for the liquids (water film, f , and oil surroundings, s) and 0 for air (a), and Ψ_2 which is 1 for the water film (f) and 0 everywhere else (figure 5.3.1b). Note that this implementation requires an implicit declaration of the surrounding phase (s), given by $\Psi_2(1 - \Psi_1)$ [315–318]. Additionally, both Ψ_1 and Ψ_2 follow the VoF tracer advection equation,

$$\left(\frac{\partial}{\partial \tilde{t}} + \tilde{\mathbf{v}} \cdot \tilde{\nabla} \right) \{\Psi_1, \Psi_2\} = 0, \quad (5.11)$$

and the dimensionless density ratio is (with $\rho_f = \rho_s$)

$$\tilde{\rho} = \Psi_1 + (1 - \Psi_1) (\rho_a / \rho_f). \quad (5.12)$$

The Ohnesorge number (Oh) is now given by

$$Oh = \Psi_1 \Psi_2 Oh_f + (1 - \Psi_2) \Psi_1 Oh_s + (1 - \Psi_1) Oh_a, \quad (5.13)$$

where Oh_f and Oh_s follow equation (5.10), and $Oh_a = \eta_a / \sqrt{\rho_f (2\gamma_{sf}) h_0}$ is the Ohnesorge number based on the viscosity of air. Both Oh_f and Oh_a are fixed at 10^{-1} and 10^{-3} , respectively, for all the three-phase simulation data presented in this chapter (see § 5.6), and we vary the control parameter Oh_s in § 5.4. Lastly, the surface tension body force takes the form

$$\tilde{\mathbf{f}}_\gamma \approx (\gamma_{sa} / \gamma_{sf}) (\tilde{\kappa}_1 / 2) \tilde{\nabla} \Psi_1 + (\tilde{\kappa}_2 / 2) \tilde{\nabla} \Psi_2, \quad (5.14)$$

with γ_{sa} and γ_{sf} being the surface tension coefficients for the surroundings-air and surroundings-film interfaces, respectively.

Physically, such a configuration (figure 5.3.1b) and equations (5.11) – (5.13) ideally imply the presence of a zero thickness precursor film of the surrounding liquid (s , represented by $(1 - \Psi_2)\Psi_1 = 1$, (equation (5.13)) over the liquid film (f , $\Psi_1\Psi_2 = 1$, (equation (5.13)). Note that this numerical assumption is applicable only when it is thermodynamically favorable for one of the fluids (here s) to spread over all the other fluids, i.e., it has a positive spreading coefficient [10, 319], $S \equiv \gamma_{af} - \gamma_{sf} - \gamma_{sa} > 0$, and the Neumann triangle collapses at the three-phase contact line. In reality, this precursor film will have a finite

thickness controlled by microscopic forces [like van der Waals forces, 303], and is much smaller than the length scales that we can resolve numerically in the continuum framework. Indeed, for our numerical simulations, this precursor film has an effective thickness of $\Delta/2$, where Δ is the size of the finest grid employed in this work. We further assume that, on the time scale of film retraction, the effective spreading coefficient of the surrounding liquid (s) is 0 [320]. Consequently, the effective surface tension coefficient between the film and air is $\gamma_{af} = \gamma_{sf} + \gamma_{sa}$. This precursor film [321] is analogous to the mathematical model for spreading of a perfectly wetting liquid on a solid substrate [10, 320], which regularizes the contact line singularity owing to the numerical slip [with an effective slip length of $\Delta/2$, 322] due to the discretization of the interface.

5.3.3 Note on non-dimensionalization in the viscous regime

For highly viscous surroundings ($Oh_s > 1$), it is convenient to scale the velocities with the visco-capillary velocity scale $V_{\eta\gamma}$, owing to the dominant interplay between viscous and capillary stresses [295]. Further, we can use the visco-capillary time $\tau_{\eta\gamma}$, film thickness h_0 , and capillary pressure P_γ to normalize the time, length, and pressure dimensions, respectively:

5

$$\tau_{\eta\gamma} = \frac{h_0}{V_{\eta\gamma}} = \frac{\eta_s h_0}{2\gamma_{sf}}, \quad V_{\eta\gamma} = \frac{2\gamma_{sf}}{\eta_s}, \quad P_\gamma = \frac{2\gamma_{sf}}{h_0}, \quad (5.15)$$

where γ_{sf} is the surface tension coefficient between the film (f) and the surroundings (s), h_0 the film thickness, and η_s the viscosity of the surrounding medium. These visco-capillary scales modify the momentum equation as

$$\frac{1}{Oh_s^2} \left(\frac{\partial(\tilde{\rho}\tilde{\mathbf{v}})}{\partial\tilde{t}} + \tilde{\nabla} \cdot (\tilde{\rho}\tilde{\mathbf{v}}\tilde{\mathbf{v}}) \right) = -\tilde{\nabla}\tilde{p} + \tilde{\nabla} \cdot (2\tilde{\eta}\tilde{\mathcal{D}}) + \tilde{\mathbf{f}}_\gamma. \quad (5.16)$$

Here, Oh_s is the surroundings Ohnesorge number (equation (5.10)), $\tilde{\rho}$ follows $\tilde{\rho} = 1$ and equation (5.12) for the two-phase and the three-phase configurations, respectively, and $\tilde{\mathbf{f}}_\gamma$ equals the corresponding expressions for the two configurations (see equations (5.8) and (5.14)). Additionally, the dimensionless viscosities are given by

$$\tilde{\eta} = \begin{cases} \Psi(\eta_f/\eta_s) + (1 - \Psi) & \text{two-phase case,} \\ \Psi_1 \Psi_2 (\eta_f/\eta_s) + (1 - \Psi_2) \Psi_1 + (1 - \Psi_1) (\eta_a/\eta_s) & \text{three-phase case.} \end{cases} \quad (5.17)$$

5.3.4 Domain size and boundary conditions

Figure 5.3.1 depicts the computational domains. The left boundary represents the axis of symmetry with origin marked at $(0, 0)$. We set no-penetration and free-slip boundary conditions to all other domain boundaries along with zero gradient conditions for pressure. These boundaries are far away from the expanding hole and do not affect its growth. Furthermore, the size of the domain is chosen such that $\mathcal{L}_{\max} \gg \max(Oh_f, Oh_s)$, with a minimum \mathcal{L}_{\max} of 200 for $Oh_s \ll 1$. We have varied this domain size to ensure that the simulations are independent of its value. Note that, if this condition is not met, the assumption of infinite film, which is essential for the theoretical scaling relations developed in this work, will fail [38].

We employ Adaptive Mesh Refinement (AMR) to correctly resolve the different interfaces as well as regions of high velocity gradients (and hence, high viscous dissipation, see appendix 5.B). To ensure that the velocity field is captured accurately, these refinement criteria [see 315] effectively maintain a minimum of 40 cells across the thickness of the film (i.e., $h_0/\Delta \geq 40$). As the apparent three-phase contact line and the viscous boundary layer are critical in the present work, the refinement criteria maintain a minimum of 40 cells in the wedge region near the apparent three-phase contact line. Furthermore, the viscous boundary layer is almost 10 times larger than the film thickness (see § 5.7.2, figure 5.7.3). Consequently, a minimum of 400 cells in the viscous boundary layer in the surrounding medium is needed to properly resolve the velocity gradients. We have conducted extensive grid independence studies so that the final results (energy transfers and the retraction velocity) are independent of the number of grid cells.

5.4 Taylor-Culick retractions: numerics

Figures 5.4.1, 5.4.2, 5.4.3, and 5.4.4 elucidate the two-phase and three-phase Taylor-Culick retractions. For low viscous surroundings ($Oh_s \leq 1$), figures 5.4.1a

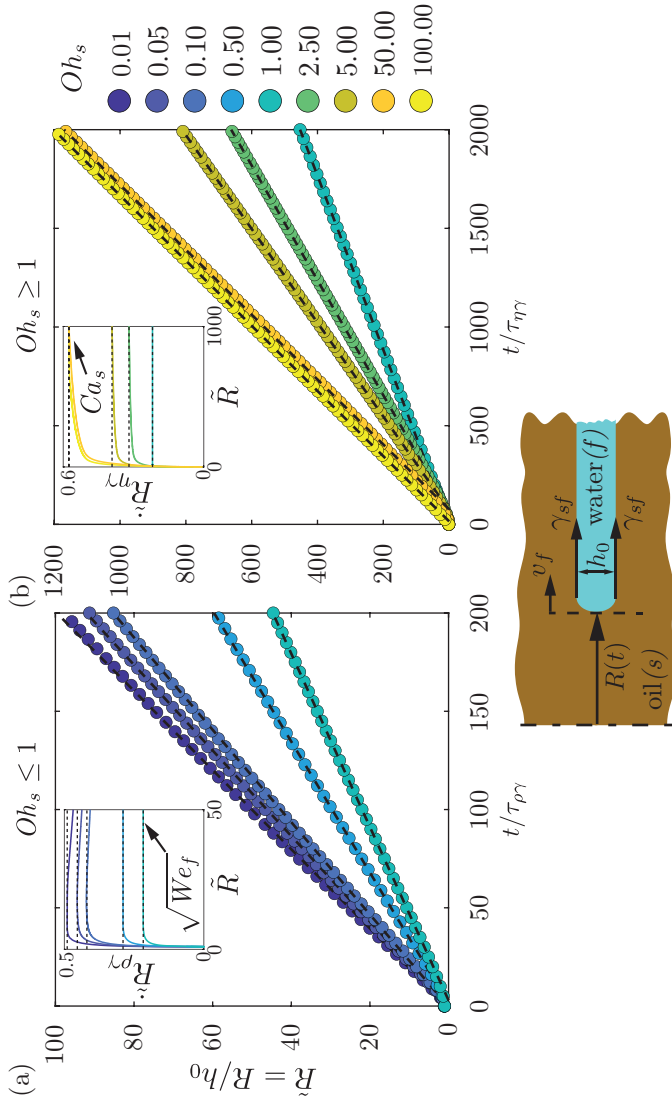


Figure 5.4.1: Two-phase Taylor-Culick retractions: temporal evolution of the dimensionless hole radius ($\tilde{R}(t)$) for (a) $Oh_s \leq 1$ and (b) $Oh_s \geq 1$. Time is normalized using the inertio-capillary time scale, $\tau_{\rho\gamma} = \sqrt{\rho_f h_0^3 / \gamma_{sf}}$ in panel (a) and the visco-capillary time scale, $\tau_{\eta\gamma} = \eta_s h_0 / \gamma_{sf}$ in panel (b). Insets of these panels show the variation of the dimensionless growth rate of the hole radius at different Oh_s , and mark the definitions of W_{ef} and Ca_s . Here, the film Ohnesorge number is $Oh_f = 0.05$.

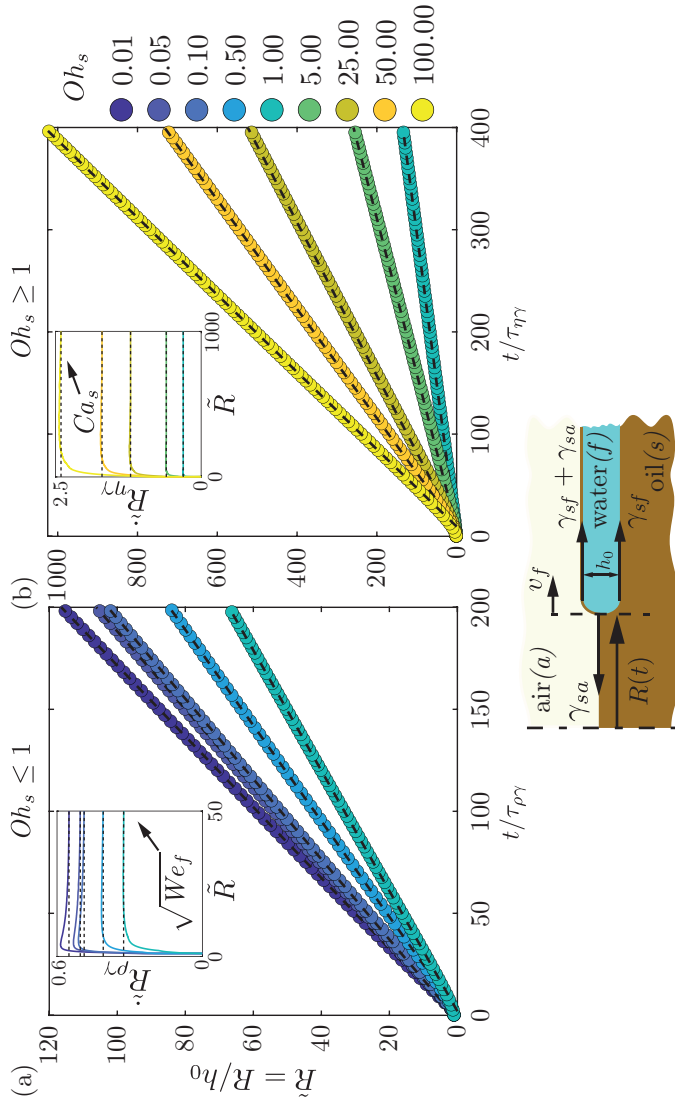


Figure 5.4.2: Three-phase Taylor-Culick retractions: temporal evolution of the dimensionless hole radius ($\tilde{R}(t)$) for (a) $Oh_s \leq 1$ and (b) $Oh_s \geq 1$. Time is normalized using the inertio-capillary time scale, $\tau_{\rho\gamma} = \sqrt{\rho_f h_0^3 / \gamma_{sf}}$ in panel (a) and the visco-capillary time scale, $\tau_{\eta\gamma} = \eta_s h_0 / \gamma_{sf}$ in panel (b). Insets of these panels show the variation of the dimensionless growth rate of the hole radius at different Oh_s , and mark the definitions of We_f and Ca_s . Here, the film Ohnesorge number is $Oh_f = 0.10$ and that of air is $Oh_a = 10^{-3}$.

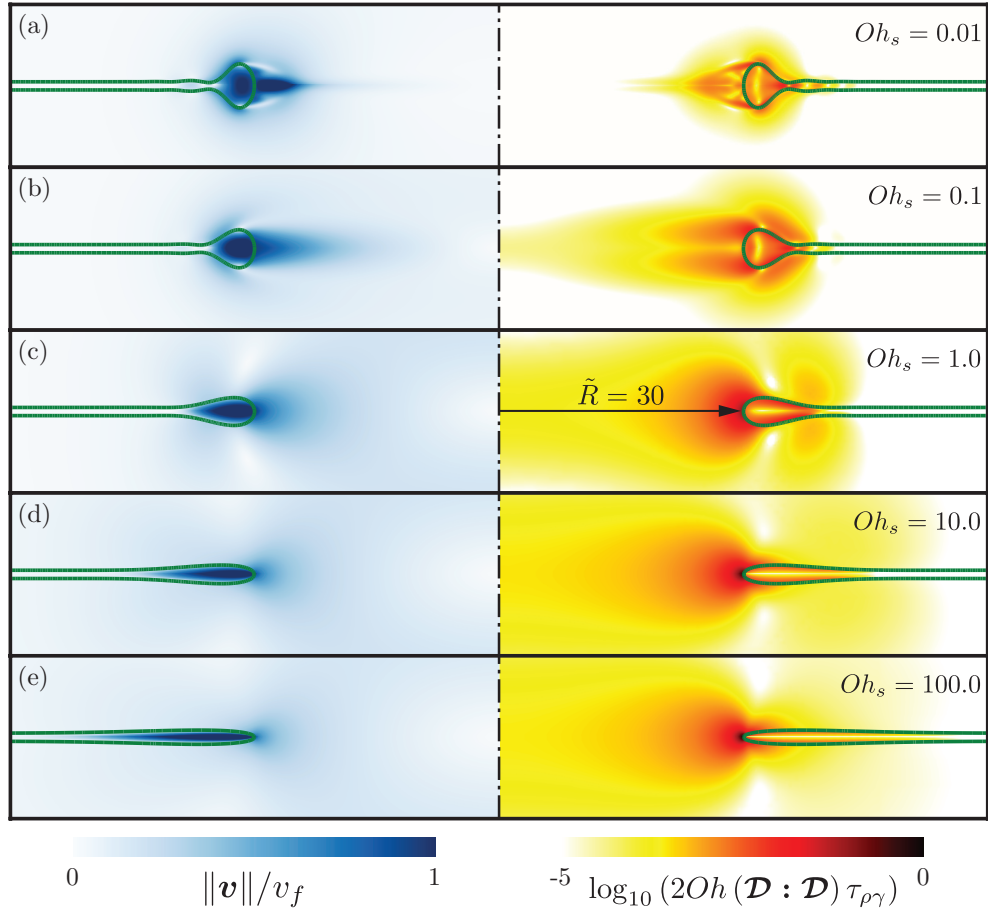


Figure 5.4.3: Two-phase Taylor-Culick retractions: the morphology of the flow at different Oh_s at $\tilde{R} = 30$. In each snapshot, the left hand side contour shows the velocity magnitude normalized with the (terminal) film velocity v_f and the right hand side shows the dimensionless viscous dissipation function normalized using the inertia-capillary scales, represented on a \log_{10} scale to differentiate the regions of maximum dissipation. Here, the film Ohnesorge number is $Oh_f = 0.05$. Also see supplemental movie 2.

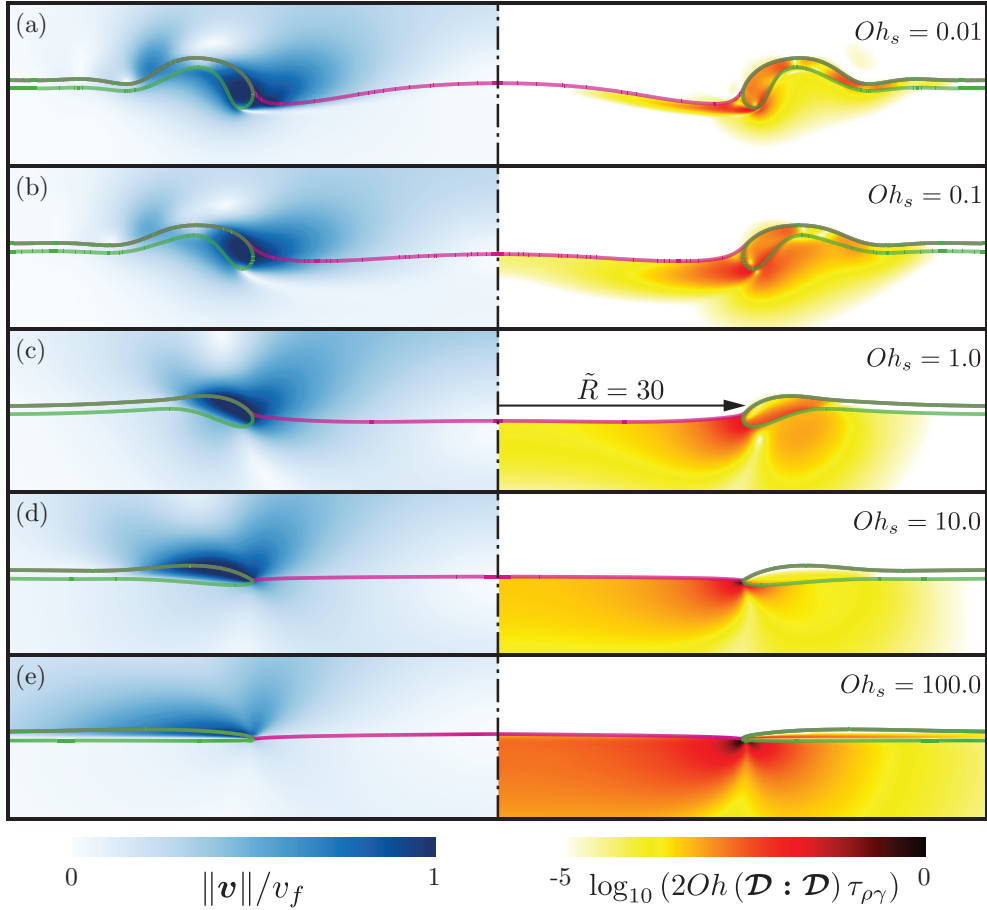


Figure 5.4.4: Three-phase Taylor-Culick retractions: the morphology of the flow at different Oh_s at $\tilde{R} = 30$. In each snapshot, the left hand side contour shows the velocity magnitude normalized with the (terminal) film velocity v_f and the right hand side shows the dimensionless viscous dissipation function normalized using the inertio-capillary scales, represented on a \log_{10} scale to differentiate the regions of maximum dissipation. Here, the film Ohnesorge number is $Oh_f = 0.10$ and that of air is $Oh_a = 10^{-3}$. Also see supplemental movie 3.

and 5.4.2a show the growth of the dimensionless hole radius ($\tilde{R}(t) = R(t)/h_0$) in time (normalized with the inertia-capillary timescale $\tau_{\rho\gamma}$), and the insets contain the growth rate of this hole: $\dot{\tilde{R}}_{\rho\gamma}(t) = \tau_{\rho\gamma} d\tilde{R}(t)/dt$. After the initial transients, the hole grows (i.e., the film retracts) linearly in time with a constant velocity (v_f). We can use this retraction velocity to calculate the film Weber number,

$$We_f \equiv \frac{\rho_f v_f^2 h_0}{2\gamma_{sf}} = \lim_{\tilde{R} \rightarrow \infty} \dot{\tilde{R}}_{\rho\gamma}^2, \quad (5.18)$$

which is represented by the black dotted lines in figures 5.4.1a and 5.4.2a. We_f is an output parameter of the retraction process. Note that, for very low Oh_s , as the rim grows with time, the inertial drag on the moving rim due to the surrounding medium overcomes the driving capillary forces, resulting in a decrease of the tip velocity [see insets of figure 5.4.1a and 293]. However, we can still calculate a velocity scale (and hence We_f) associated with the Taylor-Culick like retraction immediately after the initial transients (as marked by the black dotted lines in the insets of figure 5.4.1a for the lowest Oh_s).

Furthermore, when the surroundings is highly viscous ($Oh_s \geq 1$), we plot the growing hole radius $\tilde{R}(t)$ as a function of time, which is normalized by the visco-capillary timescale $\tau_{\eta\gamma}$, see § 5.3.3, and figures 5.4.1b and 5.4.2b. The insets of these panels contain the growth rate of the hole, calculated as $\dot{\tilde{R}}_{\eta\gamma} = \tau_{\eta\gamma} d\tilde{R}/dt$. Once again, we observe that the growth of the hole (and the film retraction) depend linearly on time with a constant velocity, which can be used to calculate the surroundings capillary number,

$$Ca_s \equiv \frac{\eta_s v_s}{2\gamma_{sf}} = \lim_{\tilde{R} \rightarrow \infty} \dot{\tilde{R}}_{\eta\gamma}, \quad (5.19)$$

marked with the black dotted lines in figures 5.4.1b, 5.4.2b, and the corresponding insets. Ca_s is another output parameter of the retraction process. Note that the velocity of the retracting film (v_f) is the same as the velocity scale in the surrounding medium (v_s), following the kinematic boundary condition at the circumference of the growing hole. Consequently, the two output parameters, We_f (equation (5.18)) and Ca_s (equation (5.19)) are related as $Ca_s = Oh_s \sqrt{We_f}$ (see § 5.6).

Lastly, figures 5.4.3 and 5.4.4 illustrate the flow morphologies for the two-phase and three-phase configurations, respectively, when the hole has grown

to $\tilde{R} = 30$. Readers can refer to supplemental movies 2, 3 for temporal dynamics of the two-phase and three-phase configurations, respectively. Similar to the classical Taylor-Culick retraction case (appendix 5.A and supplemental movie 4), both the film and the surroundings move. However, unlike the classical case, even for low Oh_s , the surrounding medium takes away momentum from the film owing to inertia (added mass-like effect), thus reducing the retraction velocity (see insets of figures 5.4.1a and 5.4.2a). Furthermore, contrary to the classical case where the dissipation is highest at the neck connecting the rim to the rest of the film (see appendix 5.A), the dissipation in the other two configurations is spread out, and also occurs in the surrounding medium.

As the hole grows, the retracting film collects fluid parcels from upstream of the moving front through inelastic collisions and forms a rim [35, 97, 98]. For the classical and two-phase configurations, this rim entails a top-bottom symmetry, which is lost in the three-phase configuration. This is due to the air medium having significantly less inertia (added mass-like effect from the properties of the film) than the oil bath, causing the film to dig into the bath and forming a hook-shaped rim (see figures 5.4.3a,b,c and 5.4.4a,b,c). Furthermore, the surrounding bath (s) engulfs the retracting film in order to feed the precursor film. This is a result of the high capillary pressure (high curvature) in the wedge region near the apparent three-phase contact line [316, 323], which also aids in the formation of the hook-shaped rim [285]. Moreover, for the cases where there is a density contrast between the film and the surroundings, the top-bottom symmetry can break down even for the two-phase configuration due to a flapping instability at very low Oh_s , as discussed by Jian et al. [293], Lhuissier and Villermaux [324]. Furthermore, as Oh_s increases, the bulbous rim disappears, leading to slender, more elongated retracting films. In the two-phase case, the retraction film maintains (top-bottom) symmetry (see figures 5.4.3c,d,e), and the dissipation is highest in the viscous boundary layer in the surrounding medium (see figure 5.4.3; further elaborated upon in § 5.7.2). However, the three-phase case features (top-bottom) asymmetric films owing to the accumulation of fluid towards the low-resistance air medium (see figures 5.4.4c,d,e), and the dissipation is highest near the apparent three-phase contact line (see figure 5.4.4; further elaborated upon in § 5.7.2). The disappearance of bulbous rims matches with the experimental observations [see § 5.2.2 and 292].

Note that the numerical results presented in this section is complementary to the experiments on a film retracting in a submerged oil bath [two-phase

case, 292] and a film bursting at an air-liquid interface (§ 5.2.2). The numerical simulations give us access to the cross-sectional view to elucidate the shape of the retracting films (figures 5.4.3 and 5.4.4), which is difficult to resolve experimentally. On the other hand, our axisymmetric (by definition) simulations do not show the azimuthal instabilities resulting in the corrugations at the oil-air-water contact line. Furthermore, as we focus only on the early time dynamics, we also neglect the curvature of the oil drop in the case of the three-phase retractions. Nonetheless, we can still sufficiently compare the dependences of the retraction velocity on the Ohnesorge number Oh_s of the surroundings (see § 5.6), along with the scaling relations that we develop in the next section for both the experimental and numerical datapoints.

5.5 Taylor-Culick retractions: a force perspective

The capillary and viscous forces, along with the inertia of the film and the surrounding media, govern the retraction dynamics. For the classical configuration (figure 5.0.1a), the viscosity and inertia of the outer medium are negligible. Furthermore, the film viscosity η_f plays no role in determining the magnitude of the retraction velocity owing to the internal nature of the associated viscous stresses [99], as long as Oh_f is less than the aspect ratio of the film [see 38]. Using these features, Taylor [34] calculated $v_f = v_{TC}$ (equation (5.1)), resulting solely from momentum equilibrium while disregarding the fate of the liquid accumulated in the rim [97]. In terms of the dimensionless numbers introduced earlier (see § 5.4, equation (5.1)) implies that $We_f = \rho_f v_f^2 h_0 / (2\gamma_{af})$ is constant and equal to 1 (see appendix 5.A for details of the retraction dynamics in the classical configuration). In this section, we delve into the different realizations of the dominating forces, and their implications, in the two-phase and three-phase configurations.

5.5.1 Two-phase Taylor-Culick retractions

For the two-phase configuration (figure 5.0.1b), if the viscosity of the oil phase is small (i.e., $Oh_s = \eta_s / \sqrt{\rho_f \gamma_{sf} h_0} \ll 1$), the Weber number based on the film velocity v_f and the driving surface tension coefficient ($2\gamma_{sf}$), $We_f = \rho_f v_f^2 h_0 / (2\gamma_{sf})$ (equation (5.18)) has a value smaller than 1 (see inset of figure 5.4.1a). Nonetheless, the driving surface tension force $F_\gamma(t) \sim \gamma_{sf} (2\pi R(t))$ (see figure 5.0.1b) still balances the inertial force $F_\rho(t) \sim \rho_f v_f^2 (2\pi R(t)) h_0$. Note that since the oil (surrounding) and water (film) densities are very similar ($\rho_f \approx \rho_s$), we can still use ρ_f for the density scale despite the added

mass-like effect. Consequently, in this regime, the Weber number is still a constant during retraction ($We_f \sim \mathcal{O}(1)$, inset of figure 5.4.1a).

On the other hand, if the viscosity of the oil phase (η_s) is significantly higher (i.e., $Oh_s \gg 1$), the resistive viscous force $F_\eta(t)$ dominates over the inertial effects, as the surroundings Reynolds number $Re_s \equiv \rho_s v_s h_0 / \eta_s \sim \mathcal{O}(10^{-2})$. In such a scenario, the retraction dynamics will be governed by the balance between the capillary ($F_\gamma(t)$) and viscous ($F_\eta(t)$) forces [325, 326], given by

$$F_\gamma(t) \sim F_\eta(t), \quad (5.20)$$

where (from figure 5.0.1b)

$$F_\gamma(t) = 2\gamma_{sf} (2\pi R(t)). \quad (5.21)$$

For $F_\eta(t)$ in equation (5.20), one can consider the retracting rim to be a cylinder translating in a viscous flow [292, 314]. Thus, the viscous drag can be described by the Oseen approximation to the Stokes flow [327, 328], which to the leading order is expressed as

$$F_\eta(t) \sim \eta_s v_f (2\pi R(t)). \quad (5.22)$$

where the $2\pi R(t)$ term is due to the axisymmetric geometry. On equating equations (5.21) and (5.22), we get

$$v_f \sim \frac{\gamma_{sf}}{\eta_s}. \quad (5.23)$$

Moreover, $v_f = v_s$ (where v_s is the velocity scale in the surrounding medium, see § 5.4). As a result, equation (5.23) implies that the capillary number Ca_s (equation (5.19)) is constant, i.e.,

$$Ca_s = \frac{\eta_s v_s}{2\gamma_{sf}} \sim \mathcal{O}(1). \quad (5.24)$$

Further, upon dividing both sides of equation (5.23) by the inertio-capillary velocity scale $V_{\rho\gamma} = \sqrt{2\gamma_{sf}/(\rho_f h_0)}$ and squaring, we obtain

$$We_f \sim Oh_s^{-2}. \quad (5.25)$$

The aforementioned equations (5.24) – (5.25) denote the scaling laws for viscous two-phase Taylor-Culick retractions.

5.5.2 Three-phase Taylor-Culick retractions

For the three-phase configuration (figure 5.0.1c), in the viscous limit ($Oh_s \gg 1$), the force balance is still given by equation (5.20), especially for the oils that are significantly more viscous than water. Here, the driving surface tension force can be expressed as (from figures 5.0.1c and 5.3.1b)

$$F_\gamma(t) = (\gamma_{sf} + \gamma_{sa} + \gamma_{sf} - \gamma_{sa}) (2\pi R(t)) = 2\gamma_{sf} (2\pi R(t)), \quad (5.26)$$

assuming the presence of a precursor film of oil on top of the water film [see § 5.3.2 and 10, 320, 321]. However, writing an expression for $F_\eta(t)$ is not as straightforward as the two-phase configuration. As can be observed from figure 5.4.4, during the retraction of the film, the oil climbs on top of the water, resulting in a strong flow in the wedge-like region close to the oil-air-water contact line. The rate of local viscous dissipation in this region is also very high (right panels of figure 5.4.4). Similar wedge flows have also been observed for moving contact lines on solid substrates [329–331]. It has been reported that the wedge flow results in a viscosity-dependence of velocity that is weaker than $1/\eta_s$ [330], but the exact nature of the dependence has hitherto not been quantified. The presence of a deformable liquid substrate on which the wedge flow occurs (the retracting water film in this case) complicates the situation even further – making it extremely difficult to arrive at the experimentally-observed $v_f(\eta_s) \sim \eta_s^{-1/2}$ dependence equation (5.2) from a simple force balance. In § 5.7.2, we attempt to explain this scaling from an energetics point of view. Nevertheless, from the experiments, we know that the $v_f(\eta_s)$ scaling is given by equation (5.2), which can be rewritten as

$$Ca_s \sim Oh_s^{1/2}. \quad (5.27)$$

Dividing both sides of equation (5.27) by $V_{\rho\gamma}$ from equation (5.5) and squaring, we obtain

$$We_f \sim Oh_s^{-1}. \quad (5.28)$$

Therefore, from equations (5.23), (5.25), (5.27), and (5.28), we hypothesize that the presence of the oil-air-water apparent contact line in the three-phase configuration dramatically alters the scaling relationships as compared to the two-phase configuration for $Oh_s > 1$ (see figures 5.4.1b and 5.4.2b). This will be further elaborated upon in § 5.7.2. Contrary to this scenario, for low Oh_s numbers, the retraction velocities in both these configurations have the same scaling behavior. Despite the presence of a hook-shaped rim in the three-phase case (figure 5.4.4a,b), we can still treat the moving rim and the surroundings as lumped elements. As a result, the driving surface tension force γ_{sf} ($2\pi R(t)$) still balances the inertial force that scales with $\rho_f v_f^2 (2\pi R(t)) h_0$, thus giving $We_f \sim \mathcal{O}(1)$ (see figure 5.4.2a). In the next section, we demonstrate the validity of the scaling relations developed in this section.

5.6 Demonstration of the scaling relationships

Figure 5.6.1 illustrates the dependence of We_f and Ca_s on the Ohnesorge number Oh_s of the surroundings for the retraction configurations described in figure 5.0.1. Note that the same datapoints are presented in both panels 5.6.1a and 5.6.1b, following the relation $Ca_s = Oh_s \sqrt{We_f}$ (as $v_f = v_s$, see § 5.4). In figure 5.6.1a, $We_f = 1$ marks the classical Taylor-Culick retraction limit, whereas for the two-phase and three-phase configurations, we identify two regimes: inertial ($Oh_s < 1$) and viscous ($Oh_s > 1$).

The inertial scaling is identical for both the two-phase and three-phase configurations: $We_f \sim \mathcal{O}(1)$, which also implies $Ca_s \sim Oh_s$ (see § 5.5.1 and 5.5.2). The brown lines in figure 5.6.1 represent these two scaling relations.

The datapoints corresponding to the two-phase numerical simulations (from figure 5.4.1) are shown by the dark blue triangles. As Oh_s increases, the retraction transitions from the inertial scaling (brown lines), to the viscous two-phase Taylor-Culick scaling: $Ca_s \sim Oh_s^0$ equation (5.24) or $We_f \sim Oh_s^{-2}$ (equation (5.25)). We also plot the experimental datapoints from Reyssat and Quéré [292] for their silicone oil (surroundings, s) – soap water (film, f) dataset, shown in figure 5.6.1 by the light blue pentagrams. In order to make these datapoints dimensionless, we use $h_0 = 100 \mu\text{m}$ and $\gamma_{sf} = 7 \text{ mN/m}$, denoting the thickness of the soap film and the surroundings-film interfacial tension coefficient, respectively, in their experiments. We also neglect any Marangoni flow, or dynamic surface tension effects. Our simulations and scaling relationships are in reasonable agreement with the experimental datapoints of Reyssat and Quéré [292]. Note that Reyssat and Quéré [292] tried to fit a trend line

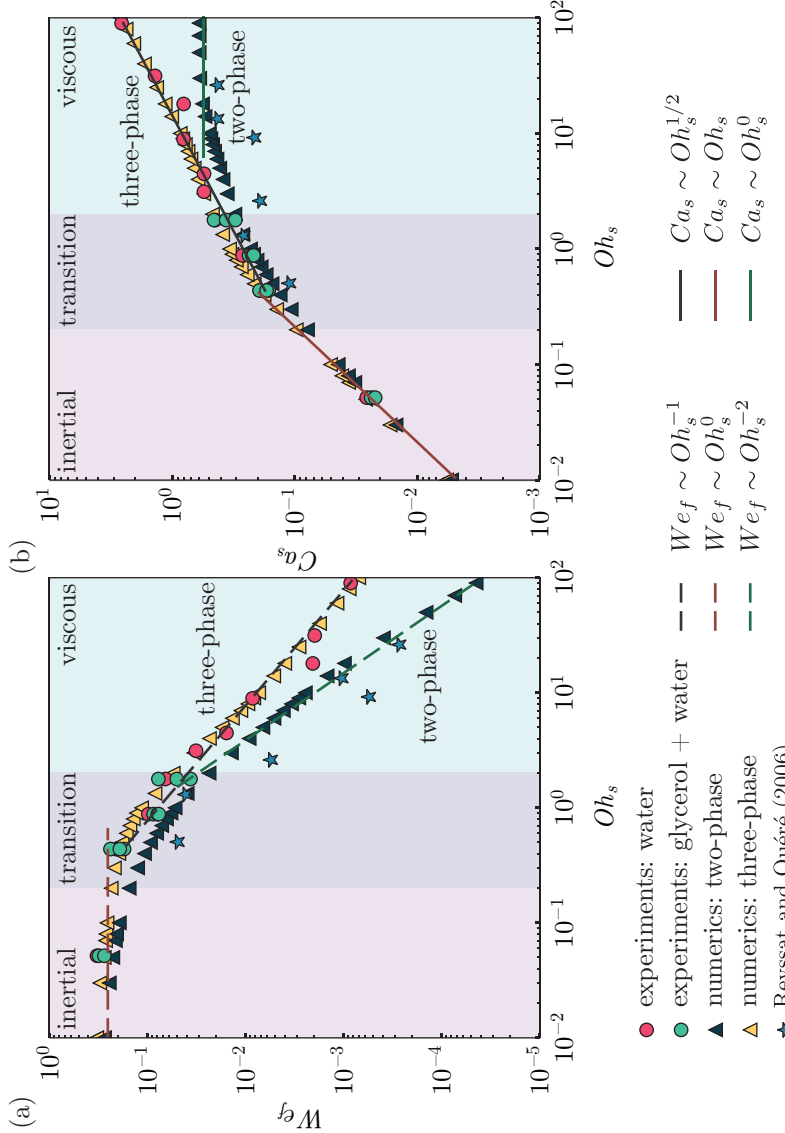


Figure 5.6.1: Regime maps visualized as We_f vs. Oh_s in (a) and as Ca_s vs. Oh_s in (b). The experimental datapoints (circles) correspond to the three-phase configuration (figure 5.0.1c) while the simulations (triangles) correspond to both the two-phase (figure 5.0.1b) and three-phase (figure 5.0.1c) configurations. The experimental datapoints (pentagrams) for the two-phase configuration have been adopted from Reyssat and Quéré [292] for their silicone oil (surroundings, s) – soap water (film, f) dataset.

of $(\ln \eta_s) / \eta_s$ (higher order Oseen correction) through all of their experimental datapoints to obtain a good fit. When the same datapoints are plotted in figure 5.6.1a and b, it is observed that some of their datapoints (corresponding to the low Oh_s numbers) are, in fact, in the transition between the inertial and the viscous regimes, while the rest of the datapoints show reasonable agreement with the viscous two-phase retraction dynamics given by equations (5.24) or (5.25).

We also plot the datapoints corresponding to our experiments (figure 5.2.3) and simulations (figure 5.4.2) for the three-phase configuration (figure 5.0.1c) in figure 5.6.1. We observe that, at low Oh_s , these datapoints follow the inertial dynamics (brown lines), while at higher Oh_s , the datapoints follow the scaling relationships given by equations (5.27) and (5.28): $Ca_s \sim Oh_s^{1/2}$ and $Wef \sim Oh_s^{-1}$, respectively (represented by the black lines in figure 5.6.1). Note that in order to non-dimensionalize the experimental datapoints shown in figure 5.2.3c (so that they can be plotted in figure 5.6.1), one needs to know the film thickness h_0 . In the present experiments, the optical resolution was insufficient for accurate measurement of the film thickness prior to rupture. Moreover, as mentioned earlier, the breakup process itself is highly sensitive to experimental noise [see § 4.2 of 97]. Similar difficulties were also presumably experienced by Eri and Okumura [314] in their experiments of two-phase retraction, and they used a fitting parameter in their $v_f(\eta_s)$ relation, which was a function of h_0 . We also know from bubble bursting experiments [84, 332] that the film thickness prior to breakup varies in the range $\mathcal{O}(100 \text{ nm}) - \mathcal{O}(10 \mu\text{m})$. Moreover, in similar studies [84, 333], the film thickness is retroactively calculated from the retraction velocity measurements. We can see from figure 5.6.1 that for low Oh_s , the dynamics are independent of the specific nature of the configuration (classical, two-phase, or three-phase). Knowing v_f , η_s , and γ_{sf} , we can calculate the Ca_s for the datapoint in figure 5.2.3c corresponding to $\eta_s = 4.94 \times 10^{-4} \text{ Pa.s}$. Fitting that Ca_s value to the $Ca_s \sim Oh_s$ trend line (brown line) in figure 5.6.1b, a value of $h_0 = 1.5 \mu\text{m}$ can be calculated, which is within the range observed for previous experiments in a similar system [84]. Using $h_0 = 1.5 \mu\text{m}$ for the remaining experimental datapoints in figure 5.2.3c (for $\eta_s > 4 \times 10^{-3} \text{ Pa.s}$) and calculating Ca_s , Oh_s , and Wef , we find that those datapoints (red circles) also collapse on the trend lines (black lines) along with the numerical simulations (yellow triangles) in figure 5.6.1. Note that a water film thickness of $h_0 = 1.5 \mu\text{m}$ sets the Oh_f at 0.1 for the three-phase case, which is different from the Oh_f that we use for the two-phase case [$Oh_f = 0.05$ based on their experiments of 292]. Therefore, to justify comparison between

the two cases, we varied Oh_f in simulations from 0.01 to 0.1 and found that the dimensionless retraction velocities (We_f and Ca_s) are Oh_f -independent for both the two-phase and three-phase configurations (for $Oh_f < 1$). We also verify the Oh_f -independence experimentally by replacing the water in our bath by glycerol-water mixtures, and the measurements thus obtained (green circles) also follow the $We_f \sim Oh_s^{-1}$ and $Ca_s \sim Oh_s^{1/2}$ trendlines (black lines) in figures 5.6.1a and 5.6.1b, respectively.

In summary, in § 5.5 – § 5.6, we discussed the forces involved during the retraction of liquid films owing to the unbalanced capillary traction, followed by identification of the inertial ($Oh_s < 1$) and viscous ($Oh_s > 1$) regimes in the We_f vs. Oh_s and Ca_s vs. Oh_s dependences. We also checked the validity of the corresponding scaling behaviors in this section. To further understand the retraction dynamics due to the capillary traction, we focus on the different thermodynamically consistent energy transfer modes in the next section. Particularly, we try to understand the scaling relationship for the viscous three-phase Taylor-Culick retraction that still eludes understanding from a momentum balance point of view (see § 5.7.2).

5.7 Taylor-Culick retractions: an energetics perspective

A retracting liquid sheet loses surface area and consequently releases energy [35, 90–92], which further increases the kinetic energy of the system (i.e., film and surroundings). A part of this energy is lost in the process due to viscous dissipation. So, the overall energy budget entails

$$E_k^f(R) + E_k^s(R) + E_k^a(R) + E_\gamma(R) + E_d^f(R) + E_d^s(R) + E_d^a(R) = E_\gamma(R=0), \quad (5.29)$$

where E_γ is the surface energy, E_k the kinetic energy, and E_d the viscous dissipation. The superscripts account for the film (f), the surroundings (s), and air (a). Of course, for the two-phase case, the terms associated with air (a) do not exist as there is no air phase. Figure 5.7.1 depicts equation (5.29) for both the two-phase and three-phase configurations. Coincidentally, even for the three-phase configuration, the energies associated with the air phase are negligible (see figure 5.7.1, the dashed and dot-dashed lines overlap), even though the velocity field in air is not negligible (figure 5.4.4). We keep $E_k^a(R)$ and $E_d^a(R)$ in the energy budget for the sake of completeness. In general, the sum of all these energies at any hole radius $R(t)$ equals the total surface energy

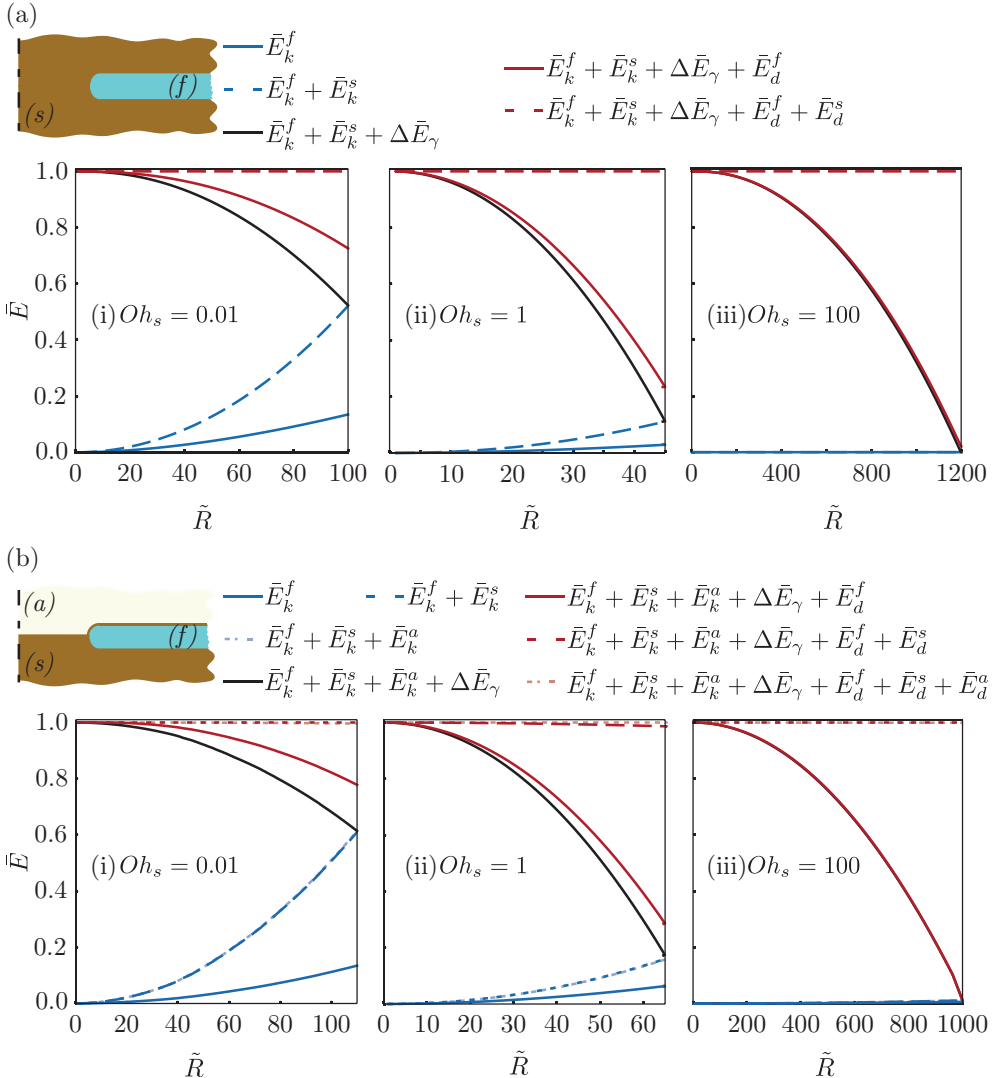


Figure 5.7.1: Energy budget at different Oh_s for the (a) two-phase and (b) three-phase configurations. The energies E are normalized by the total surface energy released as the film retracts creating a hole of radius $\tilde{R}_{\max} = 100$ for $Oh_s \leq 1$, and $\tilde{R}_{\max} = 1000$ (two-phase case) and $\tilde{R}_{\max} = 1200$ (three-phase case) for $Oh_s = 100$. Note that this \tilde{R}_{\max} , and hence the surface energy datum, are arbitrarily chosen. We use hole radii that are large enough such that the sheets approach a constant velocity. The superscripts account for the film (f), the surroundings (s), and air (a).

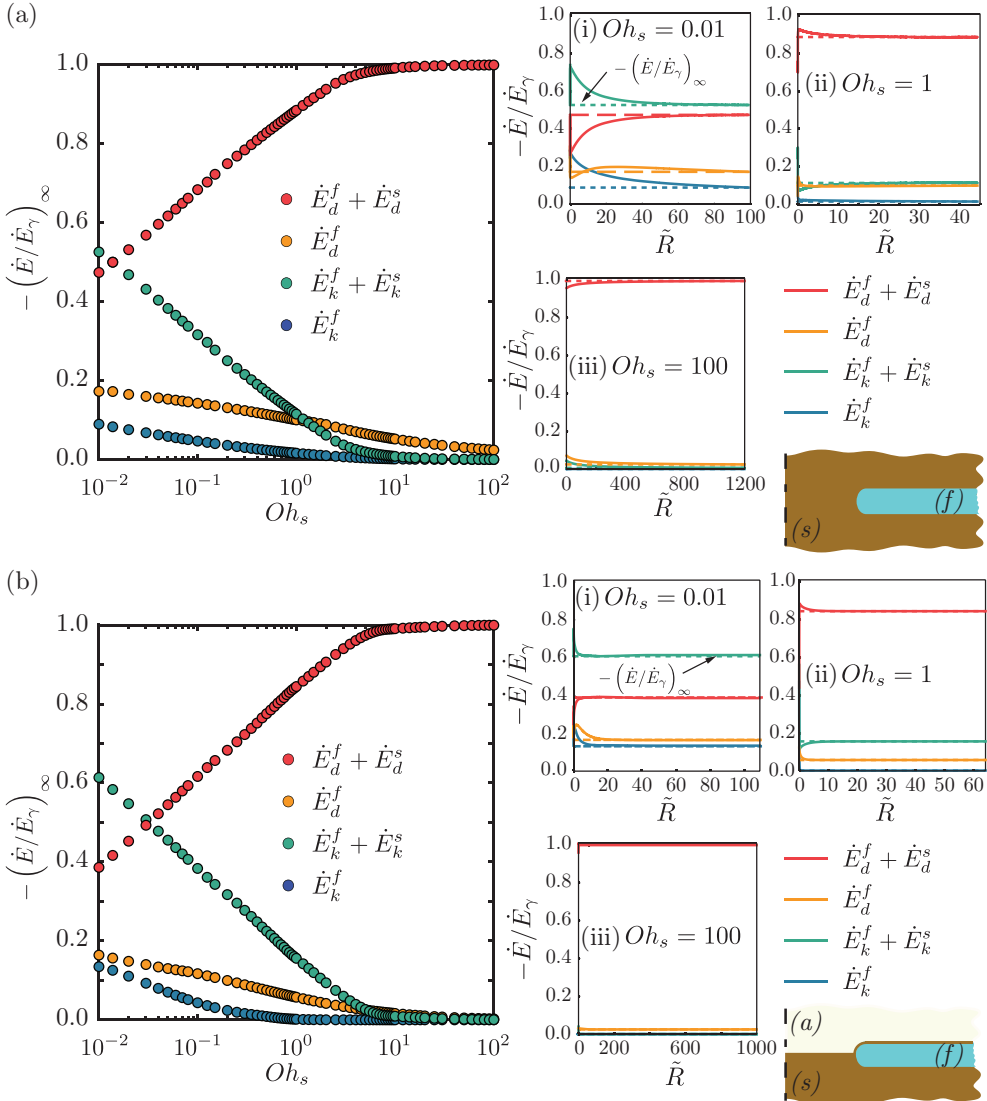


Figure 5.7.2: Variation of the rate of change of kinetic energy (\dot{E}_k) and viscous dissipation (\dot{E}_d) as proportions of the rate of energy injection ($-\dot{E}_\gamma$) with Oh_s at steady state for the (a) two-phase and (b) three-phase configurations. For both cases, in the inertial limit ($Oh_s \ll 1$), the fraction of energy that goes into kinetic energy and viscous dissipation are comparable. However, in the viscous limit ($Oh_s \gg 1$), viscous dissipation in the surroundings dominates. Insets show the representative temporal variations of the ratio of the rate of change of energy (\dot{E}) to the rate of energy injection ($-\dot{E}_\gamma$) with dimensionless hole radius \tilde{R} at three different Oh_s . The superscripts account for the film (f), the surroundings (s), and air (a).

at $R = 0$, i.e., the total energy available to the system. As the film retracts, it continuously releases energy, as its surface energy decreases. Therefore, to calculate equation (5.29), one can choose a reference for surface energy arbitrarily. In figure 5.7.1, the surface energy at a hole radius of $R = R_{\max}$ is used as this arbitrary instance. This datum is chosen such that by the time the hole expands to R_{\max} , the film would have reached a constant velocity. Furthermore, we can normalize the energies in equation (5.29) with the total surface energy released as the film retracts to a hole of radius R_{\max} . The energy budget now reads

$$\bar{E}_k^f(\tilde{R}) + \bar{E}_k^s(\tilde{R}) + \bar{E}_k^a(\tilde{R}) + \Delta\bar{E}_\gamma(\tilde{R}) + \bar{E}_d^f(\tilde{R}) + \bar{E}_d^s(\tilde{R}) + \bar{E}_d^a(\tilde{R}) = 1. \quad (5.30)$$

Here, $\bar{E}(\tilde{R}) = E(\tilde{R})/(E_\gamma(0) - E_\gamma(\tilde{R}_{\max}))$, $\Delta E_\gamma(\tilde{R}) = E_\gamma(\tilde{R}) - E_\gamma(\tilde{R}_{\max})$, and $\tilde{R} = \tilde{R}(t) = R(t)/h_0$ is the dimensionless hole radius. The reader is referred to appendix 5.B for details of the energy budget calculations.

Removing the arbitrary datum described above and noting that there is a continuous injection of surface energy ($-\dot{E}_\gamma$, minus sign because the surface energy is decreasing with the growing hole) into the system, we can also write the energy budgets in terms of rates:

5

$$\dot{E}_k^f(\tilde{R}) + \dot{E}_k^s(\tilde{R}) + \dot{E}_d^f(\tilde{R}) + \dot{E}_d^s(\tilde{R}) = \left(-\dot{E}_\gamma(\tilde{R})\right). \quad (5.31)$$

Figure 5.7.2 visualizes equation (5.31) by plotting the proportion of the rate of surface energy released that goes into the rate of increase of kinetic energy and the rate of total viscous dissipation. From the insets (i – iii) of this figure, we observe that these fractions saturate after initial transients. So, we also plot these steady state values (equation (5.32)) in panels 5.7.2a and 5.7.2b for the two-phase and three-phase configurations, respectively,

$$\left(\dot{E}/\dot{E}_\gamma\right)_\infty = \lim_{\tilde{R} \rightarrow \infty} \left(\frac{\dot{E}(\tilde{R})}{\dot{E}_\gamma(\tilde{R})}\right). \quad (5.32)$$

We devote the rest of this chapter to understanding the distribution of the energy injection rate into the rates of increase of kinetic energy and viscous dissipation for both the inertial and viscous regimes.

5.7.1 Energy transfers in the inertial regime

We first focus on the energy balance in the classical Taylor-Culick retraction and the famous Dupré-Rayleigh paradox [97]. Dupré [90, 91] hypothesized that the total surface energy released during retraction manifests as the kinetic energy of the film [92]. As a result, the predicted retraction velocity was off by a factor of $\sqrt{2}$ (see appendix 5.A), leading to discrepancies with experiments [35, 266]. Nonetheless, it is noteworthy that Dupré [90, 91] reached the correct scaling relationship by identifying the essential governing parameters of classical sheet retractions.

Culick [35] identified that the rate of surface energy released (equation (5.37)) should be distributed into an increase in kinetic energy of the rim and the viscous dissipation inside the film: $-\dot{E}_\gamma(t) = \dot{E}_k^f(t) + \dot{E}_d^f(t)$. The viscous dissipation can be attributed to the inelastic acceleration of the undisturbed film up to the velocity of the edge of the rim. Note that the dissipation is independent of the fluid viscosity and is given by [35]

$$\dot{E}_d^f(t) = \frac{1}{2} \frac{dm(t)}{dt} v_f^2, \quad (5.33)$$

where $m(t)$ is the mass of the retracting film.

Coincidentally, this rate of viscous dissipation in the film is the same as the rate of increase in its kinetic energy [constant rim velocity, 35, 97]. We confirm this hypothesis in appendix 5.A [see figures 5.A.1c, d, and 265], whereby

$$\dot{E}_k^f(t) \approx \dot{E}_d^f(t) \approx -\dot{E}_\gamma(t)/2. \quad (5.34)$$

Next, we delve into the energy transfers in the two-phase and three-phase configurations. In the inertial limit, in a manner akin to the classical case, the fraction of the rate of energy injection that goes into increasing the kinetic energy is similar to that of viscous dissipation. However, unlike the classical case, the kinetic energy as well as viscous dissipation are distributed among the film and the surrounding medium (figures 5.7.1 and 5.7.2, $Oh_s \ll 1$). We observe that

$$\left(\dot{E}_d^f(t) + \dot{E}_d^s(t) \right) \approx \left(\dot{E}_k^f(t) + \dot{E}_k^s(t) \right) \approx -\dot{E}_\gamma(t)/2. \quad (5.35)$$

In a manner reminiscent of Dupré [90, 91], we can write

$$-\dot{E}_\gamma(t) \approx \left(\dot{E}_k^f(t) + \dot{E}_k^s(t) \right) \sim (\rho_f v_f h_0 (2\pi R(t))) v_f^2, \quad (5.36)$$

where $v_f = v_s$ (kinematic boundary condition at the tip of the film) and $\rho_s = \rho_f$. Additionally, following Bohr and Scheichl [334] and appendix 5.B, the rate of change of surface energy is given by

$$\dot{E}_\gamma(t) \approx -F_\gamma(t) \frac{dR(t)}{dt} = -2\gamma_{sf} (2\pi R(t)) v_f. \quad (5.37)$$

Using equations (5.36) – (5.37), and rearranging, we get

$$We_f = \frac{\rho_f v_f^2 h_0}{2\gamma_{sf}} \sim \mathcal{O}(1), \quad (5.38)$$

which is the same as the inertial scaling derived using the force balance (insets of figures 5.4.1a and 5.4.2a).

5.7.2 Demystifying dissipation in the viscous regime

In the viscous limit ($Oh_s \gg 1$), for both the two-phase and three-phase configurations, the surface energy released is entirely dissipated in the surrounding medium (figures 5.7.1 and 5.7.2), i.e.,

$$-\dot{E}_\gamma(t) \sim \dot{E}_d^s(t). \quad (5.39)$$

In fact, this interplay between the surface energy and the viscous dissipation sets the velocity scale (v_s) in the surrounding medium, which is equal to the retraction velocity (v_f , kinematic boundary condition at the hole). Therefore, to estimate this velocity, we first calculate the rate of viscous dissipation $\dot{E}_d^s(t)$, which depends on both the viscosity η_s of the surrounding medium and the velocity gradients \mathcal{D} , following the relation (see appendix 5.B)

$$\dot{E}_d^s = \int_{\Omega_s} 2\eta_s (\mathcal{D} : \mathcal{D}) d\Omega_s = \int_{\Omega_s} \varepsilon_s d\Omega_s. \quad (5.40)$$

Here, ε_s is the viscous dissipation function of the surrounding, and the integrals are evaluated over the volume Ω_s of the surrounding medium. Note

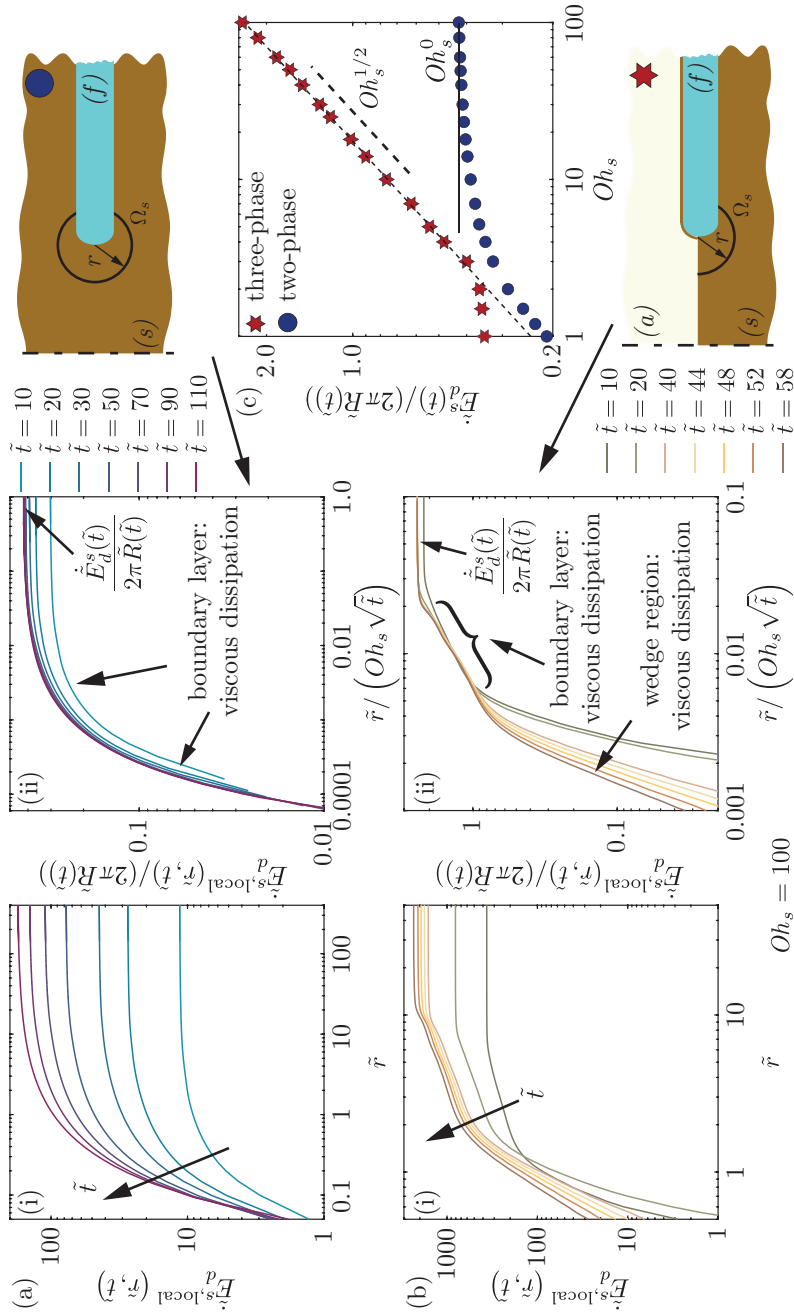


Figure 5.7.3: Dissipation in the viscous limit ($Oh_s \gg 1$) of Taylor-Culick retractions: evolution of the local rate of viscous dissipation $(\dot{E}_d^s)_{\text{local}}(\tilde{r}, \tilde{t})$ with dimensionless distance $\tilde{r} = r/h_0$ away from (a) the tip of the film in the two-phase configuration and (b) the macroscopic contact line in the three-phase configuration. In insets (ii), this distance is normalized with the dimensionless viscous boundary layer thickness in the surrounding medium, $\tilde{\delta}_\nu = \delta_\nu/h_0 = Oh_s\sqrt{\tilde{t}}$. Here, $\tilde{R} = R/h_0$ and $\tilde{t} = t/\tau_{\eta\gamma}$ are the dimensionless hole radius and dimensionless time, respectively. (c) Variation of the total viscous dissipation rate per unit circumference of the hole, $\dot{E}_d^s(\tilde{t}) / (2\pi\tilde{R}(\tilde{t}))$ at steady state with Oh_s .

that ε_s is highest at the expanding hole, i.e., the tip of the retracting film in the case of two-phase retractions (figures 5.4.3), and the macroscopic contact line in the case of three-phase retractions (figures 5.4.4). The latter is analogous to wetting and dewetting of rigid surfaces [320, 329, 331]. Motivated by this analogy, we calculate the local rate of viscous dissipation integrated over volume elements $\Omega_s(r)$ centered at the expanding hole,

$$\dot{E}_d^{s,\text{local}}(r, t) = \int_0^{\Omega_s(r)} \varepsilon_s(r, t) d\Omega_s. \quad (5.41)$$

where r is the radial distance away from the hole (see insets of figure 5.7.3c). Additionally, in the viscous regime, we can use the visco-capillary velocity $V_{\eta\gamma} = 2\gamma_{sf}/\eta_s$ and the film thickness h_0 to non-dimensionalize (equation (5.41), see § 5.3.3 and [295]),

$$\dot{\tilde{E}}_d^{s,\text{local}}(\tilde{r}, \tilde{t}) \equiv \frac{\dot{E}_d^{s,\text{local}}(\tilde{r}, \tilde{t})}{\eta_s V_{\eta\gamma}^2 h_0} = \int_0^{\tilde{\Omega}_s(\tilde{r})} \tilde{\varepsilon}_s(\tilde{r}, \tilde{t}) d\tilde{\Omega}_s. \quad (5.42)$$

Figures 5.7.3(a-i) and 5.7.3(b-i) show that the local viscous dissipation increases as we move away from the hole (increasing \tilde{r}). Furthermore, the energy dissipated increases in time as the region of flow expands, owing to the increasing hole radius and the dominant radial flow. To rationalize this increase, we plot the rate of local viscous dissipation per unit circumference of the hole in figures 5.7.3(a-ii) and 5.7.3(b-ii).

For the two-phase case, the viscous dissipation occurs in the viscous boundary layer ($\tilde{\delta}_\nu \sim Oh_s \sqrt{\tilde{t}}$) and saturates at $\tilde{r} \approx \tilde{\delta}_\nu$ (figure 5.7.3a-ii). However, for the three-phase case, we can identify two distinct regions of viscous dissipation, the wedge region close to the macroscopic contact line, where the viscous dissipation per unit circumference of the expanding hole increases steeply ($\tilde{r} < 0.01\tilde{\delta}_\nu$), and the viscous boundary layer ($\tilde{r} < 0.1\tilde{\delta}_\nu$), beyond which it saturates (figure 5.7.3b-ii). Furthermore, this saturation value gives the total viscous dissipation per unit circumference of the hole,

$$\frac{\dot{\tilde{E}}_d^s(\tilde{t})}{(2\pi\tilde{R}(\tilde{t}))} = \lim_{\tilde{r} \rightarrow \infty} \frac{\dot{\tilde{E}}_d^{s,\text{local}}(\tilde{r}, \tilde{t})}{(2\pi\tilde{R}(\tilde{t}))}, \quad (5.43)$$

which is shown in figure 5.7.3(c) as a function of Oh_s . We observe that for the two-phase case, the total dissipation is independent of Oh_s , whereas in the three-phase case, it scales with $Oh_s^{1/2}$.

$$\dot{\tilde{E}}_d^s(\tilde{t}) \sim \begin{cases} Oh_s^0 (2\pi\tilde{R}(\tilde{t})) & \text{two-phase case,} \\ Oh_s^{1/2} (2\pi\tilde{R}(\tilde{t})) & \text{three-phase case.} \end{cases} \quad (5.44)$$

Moreover, upon non-dimensionalizing equation (5.37) using the same scales as used in equation (5.42), and noting that $v_f = v_s$ and $Ca_s = \eta_s v_s / (2\gamma_{sf})$, we get

$$-\dot{\tilde{E}}_\gamma(t) \equiv \frac{\gamma_{sf} v_f (2\pi R(t))}{\eta_s V_{\eta\gamma}^2 h_0} = Ca_s (2\pi\tilde{R}(\tilde{t})). \quad (5.45)$$

Lastly, equating equations (5.44) and (5.45), we get,

$$Ca_s \sim \begin{cases} Oh_s^0 & \text{two-phase case,} \\ Oh_s^{1/2} & \text{three-phase case.} \end{cases} \quad (5.46)$$

In summary, in this section, we confirmed our hypothesis that the presence of the oil-air-water contact line in the three-phase configuration dramatically alters the scaling relationships and dynamics as compared to the two-phase configuration (see § 5.5.2). We also relate the dimensionless retraction velocity Ca_s with the control parameter Oh_s in the viscous limit by following the location and magnitude of the local rate of viscous dissipation during Taylor-Culick retractions in viscous surroundings.

5.8 Conclusions and outlook

In this chapter, we have studied the effects of the surrounding media on the retraction dynamics of liquid sheets in three canonical configurations. In the *classical* Taylor-Culick configuration, the interplay between capillarity and inertia of the film results in a constant retraction velocity. We can further neglect the surrounding medium as it does not influence the retraction process.

However, for a film retracting in a dense and viscous oil (*two-phase* configuration), and that at an oil-air interface (*three-phase*), both inertia and viscosity of the oil phase influence the retraction process. The former presents itself as an added mass-like effect. Even though capillarity still governs the constant retraction velocity, the surrounding medium's inertia reduces the magnitude of the film's momentum as it retracts.

Moreover, when the viscosity of the oil is significantly higher than that of the film, the viscous stresses dictate the retraction process and set the velocity scale. To further demystify the energy balance in this process, we used thermodynamically consistent energy transfer mechanisms to understand the fate of the released surface energy owing to the loss of surface area of the retracting film. This energy is injected into the system and manifests itself as kinetic energy and viscous dissipation. In the inertial regime, the proportions of kinetic energy and viscous dissipation are the same, conforming to the analyses of Culick [35]. However, in the viscous regime, the total surface energy released goes into viscous dissipation in the surroundings.

Following the lumped elements analysis, motivated by Taylor [34], Culick [35], we also developed scaling relations to relate the non-dimensionalized retraction velocity (We_f and Ca_s) with the control parameter Oh_s . In the inertial limit, the Weber number We_f based on the retraction velocity is a constant for all three configurations. On the other hand, in the viscous limit, the retraction velocity in the *two-phase* configuration scales with the visco-capillary velocity scale (constant capillary number, $Ca_s \sim \mathcal{O}(1)$); while for the *three-phase* configuration, the capillary number Ca_s increases with increasing Oh_s , owing to the localization of viscous dissipation near the three-phase contact line.

A natural extension of the present work would be to understand the retraction of non-Newtonian sheets and filaments [276] in similar surroundings. In such scenarios, the retraction dynamics will depend not only on capillarity and viscosity as described in this work, but also on the rheological properties of both the film and the surroundings. Furthermore, in a broader perspective, the precursor film-based three-fluid volume of fluid method can be used to elucidate several spreading phenomena, both at small and large scales, e.g., drop-film interactions in the inkjet printing process [16] and late time spreading during oil spillage [335], respectively.

Acknowledgments

We acknowledge Pim Dekker for carrying out initial experiments. We would like to thank Maziyar Jalaal, Jacco Snoeijer, and Andrea Prosperetti for discussions.

Appendix

5.A Classical Taylor-Culick retractions

In this section, we discuss the classical Taylor-Culick retractions, which is modeled using the numerical method used for the two-phase configuration (see § 5.3.2) by replacing the surrounding medium (s) with air (a). The volume of fluid (VoF) tracer advection equation (5.7), and the Brackbill et al. [157] surface tension force formulation (equation (5.8)) remain the same, whereas, the VoF property equations are modified as

$$\tilde{\rho} = \Psi + (1 - \Psi) \frac{\rho_a}{\rho_f}, \quad (5.47)$$

$$Oh = \Psi Oh_f + (1 - \Psi) Oh_a, \quad (5.48)$$

where ρ_a/ρ_f is the air to film density ratio (fixed at 10^{-3}), and the two dimensionless groups

$$Oh_f = \frac{\eta_f}{\sqrt{\rho_f (2\gamma_{af}) h_0}}, \quad Oh_a = \frac{\eta_a}{\sqrt{\rho_f (2\gamma_{af}) h_0}} \quad (5.49)$$

represent the film Ohnesorge number and the air Ohnesorge number (fixed at 10^{-5}), respectively.

Figure 5.A.1 summarizes the results of the classical Taylor-Culick retractions for a typical $Oh_f = 0.05$. After the initial transients, the growing hole follows a linear evolution in time and the growth rate approaches the Taylor-Culick velocity (equation (5.1)), see figure 5.A.1b and its inset). In the steady state, both the water film and the ambient air move (figure 5.A.1a), but the density of air is negligible as compared to that of the film. Consequently, the air does not contribute to the force or energy equilibrium described below.

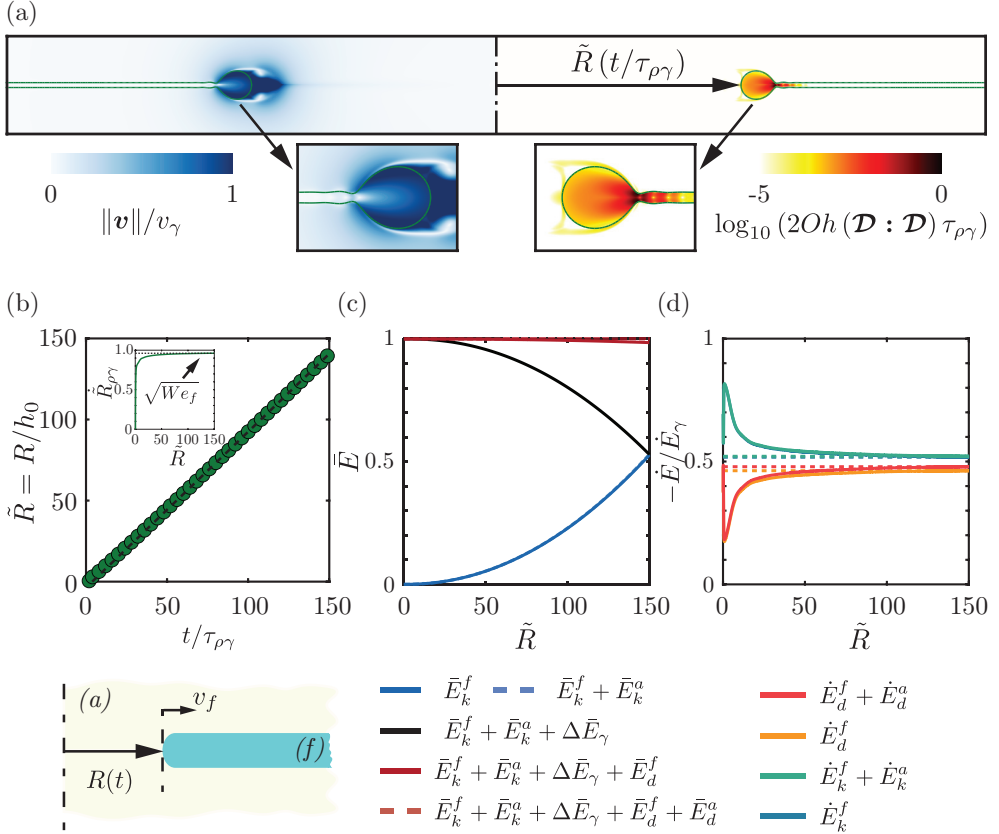


Figure 5.A.1: Classical Taylor-Culick retractions: (a) The morphology of the flow when the dimensionless hole radius $\tilde{R} = 50$. The left hand side contour shows the velocity magnitude normalized with the inertio-capillary velocity scale ($\|\mathbf{v}\|/V_{\rho\gamma}$), while the right hand side shows the dimensionless viscous dissipation function normalized using the inertio-capillary scales ($2Oh(\mathcal{D}:\mathcal{D})\tau_{\rho\gamma}^2$), represented on a \log_{10} scale to differentiate the regions of maximum dissipation. (b) Temporal evolution of $\tilde{R}(t)$. Time is normalized using the inertio-capillary time scale, $\tau_{\rho\gamma} = \sqrt{\rho_f h_0^3 / \gamma_{sf}}$. Inset of panel (b) shows the variation of dimensionless growth rate of the hole radius. Notice that $\sqrt{We_f} = \lim_{\tilde{R} \rightarrow \infty} \dot{\tilde{R}}_{\rho\gamma} = 1$. (c) Energy budget where the energies (E) are normalized using the total surface energy released as the film retracts, creating a hole of radius $\tilde{R}_{\max} = 150$. (d) Variations of the rate of change of energy $\dot{E}(t)$ as a fraction of the rate of energy injection into the system ($-\dot{E}_\gamma(t)$) with dimensionless hole radius $\tilde{R}(t)$. The superscripts account for the film (f) and air (a). The Ohnesorge number of the film for this simulation is $Oh_f = 0.05$, and that of air is $Oh_a = 10^{-5}$ to respect the assumption that the surrounding medium has negligible effect on the retraction process [34, 35]. Additionally, the air-to-film density ratio is $\rho_a/\rho_f = 10^{-3}$. Also see supplemental movie 4.

5.A.1 Force balance

For the classical configuration (figure 5.0.1a), the force balance strictly implies that the capillary force ($F_\gamma(t)$) equals the rate of change of momentum ($P(t)$) of the moving rim written as [34]

$$F_\gamma(t) = \frac{dP(t)}{dt} = \frac{d}{dt} (m(t)v_f), \quad (5.50)$$

where the capillary force is given by $F_\gamma(t) = 2\gamma_{af} (2\pi R(t))$, γ_{af} is the surface tension coefficient between the film and the surrounding air. Assuming that the film velocity v_f is a constant, we can simplify equation (5.50) to

$$2\gamma_{af} (2\pi R(t)) = v_f \frac{dm(t)}{dt}, \quad (5.51)$$

where we can employ the continuity equation to get

$$\frac{dm(t)}{dt} = \rho_f v_f h_0 (2\pi R(t)). \quad (5.52)$$

Further, using equations (5.51) and (5.52),

$$2\gamma_{af} (2\pi R(t)) = \rho_f v_f^2 h_0 (2\pi R(t)), \quad (5.53)$$

for the classical configuration (figure 5.0.1a), giving

$$v_f = \sqrt{\frac{2\gamma_{af}}{\rho_f h_0}}. \quad (5.54)$$

Note that equations (5.50)–(5.53) are similar to the calculations of Taylor [34], and only considers momentum equilibrium while disregarding the fate of the liquid accumulated in the rim [97]. Furthermore, it assumes no interaction with the surrounding medium (air). In terms of the dimensionless numbers, (equation (5.54)) implies that $Wef = \rho_f v_f^2 h_0 / (2\gamma_{af})$ is constant and equal to 1 (i.e., $v_f = v_{TC}$, see equation (5.1)).

5.A.2 Energy balance

Dupré [90, 91] wrongly assumed that the entire surface energy released during the retraction manifests as the kinetic energy of the film [92], giving

$$-\dot{E}_\gamma(t) = \dot{E}_k^f(t), \quad (5.55)$$

$$2\gamma_{af} (2\pi R(t)) v_f = \frac{d}{dt} \left(\frac{1}{2} m(t) v_f^2 \right). \quad (5.56)$$

Using conservation of mass $dm(t) = \rho v h_0 (2\pi R(t)) dt$, Dupré [90, 91] calculated the retraction velocity to be

$$v_f = \sqrt{\frac{4\gamma_{af}}{\rho_f h_0}} = \sqrt{2} v_{TC}, \quad (5.57)$$

which is off by a factor of $\sqrt{2}$ [see Dupré-Rayleigh paradox in 97].

Culick [35] realized that the correct energy balance entails that the rate of surface energy released should be distributed equally into an increase in kinetic energy of the rim and the viscous dissipation inside the film (equation (5.58)). Figures 5.A.1c and d illustrate the energy balance associated with the classical Taylor-Culick retractions (note that $\bar{E}_k^f(t) \approx \bar{E}_d^f(t)$ in figure 5.A.1c and $\dot{E}_k^f(t) \approx \dot{E}_d^f(t)$ in figure 5.A.1d).

$$-\dot{E}_\gamma(t) = \dot{E}_k^f(t) + \dot{E}_d^f(t), \quad (5.58)$$

where $-\dot{E}_\gamma(t) \approx 2\gamma_{af} (2\pi R(t)) v_f$ [see appendix 5.B and 334]. Note that the rate of viscous dissipation at any given instant is analogous to the inelastic collision of a tiny fluid parcel in the film with the massive rim. Indeed, the local viscous dissipation ($2Oh(\mathcal{D} : \mathcal{D})\tau_{\rho\gamma}^2$) is maximum in the region connecting the rim to the film (figure 5.A.1a). Consequently [35],

$$2\gamma_{af} (2\pi R(t)) v_f = \frac{d}{dt} \left(\frac{1}{2} m(t) v_f^2 \right) + \frac{1}{2} \frac{dm(t)}{dt} v_f^2. \quad (5.59)$$

Again, using conservation of mass $dm = \rho v h_0 (2\pi R(t)) dt$ and rearranging equation (5.59), we get

$$v_f = v_{TC} = \sqrt{\frac{2\gamma_{af}}{\rho_f h_0}} \quad (5.60)$$

for the classical configuration.

5.B Energy calculations

This appendix explains the motivation and mathematical expressions used in the present study to describe different energy transfers, and their rates, as discussed in § 5.7. Similar approaches have been used in the literature to study the dynamics of two-phase flows [149, 334]. Here, we extend these formulations to three-phase flows.

The kinetic energies and viscous dissipations associated with the three fluids are given by [160, p. 50-51]

$$E_k^j = \frac{1}{2} \rho_j \int_{\Omega_j} \|\mathbf{u}\|^2 d\Omega_j, \quad (5.61)$$

$$E_d^j = 2 \int_t \left(\int_{\Omega_j} \eta_j (\mathcal{D} : \mathcal{D}) d\Omega_j \right) dt = \int_t \left(\int_{\Omega_j} \varepsilon_j d\Omega_j \right) dt. \quad (5.62)$$

where ε_j and $d\Omega_j$ are the viscous dissipation function and the differential volume element associated with the j^{th} fluid. Additionally, ρ_j and η_j denote the density and viscosity, respectively, of the j^{th} fluid. In the present work, $j = f$ (film, water), s (surroundings, oil), and a (air). Furthermore, in terms of rates,

$$\frac{dE_k^j}{dt} = \frac{d}{dt} \left(\frac{1}{2} \rho_j \int_{\Omega_j} \|\mathbf{u}\|^2 d\Omega_j \right), \quad (5.63)$$

$$\frac{dE_d^j}{dt} = \int_{\Omega_j} \varepsilon_j d\Omega_j. \quad (5.64)$$

Next, the total surface energy E_γ of the system for the three-phase configuration is

$$E_\gamma = \int_{\mathcal{A}_{sf}} \gamma_{sf} d\mathcal{A}_{sf} + \int_{\mathcal{A}_{sa}} \gamma_{sa} d\mathcal{A}_{sa}, \quad (5.65)$$

where γ_{ij} and \mathcal{A}_{ij} are the interfacial tension coefficient and area, respectively, associated with an interface between the i^{th} and the j^{th} fluids. Note that,

the assumption of a precursor film of oil (surroundings, s) on the water film (f) implies that there is no film-air interface. Additionally, $\gamma_{sf} = 2\gamma_{sa}$ (see § 5.3.2).

$$E_\gamma = \gamma_{sf} (\mathcal{A}_{sf} + \mathcal{A}_{sa}/2), \quad (5.66)$$

So, the rate of surface energy released during the retraction process in the three-phase configuration is

$$\dot{E}_\gamma = \gamma_{sf} \left(\dot{\mathcal{A}}_{sf} + \dot{\mathcal{A}}_{sa}/2 \right), \quad (5.67)$$

where $\dot{\mathcal{A}}_{ij}$ is the rate of change of interfacial area.

For the two-phase configuration, there is no air ($\mathcal{A}_{sa} = 0$), and the rate of change of surface energy is simply

$$\dot{E}_\gamma = \gamma_{sf} \dot{\mathcal{A}}_{sf}. \quad (5.68)$$

Note that we use equations (5.62) – (5.68) for calculating the energies, and their rates of change, in figures 5.7.1, 5.7.2, and 5.A.1. However, to better understand the individual contributions of the two terms on the right hand side of equation (5.67), figure 5.B.1 illustrates the ratio of the rate of change of surroundings-air interfacial area ($\dot{\mathcal{A}}_{sa}$) to that of the surroundings-film ($\dot{\mathcal{A}}_{sf}$). Initially, at very small hole radii ($\tilde{R} \rightarrow 0$), the two rates are comparable ($\dot{\mathcal{A}}_{sa} \sim \dot{\mathcal{A}}_{sf}$). But, after these initial transients, the rate of change in the surroundings-film interface area dominates ($\dot{\mathcal{A}}_{sf} \gg \dot{\mathcal{A}}_{sa}$). Therefore, even for the three-phase configuration, in the steady state,

$$\dot{E}_\gamma \approx \gamma_{sf} \dot{\mathcal{A}}_{sf}. \quad (5.69)$$

As a result, we only need to evaluate $\dot{\mathcal{A}}_{sf}$ for developing a scaling for the rate of change of surface energy. For doing this, we use the analysis presented in [334], written in our notations as

$$\dot{\mathcal{A}}_{sf} = \int_{\mathcal{A}_{sf}} \kappa (\mathbf{U} \cdot \mathbf{n}) d\mathcal{A}_{sf} + \int_{\mathcal{C}} (\mathbf{U} \cdot \mathbf{m}) d\mathcal{C} \quad (5.70)$$

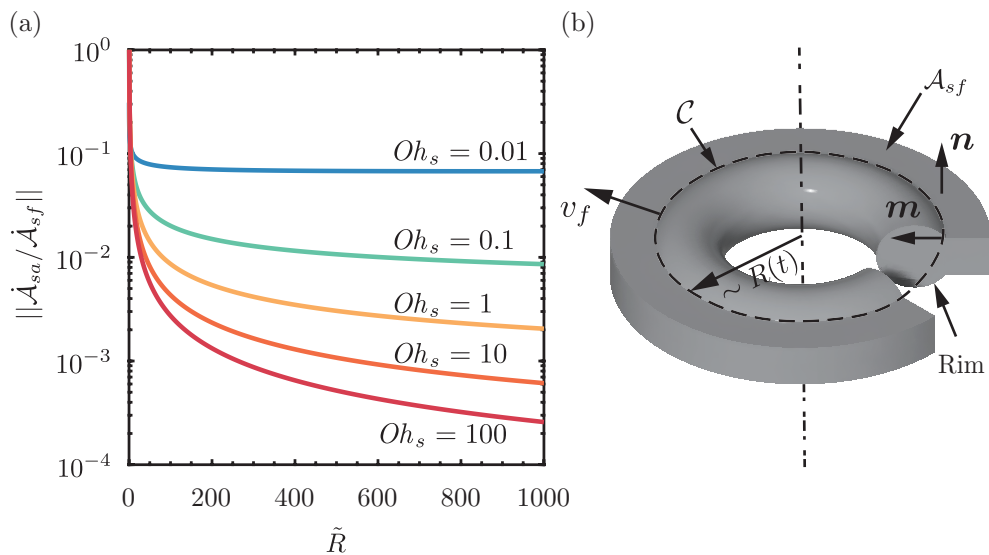


Figure 5.B.1: (a) Variation of the ratio of the magnitudes of the rate of change of surroundings-air interfacial area (\dot{A}_{sa}) to that of the surroundings-film (\dot{A}_{sf}) with the dimensionless hole radius $\tilde{R} = R/h_0$. (b) Schematic showing the control surface A_{sf} (free surface of the film without the rim) used for the calculation of the rate of change of surface energy.

for a control volume bounded by the control surface \mathcal{A}_{sf} (free surface of the film without the rim, figure 5.B.1b). Here, \mathbf{U} is the velocity of differential control volume bounded by $d\mathcal{A}_{sf}$, κ the curvature at this location, and \mathbf{n} is a unit vector normal to $d\mathcal{A}_{sf}$. Lastly, the control surface \mathcal{A}_{sf} is bounded by the contour \mathcal{C} , and \mathbf{m} is a unit vector perpendicular to this contour. Note that capillary traction acts perpendicular to \mathcal{C} away from the axis of symmetry. The first term on the right hand side of equation (5.70) accounts for the change in surface area due to inflation normal to \mathcal{A}_{sf} , and the second term is a consequence of the distortion of \mathcal{A}_{sf} in the tangential direction, i.e., stretching, or in this case, compression (the growing hole). With this choice of the control surface, the dilation normal to \mathcal{A}_{sf} is zero (area inflation only occurs at the rim which we ignore), and

$$\dot{\mathcal{A}}_{sf}(t) \approx \int_{\mathcal{C}(t)} (\mathbf{U} \cdot \mathbf{m}) d\mathcal{C} = -2v_f(2\pi R(t)), \quad (5.71)$$

where the factor 2 comes in because of the two surfaces (top and bottom). Therefore, for both the two-phase as well as three-phase Taylor-Culick retractions, the rate of injection of energy in the system is

$$-\dot{E}_\gamma(t) \approx 2\gamma_{sf} v_f(2\pi R(t)). \quad (5.72)$$

Note that while calculating the rate of change of surface energy, we did not account for the growth of the rim because it is much slower than the growth of the hole, and the flow is predominantly in the radial direction [see figures 5.4.3 and 5.4.4, and 336].

5.C Code availability

The codes used in the present article are permanently available at Sanjay [315].

5.D Supplemental movies

These supplemental movies are available at Sanjay [[external YouTube link](#), 337].

SM1: Post-rupture retraction of a water film in a three-phase Taylor-Culick configuration for different viscosities of the surroundings.

- SM2: Morphology of the flow at different Oh_s in the case of two-phase Taylor-Culick retractions. In this video, the left hand side contour shows the velocity magnitude normalized with the (terminal) film velocity v_f and the right hand side shows the dimensionless viscous dissipation function normalized using the inertio-capillary scales, represented on a \log_{10} scale to differentiate the regions of maximum dissipation.
- SM3: Morphology of the flow at different Oh_s in the case of three-phase Taylor-Culick retractions. In this video, the left hand side contour shows the velocity magnitude normalized with the (terminal) film velocity v_f and the right hand side shows the dimensionless viscous dissipation function normalized using the inertio-capillary scales, represented on a \log_{10} scale to differentiate the regions of maximum dissipation.
- SM4: Morphology of the flow for classical Taylor-Culick retractions. In this video, the left hand side contour shows the velocity magnitude normalized with the (terminal) film velocity v_f and the right hand side shows the dimensionless viscous dissipation function normalized using the inertio-capillary scales, represented on a \log_{10} scale to differentiate the regions of maximum dissipation.
- Bonus 1: Talk titled “Precursor films help simulate three-phase flows” delineating the precursor film-based three-fluid volume of fluid method.
- Bonus 2-3: Conference (APS-DFD 2021) talks titled “Viscous dissipation dictates Taylor-Culick type retractions” and “Revisiting Taylor-Culick retractions” presenting the results from this chapter.

chapter 5: Taylor-Culick retractions and
the influence of the surroundings



source code



supplemental movies

Chapter 6

Bursting bubbles in a viscoplastic medium^o

When a rising bubble in a Newtonian liquid reaches the liquid-air interface, it can burst, leading to the formation of capillary waves and a jet on the surface. Here, we numerically study this phenomenon in a yield stress fluid. We show how viscoplasticity controls the fate of these capillary waves and their interaction at the bottom of the cavity. Unlike Newtonian liquids, the free-surface converges to a non-flat final equilibrium shape once the driving stresses inside the pool fall below the yield stress. Details of the dynamics, including the flow's energy budgets, are discussed. The work culminates in a regime map with four main regimes with different characteristic behaviours.

^oPublished as: **Vatsal Sanjay**, Detlef Lohse, and Maziyar Jalaal, *Bursting bubbles in a viscoplastic medium*, J. Fluid Mech. **922**, A2 (2021). Simulations and analysis are done by Sanjay; writing by Sanjay and Jalaal; and supervision by Lohse and Jalaal. Proofread by everyone.

6.1 Introduction

Bubble bursting processes abound in nature and technology and have been studied for long in fluid mechanics [338]. For example, they play a vital role in transporting aromatics from champagne [85, 104–106], and pathogens from contaminated water [263, 339]. The process is also responsible for forming sea spray due to ejecting myriads of droplets [340, 341]. Bursting bubbles also play an important role in geophysical phenomena such as volcanic eruptions [342].

In Newtonian liquids, the bubble bursting mechanism is controlled by buoyancy, surface tension, and viscosity. First, the air bubble (figure 6.1.1a) being lighter than the surrounding medium, rises and approaches the liquid-air interface (figure 6.1.1b). The thin film between the bubble and the free-surface then gradually drains [343, 344] and eventually ruptures, resulting in an open cavity (figure 6.1.1c, [100]).

The collapse of this cavity leads to a series of rich dynamical processes that involve flow focusing owing to capillary waves [101, 102] and may lead to the formation of Worthington jet [103]. A perfect flow focusing can also result in an ultra-thin and fast singular jet. We investigated one such manifestation in chapter 1 where this singular jet was responsible for strong normal reaction forces during drop impact on a non-wetting substrates [also see 44, 178].

Furthermore, in some cases, the jet might break via a Rayleigh-Plateau instability, forming droplets [106, 345]. Walls et al. [346] studied how gravity and viscosity conspire to inhibit this breakup. This phenomenon of cavity collapse and Worthington jet formation is so robust that it even occurs in soft granular matter, when a rising bubble also bursts at the surface, leading to a granular jet [139].

The earlier work on bursting bubbles used boundary integral methods in an inviscid limit [347, 348]. However, the progress in the direct numerical simulation (DNS) tools for multiphase flows [2, 156, 158, 349] has resulted in models that consider the effects of viscosity. In fact, some recent studies revealed how liquid's viscosity affects the dynamics of the bursting bubbles [103, 108].

For Newtonian liquids, Deike et al. [108] have provided quantitative cross-validation of the numerical and experimental studies. They have also given a complete quantitative description of the influence of viscosity, gravity, and capillarity on the process, extending the earlier work of Duchemin et al. [102]. More recently, the experiments and simulations are complemented by theoreti-

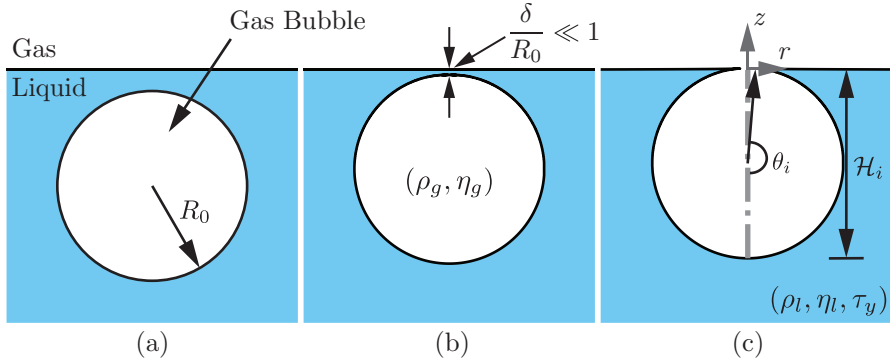


Figure 6.1.1: Schematics for the process of a bursting bubble: (a) A gas bubble in bulk. (b) The bubble approaches the free-surface forming a liquid film (thickness δ) between itself and the free-surface. (c) A bubble cavity forms when the thin liquid film disappears.

cal frameworks [103, 107], resulting in a profound understanding of the physics of bubble bursting in Newtonian fluids. Appendix 6.B provides more details on the previous studies in the Newtonian limit and compares our results with those available in the literature.

Notably, despite many applications, such as in the food industry and geophysics, the influence of rheological properties on the collapse of bubble cavities is yet to be understood. Here, we study the dynamics of bursting bubbles in a viscoplastic medium using direct numerical simulations (DNS). Viscoplastic or yield stress fluids manifest a mix of solid and fluid behavior. The materials behave more like an elastic solid below critical stress (yield stress); however, they flow like a viscous liquid above this critical stress. Readers can find detailed reviews on yield stress fluids in Balmforth et al. [86], Bird et al. [109], Coussot [110], Bonn et al. [111].

Previous experiments and simulations have studied trapped bubbles in a viscoplastic medium [350–352], rising bubbles in yield stress fluids [353–359], and bubbles moving inside tubes filled with viscoplastic fluids [360–362]. We will show that the introduction of non-Newtonian properties can significantly influence the bursting behavior of bubbles on a free-surface. At moderate values of yield stress, the collapse of the cavity can still lead to the formation of a Worthington jet, but the droplet formation might be suppressed. At high yield stress values, the unyielded region of the viscoplastic fluid can seize the collapse of this cavity, which leads to distinct final crater shapes.

The chapter is organized as follows: § 6.2 describes the problem and the

governing parameters. § 6.3 provides a phenomenological analysis, and § 6.4 presents the different modes of energy transfer during the viscoplastic bursting process. § 6.5 presents the final equilibrium shapes. The work culminates in § 6.6 where we summarize the different regimes observed in the process of bursting in a phase diagram. The chapter ends with conclusions in § 6.7.

6.2 Numerical framework & problem description

6.2.1 Governing equations

We consider the burst of a small axisymmetric bubble at a surface of an incompressible Bingham fluid. To nondimensionalise the governing equations, we remove the length and velocity scales using the initial bubble radius R_0 and inertia-capillary velocity $V_{\rho\gamma}$, scales, respectively. Pressure and stresses are scaled with the characteristic capillary pressure P_γ (see appendix 6.A). The dimensionless equations for mass and momentum conservation, for the liquid phase, then read (tildes denote dimensionless quantities throughout this chapter)

$$\tilde{\nabla} \cdot \tilde{\mathbf{v}} = 0, \quad (6.1)$$

$$\frac{\partial \tilde{\mathbf{v}}}{\partial \tilde{t}} + \tilde{\nabla} \cdot (\tilde{\mathbf{v}} \tilde{\mathbf{v}}) = -\tilde{\nabla} \tilde{p} + \tilde{\nabla} \cdot \tilde{\boldsymbol{\sigma}} - Bo \hat{\mathbf{e}}_z, \quad (6.2)$$

where \mathbf{v} is the velocity vector, t is time, p is the pressure and $\boldsymbol{\sigma}$ represents the deviatoric stress tensor. We use a regularized Bingham model with

$$\tilde{\boldsymbol{\sigma}} = 2 \min \left(\frac{\mathcal{J}}{2\|\tilde{\boldsymbol{\mathcal{D}}}\|} + Oh, Oh_{\max} \right) \tilde{\boldsymbol{\mathcal{D}}}, \quad (6.3)$$

where $\|\tilde{\boldsymbol{\mathcal{D}}}\|$ is the dimensionless second invariant of the deformation rate tensor, $\tilde{\boldsymbol{\mathcal{D}}} = \boldsymbol{\mathcal{D}}/(V_{\rho\gamma}/R_0)$, and Oh_{\max} is the viscous regularization parameter. The three dimensionless numbers controlling the equations above are the plastocapillary number (\mathcal{J}), which accounts for the competition between the capillary and yield stresses, the Ohnesorge number (Oh) that compares the inertio-capillary to inertio-viscous time scales, and the Bond number (Bo), which compares gravity and surface tension forces:

$$\mathcal{J} = \frac{\sigma_y R_0}{\gamma}, \quad Oh = \frac{\eta}{\sqrt{\rho_l \gamma R_0}}, \quad Bo = \frac{\rho_l g R_o^2}{\gamma}. \quad (6.4)$$

Here, γ is the liquid-gas surface tension coefficient, and σ_y and ρ_l are the liquid's yield stress and density, respectively. Next, η_l is the constant viscosity in the Bingham model. Note that in our simulations, we also solve the fluid's motion in the gas phase, using a similar set of equations (see appendix 6.A). Hence, the further relevant non-dimensional groups in addition to those in equation (6.4) are the ratios of density ($\rho_r = \rho_g/\rho_l$) and viscosity ($\eta_r = \eta_g/\eta_l$). In the present study, these ratios are kept fixed at 10^{-3} and 2×10^{-2} , respectively.

6.2.2 Method

For our calculations, we use the free software program Basilisk C [143, 161]. The code uses the volume of fluid (VoF) technique [2, 156] to track the interface, introducing a concentration field Ψ , that satisfies the scalar advection equation. Hence, equations (6.1) - (6.2) and their counterparts for the gas phase are solved using the one-fluid approximation, where the surface tension acts as a body force, $\tilde{\mathbf{f}}_\gamma$ only at the gas-liquid interface [157, 158]. In dimensionless form,

$$\tilde{\mathbf{f}}_\gamma = \tilde{\kappa} \tilde{\delta}_s \hat{\mathbf{n}} \approx \tilde{\kappa} \tilde{\nabla} \Psi, \quad (6.5)$$

where, δ_s is the interface Dirac function, $\hat{\mathbf{n}}$ is a unit vector normal to the interface [2], and κ is the curvature of the interface, $z = S(r)$, given by [363, p. 14-16] (in dimensionless form):

$$\tilde{\kappa} = R_0 \left(\frac{\frac{d^2 S}{dr^2}}{\left(1 + \left(\frac{dS}{dr}\right)^2\right)^{3/2}} + \frac{\frac{dS}{dr}}{r \left(1 + \left(\frac{dS}{dr}\right)^2\right)^{1/2}} \right). \quad (6.6)$$

In Basilisk C, the curvature in equation (6.6) is calculated using the height-function method. As the surface-tension scheme is explicit in time, the maximum time-step is maintained at most at the oscillation period of the smallest wave-length capillary wave [158, 159]. Note that the curvature above is, in fact, the dimensionless capillary pressure. Hence, in the text, the wave with the largest curvature is called the “strongest wave”.

Basilisk C also provides Adaptive Mesh Refinement (AMR). We use this feature to minimize errors in the VoF tracer (tolerance threshold: 10^{-3}) and interface curvature (tolerance threshold: 10^{-4}). Additionally, we also refine based on velocity (tolerance threshold: 10^{-2}) and vorticity (tolerance threshold: 10^{-3}) fields to accurately resolve the regions of low strain rates. For AMR,

we use a grid resolution such that the minimum cell size is $\Delta = R_0/512$, which implies that to get similar results, one will need 512 cells across the bubble radius while using uniform grids. We have also carried out extensive grid independence studies to ensure that changing the grid size does not influence the results. Moreover, we employ free-slip and no-penetration boundary conditions for both liquid and gas at the domain boundaries. For pressure, zero gradient condition is employed at the boundaries. For the cases where the Worthington jet breaks into droplets, an outflow boundary condition is employed at the top boundary to ensure that the drop does not bounce off the boundary. These boundaries are far away from the bubble (size of the domain is $8R_0$) such that they do not influence the process.

Note that our numerical method uses a regularized form of the Bingham constitutive equations (see equation (6.3) and appendix 6.A). Hence, we cannot resolve the exact position of the yield surface as $\|\tilde{\mathcal{D}}\|$ is never precisely zero. However, we can safely assume that low values of $\|\tilde{\mathcal{D}}\|$ will be associated with the plastic regions. In our simulations, $Oh_{\max} = 10^8$. We have ensured that our results are independent of this regularization parameter (appendix 6.E.1). The regularization of the constitutive model also forces us to choose a criterion for the stoppage time, t_s . In our simulations, we consider a significantly small cut-off kinetic energy to stop the simulations (see appendix 6.E.2 for details).

6.2.3 Initial Condition

This initial shape of a bubble at a fluid-fluid interface (figure 6.1.1b) can be calculated by solving the Young-Laplace equations to find the quasi-static equilibrium state for an arbitrary Bond number, Bo (see [84, 108, 346, 364]). As a starting point, this study only concerns the limit of $Bo \rightarrow 0$, i.e., when capillary effects dominate the gravitational ones. We choose $Bo = 10^{-3}$ for all the simulations in this work. For this value, the initial bubble is nearly spherical in a surrounding Newtonian liquid. Note that the bubble sphericity is a crucial assumption (simplification) in our work. The actual initial shape of the bubble depends on its size (Bo), material properties (\mathcal{J}, Oh), the method of generation, and its dynamics before approaching the interface [350, 357, 365]. Furthermore, for a bubble to rise in a viscoplastic medium, the buoyancy forces should be strong enough to yield the flow [86, 350, 353], i.e., $Bo \gg \mathcal{J}$. Hence, non-spherical and non-trivial shapes could be expected [355]. For such a limit, one should first solve the full dynamics of rising bubbles to achieve the correct initial condition for the bursting problem. Note that low Bo bubbles could still form near a free-surface in other situations. One example is the

process of Laser-Induced Forward Transfer (LIFT), in which a laser pulse generates a bubble near the free-surface of a viscoplastic liquid [366].

For our given initial shape, the value of \mathcal{J} varies between 0 and 64. This range is selected such that we will study a full range of yield stress effects, from the Newtonian limit ($\mathcal{J} = 0$) to a medium that barely deforms due to a large yield stress ($\mathcal{J} = 64$).

Following the common assumption in these types of problems [103, 108], we assume that the thin liquid cap of thickness δ (figure 6.1.1b) disappears at $t = 0$, resulting in the configuration shown in figure 6.1.1(c), i.e. the initial condition for our simulations. In figure 6.1.1(c), (r, z) denotes the radial and axial coordinate system. Furthermore, $\tilde{\mathcal{H}}_i = \mathcal{H}_i/R \approx 2$ is the initial bubble depth, and θ_i is the initial location of the cavity and free-surface intersection. Note that the curvature diverges at this intersection in such a configuration. We smooth the sharp edge using a small circular arc to circumvent this singularity, introducing a rim with a finite curvature κ_0 that connects the bubble to the free-surface. We ensured that the curvature of the rim is high enough such that the subsequent dynamics are independent of its finite value (for details, see appendix 6.E.3).

6.3 Effects of yield stress on the bursting bubble

6.3.1 Phenomenology

This section describes the dynamics of bursting bubbles and the qualitative effects of the plastocapillary number (\mathcal{J}). Figure 6.3.1 illustrates four representative cases for this purpose. For a Newtonian liquid (figure 6.3.1a, $\mathcal{J} = 0$), the retraction of the rim (see figure 6.3.1a: $\tilde{t} = 0.10$) leads to the formation of capillary waves.

Part of these waves travels away from the cavity, forming regions of small strain rates (black dots in figure 6.3.1a: $\tilde{t} = 0.45$), which are advected with the train of capillary waves. Meanwhile the other part of the waves travel down the cavity (figure 6.3.1a: $\tilde{t} = 0.1$) and focuses on the cavity's bottom (figure 6.3.1a: $\tilde{t} = 0.45$).

Consequently, a Worthington jet is formed as depicted in figure 6.3.1(a): $\tilde{t} = 0.65$. Furthermore, due to the conservation of momentum, a high-velocity jet is also formed opposite to this Worthington jet inside the liquid pool (figure 6.3.1a: $\tilde{t} = 0.65$), a reminiscent of the momentum jet that we investigated in chapter 1. The Worthington jet can then break into multiple droplets due

to the Rayleigh-Plateau instability [346]. In the Newtonian limit, the flow continues until the free-surface is fully flat, when the surface energy is minimized (figure 6.3.1a: $\tilde{t} = 4.00$).

The introduction of the yield stress, in general, slows down the flow due to a larger apparent viscosity. Remarkably, even at large yield stresses, the early time dynamics near the retracting rim remain unchanged due to the highly curved interface, as clearly shown in the first panels ($\tilde{t} = 0.1$) of figures 6.3.1. On the contrary, the anatomy of the flow inside the pool is considerably affected due to the yield stress. At low yield stresses ($\mathcal{J} = 0.1$ in figure 6.3.1b: $\tilde{t} = 0.1$), everywhere near the bubble cavity yields at early times. However, as the values of plastocapillary number increases, the size of the yielded region decreases ($\mathcal{J} = 0.5$ & $\mathcal{J} = 1.0$ in figures 6.3.1c and 6.3.1d, respectively).

Furthermore, at low values of \mathcal{J} , the flow focusing at the bottom of the cavity persists (figure 6.3.1b: $\tilde{t} = 0.50$), although, due to the increased dissipation, it is less vigorous. As a result, the jet formed post-collapse is thicker, slower, and less prominent (figure 6.3.1b: $\tilde{t} = 1.00$) as compared to the Newtonian case (figure 6.3.1a: $\tilde{t} = 0.65$). Notably, for small values of \mathcal{J} , the Worthington jet still forms and breaks up into droplets due to the Rayleigh-Plateau instability.

Note that unlike for the Newtonian case, where the final shape is always a flat free-surface, a viscoplastic medium (i.e., finite \mathcal{J}) comes to a halt when stress inside the liquid drops below the yield stress. Hence, the final state can feature non-zero surface energy (figure 6.3.1b: $\tilde{t} \geq 4.00$).

At higher values of \mathcal{J} , the capillary waves are so damped that flow focusing at the bottom of the cavity vanishes. At moderate \mathcal{J} (figure 6.3.1c where $\mathcal{J} = 0.5$), the capillary waves are still strong enough to travel over the entire cavity (figure 6.3.1c: $\tilde{t} = 0.25 - 0.80$). As a result, the entire cavity yields, nonetheless, the final shape still features a deep crater (figure 6.3.1c: $\tilde{t} = 1.60$).

On further increasing \mathcal{J} such that yield stress is as strong as the capillary stress ($\sigma_y \sim \gamma/R_0$, i.e., $\mathcal{J} \sim \mathcal{O}(1)$), the capillary waves do not yield the entire cavity (figure 6.3.1(c): $\tilde{t} = 0.25 - 0.75$). Hence, the final shape furnishes a deep crater that stores a large surface energy, contrary to the final shapes at small \mathcal{J} values.

In this section, we mainly focus on the effect of yield stress (via \mathcal{J}) on the process of bursting bubbles. Appendix 6.C contains the discussion on the effect of Oh . Furthermore, in the subsequent sections, we will discuss the features explained above in more quantitative details. § 6.3.2 and § 6.3.3 delineate the traveling capillary waves and the subsequent jet formation (or

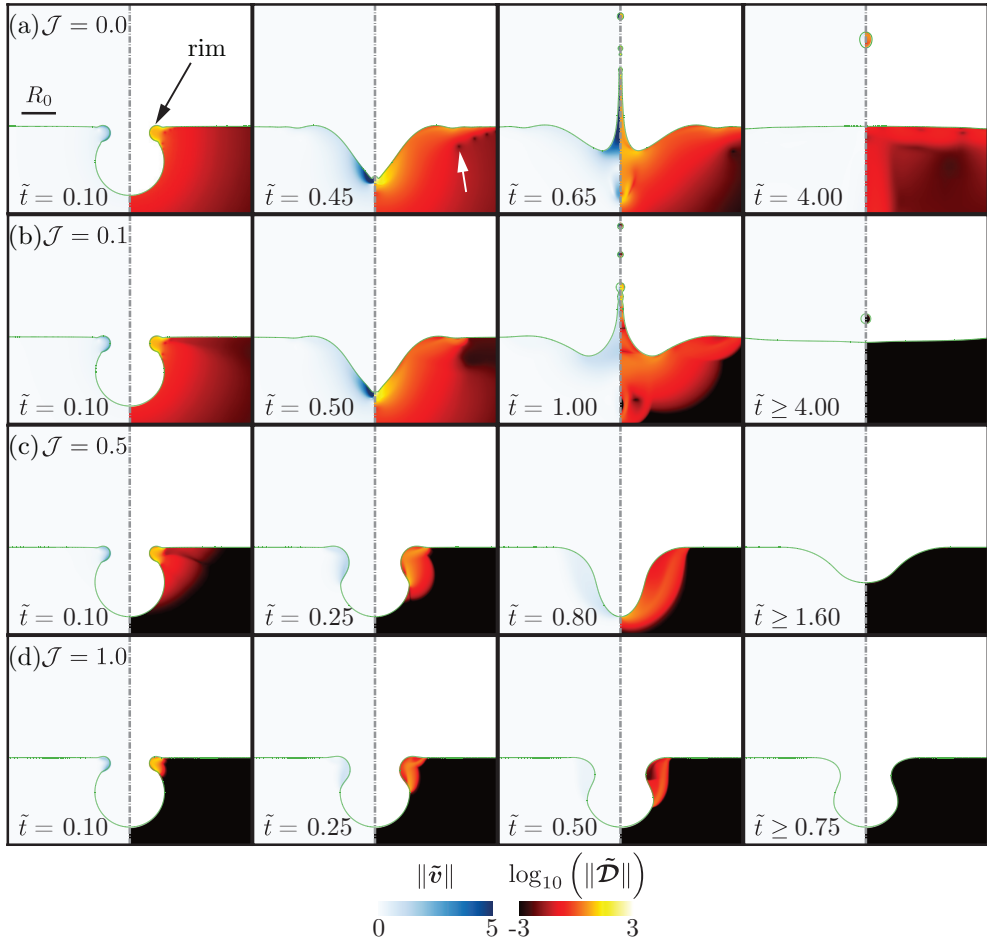


Figure 6.3.1: Bursting bubble dynamics for different plastocapillary numbers. (a) $\mathcal{J} = 0.0$: a typical case with a Newtonian liquid medium, (b) $\mathcal{J} = 0.1$: a weakly viscoplastic liquid medium in which the process still shows all the major characteristics of the Newtonian liquid, (c) $\mathcal{J} = 0.5$: a case of moderate yield stress whereby the jetting is suppressed, nonetheless the entire cavity still yields, and (d) $\mathcal{J} = 1.0$: a highly viscoplastic liquid medium whereby a part of the cavity never yields. The left part of each panel shows the magnitude of the velocity field, and the right part shows the magnitude of the deformation tensor on a \log_{10} scale. The transition to the black region (low strain rates) marks the yield-surface location in the present study. Here, time is normalized with the inertia-capillary time scale, $\tau_{\rho\gamma} = \sqrt{\rho_d R_0^3 / \gamma}$ and the time instances in this figure are chosen to show significant events throughout the process of bursting bubbles for different \mathcal{J} . For all the cases in this figure, $Oh = 10^{-2}$. Also see supplemental movies 1 – 4.

lack of it), respectively.

6.3.2 Capillary waves in the presence of yield stress

Capillary waves are critical in the bubble bursting process [103]. Initially, the breakage of the film and the retraction of the rim create a train of capillary waves of varying strengths [367]. However, sharper waves experience very high viscous dampening. As a result, the wave focusing and jet formation are controlled by the strongest wave, which is not ceased by viscous damping. We follow Gordillo and Rodríguez-Rodríguez [103] and track the strongest wave by chasing the maximum curvature of the free-surface wave ($\|\tilde{\kappa}_c\|$). The location of this wave, on the cavity, is denoted by the angular position, θ_c (see inset in figure 6.3.2a).

For a Newtonian liquid ($\mathcal{J} = 0$), at low Ohnesorge numbers (e.g., figure 6.3.2), the strongest capillary wave propagates at a constant velocity $V_{p\gamma}$, dashed line in figure 6.3.2a). The viscous stress attenuates these waves but does not influence θ_c . Previous studies [103, 368] have found similar results for Newtonian liquids (see appendix 6.B for more details). The strength of this wave decreases as it propagates down the cavity due to continuous viscous dissipation. Around $\theta_c \approx \pi/2$, the geometry changes leading to flow focusing resulting in an increase in the strength ($\tilde{\kappa}_c$) of the wave (see figure 6.3.2c: $\tilde{t} = 0.2$ to $\tilde{t} = 0.35$). This minimum value of $\|\tilde{\kappa}_c\|$ non-linearly depends on Oh (see Gordillo and Rodríguez-Rodríguez [103] & appendix 6.B for details).

As shown in figure 6.3.2(a,b) (and also discussed in § 6.3.1), the initial changes in $\|\theta_c\|$ and $\|\tilde{\kappa}_c\|$ remain similar to the Newtonian limit, since the highly curved region near the initial rim retraction fully yields the fluid around it. As the flow develops, the plasticity effects become more pronounced as compared to the capillary effects, and the capillary waves no longer follow the path taken by their Newtonian counterpart. The larger the value of \mathcal{J} , the sooner the dynamics of the capillary waves deviate from the Newtonian limit, and they become weaker. Eventually, the waves stop at a finite stoppage time, furnishing a finite final θ_c and $\|\tilde{\kappa}_c\|$ (represented by θ_f and $\|\tilde{\kappa}_f\|$, respectively). In section § 6.5, we will discuss the variation of these parameters for the final crater shapes.

6.3.3 Jet formation in the presence of yield stress

Another interesting feature of the bubble bursting process is the Worthington jet's formation as the bubble cavity collapses. To characterize this jet, we

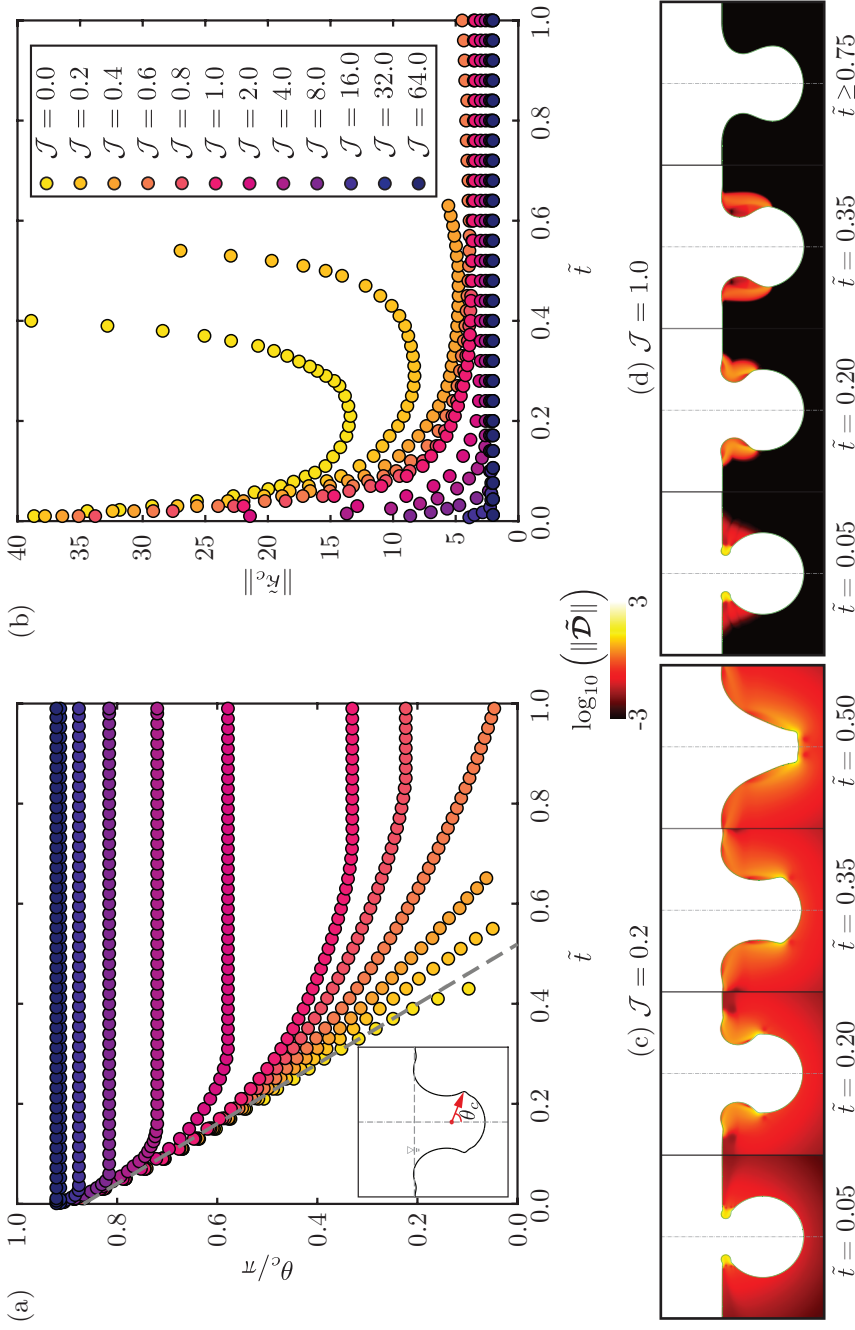


Figure 6.3.2: Effects of viscoplasticity on the traveling capillary waves. (a) Variation of the location (θ_c) of strongest capillary with time. The gray dotted line denotes the Newtonian limit, $\theta_c - \theta_i \sim -\tilde{t}$ as described by [103]. (b) Variation of the strength ($\|\tilde{\kappa}_c\|$) of the strongest capillary wave with time. Snapshots of the deformation tensor modulus $\|\tilde{\mathcal{D}}\|$ for $J = (c) 0.2$, and (d) 1.0. Here, time is normalized with the inertio-capillary time scale, $\tau_{\rho\gamma} = \sqrt{\rho_d R_0^3/\gamma}$. For all the cases in this figure, $Oh = 10^{-2}$. Also see supplemental movies 5 – 7.

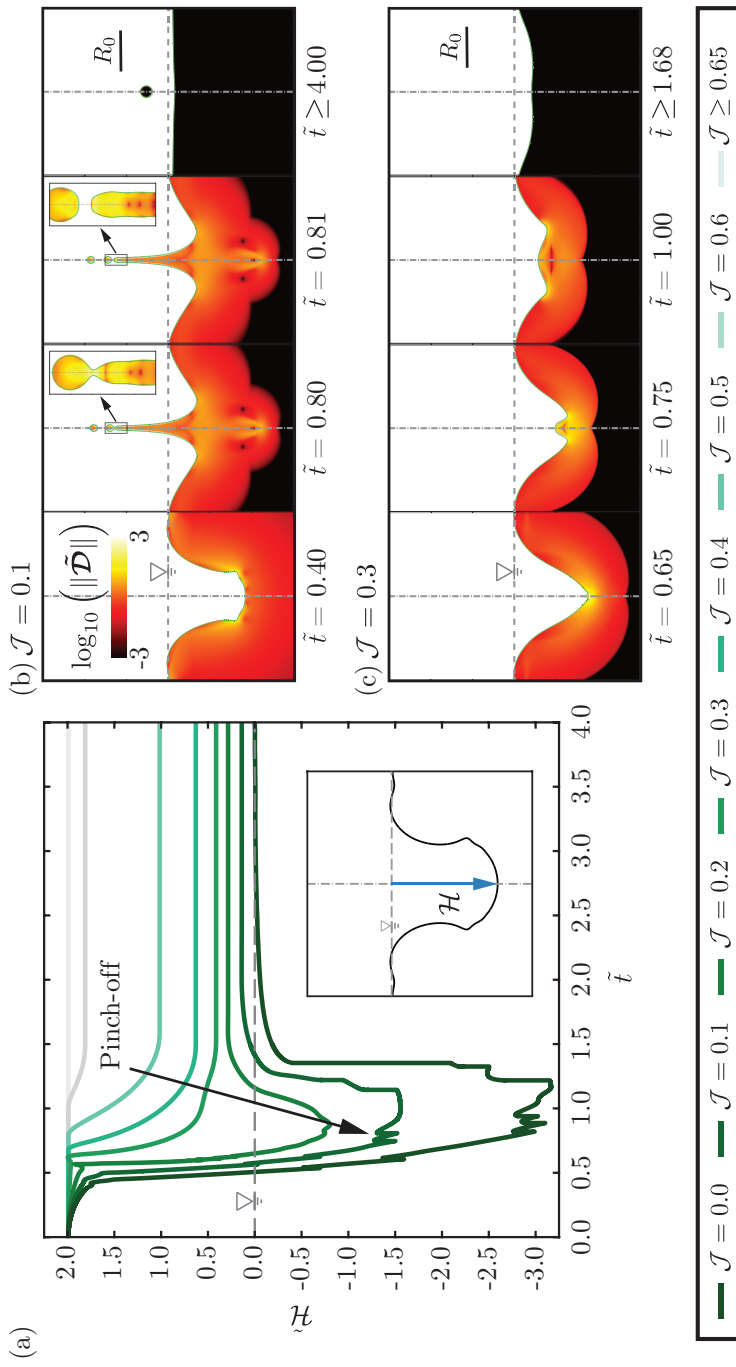


Figure 6.3.3: Effects of viscoplasticity on the formation of the jet as a result of the collapsing cavity: (a) Variation of the dimensionless depth $\tilde{\mathcal{H}} = \mathcal{H}/R_0$ of the cavity at its axis with time. The inset shows the definition of \mathcal{H} . Modulus of the deformation tensor $\|\tilde{\mathcal{D}}\|$ for the collapse of the bubble cavity and formation of the jet for $\mathcal{J} = (b) 0.1$ and (c) 0.3. Here, time is normalized with the inertio-capillary time scale, $\tau_{\rho\gamma} = \sqrt{\rho_d R_0^3/\gamma}$. Note that each kink in panel (a) is associated with the formation of a drop, as illustrated in the insets of the panel (b). For all the cases in this figure, $Oh = 10^{-2}$. See supplemental movies 8 – 10.

track the dimensionless location $(\tilde{\mathcal{H}} = \mathcal{H}/R_0)$ of the interface at the center $r = 0$. Figure 6.3.3(a) shows the temporal variation of $\tilde{\mathcal{H}}$ for different values of \mathcal{J} at fixed $Oh = 10^{-2}$. As the waves propagate, the cavity begins to collapse; hence the value of $\tilde{\mathcal{H}}$ decreases. A jet forms when the bottom of the cavity crosses the free-surface, and $\tilde{\mathcal{H}}$ becomes negative (see figure 6.3.3b). For small values of \mathcal{J} , the Rayleigh-Plateau instability and a subsequent pinch-off occur, resulting in the kinks shown in figure 6.3.3(a). The jets eventually retract, and $\tilde{\mathcal{H}}$ approaches 0, i.e., a flat final interface. As the value of \mathcal{J} increases, the final value of $\tilde{\mathcal{H}}$ increases, approaching the upper bound of $\tilde{\mathcal{H}} = \tilde{\mathcal{H}}_i = 2$, which is set by the initial condition (twice the bubble radius, i.e., the bottom of the cavity never yields). In fact, for $\mathcal{J} \geq 0.65$, this value remains unchanged, meaning the plug region attached to the bottom of the cavity never yields. Note that, in an intermediate range of $\mathcal{J} \approx 0.35$, the interplay of the capillary waves and the yield stress results in a dimple (underdeveloped jet) that never crosses the free-surface (see figure 6.3.3c).

6.4 What happens to the initial surface energy?

To better understand the bubble bursting dynamics in a viscoplastic medium, we also looked at the energy budgets. The total energy $\tilde{E} = E/(\gamma R_0^2)$ is the sum of the total kinetic energy of the liquid pool \tilde{E}_k , its surface energy \tilde{E}_s , and the energy dissipation \tilde{E}_d . The latter contains two parts due to viscous (\tilde{E}_d^{Oh}) and yield stress ($\tilde{E}_d^{\mathcal{J}}$) contributions, $\tilde{E}_d = \tilde{E}_d^{Oh} + \tilde{E}_d^{\mathcal{J}}$. Lastly, small energies associated with jet breakup and airflow are summarized in \tilde{E}_m . Hence,

$$\tilde{E}(\tilde{t}) = \tilde{E}_k(\tilde{t}) + \tilde{E}_s(\tilde{t}) + \tilde{E}_d(\tilde{t}) + \tilde{E}_m(\tilde{t}) = \tilde{E}_i, \quad (6.7)$$

where, \tilde{E}_i is the initial energy that is purely the surface energy. Readers are referred to appendix 6.D for details for calculating the energy budget.

Figure 6.4.1 shows three representative examples of these energy budgets, normalized by the initial energy E_i . In figure 6.4.1, the time is normalized by the stoppage time t_s . Panel (a) shows the temporal evolution of different modes of the energy transfer for a low \mathcal{J} . Initially, at $t = 0$, the system's total energy is stored as the bubble cavity's surface energy. As the flow starts, a part of this surface energy converts to the kinetic energy of the flow generated by the traveling capillary waves. The kinetic energy reaches a maximum when the capillary waves focus at the bottom of the cavity, as the focusing process forms a region of high velocity. At the instant of focusing, for $\mathcal{J} = 0.1$ & $Oh = 10^{-1}$,

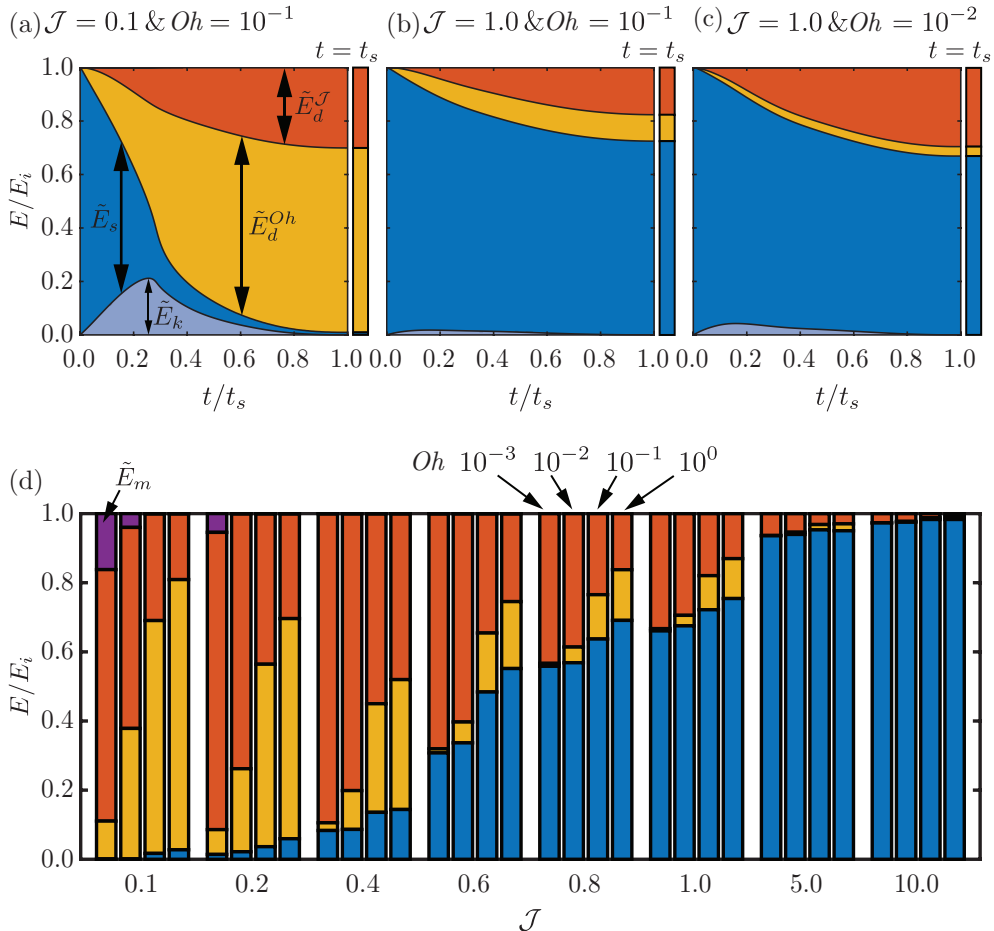


Figure 6.4.1: Energy budget for the process of the bubble bursting in a viscoplastic medium: Temporal evolution of the different modes of energy transfers for (a) $\mathcal{J} = 0.1$ & $Oh = 10^{-1}$, (b) $\mathcal{J} = 1.0$ & $Oh = 10^{-1}$, and (c) $\mathcal{J} = 1.0$ & $Oh = 10^{-2}$. (d) Comparison of the energy footprint at the stoppage time, $t = t_s$ for different \mathcal{J} and Oh .

$\approx 60\%$ of the initial energy is still present in the system as a sum of the kinetic and surface energy of the liquid pool. Subsequently, the Worthington jet forms and high dissipation is observed due to an increase in the strain rate (see equation (6.16)). The surface energy decreases monotonically throughout the process and reaches a finite near-zero value at the stoppage time t_s . This behavior is different from a Newtonian liquid, where the surface energy would become exactly zero, as $t \rightarrow \infty$.

For $\mathcal{J} = 1.0$ (figure 6.4.1b,c), initially, the surface energy decreases monotonically until it reaches a plateau at $t = t_s$. However, contrary to the example with a small value of \mathcal{J} , in these cases, a major part of the cavity never yields. Consequently, more than 70% for $Oh = 10^{-1}$ and over 60% for $Oh = 10^{-2}$ of the initial energy is still stored as the crater's surface energy. Also note that in the limit of large \mathcal{J} (and low Oh), yield stress is responsible for the majority of energy dissipation, i.e., $\tilde{E}_d^{Oh} \ll \tilde{E}_d^{\mathcal{J}}$.

The energy footprint at $t = t_s$ gives further insights into the bubble cavity's final static shape. Therefore, we compare these energies for different \mathcal{J} and Oh in figure 6.4.1(d). For all the conditions, $\tilde{E}_k \rightarrow 0$, and only surface energy remain in the system at the stoppage time. Rest of the energy $(\tilde{E}_i - \tilde{E}_s(t_s))$ features as dissipation (except for those cases where drops form and E_m is not negligible).

For low values of \mathcal{J} , the final surface energy \tilde{E}_s is close to zero because the final craters are shallow (see § 6.5 for details). This residual surface energy increases with increasing \mathcal{J} and Oh ; however, the dependency on Oh is negligible at higher values of \mathcal{J} . Lastly, the dissipation due to the yield stress $(\tilde{E}_d^{\mathcal{J}})$ contributes more to the overall dissipation for small Oh .

6.5 Final crater shapes

The process of bubble bursting in yield-stress fluids results in non-flat final shapes. Figure 6.5.1 shows the final crater shapes as observed for different \mathcal{J} and Oh , and figure 6.5.2 quantifies the different features of these final shapes by analyzing the location (θ_f) and strength ($\|\tilde{\kappa}_f\|$) of the strongest capillary wave, and the final depth of the crater ($\tilde{\mathcal{H}}_f$). For the convenience of comparison, we normalize $\tilde{\mathcal{H}}_f$ by its initial value $\tilde{\mathcal{H}}_i \approx 2$, and $\|\tilde{\kappa}_f\|$ by the initial curvature of the cavity's bottom $\|\tilde{\kappa}_i\| \approx 2$.

At low values of yield stress ($\mathcal{J} \leq 0.4$), the final shape of the crater strongly depends on Oh (see figures 6.5.1a,b, and 6.5.2a). When both \mathcal{J} & Oh are

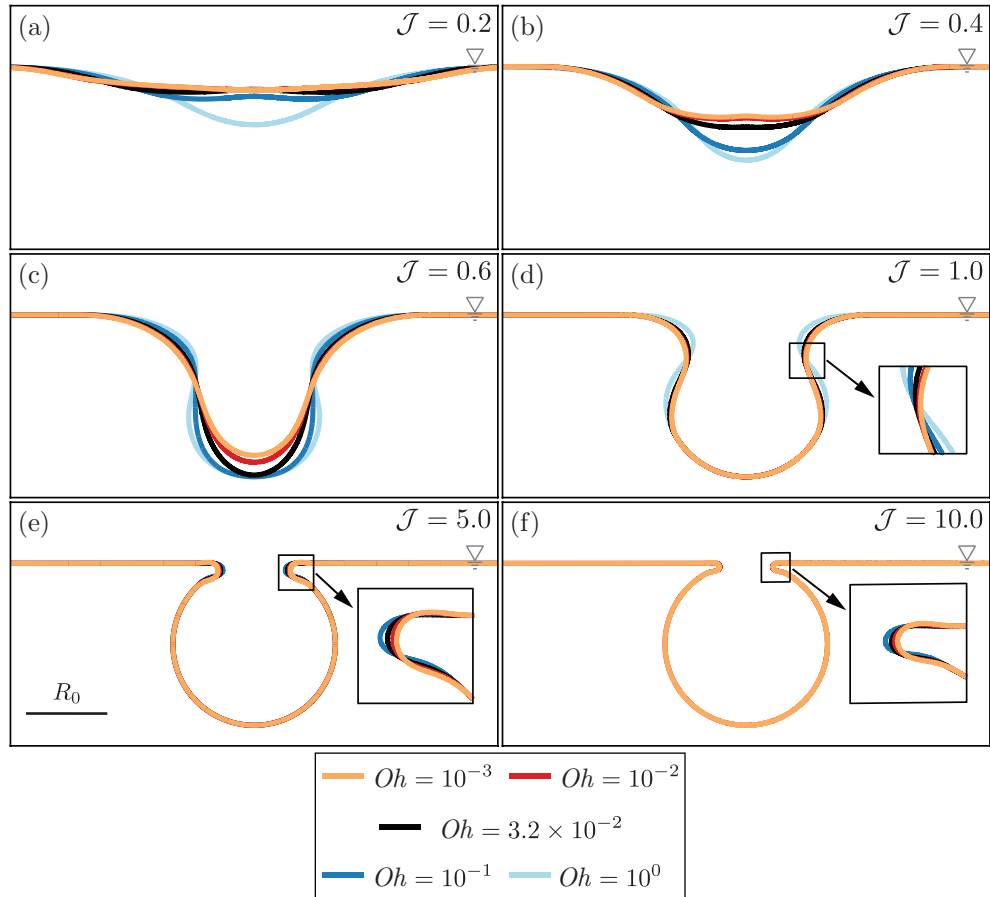


Figure 6.5.1: Final crater shapes: Variation of the final shapes with the Oh at $\mathcal{J} =$ (a) 0.2, (b) 0.4, (c) 0.6, (d) 1.0, (e) 5.0, and (f) 10.0.

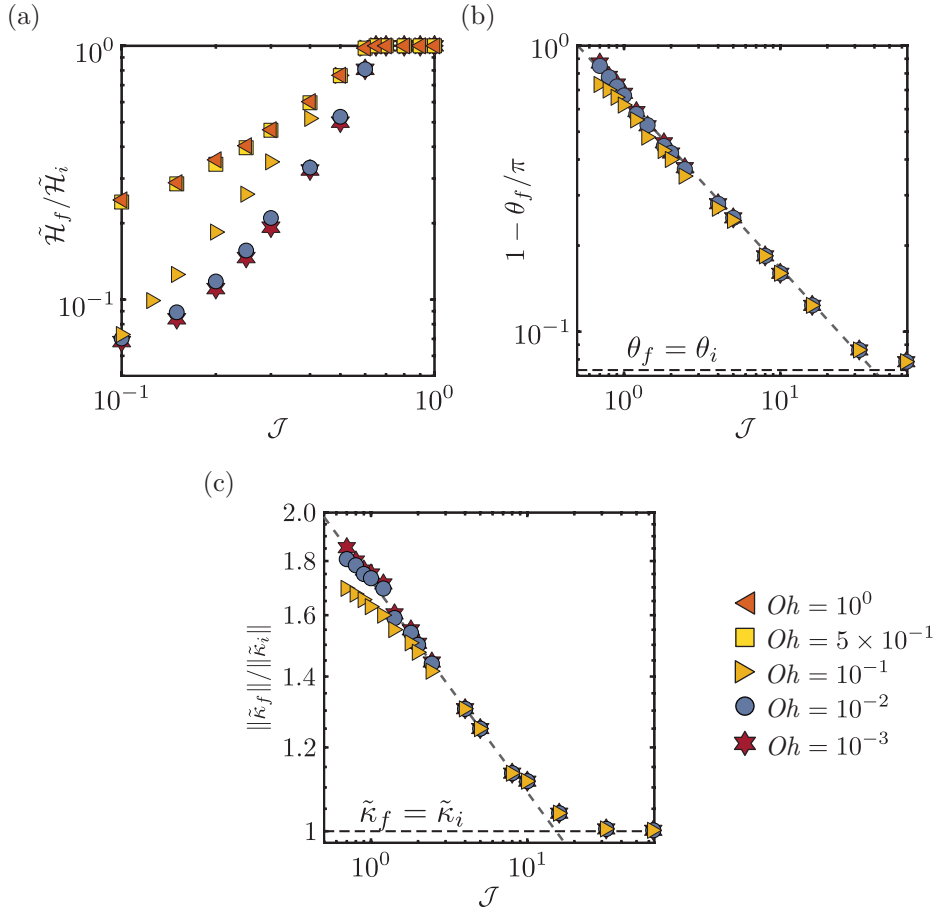


Figure 6.5.2: Quantifying the characteristics of the final shapes as a function of \mathcal{J} at different Oh : (a) Depth \mathcal{H}_f of centre-line of the final cavity surface. (b) Location θ_f and (c) Strength $\|\kappa_f\|$ of the strongest capillary wave in the final crater. The grey dashed lines in panels b and c are guides to the eye.

small, the Worthington jet forms (see § 6.3.3 for detailed discussions) which relaxes back towards the flat surface as $\tilde{t} \rightarrow \infty$. This jet relaxation results in shallow final cavities. As Oh increases, the viscous dissipation dominates the flow, the capillary waves are damped, and the change in the final cavity height becomes minimal; hence, $\tilde{\mathcal{H}}_f \approx \tilde{\mathcal{H}}_i$. In fact, for $Oh > 10^{-1}$, the capillary wave's amplitude is so close to zero that it becomes impossible to track.

As the value of yield stress (\mathcal{J}) increases, the effective viscosity of the flow increases and hence the initial cavity deforms less. For a highly plastic medium, the capillary waves cannot yield the entire cavity. As a result, $\tilde{\mathcal{H}}_f = \tilde{\mathcal{H}}_i$ for $\mathcal{J} \geq 0.65$, independent of the values of Oh . For higher Oh , this transition is reached (marginally) earlier (e.g., $\mathcal{J} \geq 0.5$ for $Oh \geq 1.0$).

For the cases where the bottom of the cavity never yields (figure 6.5.1d,e,f), we characterize the final crater shapes based on the location and strength of the frozen capillary wave (θ_f and $\tilde{\kappa}_f$, respectively). The variations of these values are shown in figure 6.5.2(b,c). As \mathcal{J} increases, the final location of the wave is closer to the initial value, $\theta_f \approx \theta_i$. Similarly, the strength of the final wave approaches the value defined by the initial condition, as \mathcal{J} increases. For this regime, the effects of Oh on the final shape seem to be negligible for $\mathcal{J} > 2$.

6.6 Regime map

In the present study, the two crucial control parameters to describe the process of bursting bubbles in a viscoplastic medium are the plastocapillary number \mathcal{J} , and the Ohnesorge number Oh . This section uses these dimensionless numbers to summarize the observed features explained in the text, providing a regime map (or phase diagram). Figure 6.6.1 shows this map for the bursting bubble process in a viscoplastic medium. Note that we have run more than 750 simulations to arrive at this regime map, but in figure 6.6.1 we only show a few representatives at the transition lines.

For Newtonian fluids, the previous studies have found that for $Oh > 0.03$, viscous stresses dominate over the surface tension, such that the Worthington jet does not break up into droplets [106, 346, 369]. In this work, at $\mathcal{J} = 0$, we have reproduced this transition Oh (see left axis in figure 6.6.1). Increasing \mathcal{J} has a similar effect on the jet breakup as it manifests itself as increased apparent viscosity of the liquid. Consequently, even when $Oh \rightarrow 0$ the capillary waves get severely damped for $\mathcal{J} > 0.3$, and no droplets are formed. The blue area in figure 6.6.1 highlights the region in which a Worthington jet forms and

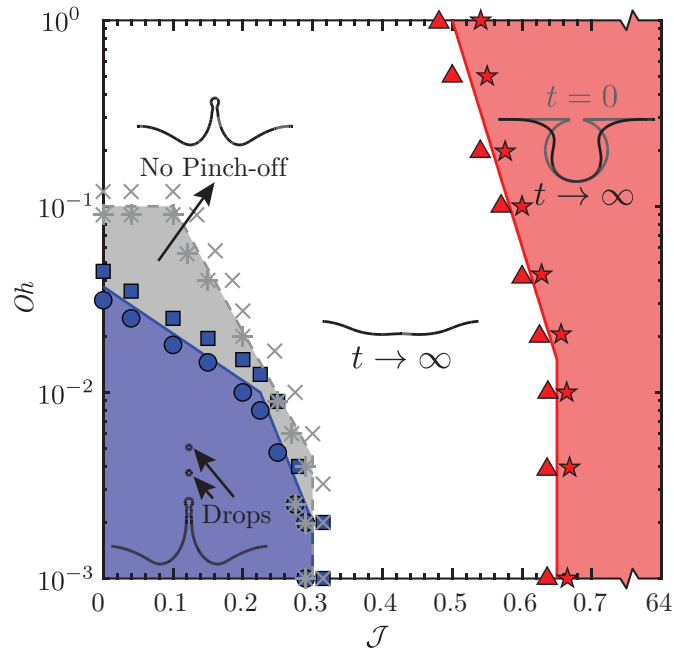


Figure 6.6.1: Regime map in terms of the plastocapillary number \mathcal{J} and the Ohnesorge number Oh showing the transitions between the different categories identified in the current study. The insets show a representative case from each of the four regimes, namely formation of jet which breaks into droplets (blue), formation of jet without droplets (gray), the entire cavity collapses but the cavity center never crosses the initial pool free-surface (white), and a part of the cavity never yields (red). The symbols represent simulations at the different transition lines.

disintegrates.

The gray area in figure 6.6.1 shows an intermediate regime in which the jet forms and crosses the free-surface line ($z = 0$) but does not breakup. This transition, for $\mathcal{J} = 0$, occurs at $Oh \approx 10^{-1}$. For non-zero \mathcal{J} , the transition occurs at smaller values of Oh as the jet (if it forms) has less kinetic energy and cannot cross the $z = 0$ line. If the jet does not form (beyond the grey area), the collapse of the cavity results in a crater (for $\mathcal{J} \neq 0$).

As discussed in § 6.3.2, if the surface tension stresses are high enough, the whole cavity yields. Otherwise, for large values of the yield stress ($\mathcal{J} \sim \mathcal{O}(1)$), the plug region attached to the bottom of the cavity never yields. As a result, the bottom of the cavity does not move, i.e., $\tilde{\mathcal{H}}_f = \tilde{\mathcal{H}}_i$. This transition from a fully yielded cavity to the cavity with an unyielded bottom is highlighted in figure 6.6.1 with the red line.

6.7 Conclusions and outlook

In this work, we have studied the capillary-driven process of bursting bubbles in a viscoplastic medium. Like in Newtonian fluids, flow begins when the rim, which connects the bubble cavity to the free-surface. Consequently, the fluid is yielded, and a train of capillary waves is generated. The yield stress significantly affects the flow structure inside the pool by making plug regions. The higher the value of the yield stress, the larger the deviation from the Newtonian counterpart is.

Following the analyses of Deike et al. [108] and Gordillo and Rodríguez-Rodríguez [103], we provided information on the dynamics of the capillary waves as they travel down the bubble cavity. In liquids with low yield stresses, the cavity collapse leads to a Worthington jet that might break up into drops by a Rayleigh-Plateau instability. However, for liquids with a large yield stress, the jet vanishes. The energy budgets analysis gives insight into the dynamics by showing how the initial surface energy is dissipated. Eventually, in contrast to the Newtonian fluids, where the final state is always a flat film, bubble bursting in viscoplastic medium results in final crater shapes with high residual surface energy. We analysed the geometry of these shapes as a function of the governing control parameters, namely the Ohnesorge and the plastocapillary numbers. Lastly, we use the same numbers to categorise the four different regimes in viscoplastic bubble bursting (see the phase diagram in figure 6.6.1).

Our study has direct applications in a range of industrial operations, where

bubbles are present at the surface of a yield stress fluids. The focus of this work is to compare the bursting bubble process in a yield stress fluid to that in a Newtonian fluid, without the initial shape effects. However, once the exact shape of the bubble at the free-surface is known, either from experiments or theory, one can calculate the resulting flow and compare them to the present study. Moreover, the current results could be useful in analysing some geo-physical flows, such as those in volcanic eruptions. In a broader perspective, the work presents a system in which surface tension and yield stress are the main factors. Such a system is of fundamental interest in design and manufacturing at small scales when capillary action is competing with the yield stress, e.g., in 3D printing and coatings polymeric fluids [366, 370–372].

Acknowledgments

We thank Andrea Prosperetti, Arup Kumar Das and Stéphane Zaleski for insightful discussions about the Newtonian limit of the bursting-bubble process. We also want to thank Uddalok Sen, Rodrigo Ezeta and Carola Seyfert for comments on the manuscript.

Appendix

6.A Governing equations

In this appendix, we describe the governing equations that describe the process of bursting bubbles in a viscoplastic medium. For an incompressible liquid, the continuity and momentum equations read

$$\nabla \cdot \mathbf{v} = 0, \quad (6.8)$$

$$\frac{\partial(\rho_l \mathbf{v})}{\partial t} + \nabla \cdot (\rho_l \mathbf{v} \mathbf{v}) = -\nabla p + \nabla \cdot \boldsymbol{\sigma} + \rho_l \mathbf{g}, \quad (6.9)$$

where \mathbf{v} is the velocity vector, ρ_l is the density of the liquid, p is the pressure field, $\boldsymbol{\sigma}$ is the stress tensor in liquid, and \mathbf{g} is the acceleration due to gravity. We model the viscoplastic liquid medium as a non-Newtonian Bingham fluid with a yield stress, σ_y . For such liquids, the constitutive equation are

$$\begin{cases} \mathcal{D} = 0 & \|\boldsymbol{\sigma}\| < \sigma_y \\ \boldsymbol{\sigma} = 2 \left(\frac{\sigma_y}{2\|\mathcal{D}\|} + \eta_l \right) \mathcal{D} & \|\boldsymbol{\sigma}\| \geq \sigma_y \end{cases} \quad (6.10)$$

In the equation above, $\mathcal{D} = (\nabla \mathbf{v} + (\nabla \mathbf{v})^T)/2$ is the deformation tensor and η_l the constant viscosity in the Bingham model. We adopt a regularised revision of equation (6.10) in our numerical simulations, given by:

$$\boldsymbol{\sigma} = 2 \min \left(\frac{\sigma_y}{2\|\mathcal{D}\|} + \eta_l, \eta_{max} \right) \mathcal{D} \quad (6.11)$$

In equation (6.11), $\sigma_y/(2\|\mathcal{D}\|) + \eta_l$ is essentially the apparent viscosity (η_{eff}) of the liquid and η_{max} is the “large” regularization viscosity, such that $\eta_{eff} \leftarrow \min(\eta_{eff}, \eta_{max})$.

The same sets of mass and momentum conservation equations (6.8) – (6.9) are also solved for the gas phase, but now with constant density and viscosity. We use the inertia-capillary velocity ($V_{\rho\gamma}$) and inertia-capillary time $\tau_{\rho\gamma}$, and the capillary stress P_γ defined as

$$V_{\rho\gamma} = \sqrt{\frac{\gamma}{\rho_l R_0}}, \quad \tau_{\rho\gamma} = \frac{R_0}{V_{\rho\gamma}} = \sqrt{\frac{\rho_l R_0^3}{\gamma}}, \quad (6.12)$$

$$P_\gamma = \frac{\gamma}{R_0}, \quad (6.13)$$

to non-dimensionalize above governing equations to find equations (6.1) to (6.4).

6.B The Newtonian limit

One of the essential and widely studied features of the bursting bubble process in a Newtonian liquid is the resulting Worthington jet's velocity. This jet is formed because of the strong flow-focusing caused by the capillary waves at the bubble cavity's bottom. In general, this process is very fast, as shown in figure 6.B.1(a). Over a small time span of $\approx 0.1\tau_{\rho\gamma}$ (see insets of figure 6.B.1), the jet traverses a distance of $\approx 1.5R_0$. Moreover, the inception of this jet is characterized by velocities as high as $50V_{\rho\gamma}$. This jet's flow is also associated with high viscous dissipation (because of the high strain rates resulting from such high velocities). As a result of these two processes, there is a distinct maximum at the instant of jet inception ($v_{j,1}$). This velocity could be difficult to calculate, especially at low Oh because of high-frequency capillary waves. Numerically, it is easiest to calculate the velocity of the jet as it crosses the free-surface, $z = 0$ (grey dotted line in figure 6.B.1a). However, in experiments, it is easier to calculate the velocity of the first droplet that forms as a result of the jet breakup. In the inset of figure 6.B.1(a), the instant immediately before jet breakup into a droplet gives a velocity of $v_{j,3}$. As a result, in the literature, different authors have reported different jet velocities. We have decided to plot all three velocities (wherever applicable) in figure 6.B.1(b) along with the scaling laws proposed by Deike et al. [108] (grey line) and Gordillo and Rodríguez-Rodríguez [103] (green, magenta, and purple lines). Our results agree well with the previously published works, which have been extensively validated with experimental data. Note that the differences between our data points and those of Gordillo and Rodríguez-Rodríguez [103] also arise because of a slight difference in Bond numbers for the two studies ($Bo = 5 \times 10^{-2}$ in

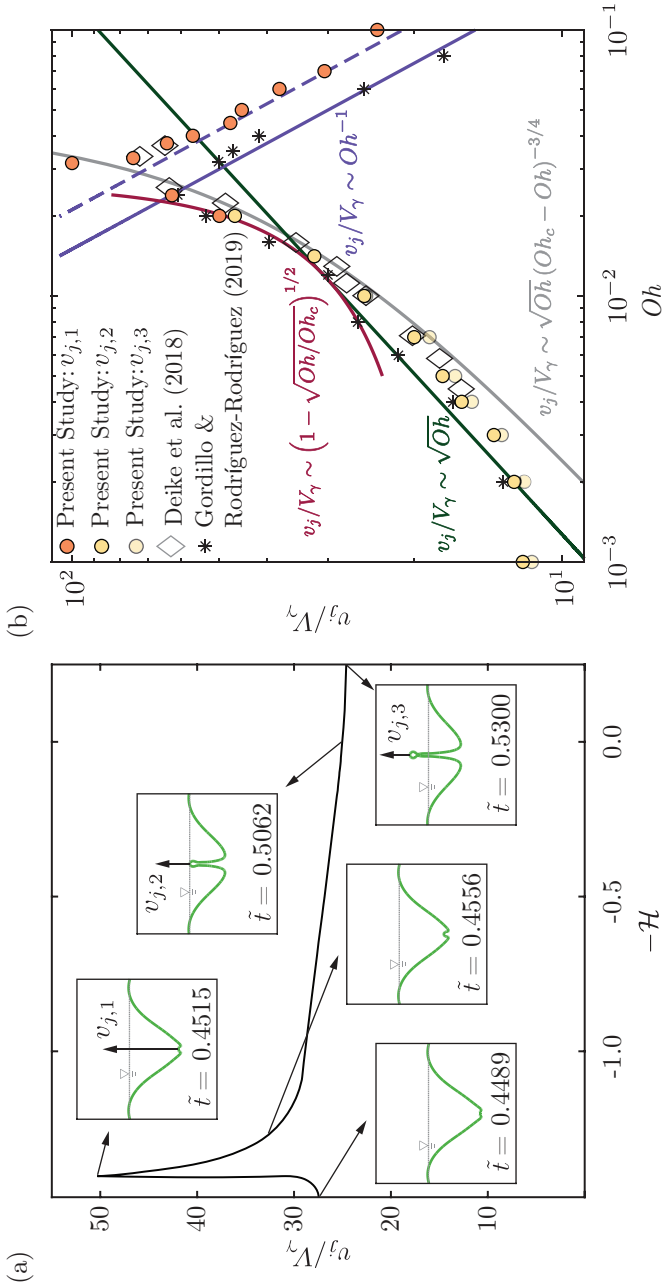


Figure 6.B.1: Characterization of the Worthington jet's velocity formed as a result of the bursting bubble process in Newtonian liquids: (a) Variation of the jet's velocity as it travels through different axial locations ($Oh = 10^{-2}$). The inset shows the shape of this jet at different time. The grey dotted line represents the free-surface, $z = 0$. (b) Comparison of the jet's velocity with the data and scaling laws available in the literature for the range of Ohnesorge numbers used in this study. Note that the scaling law in solid black line comes from Deike et al. [108], whereas the other lines are from Gordillo and Rodríguez-Rodríguez [103] as noted in the figure.

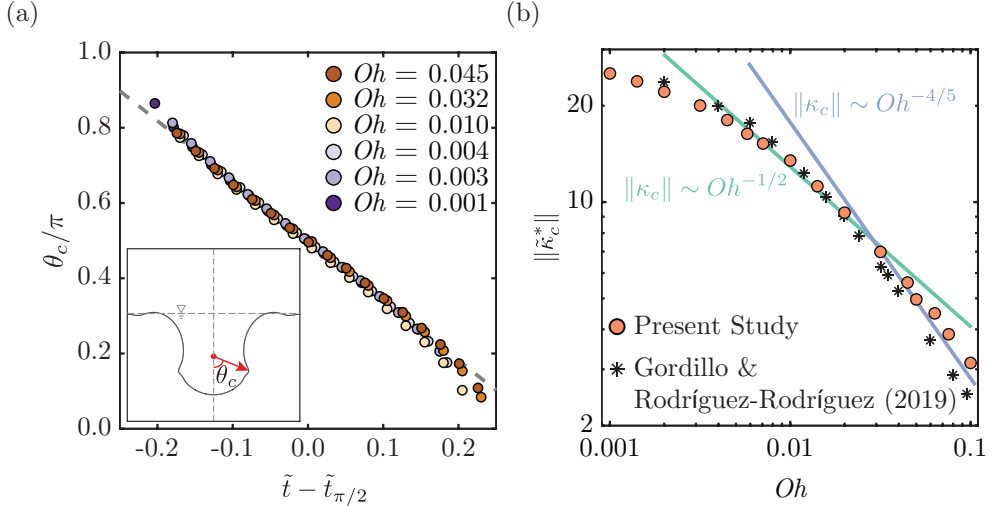


Figure 6.B.2: (a) Variation of the location θ_c of the strongest capillary wave with time. The gray dotted line denotes $\theta_c - \theta_i \sim -\tilde{t}$ as described by [103]. Here, time is normalized with the inertio-capillary time scale, $\tau_{\rho\gamma} = \sqrt{\rho_d R_0^3}/\gamma$. (b) Variation of the strength $\|\tilde{\kappa}_c^*\|$ at $\theta_c = \pi/2$ with the Oh . The scaling laws are taken from Gordillo and Rodríguez-Rodríguez [103].

Gordillo and Rodríguez-Rodríguez [103] as compared to $Bo = 10^{-3}$ in Deike et al. [108] and in the present work). This disagreement is higher for high Oh . Furthermore, as pointed out by Deike et al. [108], at lower Bo , the maxima in the $v_j - Oh$ plot shifts to the right with higher velocities, a feature which is distinctly captured by figure 6.B.1(b).

Figure 6.B.2(a) shows the temporal evolution of the angular trajectory of the strongest capillary wave as it travels down the bubble cavity. As predicted by Gordillo and Rodríguez-Rodríguez [103] and shown experimentally by Krishnan et al. [368], this wave travels at a constant angular velocity, implying $\theta_c - \theta_i \sim -t/\tau_{\rho\gamma}$ (gray dotted line in figure 6.B.2a). Furthermore, we also compare the strength of this wave with those predicted by the scaling laws given in Gordillo and Rodríguez-Rodríguez [103] and found good agreement (figure 6.B.2b).

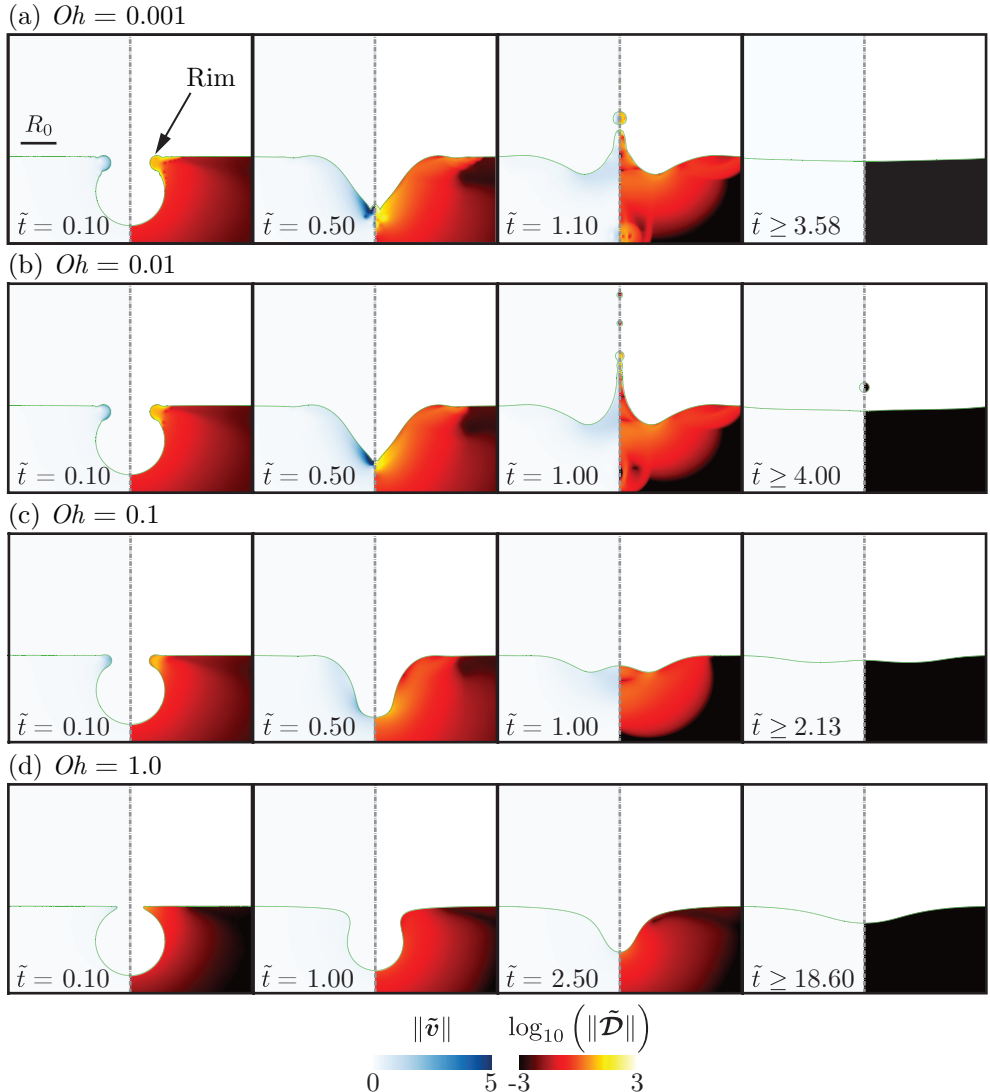


Figure 6.C.1: Bursting bubble dynamics for different Ohnesorge numbers: (a) $Oh = 10^{-3}$, (b) $Oh = 10^{-2}$, (c) $Oh = 10^{-1}$, and (d) $Oh = 10^0$. Here, time is normalized with the inertia-capillary time scale, $\tau_{\rho\gamma} = \sqrt{\rho_d R_0^3 / \gamma}$. In the background, the left part of each panel shows the magnitude of the velocity field and the right part shows the deformation tensor's magnitude on a \log_{10} scale. For all the cases in this figure, $\mathcal{J} = 0.1$. Also see supplemental movies 2, 11 – 13.

6.C The effect of the Ohnesorge number, Oh

This appendix describes the dynamics of bursting bubbles and the qualitative effects of varying Ohnesorge number Oh at given plastocapillary number of $\mathcal{J} = 0.1$. Figure 6.C.1 illustrates four representative cases for this purpose. As noted in the text and several previous studies [102, 103, 108], the initial retraction of the rim forms a train of capillary waves. For low Ohnesorge numbers, e.g., $Oh = 10^{-3}$ in figure 6.C.1(a), the viscous dissipation is very small, and as a result, most of these capillary waves converge at the bottom of the cavity and result in vigorous surface undulations at the cavity's bottom (figure 6.C.1a: $\tilde{t} = 0.1 - 0.50$). These waves result in a thick Worthington jet. As the Oh increases ($Oh = 10^{-2}$ in figure 6.C.1b), viscous dissipation damps the high-frequency capillary waves and improves the flow focusing at the cavity's bottom, leading to thinner and faster jets. This process is similar to what has been reported in the literature for Newtonian liquids [102, 106, 108]. Note that figure 6.C.1(b) is the same as figure 6.3.1(b) and has been presented again for completeness.

Larger Oh (10^{-1} & 10^0 in figures 6.C.1c and 6.C.1d, respectively), result in a longer flow time scales. Nonetheless, at low \mathcal{J} (such as 0.1 in figure 6.C.1), the entire cavity still yields and the center gently approaches the free-surface at $z = 0$ (figure 6.C.1b,c: first three columns). Most of the initial surface energy is lost as viscous dissipation (both \tilde{E}_d^{Oh} & $\tilde{E}_d^{\mathcal{J}}$) and the flow stops as the internal stresses in the fluid falls below the yield stress (figure 6.C.1b,c: last column).

6.D Energy budget calculations

Here, we describe the formulation used to evaluate the different energy transfer modes discussed in § 6.4. A similar approach has been used throughout this thesis to investigate bouncing and non-bouncing drops in Part I, and to demystify the role of viscous surroundings in Taylor-Culick retractions (chapter 5). In this chapter, we have extended the methodology to yield-stress liquids. The kinetic and the surface energy of the liquid are given by

$$\tilde{E}_k = \frac{1}{2} \int_{\tilde{\Omega}_p} \|\tilde{\mathbf{v}}\|^2 d\tilde{\Omega}_p, \quad (6.14)$$

$$\tilde{E}_s = \int_{\tilde{\Gamma}_p} d\tilde{\Gamma}_p, \quad (6.15)$$

where the energies are non-dimensionalized by the surface energy γR_0^2 . The integrals are evaluated over the volume $(\tilde{\Omega}_p)$ and the surface $(\tilde{\Gamma}_p)$ of the biggest liquid continuum in the domain, disregarding the drops (which are included in the energy budget in a different way described below). The state of liquid pool with a flat free-surface is taken as the reference to calculate \tilde{E}_s .

Extending the Newtonian fluid's formulation in Landau and Lifshitz [160, p. 50-51], the total dissipation in our system can be calculated as

$$\tilde{E}_d = 2 \int_{\tilde{t}} \left(\int_{\tilde{\Omega}_p} \left(Oh + \frac{\mathcal{J}}{2\|\tilde{\mathcal{D}}\|} \right) \|\tilde{\mathcal{D}}\|^2 d\tilde{\Omega}_p \right) d\tilde{t}. \quad (6.16)$$

Note that by writing the equation in this form, we assume that the yield stress contributes to the energy dissipation only through an increase in the effective viscosity (see appendix 6.A). In order to isolate the effects of the viscosity and yield-stress associated viscosity, we can rewrite equation (6.16) as $\tilde{E}_d = \tilde{E}_d^{Oh} + \tilde{E}_d^{\mathcal{J}}$, where

$$\tilde{E}_d^{Oh} = 2 Oh \int_{\tilde{t}} \left(\int_{\tilde{\Omega}_p} \|\tilde{\mathcal{D}}\|^2 d\tilde{\Omega}_p \right) d\tilde{t}, \quad (6.17)$$

$$\tilde{E}_d^{\mathcal{J}} = \mathcal{J} \int_{\tilde{t}} \left(\int_{\tilde{\Omega}_p} \|\tilde{\mathcal{D}}\| d\tilde{\Omega}_p \right) d\tilde{t}. \quad (6.18)$$

We present together all other forms of energy as

$$\tilde{E}_m = \tilde{E}_k^{\text{Drops}} + \tilde{E}_s^{\text{Drops}} + \tilde{E}_d^{\text{Drops}} + \int_{\tilde{\Omega}_p + \tilde{\Omega}_d} Bo \tilde{z} d(\tilde{\Omega}_p + \tilde{\Omega}_d) + \tilde{E}_g. \quad (6.19)$$

In equation (6.19), the first two terms, $\tilde{E}_k^{\text{Drops}}$ & $\tilde{E}_s^{\text{Drops}}$ denote the kinetic and the surface energies of the ejected drops, respectively. The third term, $\tilde{E}_d^{\text{Drops}}$, is the sum of the effective dissipation inside the drop. Note that all these three terms are evaluated like equations (6.14) to (6.18) with one difference that the volume and surface integrals are performed over the drops ($\tilde{\Omega}_d$ and $\tilde{\Gamma}_d$, respectively), instead of over the pool ($\tilde{\Omega}_p$ and $\tilde{\Gamma}_p$, respectively). The next term evaluates the gravitational potential energy for the liquid (both the pool and the drops). As $Bo \rightarrow 0$, this term is insignificant. Lastly, \tilde{E}_g denotes the sum of energies stored in the gas medium and viscous dissipation due to velocity gradients inside it:

$$\tilde{E}_g = \rho_r \int_{\tilde{\Omega}_g} \left(\frac{\|\tilde{\mathbf{v}}\|^2}{2} + Bo \tilde{z} \right) d\tilde{\Omega}_g + 2\eta_r Oh \int_{\tilde{t}} \left(\int_{\tilde{\Omega}_g} \|\tilde{\mathcal{D}}\|^2 d\tilde{\Omega}_g \right) d\tilde{t}. \quad (6.20)$$

\tilde{E}_m (equation (6.19)) is only significant when the resultant Worthington jet leads to the formation of droplets (figure 6.4.1c).

6.E Code availability & choosing numerical parameters

For our calculations, we use the free software program Basilisk C [143, 161]. To ensure reproducibility, the codes used in the present article are permanently available at Sanjay [373]. Furthermore, § 6.2 contains major computational choices and parameters employed in the current study. In this appendix, we provide further details and reasons for selecting the critical parameters in light of the regularization method.

6.E.1 Viscous regularization parameter

To verify that the macroscopic flow features were independent of the regularization parameter, we conducted simulations for different Oh_{\max} . We show a representative case for this test in figure 6.E.1. Using a small value of Oh_{\max} , such as 10^0 in figure 6.E.1(a - i), the process resembles a case with increased effective viscosity. However, at higher values of Oh_{\max} (10^4 for figure 6.E.1a - ii or 10^8 for figure 6.E.1a - iii), the process is independent of viscous regularization parameter. To ensure that the flow is captured precisely, the liquid kinetic energy is tracked over time as well (figure 6.E.1b). For $Oh_{\max} > 10^2$, there is negligible differences between the cases.

Comparing the values of $\|\tilde{\mathcal{D}}\|$, it is shown that the flow patterns are unchanged for a given large values of Oh_{\max} and once could clearly distinguish a sharp transition between a weakly deformed region and a strongly deformed one. That being said, we would like to mention that the identification of the yield surface is obscured, when regularized constitutive models are used (*cf.* [374]). Nevertheless, irrespective of such details, the map of the second invariant of the deformation rate tensor provides important information on flow patterns inside viscoplastic medium.

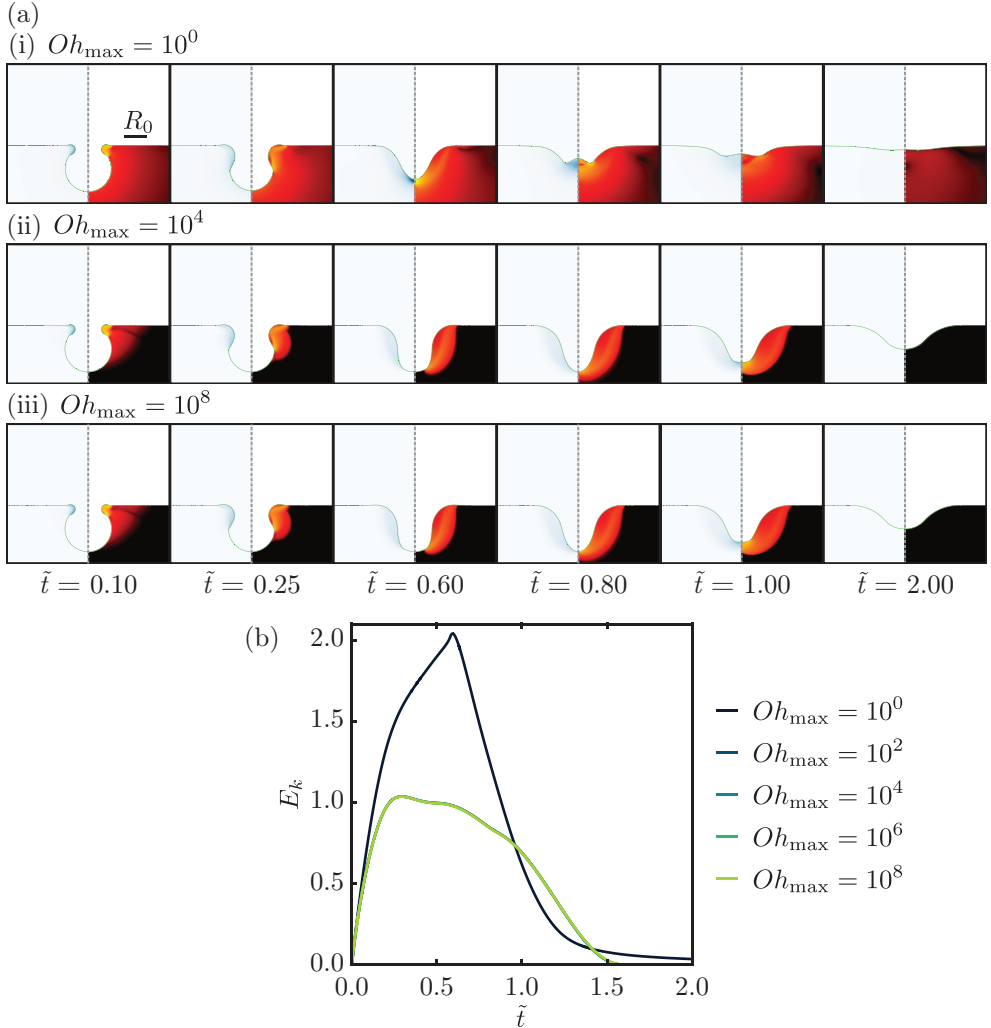


Figure 6.E.1: Sensitivity to viscous regularization parameter Oh_{\max} : Temporal evolution of the bubble cavity for (a) $Oh_{\max} =$ (i) 10^0 , (ii) 10^4 , and (iii) 10^8 , and (b) Kinetic energy evolution in time. Here, time is normalized with the inertio-capillary time scale, $\tau_{\rho\gamma} = \sqrt{\rho_d R_0^3 / \gamma}$. The results show negligible differences for $Oh_{\max} > 10^2$.

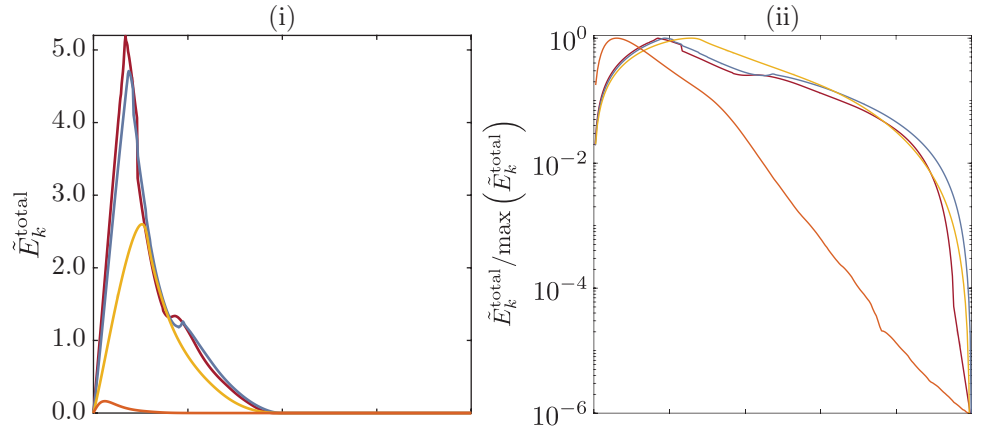
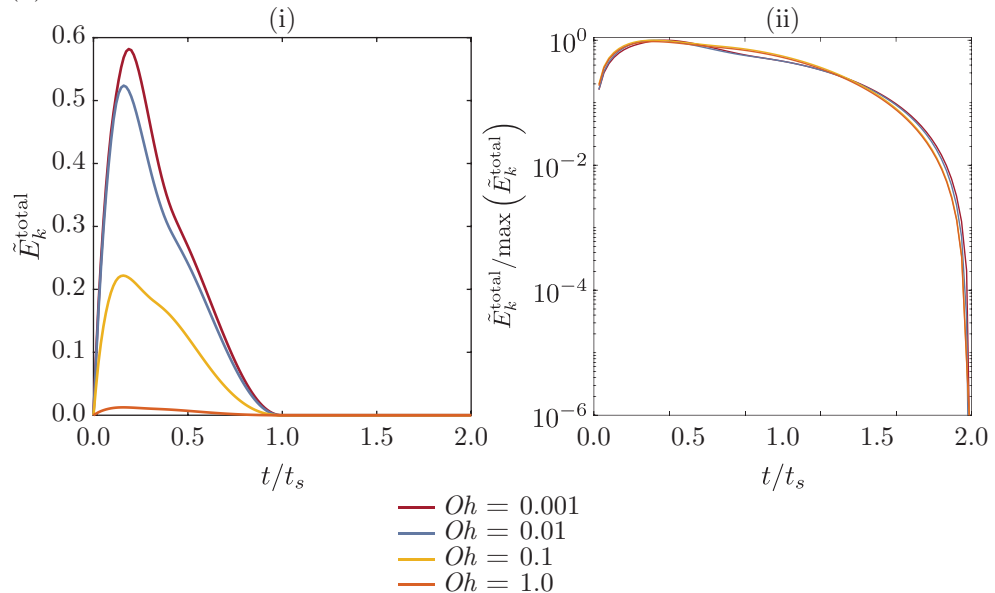
(a) $\mathcal{J} = 0.1$ (b) $\mathcal{J} = 1.0$ 

Figure 6.E.2: Selection of stoppage time: variation of the kinetic energy of the liquid, \tilde{E}_k^{\max} (see equation (6.21)) with time for eight representative cases: (a) $\mathcal{J} = 0.1$ & $Oh = 10^{-3} - 10^0$ and (b) $\mathcal{J} = 1.0$ & $Oh = 10^{-3} - 10^0$. Here, we plot the temporal evolution of the kinetic energy, both on a linear (energy) – linear (time) in (i) and on a log (energy) – linear (time) in (ii). For the latter, the kinetic energy is normalized by its maximum value during the process to ease comparison between different Oh , and shows a sharp decrease in the total kinetic energy as the stoppage time, $t = t_s$ is approached independent of the Oh . We define t_s as the instant beyond which the flow is too slow to cause any macroscopic changes in the time-scales that we want to study.

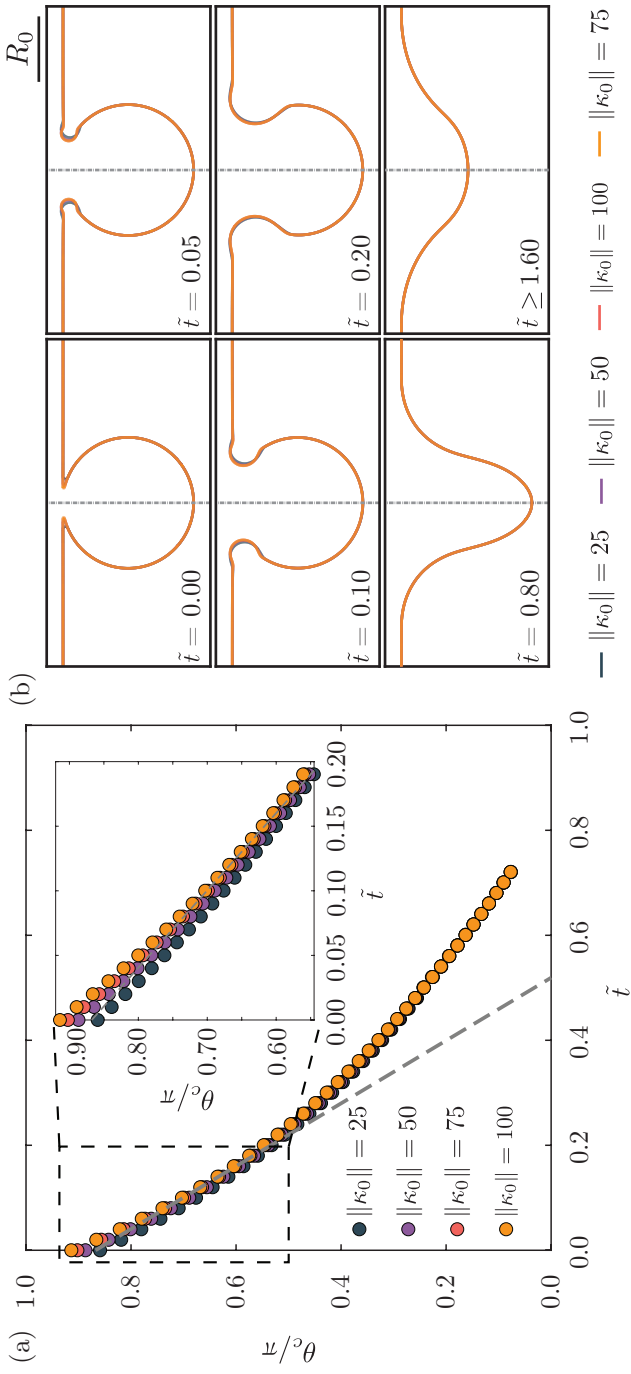


Figure 6.E.3: Sensitivity to initial rim curvature: (a) Temporal evolution of the location of the strongest capillary wave θ_c , and (b) Influence on the overall process of cavity collapse. Beyond, $\tilde{t} = 0.2$, there is negligible difference between the interfaces as the effect of initial condition vanishes. Here, time is normalized with the inertio-capillary time scale, $\tau_{\rho\gamma} = \sqrt{\rho_d R_0^3/\gamma}$. Inset in (a) zooms into the initial stages of the process where influence of $\|\tilde{\kappa}_0\|$ is apparent.

6.E.2 Stoppage time

Another important consequence of yield stress is a finite stoppage time. The flow in a liquid will stop if the stress falls below the yield stress. This implies that $\|\tilde{\mathcal{D}}\|$ should vanish. Since we use a regularization method, the flow in our simulations never truly stops. Hence, we consider a cut-off kinetic energy of $10^{-6} \times \max(E_k^{\text{Total}})$, where

$$\tilde{E}_k^{\text{Total}} = 0.5 \int_{\tilde{\Omega}} (\|\tilde{\mathbf{v}}\|^2 + \rho_r \|\tilde{\mathbf{v}}\|^2) d\tilde{\Omega} \quad (6.21)$$

is the total kinetic energy of the system. We stop the calculations when the total kinetic energy of the system is below the cut-off. To verify the sensitivity of this cut-off, we ran a number of simulations till $\tilde{t} = 2\tilde{t}_s$ (figure 6.E.2). Clearly, independent of the Oh , the flow becomes asymptotically stationary beyond $t = t_s$. A sharp decrease in the total kinetic energy can be observed in the semi-log plots (figures 6.E.2a-ii,b-ii) as the stoppage time is approached. Note that, this analysis only provides an estimation for the stoppage time, t_s and a more comprehensive study is required to find the exact values of t_s . Nonetheless, as clear from our results like those shown in figures 6.3.1 and 6.E.2, beyond this time, the flow dynamics are too slow for any macroscopic change in the location or the strength of capillary waves, or the shape of the final cavity.

6.E.3 Initial rim curvature effects

As mentioned in § 6.2.3, in our initial shape, we introduced a rim with a finite curvature $\tilde{\kappa}_0$ that connects the bubble to the free-surface. The initial location of the cavity-free-surface intersection θ_i also changes (inset of figure 6.E.3a), depending on this regularized curvature. In this appendix, we will show how this initial condition affects the bubble bursting process. For all the cases presented in this work, we have used $\tilde{\kappa}_0 = 100$. For Newtonian cases, Deike et al. [108] has carried out a more extensive sensitivity test to ascertain the importance of initial cavity shape on the process. For $\mathcal{J} = 0$, our results support their findings that the size of the initial hole around the axis ($r = 0$) is crucial and can manifest into changes in the jet velocity. Furthermore, κ_0 controls the first capillary waves that appear as the bubble cavity collapses (§ 6.3.2). Figures 6.B.1 and 6.B.2 show that our results agree with [103, 108] which have been validated with experiments.

For higher \mathcal{J} values, it is essential that $\|\tilde{\kappa}_0\| > \mathcal{J}$ for flow initiation.

We have restricted our study to $\mathcal{J} = 64$ where the flow is confined in the region of this high curvature (see § 6.5). Furthermore, figure 6.E.3 contains one representative case where we show the influence of κ_0 on the temporal evolution of the strongest capillary wave as it travels down the bubble cavity (figure 6.E.3a) and also on the interface deformations (figure 6.E.3b). As shown in these curves the difference in the results is negligible when $\|\kappa_0\| > 75$.

6.F Supplemental movies

These supplemental movies are available at Sanjay [[external YouTube link](#), 375]. In all the supplemental videos, the left part shows the magnitude of the velocity field, and the right part shows the magnitude of the Deformation tensor on a \log_{10} scale (also see figures 6.3.1, 6.3.2, 6.3.3, and 6.C.1).

- SM1: A typical case of bursting bubble in a Newtonian liquid medium: $\mathcal{J} = 0.0$ and $Oh = 10^{-2}$.
- SM2: Bursting bubble in a weakly viscoplastic liquid medium in which the process still shows all the major characteristics of the Newtonian liquid: $\mathcal{J} = 0.1$ and $Oh = 10^{-2}$.
- SM3: Bursting bubble in a liquid medium with medium yield stress whereby the jetting is suppressed, nonetheless the entire cavity yields: $\mathcal{J} = 0.5$ and $Oh = 10^{-2}$.
- SM4: Bursting bubble in a highly viscoplastic liquid medium: $\mathcal{J} = 1.0$ and $Oh = 10^{-2}$.
- SM5: Angular trajectory of the traveling capillary wave during bursting bubble in a Newtonian liquid medium: $\mathcal{J} = 0.0$ and $Oh = 10^{-2}$. The grey dotted line denotes the Newtonian limit, $\theta_c - \theta_i \sim -t/\tau_{\rho\gamma}$ as described by Gordillo and Rodríguez-Rodríguez [103]. The blue dot in the right panel of the video shows the position of the capillary wave.
- SM6: Angular trajectory of the traveling capillary wave during bursting bubble in a viscoplastic liquid medium: $\mathcal{J} = 0.2$ and $Oh = 10^{-2}$. The blue dot in the right panel of the video shows the position of the capillary wave.
- SM7: Angular trajectory of the traveling capillary wave during bursting bubble in a viscoplastic liquid medium: $\mathcal{J} = 1.0$ and $Oh = 10^{-2}$. The blue dot in the right panel of the video shows the position of the capillary wave.

chapter 6: bursting bubbles in a viscoplastic medium



source code



supplemental movies

- SM8: Formation of the jet as a result of collapsing cavity in a Newtonian liquid medium: $\mathcal{J} = 0.0$ and $Oh = 10^{-2}$. The blue dot in the right panel of the video shows the center line interface location being tracked.
- SM9: Effects of viscoplasticity on the formation of the jet as a result of collapsing cavity: $\mathcal{J} = 0.1$ and $Oh = 10^{-2}$. The blue dot in the right panel of the video shows the center line interface location being tracked.
- SM10: Effects of viscoplasticity on the formation of the jet as a result of collapsing cavity (jetting is suppressed): $\mathcal{J} = 0.3$ and $Oh = 10^{-2}$. The blue dot in the right panel of the video shows the center line interface location being tracked.
- SM11: Bursting bubble in a viscoplastic liquid medium: $\mathcal{J} = 0.1$ and $Oh = 10^{-3}$.
- SM12: Bursting bubble in a viscoplastic liquid medium: $\mathcal{J} = 0.1$ and $Oh = 10^{-1}$.
- SM13: Bursting bubble in a viscoplastic liquid medium: $\mathcal{J} = 0.1$ and $Oh = 10^0$.
- Bonus: Conference (International Congress on Rheology 2020) talk titled “Bursting Bubble in a Viscoplastic medium” presenting the results from this chapter.

Conclusion and outlook

In this thesis, we elucidated two classes of the commonly encountered free-surface phenomena: the impact of liquid drops on non-wetting substrates (part I), and capillary-driven retraction and bursting of films and free-surface bubbles (part II). Figure C1 summarizes the different regimes observed in this thesis. We also show the range of dimensionless numbers simulated to explore these regimes. In this section, we will briefly revisit each chapter to summarize the key results and answer the questions posed in the introduction to this thesis. We also point out open issues and propose follow-up studies that may stem from the various chapters.

Part I

In **chapter 1**, we study water drops impacting non-wetting substrates and find that not only is the inertial shock at impact associated with a distinct peak in the temporal evolution of the normal force, but so is the jump-off, which was hitherto unknown. We also give the following takeaway messages:

Takeaway messages **Chapter 1**

1. For most cases, the inertial pressure force sets the magnitude of both the peaks in the normal reaction force. But, surprisingly, even low-velocity impacts can lead to a remarkably high second peak in the normal force, which can even be larger than the first one.
2. The first peak occurs immediately after impact at a time instant that conforms to the inertial shock of impact, whereas the time at which the second peak occurs scales with the inertio-capillary time owing to the drop impact and drop oscillation analogy.

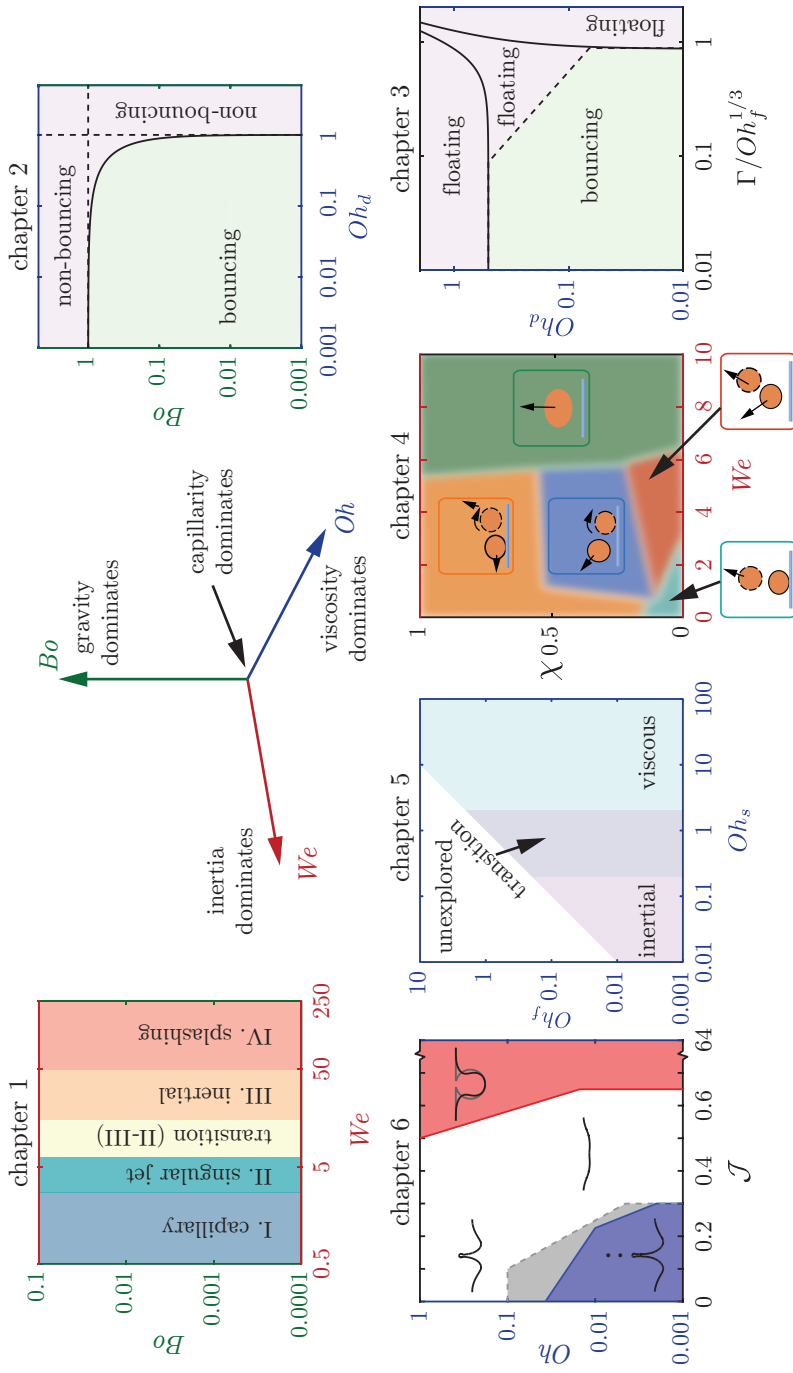


Figure C1: Summary of the different regimes and the range of the dimensionless numbers simulated to explore these regimes. The different regime maps contain the Weber number We (equation (2), chapters 1 and 4), the Bond number B_o (equation (7), chapters 1 and 2), dimensionless film thickness Γ (equation (10), chapter 3), the dimensionless offset χ (equation (9)) between the impacting and sessile drops (chapter 4), and the plasto-capillary number \mathcal{J} (equation (8), chapter 6). A common theme among most of these regime maps is the use of Ohnesorge numbers Oh (equation (5)) which can be further classified as: the drop Ohnesorge number (chapters 2 and 3), the film Ohnesorge number Oh_f (chapters 3 and 5), and the surroundings Ohnesorge number Oh_s (chapter 5). Please refer to the individual chapters for the details of each regime map.

The amplitude of the second peak further divides the drop impact dynamics into four distinct regimes based on the Weber number We , I. capillary, II. singular, III. inertial, and IV. splashing. These regimes are independent of the Bond number Bo (figure C1) for $0 < Bo < 0.1$. In the inertial limit (low Ohnesorge numbers Oh), gravity only dictates the dynamics of the falling drop prior to its impact on the substrate. This effect is accounted in the impact velocity and hence We . The insights from this chapter are crucial to develop countermeasures to the failure of superhydrophobicity in technological applications. Exciting and relevant extensions of our work include the study of impact forces of viscous drops, which will show quite different scaling behavior [153], and of Leidenfrost drops [6]. It will also be interesting to extend this work to less superhydrophobic substrates where contact line motion (viscous stresses vs. capillary traction) may significantly affect the flow focusing and hence the theoretical model. For such cases, we speculate the absolute numbers might change; however, the scaling relations would be the same.

In [chapter 2](#), we observed that close to the bouncing to non-bouncing transition of drops falling on a non-wetting substrate, the rebound process is independent of the impact parameters. This observation disentangles the later stages of the rebound from the initial impact dynamics. Consequently, we draw an analogy to the case of coalescence-induced jumping of two identical drops [175–177] to give a simple criterion for the bouncing to non-bouncing transition, namely that the sum of the drop Ohnesorge and Bond numbers is unity ($Oh + Bo = 1$), for the bouncing to non-bouncing transition (figure C1). We further provide the following takeaway messages:

Takeaway messages [Chapter 2](#)

1. Throughout the drop impact process, viscous dissipation enervates internal momentum. A drop will cease bouncing and stay on the substrate if its upward momentum (driven by capillarity and resisted by viscous stresses) after the retraction stage is insufficient to overcome gravity.
2. Drops smaller than their visco-capillary length stop bouncing due to viscous dissipation [153].
3. On the other hand, drops larger than their gravito-capillary length cannot bounce due to their own weight [174].

We stress that this chapter only deciphers the theoretical upper bound of the bouncing to non-bouncing transition on an ideal non-wetting substrate. A natural extension of this work would be to non-ideal superhydrophobic substrates and understand why the transition to non-bouncing occurs way below [183] the threshold proposed in this chapter. Furthermore, we solely focus on drops impacting with velocities exceeding their inertia-capillary velocity, i.e., the impact Weber numbers greater than unity. It will be interesting to extend this work for cases where the drops only deform weakly, i.e., capillarity dominates over inertia. One can either use a quasi-static model of bouncing drops [150] or an analogy to non-linear springs [185] to probe that regime. Lastly, it will be interesting to investigate whether the bouncing inhibition criterion found in this chapter also applies to the coalescence-induced bouncing of drops.

In **chapter 3**, we investigated drops bouncing off viscous liquid films that mimic atomically smooth substrates. The repellent behavior of such substrates entails the presence of an air layer trapped between it and the impacting drop. This chapter probes these repellent properties and provides the following key insights:

Takeaway messages **Chapter 3**

1. Drops impacting on viscous liquid films show two distinct bouncing regimes, namely, the substrate-independent and substrate-dependent bouncing. In the former, the impact dynamics are not affected by the presence of the viscous film owing to its high viscosity or negligible thickness, i.e., the effective film mobility $\Gamma/Oh_f^{1/3} \rightarrow 0$. However, in the latter, both the drop and film properties influence the rebound dynamics.
2. Within the substrate-independent limit, repellency is suppressed once the drop viscosity exceeds a critical value as on superamphiphobic substrates discussed in chapter 2 ($Oh_d > Oh_{d,c}$). The substrate-dependent regime also admits a limit for low viscosity drops, in which the film properties alone determine the inhibition of repellency (figure C1).

Here, we emphasize that this study does not present an exhaustive exploration of all bouncing regimes. Interestingly, Galeano-Rios et al. [182] have shown that spherical hydrophobic solid spheres can bounce off deep low viscosity pools. Consequently, we hypothesize that the bouncing regime could

resurrect for highly viscous drops on large inviscid pools, evidencing non-monotonic energy transfer. It will be interesting to probe such a regime in future work.

In [chapter 4](#), we found that in the presence of a non-wetting substrate, the drop-on-drop impact results in five rebound scenarios, four of which do not involve coalescence. These Four non-coalescing outcomes are attainable by varying the Weber number We and the offset from head-on alignment of the impacting drops χ as illustrated in figure [C1](#). One-to-one comparisons between the experimentally and numerically determined drop boundaries and center of mass mechanical energies illustrate the power of the direct numerical simulations for quantitatively predicting the dynamics of drop-on-drop impact. More specifically, our numerical simulations illustrate that these general outcomes are governed by the average direction of the flow velocity vectors during the retraction phase, which are associated with We and χ . The key takeaway messages of this chapter are:

Takeaway messages [Chapter 4](#)

1. As the two drops collide, the kinetic energy of the impacting drop is converted into the surface energy of both drops. A recovery phase follows this transfer whereby the surface energy of the system returns to the kinetic energies of the drops. Throughout the process, viscous dissipation enervates the internal momenta of the drops.
2. The impacting drop lifts a lazy sessile one in two of the four rebound scenarios. If sufficient energy is transferred between the drops, both drops can take off the substrate, while in some cases, the impacting drop kicks the sessile drop off the substrate but itself cannot bounce.

Part II

In [chapter 5](#), we found that even when the surrounding medium interacts with the Taylor-Culick retraction of a film, the film still retracts with a constant velocity provided that it is long enough to avoid finite film size and internal viscous effects. However, both the inertia and viscosity of the surroundings influence the magnitude of this constant velocity. Here, we used the lumped elements analysis, motivated by Taylor [\[34\]](#) and Culick [\[35\]](#), to understand

both inertial and viscous regimes in the three canonical configurations. This chapter culminates with the following takeaway messages:

Takeaway messages **Chapter 5**

1. For the generalized Taylor-Culick retractions, even when the surroundings have negligible viscosity (surrounding Ohnesorge number $Oh_s \ll 1$, figure C1), they still influence the retraction process through inertial (added mass-like) effects. Hence, for such a scenario, the constant retraction velocity still follows the scaling proposed by Taylor [34] and Culick [35] for the classical case. However, the coefficient of this scaling relationship decreases owing to inertial resistance from the surroundings.
2. On the other hand, for highly viscous surroundings ($Oh_s \gg 1$, figure C1), viscous dissipation dictates the retraction velocity scale. The exact nature of this variation depends on the geometry of the canonical configuration in question. For example, for retracting sheets submerged in a viscous oil, the retraction velocity scales with the visco-capillary velocity (i.e., the Capillary number is a constant). However, for sheets retracting at an oil-air interface, the Capillary number shows a power-law behavior with the dimensionless viscosity (Ohnesorge number) of the surrounding viscous medium.
3. For the case of classical Taylor-Culick retraction, it is known that the viscous dissipation is highest in the neck region connecting the film to its bulbous rim. Intuitively, for film retracting sheets fully submerged in a viscous oil, dissipation occurs throughout the viscous boundary layer in the surroundings. However, for films retracting at an oil-air interface, the viscous dissipation occurs not only in the viscous boundary layer but is also concentrated in the wedge region at the apparent film-oil-air three-phase contact line.

Here, we restrict ourselves to cases where film Ohnesorge number Oh_f is smaller than that of the surroundings ($Oh_f \leq Oh_s$, figure C1). To further understand such retraction processes and demystify the role of finite film length and viscosity, particularly for $Oh_f \geq Oh_s$, one can use the similarity solutions proposed by Pierson et al. [37] and Deka and Pierson [38] coupled with an Oseen-type approximation to Stokes flow to incorporate the influence of the surroundings. Furthermore, one can study the retraction of non-Newtonian

sheets and filaments [276] in similar surroundings. In such scenarios, the retraction dynamics will depend not only on capillarity and viscosity, as described in this work, but also on the rheological properties of both the film and the surroundings.

In **chapter 6**, we revealed that the influence of viscoplasticity on the capillary-driven bursting of a bubble at a liquid-gas free-surface is twofold: (i) it manifests as an increase in effective viscosity to attenuate the capillary waves that control the bursting process, and (ii) the plasticity of the medium resists any attempts to deform its free-surface. We give the following takeaway messages:

Takeaway messages **Chapter 6**

1. Immediately after bursting, the large capillary stresses localized at the intersection of the bubble cavity and the free-surface result in a train of capillary waves that travel down the bubble cavity. In liquids with low yield stresses, these waves still follow the same behavior as their Newtonian counterpart. Subsequently, the cavity collapse leads to a Worthington jet that might break into droplets owing to the Rayleigh-Plateau instability. However, for liquids with a large yield stress, the capillary waves and the Worthington jet vanish.
2. Yield-stress fluids can sustain deformations. Consequently, even after waiting for a long time, the cavity never returns to its zero surface energy configuration (a flat free-surface). For high yield stress liquids, the plasticity of the medium can even overcome the capillary waves that try to yield the free-surface, thus freezing a zoo of final crater shapes.

Consequently, we identified four distinct regimes: I. formation of the Worthington jet, which breaks up into droplets, II. formation of jet without droplets, III. the entire cavity collapses, but the cavity center never crosses the initial pool free-surface, and IV. a part of the cavity never yields based on the plasto-capillary number \mathcal{J} and the Ohnesorge number Oh (figure C1). The focus of this chapter was to compare the bursting bubble process in a yield stress fluid to that in a Newtonian fluid, without the initial shape effects. However, once the exact shape of the bubble at the free-surface is known, either from experiments or theory, one can calculate the resulting flow and compare them to the

present study forming a natural extension to this work. Moreover, the current results could also be useful in analyzing some geophysical flows, such as those in volcanic eruptions [342].

A common theme in analyzing these processes is that we elaborated upon the energetics of each process and demystified the role of viscous dissipation. To this end, we employed direct numerical simulations with the free software program Basilisk C [143] that tracks the interface between two fluids using the volume of fluid method [2, 156]. We also extended the energy calculations [30, 160, 334] to these configurations. We found that we can use the Ohnesorge number (Oh) as a proxy to estimate the importance of viscous dissipation in these processes. Indeed, in all the capillary-driven phenomena (drop oscillation, retraction, and take-off in chapters 1– 4, and rupture and bursting in chapters 5– 6), a large Ohnesorge number ($Oh \gg 1$) implies dominance of viscous dissipation (figure C1). Surprisingly, even at low Ohnesorge numbers ($Oh \ll 1$), viscous dissipation can still enervate internal momentum. In fact, in the inertial limit, viscous dissipation accounts for almost 50% of the released energy during both classical and generalized Taylor-Culick retractions.

Similarly, for drop impact processes, again in the inertial limit, viscous dissipation can amount to almost 20% of the initial energy. Following this insight, we also delineated when these drops stop bouncing on an ideal non-wetting substrate and found the theoretical upper limit for bouncing drops, which is greatly influenced by viscous dissipation and gravity (figure C1). The knowledge about this bouncing to non-bouncing transition is helpful in inkjet printing [16], or pesticide deposition on plants [20, 21] where one would like the drops to stay on the substrate. This transition is also vital in spray cooling applications [17, 18] whereby bouncing may lead to dry-out and locally high temperature hot spots, which is detrimental for the device integrity. However, we do not consider heat transfer or phase-change effects in our simulations to account for such behaviors. We also do not consider non-Newtonian rheology of the ink or the pesticides. These effects can be implemented in the future to optimize such processes further. Note that, while studying the drop impact process in part I using our continuum-based numerical simulations, the biggest idealization we make is the presence of a thin air layer between the impacting drop and the substrate even at high impact velocities. Such an idealization is incomprehensible in experiments as the drop always contacts the substrate owing to surface asperities, flow, or inter-molecular forces [11, 12, 80, 204]. Consequently, our continuum-based direct numerical simulations are inadequate to predict whether or not a drop will coalesce with another drop or with

the substrate. We take this information from the experiments. Prediction of such coalescence (or rupture) behaviors is beyond the scope of the present thesis, but one can couple a consistent molecular dynamics technique (like gas kinetic theory) with the continuum-based volume of fluid method to bridge this lacuna in our model in the future. Nonetheless, employing this idealization gives good agreement with the macroscopic features of the drop impact processes, including normal reaction forces between the drop and the substrate, maximum spreading diameter, contact time, and restitution coefficient of the impacting drop. Indeed, it is crucial to benchmark the simulation codes against experiments with well-defined geometries and theoretical predictions from first principles. The remarkable agreement between our simulations on ideal non-wetting substrates and experiments evidences that the air layer is essential to avoid pinning of the contact line but otherwise has no significant influence on the fundamental physics of the process. The results from this part of the thesis will help further the fundamental understanding of the drop impact process and have various natural and industrial consequences. For example, understanding the normal reaction force between the impact drop and substrate will help mitigate soil erosion [58] and develop countermeasures against the damage to engineered surfaces [59–61].

Lastly, to investigate Taylor-Culick retractions at a liquid-gas free-surface in chapter 5, we developed a precursor film-based three-fluid volume of fluid method that captures the experimentally-observed scaling behavior very well. In a broader perspective, one can use this method to elucidate several spreading phenomena, both at small and large scales, such as, drop-film interactions in the inkjet printing process [16] and late time spreading during oil spillage [335], respectively. However, this numerical assumption is applicable only when it is thermodynamically favorable for one of the fluids to spread over the other fluids it comes in contact with, i.e., it has a positive spreading coefficient [10, 319]. Indeed, extending this method to generalized three-phase contact line motions is expected to yield interesting results. The current three-fluid model can also handle different surface tension forces for the three interfaces and can be used as a base model to incorporate multi-physical aspects, such as Marangoni flows and multicomponent systems [376].

References

- [1] M. Miodownik. *Liquid rules: The delightful and dangerous substances that flow through our lives*. HarperCollins, 2019.
- [2] G. Tryggvason, R. Scardovelli, and S. Zaleski. *Direct Numerical Simulations of Gas–Liquid Multiphase Flows*. Cambridge university press, 2011.
- [3] U. Jain. *Slamming Liquid Impact and the Mediating Role of Air*. PhD thesis, University of Twente, 2020.
- [4] H. Boerhaave. *Elementae Chemiae, Vol. 1*. Leiden: Lugduni Batavorum, 1732.
- [5] J. G. Leidenfrost. *De aquae communis nonnullis qualitatibus tractatus*. Ovenirus, 1756.
- [6] D. Quéré. Leidenfrost dynamics. *Annu. Rev. Fluid Mech.*, 45:197–215, 2013.
- [7] G. I. Taylor. Disintegration of water drops in an electric field. *Proc. R. Soc. London, Ser. A*, 280(1382):383–397, 1964.
- [8] N. Ashgriz. *Handbook of atomization and sprays: theory and applications*. Springer Science & Business Media, 2011.
- [9] A. E. Hosoi and J. W. M. Bush. Evaporative instabilities in climbing films. *J. Fluid Mech.*, 442:217–239, 2001.
- [10] P.-G. de Gennes, F. Brochard-Wyart, and D. Quéré. *Capillarity and Wetting Phenomena: Drops, Bubbles, Pearls, Waves*. Springer, 2004.

- [11] S. Kim, Z. Wu, E. Esmaili, J. J Dombroskie, and S. Jung. How a raindrop gets shattered on biological surfaces. *Proc. Natl. Acad. Sci. U.S.A.*, 117(25):13901–13907, 2020.
- [12] D. Lohse and E. Villermaux. Double threshold behavior for breakup of liquid sheets. *Proc. Natl. Acad. Sci. U.S.A.*, 117:18912–18914, 2020.
- [13] L. da Vinci. *Codex Hammer (earlier Codex Leicester)*. In *The Notebooks of Leonardo da Vinci (ed. and trans. E. MacCurdy)*. George Braziller, 1508.
- [14] A. M. Worthington. On the forms assumed by drops of liquids falling vertically on a horizontal plate. *Proc. R. Soc. London, Ser. A*, 25(171–178):261–272, 1877.
- [15] A. M. Worthington. A second paper on the forms assumed by drops of liquids falling vertically on a horizontal plate. *Proc. R. Soc. London*, 25:498–503, 1877.
- [16] D. Lohse. Fundamental fluid dynamics challenges in inkjet printing. *Annu. Rev. Fluid Mech.*, 54:349–382, 2022.
- [17] J. Kim. Spray cooling heat transfer: The state of the art. *Int. J. Heat Fluid Flow*, 28(4):753–767, 2007.
- [18] S. Shiri and J. C. Bird. Heat exchange between a bouncing drop and a superhydrophobic substrate. *Proc. Natl. Acad. Sci. U.S.A.*, 114(27):6930–6935, 2017.
- [19] S. Jowkar and M. R. Morad. Rebounding suppression of droplet impact on hot surfaces: effect of surface temperature and concaveness. *Soft Matter*, 15(5):1017–1026, 2019.
- [20] L. He, L. Ding, B. Li, W. Mu, P. Li, and F. Liu. Optimization strategy to inhibit droplets rebound on pathogen-modified hydrophobic surfaces. *ACS Appl. Mater. Interfaces*, 13(32):38018–38028, 2021.
- [21] H. Hoffman, R. Sijs, T. de Goede, and D. Bonn. Controlling droplet deposition with surfactants. *Phys. Rev. Fluids*, 6(3):033601, 2021.
- [22] F. R. Smith, C. Nicloux, and D. Brutin. Influence of the impact energy on the pattern of blood drip stains. *Phys. Rev. Fluids*, 3(1):13601, 2018.

- [23] C. Seyfert. *Shaping Droplets: Colloids and Instabilities*. PhD thesis, University of Twente, 2022.
- [24] A. K. Dickerson, P. G. Shankles, N. M. Madhavan, and D. L. Hu. Mosquitoes survive raindrop collisions by virtue of their low mass. *Proc. Natl. Acad. Sci. U.S.A.*, 109(25):9822–9827, 2012.
- [25] H. Wagner. Über Stoß- und Gleitvorgänge an der Oberfläche von Flüssigkeiten. *Z. Angew. Math. Mech.*, 12(4):193–215, 1932.
- [26] J. Philippi, P.-Y. Lagrée, and A. Antkowiak. Drop impact on a solid surface: short-time self-similarity. *J. Fluid Mech.*, 795:96–135, 2016.
- [27] L. Gordillo, T.-P. Sun, and X. Cheng. Dynamics of drop impact on solid surfaces: evolution of impact force and self-similar spreading. *J. Fluid Mech.*, 840:190–214, 2018.
- [28] C. Clanet, C. Béguin, D. Richard, and D. Quéré. Maximal deformation of an impacting drop. *J. Fluid Mech.*, 517:199–208, 2004.
- [29] N. Laan, K. G. de Bruin, D. Bartolo, C. Josserand, and D. Bonn. Maximum diameter of impacting liquid droplets. *Phys. Rev. Appl.*, 2(4):44018, 2014.
- [30] S. Wildeman, C. W. Visser, C. Sun, and D. Lohse. On the spreading of impacting drops. *J. Fluid Mech.*, 805:636–655, 2016.
- [31] J. M. Gordillo, G. Riboux, and E. S. Quintero. A theory on the spreading of impacting droplets. *J. Fluid Mech.*, 866:298–315, 2019.
- [32] C. Neinhuis and W. Barthlott. Characterization and distribution of water-repellent, self-cleaning plant surfaces. *Ann. Bot.*, 79(6):667–677, 1997.
- [33] D. Quéré. Wetting and roughness. *Annu. Rev. Mater. Res.*, 38:71–99, 2008.
- [34] G. I. Taylor. The dynamics of thin sheets of fluid. III. Disintegration of fluid sheets. *Proc. R. Soc. London, Ser. A*, 253:313–321, 1959.
- [35] F. E. C. Culick. Comments on a ruptured soap film. *J. Appl. Phys.*, 31:1128–1129, 1960.

- [36] D. Bartolo, C. Josserand, and D. Bonn. Retraction dynamics of aqueous drops upon impact on non-wetting surfaces. *J. Fluid Mech.*, 545:329–338, 2005.
- [37] J.-L. Pierson, J. Magnaudet, E. J. Soares, and S. Popinet. Revisiting the Taylor-Culick approximation: Retraction of an axisymmetric filament. *Phys. Rev. Fluids*, 5(7):073602, 2020.
- [38] H. Deka and J.-L. Pierson. Revisiting the Taylor-Culick approximation. II. Retraction of a viscous sheet. *Phys. Rev. Fluids*, 5(9):093603, 2020.
- [39] V. Sanjay, U. Sen, P. Kant, and D. Lohse. Taylor-Culick retractions and the influence of the surroundings. *arXiv Preprint. arXiv:2202.13400*, 2022.
- [40] D. Richard and D. Quéré. Bouncing water drops. *Europhys. Lett.*, 50(6):769, 2000.
- [41] A. L. Yarin. Drop impact dynamics: Splashing, Spreading, Receding, Bouncing... *Annu. Rev. Fluid Mech.*, 38:159–192, 2006.
- [42] C. Josserand and S. T. Thoroddsen. Drop impact on a solid surface. *Annu. Rev. Fluid Mech.*, 48:365–391, 2016.
- [43] Y. Renardy, S. Popinet, L. Duchemin, M. Renardy, S. Zaleski, C. Josserand, M. A. Drumright-Clarke, D. Richard, C. Clanet, and D. Quéré. Pyramidal and toroidal water drops after impact on a solid surface. *J. Fluid Mech.*, 484:69–83, 2003.
- [44] D. Bartolo, C. Josserand, and D. Bonn. Singular jets and bubbles in drop impact. *Phys. Rev. Lett.*, 96(12):124501, 2006.
- [45] A. L. Yarin, I. V. Roisman, and C. Tropea. *Collision Phenomena in Liquids and Solids*. Cambridge University Press, 2017.
- [46] R. Blossey. Self-cleaning surfaces—virtual realities. *Nat. Mater.*, 2(5):301–306, 2003.
- [47] Y. Liu, X. Chen, and J. H. Xin. Hydrophobic duck feathers and their simulation on textile substrates for water repellent treatment. *Bioinspiration Biomimetics*, 3(4):046007, 2008.

- [48] T. Mouterde, G. Lehoucq, S. Xavier, A. Checco, C. T. Black, A. Rahaman, T. Midavaine, C. Clanet, and D. Quéré. Antifogging abilities of model nanotextures. *Nat. Mater.*, 16(6):658–663, 2017.
- [49] A. Lafuma and D. Quéré. Superhydrophobic states. *Nat. Mater.*, 2(7):457–460, 2003.
- [50] M. Callies and D. Quéré. On water repellency. *Soft Matter*, 1(1):55–61, 2005.
- [51] M. Sbragaglia, A. M. Peters, C. Pirat, B. M. Borkent, R. G. H. Lammertink, M. Wessling, and D. Lohse. Spontaneous breakdown of superhydrophobicity. *Phys. Rev. Lett.*, 99(15):156001, 2007.
- [52] Y. Li, D. Quéré, C. Lv, and Q. Zheng. Monostable superrepellent materials. *Proc. Natl. Acad. Sci. U.S.A.*, 114(13):3387–3392, 2017.
- [53] P. Tsai, R. G. H. Lammertink, M. Wessling, and D. Lohse. Evaporation-triggered wetting transition for water droplets upon hydrophobic microstructures. *Phys. Rev. Lett.*, 104(11):116102, 2010.
- [54] X. Chen, R. Ma, J. Li, C. Hao, W. Guo, B. L. Luk, S. C. Li, S. Yao, and Z. Wang. Evaporation of droplets on superhydrophobic surfaces: Surface roughness and small droplet size effects. *Phys. Rev. Lett.*, 109(11):116101, 2012.
- [55] P. Papadopoulos, L. Mammen, X. Deng, D. Vollmer, and H.-J. Butt. How superhydrophobicity breaks down. *Proc. Natl. Acad. Sci. U.S.A.*, 110(9):3254–3258, 2013.
- [56] E. Bormashenko, R. Pogreb, G. Whyman, and M. Erlich. Resonance Cassie-Wenzel wetting transition for horizontally vibrated drops deposited on a rough surface. *Langmuir*, 23(24):12217–12221, 2007.
- [57] D. Bartolo, F. Bouamrane, E. Verneuil, A. Buguin, P. Silberzan, and S. Moulinet. Bouncing or sticky droplets: Impalement transitions on superhydrophobic micropatterned surfaces. *Eur. Lett.*, 74(2):299, 2006.
- [58] M. A. Nearing, J. M. Bradford, and R. D. Holtz. Measurement of force vs. time relations for waterdrop impact. *Soil Sci. Soc. Am. J.*, 50:1532–1536, 1986.

- [59] M. Ahmad, M. Schatz, and M. V. Casey. Experimental investigation of droplet size influence on low pressure steam turbine blade erosion. *Wear*, 303:83–86, 2013.
- [60] B. Amirzadeh, A. Louhghalam, M. Raessi, and M. Tootkaboni. A computational framework for the analysis of rain-induced erosion in wind turbine blades. *J. Wind Eng. Ind. Aerodyn.*, 163:33–43, 2017.
- [61] O. Gohardani. Impact of erosion testing aspects on current and future flight conditions. *Prog. Aerosp. Sci.*, 47(4):280–303, 2011.
- [62] X. Cheng, T.-P. Sun, and L. Gordillo. Drop impact dynamics: Impact force and stress distributions. *Annu. Rev. Fluid Mech.*, 54, 2021.
- [63] s. Gart, J. E. Mates, C. M. Megaridis, and S. Jung. Droplet impacting a cantilever: A leaf-raindrop system. *Phys. Rev. A*, 93(3):0344019, 2015.
- [64] O. Reynolds. On the floating of drops on the surface of water depending only on the purity of the surface. *Proc. Lit. Phil. Soc.*, 21(1):413–414, 1881.
- [65] M. Geri, B. Keshavarz, G. H. McKinley, and J. W. M. Bush. Thermal delay of drop coalescence. *J. Fluid Mech.*, 833, 2017.
- [66] S. Chandra and C. T. Avedisian. On the collision of a droplet with a solid surface. *Proc. R. Soc. A*, 432(1884):13–41, 1991.
- [67] T. Tran, H. J. J. Staat, A. Prosperetti, C. Sun, and D. Lohse. Drop impact on superheated surfaces. *Phys. Rev. Lett.*, 108(3):36101, 2012.
- [68] M. Shirota, M. A. J. van Limbeek, C. Sun, A. Prosperetti, and D. Lohse. Dynamic leidenfrost effect: Relevant time and length scales. *Phys. Rev. Lett.*, 116(6):064501, 2016.
- [69] P. Chantelot and D. Lohse. Leidenfrost effect as a directed percolation phase transition. *Phys. Rev. Lett.*, 127(12):124502, 2021.
- [70] M. Adda-Bedia, S. Kumar, F. Lechenault, S. Moulinet, M. Schillaci, and D. Vella. Inverse leidenfrost effect: Levitating drops on liquid nitrogen. *Langmuir*, 32(17):4179–4188, 2016.
- [71] A. Gauthier, D. van der Meer, J. H. Snoeijer, and G. Lajoinie. Capillary orbits. *Nat. Commun.*, 10(1):1–5, 2019.

- [72] A. Gauthier, C. Diddens, R. Proville, D. Lohse, and D. van der Meer. Self-propulsion of inverse leidenfrost drops on a cryogenic bath. *Proc. Natl. Acad. Sci. U.S.A.*, 116(4):1174–1179, 2019.
- [73] S. Pal, A. M. Miqdad, S. Datta, A. K. Das, and P. K. Das. Control of drop impact and proposal of pseudo-superhydrophobicity using electrostatics. *Ind. Eng. Chem. Res.*, 56(39):11312–11319, 2017.
- [74] C. Singh, A. K. Das, and P. K. Das. Levitation of non-magnetizable droplets inside ferrofluid. *J. Fluid Mech.*, 857:398–448, 2018.
- [75] J. M. Kolinski, S. M. Rubinstein, S. Mandre, M. P. Brenner, D. A. Weitz, and L. Mahadevan. Skating on a film of air: drops impacting on a surface. *Phys. Rev. Lett.*, 108(7):074503, 2012.
- [76] R. C. A. van der Veen, T. Tran, D. Lohse, and C. Sun. Direct measurements of air layer profiles under impacting droplets using high-speed color interferometry. *Phys. Rev. E*, 85(2):026315, 2012.
- [77] S. Mandre, M. Mani, and M. P. Brenner. Precursors to splashing of liquid droplets on a solid surface. *Phys. Rev. Lett.*, 102(13):134502, 2009.
- [78] M. M. Driscoll and S. R. Nagel. Ultrafast interference imaging of air in splashing dynamics. *Phys. Rev. Lett.*, 107(15):154502, 2011.
- [79] W. Bouwhuis, R. C. A. van der Veen, T. Tran, D. L. Keij, K. G. Winkels, I. R. Peters, D. van der Meer, C. Sun, J. H. Snoeijer, and D. Lohse. Maximal air bubble entrainment at liquid-drop impact. *Phys. Rev. Lett.*, 109(26):264501, 2012.
- [80] J. M. Kolinski, L. Mahadevan, and S. M. Rubinstein. Drops can bounce from perfectly hydrophilic surfaces. *Europhys. Lett.*, 108(2):24001, 2014.
- [81] Y. J. Jiang, A. Umemura, and C. K. Law. An experimental investigation on the collision behaviour of hydrocarbon droplets. *J. Fluid Mech.*, 234:171–190, 1992.
- [82] J. Qian and C. K. Law. Regimes of coalescence and separation in droplet collision. *J. Fluid Mech.*, 331:59–80, 1997.
- [83] É. Guyon, J. Bico, É. Reyssat, and B. Roman. *Hidden Wonders: The Subtle Dialogue Between Physics and Elegance*. MIT Press, 2021.

- [84] H. Lhuissier and E. Villermaux. Bursting bubble aerosols. *J. Fluid Mech.*, 696:5–44, 2012.
- [85] E. Ghabache, G. Liger-Belair, A. Antkowiak, and T. Séon. Evaporation of droplets in a champagne wine aerosol. *Sci. Rep.*, 6:25148, 2016.
- [86] N. J. Balmforth, I. A. Frigaard, and G. Ovarlez. Yielding to stress: recent developments in viscoplastic fluid mechanics. *Annu. Rev. Fluid Mech.*, 46:121–146, 2014.
- [87] F. Savart. Mémoire sur le choc de deux veines liquides animées de mouvements directement opposés. *Ann. Chim. Phys.*, 55:257–310, 1833.
- [88] F. Savart. Mémoire sur le choc d'une veine liquide lancée contre un plan circulaire. *Ann. Chim. Phys.*, 54:56–57, 1833.
- [89] F. Savart. Suite du mémoire sur le choc d'une veine liquide lancée contre un plan circulaire. *Ann. Chim. Phys.*, 54:113–145, 1833.
- [90] A. Dupré. Théorie mécanique de la chaleur. *Ann. Chim. Phys.*, 11:194–219, 1867.
- [91] A. Dupré. *Théorie mécanique de la chaleur*. Gauthier-Villars, 1869.
- [92] Lord Rayleigh. Some applications of photography. *Nature*, 44:249, 1891.
- [93] W. R. McEntee and K. J. Mysels. The bursting of soap films. I. An experimental study. *J. Phys. Chem.*, 73:3018–3028, 1969.
- [94] N. Bremond and E. Villermaux. Bursting thin liquid films. *J. Fluid Mech.*, 524:121–130, 2005.
- [95] F. Müller, U. Kornek, and R. Stannarius. Experimental study of the bursting of inviscid bubbles. *Phys. Rev. E*, 75:065302 (R), 2007.
- [96] J. P. Munro, C. R. Anthony, O. A. Basaran, and J. R. Lister. Thin-sheet flow between coalescing bubbles. *J. Fluid Mech.*, 773:R3, 2015.
- [97] E. Villermaux. Fragmentation versus cohesion. *J. Fluid Mech.*, 898:P1, 2020.
- [98] P.-G. de Gennes. Introductory lecture. mechanics of soft interfaces. *Faraday Discuss.*, 104:1–8, 1996.

- [99] N. Savva and J. W. M. Bush. Viscous sheet retraction. *J. Fluid Mech.*, 626:211–240, 2009.
- [100] B. J. Mason. Bursting of air bubbles at the surface of sea water. *Nature*, 174(4427):470, 1954.
- [101] B. W. Zeff, B. Kleber, J. Fineberg, and D. P. Lathrop. Singularity dynamics in curvature collapse and jet eruption on a fluid surface. *Nature*, 403(6768):401, 2000.
- [102] L. Duchemin, S. Popinet, C. Josserand, and S. Zaleski. Jet formation in bubbles bursting at a free surface. *Phys. Fluids*, 14(9):3000–3008, 2002.
- [103] J. M. Gordillo and J. Rodríguez-Rodríguez. Capillary waves control the ejection of bubble bursting jets. *J. Fluid Mech.*, 867:556–571, 2019.
- [104] G. Liger-Belair. The physics behind the fizz in champagne and sparkling wines. *Eur. Phys. J. Spec. Top.*, 201(1):1–88, 2012.
- [105] M. Vignes-Adler. The fizzling foam of champagne. *Angew. Chem. Int. Ed.*, 52(1):187–190, 2013.
- [106] E. Ghabache, A. Antkowiak, C. Josserand, and T. Séon. On the physics of fizziness: How bubble bursting controls droplets ejection. *Phys. Fluids*, 26(12):121701, 2014.
- [107] A. M. Gañán-Calvo. Revision of bubble bursting: Universal scaling laws of top jet drop size and speed. *Phys. Rev. Lett.*, 119(20):204502, 2017.
- [108] L. Deike, E. Ghabache, G. Liger-Belair, A. K. Das, S. Zaleski, S. Popinet, and T. Séon. Dynamics of jets produced by bursting bubbles. *Phys. Rev. Fluids*, 3(1):13603, 2018.
- [109] R. B. Bird, G. C. Dai, and B. J. Yarusso. The rheology and flow of viscoplastic materials. *Rev. Chem. Eng.*, 1(1):1–70, 1983.
- [110] P. Coussot. Yield stress fluid flows: A review of experimental data. *J. Non-Newton. Fluid Mech.*, 211:31–49, 2014.
- [111] D. Bonn, M. M. Denn, L. Berthier, T. Divoux, and S. Manneville. Yield stress materials in soft condensed matter. *Rev. Mod. Phys.*, 89(3):35005, 2017.

- [112] E. Buckingham. On physically similar systems; illustrations of the use of dimensional equations. *Phys. Rev.*, 4(4):345, 1914.
- [113] E. Buckingham. The principle of similitude. *Nature*, 96(2406):396–397, 1915.
- [114] J. Eggers and M. A. Fontelos. *Singularities: formation, structure, and propagation*, volume 53. Cambridge University Press, 2015.
- [115] Lord Rayleigh. On the capillary phenomena of jets. *Proc. R. Soc. London*, 29(196–199):71–97, 1879.
- [116] J. Eggers, M. A. Fontelos, C. Josserand, and S. Zaleski. Drop dynamics after impact on a solid wall: Theory and simulations. *Phys. Fluids*, 22(6):062101, 2010.
- [117] G. H. McKinley and M. Renardy. Wolfgang von Ohnesorge. *Phys. Fluids*, 23(12):127101, 2011.
- [118] X. Tang, A. Saha, C. K. Law, and C. Sun. Bouncing drop on liquid film: Dynamics of interfacial gas layer. *Phys. Fluids*, 31(1):013304, 2019.
- [119] S. P. Lin and R. D. Reitz. Drop and spray formation from a liquid jet. *Annu. Rev. Fluid Mech.*, 30:85–105, 1998.
- [120] P. K. Notz and O. A. Basaran. Dynamics and breakup of a contracting liquid filament. *J. Fluid Mech.*, 512:223–256, 2004.
- [121] H. Dong, W. W. Carr, and J. F. Morris. An experimental study of drop-on-demand drop formation. *Phys. Fluids*, 18(7):072102, 2006.
- [122] L. Xu, T. Shi, and L. An. Nonsolvent-induced dewetting of thin polymer films. *Langmuir*, 23(18):9282–9286, 2007.
- [123] B. Derby. Inkjet printing of functional and structural materials: fluid property requirements, feature stability, and resolution. *Annu. Rev. Mater. Res.*, 40:395–414, 2010.
- [124] W. von Ohnesorge. *Anwendung eines kinematographischen Hochfrequenz- apparates mit mechanischer Regelung der Belichtung zur Aufnahme der Tropfenbildung und des Zerfalls flüssiger Strahlen*. PhD thesis, Konrad Triltsch, Würzburg, 1937.

- [125] J. Li, B. Zhang, P. Guo, and Q. Lv. Impact force of a low speed water droplet colliding on a solid surface. *J. Appl. Phys.*, 116(21):214903, 2014.
- [126] D. Soto, A. B. de Lariviere, X. Boutillon, C. Clanet, and D. Quéré. The force of impacting rain. *Soft Matter*, 10(27):4929–4934, 2014.
- [127] B. Zhang, J. Li, P. Guo, and Q. Lv. Experimental studies on the effect of reynolds and weber numbers on the impact forces of low-speed droplets colliding with a solid surface. *Exp. Fluids*, 58(9):1–12, 2017.
- [128] B. R. Mitchell, J. C. Klewicki, Y. P. Korkolis, and B. L. Kinsey. The transient force profile of low-speed droplet impact: measurements and model. *J. Fluid Mech.*, 867:300–322, 2019.
- [129] R. Zhang, B. Zhang, Q. Lv, J. Li, and P. Guo. Effects of droplet shape on impact force of low-speed droplets colliding with solid surface. *Exp. Fluids*, 60(4):64, 2019.
- [130] V. Bergeron and D. Quéré. Water droplets make an impact. *Phys. World*, 14(5):27, 2001.
- [131] D. Richard, C. Clanet, and D. Quéré. Contact time of a bouncing drop. *Nature*, 417(6891):811–811, 2002.
- [132] T. Onda, S. Shibuichi, N. Satoh, and K. Tsujii. Super-water-repellent fractal surfaces. *Langmuir*, 12(9):2125–2127, 1996.
- [133] A. Tuteja, W. Choi, M. Ma, J. M. Mabry, S. A. Mazzella, G. C. Rutledge, G. H. McKinley, and R. E. Cohen. Designing superoleophobic surfaces. *Science*, 318(5856):1618–1622, 2007.
- [134] H. J. Cho, D. J. Preston, Y. Zhu, and E. N. Wang. Nanoengineered materials for liquid–vapour phase-change heat transfer. *Nat. Rev. Mater.*, 2(2):16092, 2016.
- [135] M. Liu, S. Wang, and L. Jiang. Nature-inspired superwettability systems. *Nat. Rev. Mater.*, 2(7):17036, 2017.
- [136] C. Hao, Y. Liu, X. Chen, J. Li, M. Zhang, Y. Zhao, and Z. Wang. Bioinspired interfacial materials with enhanced drop mobility: From fundamentals to multifunctional applications. *Small*, 12(14):1825–1839, 2016.

- [137] S. Wu, Y. Du, Y. Alsaïd, D. Wu, M. Hua, Y. Yan, B. Yao, Y. Ma, X. Zhu, and X. He. Superhydrophobic photothermal icephobic surfaces based on candle soot. *Proc. Natl. Acad. Sci. U.S.A.*, 117(21):11240–11246, 2020.
- [138] H. Zhan, C. Lu, C. Liu, Z. Wang, C. Lv, and Y. Liu. Horizontal motion of a superhydrophobic substrate affects the drop bouncing dynamics. *Phys. Rev. Lett.*, 126(23):234503, 2021.
- [139] D. Lohse, R. Bergmann, R. Mikkelsen, C. Zeilstra, D. van der Meer, M. Versluis, K. van der Weele, M. van der Hoef, and H. Kuipers. Impact on soft sand: Void collapse and jet formation. *Phys. Rev. Lett.*, 93(19):198003, 2004.
- [140] D. Lohse. Bubble puzzles: From fundamentals to applications. *Phys. Rev. Fluids.*, 3(11):110504, 2018.
- [141] S.-H. Lee, M. Rump, K. Harth, M. Kim, D. Lohse, K. Fezzaa, and J. H. Je. Downward jetting of a dynamic leidenfrost drop. *Phys. Rev. Fluids*, 5(7):074802, 2020.
- [142] S. Mitra, Q. Vo, and T. Tran. Bouncing-to-wetting transition for impact of water droplets on soft solids. *arXiv preprint arXiv:2103.09473*, 2021.
- [143] S. Popinet and collaborators. Basilisk C. [Basilisk](#) (Last accessed: February 1, 2022), 2013-2022.
- [144] A. Gauthier, S. Symon, C. Clanet, and D. Quéré. Water impacting on superhydrophobic macrotextures. *Nat. Commun.*, 6(1):1–6, 2015.
- [145] O. Ramírez-Soto, V. Sanjay, D. Lohse, J. T. Pham, and D. Vollmer. Lifting a sessile oil drop from a superamphiphobic surface with an impacting one. *Sci. Adv.*, 6(34):eaba4330, 2020.
- [146] P. Chantelot and D. Lohse. Drop impact on superheated surfaces: short-time dynamics and transition to contact. *J. Fluid Mech.*, 928:A36, 2021.
- [147] P. Chantelot. *Rebonds spéciaux de liquides*. PhD thesis, Université Paris-Saclay (ComUE), 2018.
- [148] A. H. Woodcock, C. F. Kientzler, A. B. Arons, and D. C. Blanchard. Giant condensation nuclei from bursting bubbles. *Nature*, 172(4390):1144–1145, 1953.

- [149] V. Sanjay, D. Lohse, and M. Jalaal. Bursting bubble in a viscoplastic medium. *J. Fluid Mech.*, 922:A2, 2021.
- [150] J. Moláček and J. W. M. Bush. A quasi-static model of drop impact. *Phys. Fluids*, 24(12):127103, 2012.
- [151] G. Riboux and J. M. Gordillo. Experiments of drops impacting a smooth solid surface: A model of the critical impact speed for drop splashing. *Phys. Rev. Lett.*, 113(2):24507, 2014.
- [152] L. Xu, W. W. Zhang, and S. R. Nagel. Drop splashing on a dry smooth surface. *Phys. Rev. Lett.*, 94(18):184505, 2005.
- [153] A. Jha, P. Chantelot, C. Clanet, and D. Quéré. Viscous bouncing. *Soft Matter*, 16(31):7270–7273, 2020.
- [154] S. Popinet. Numerical models of surface tension. *Annu. Rev. Fluid Mech.*, 50:49–75, 2018.
- [155] S. Popinet and collaborators. Basilisk C: reduced pressure library. [Basilisk](#) (Last accessed: April 4, 2022), 2013-2022.
- [156] A. Prosperetti and G. Tryggvason. *Computational Methods for Multiphase Flow*. Cambridge university press, 2009.
- [157] J. U. Brackbill, D. B. Kothe, and C. Zemach. A continuum method for modeling surface tension. *J. Comput. Phys.*, 100(2):335–354, 1992.
- [158] S. Popinet. An accurate adaptive solver for surface-tension-driven interfacial flows. *J. Comput. Phys.*, 228(16):5838–5866, 2009.
- [159] S. Popinet and collaborators. Basilisk C: surface tension library. [Basilisk](#) (Last accessed: March 31, 2021), 2013-2022.
- [160] L. D. Landau and E. M. Lifshitz. *Fluid Mechanics – Volume 6: Course of Theoretical Physics*. Elsevier, 2 edition, 1987.
- [161] S. Popinet. A quadtree-adaptive multigrid solver for the Serre–Green–Naghdi equations. *J. Comput. Phys.*, 302:336–358, 2015.
- [162] V. Sanjay. Code repository: Impact forces of water drops falling on superhydrophobic surfaces. [GitHub](#) (Last accessed: February 4, 2022), 2022.

- [163] S.-H. Lee, K. Harth, M. Rump, M. Kim, D. Lohse, K. Fezzaa, and J. H. Je. Drop impact on hot plates: contact times, lift-off and the lamella rupture. *Soft Matter*, 16(34):7935–7949, 2020.
- [164] B. R. Mitchell, A. Nassiri, M. R. Locke, J. C. Klewicki, Y. P. Korkolis, and B. L. Kinsey. Experimental and numerical framework for study of low velocity water droplet impact dynamics. In *International Manufacturing Science and Engineering Conference*, volume 49897, page V001T02A047. American Society of Mechanical Engineers, 2016.
- [165] A. S. Grinspan and R. Gnanamoorthy. Impact force of low velocity liquid droplets measured using piezoelectric pvdf film. *Colloids Surf., A*, 356(1-3):162–168, 2010.
- [166] B. Samuel, H. Zhao, and K.-Y. Law. Study of wetting and adhesion interactions between water and various polymer and superhydrophobic surfaces. *J. Phys. Chem. C*, 115(30):14852–14861, 2011.
- [167] V. Liimatainen, M. Vuckovac, V. Jokinen, V. Sariola, M. J. Hokkanen, Q. Zhou, and R. H. A. Ras. Mapping microscale wetting variations on biological and synthetic water-repellent surfaces. *Nat. Commun.*, 8(1):1–7, 2017.
- [168] C. W. Visser, P. E. Frommhold, S. Wildeman, E. Mettin, D. Lohse, and C. Sun. Dynamics of high-speed micro-drop impact: numerical simulations and experiments at frame-to-frame times below 100 ns. *Soft Matter*, 11(9):1708–1722, 2015.
- [169] V. Sanjay. Supplemental movies: Impact forces of water drops falling on superhydrophobic surfaces. [YouTube](#) (Last accessed: April 4, 2022), 2022.
- [170] M. Rein. Phenomena of liquid drop impact on solid and liquid surfaces. *Fluid Dyn. Res.*, 12(2):61, 1993.
- [171] E. Villermaux and B. Bossa. Drop fragmentation on impact. *J. Fluid Mech.*, 668:412–435, 2011.
- [172] S. T. Thoroddsen, T. G. Etoh, and K. Takehara. High-speed imaging of drops and bubbles. *Annu. Rev. Fluid Mech.*, 40:257–285, 2008.

- [173] P. Tsai, S. Pacheco, C. Pirat, L. Lefferts, and D. Lohse. Drop impact upon micro-and nanostructured superhydrophobic surfaces. *Langmuir*, 25(20):12293–12298, 2009.
- [174] A.-L. Biance, F. Chevy, C. Clanet, G. Lagubeau, and D. Quéré. On the elasticity of an inertial liquid shock. *J. Fluid Mech.*, 554:47–66, 2006.
- [175] J. B. Boreyko and C. H. Chen. Self-propelled dropwise condensate on superhydrophobic surfaces. *Phys. Rev. Lett.*, 103(18), 2009.
- [176] T. Mouterde, T.-V. Nguyen, H. Takahashi, C. Clanet, I. Shimoyama, and D. Quéré. How merging droplets jump off a superhydrophobic surface: Measurements and model. *Phys. Rev. Fluids*, 2(11):112001, 2017.
- [177] P. Lecointre, T. Mouterde, A. Checco, C. T. Black, A. Rahman, C. Clanet, and D. Quéré. Ballistics of self-jumping microdroplets. *Phys. Rev. Fluids*, 4(1):013601, 2019.
- [178] B. Zhang, V. Sanjay, S. Shi, Y. Zhao, C. Lv, and D. Lohse. Impact forces of water drops falling on superhydrophobic surfaces. *arXiv Preprint. arXiv:2202.02437*, 2022.
- [179] V. Sanjay. Code repository: When does a drop stop bouncing? [GitHub](#) (Last accessed: April 20, 2022), 2022.
- [180] V. Sanjay, S. Lakshman, P. Chantelot, J. H. Snoeijer, and D. Lohse. Drop impact on viscous liquid films. *In preparation*, 2022.
- [181] L. H. J. Wachters and N. A. J. Westerling. The heat transfer from a hot wall to impinging water drops in the spheroidal state. *Chem. Eng. Sci.*, 21(11):1047–1056, 1966.
- [182] C. A. Galeano-Rios, R. Cimpeanu, I. A. Bauman, A. MacEwen, P. A. Milewski, and D. M. Harris. Capillary-scale solid rebounds: experiments, modelling and simulations. *J. Fluid Mech.*, 912, 2021.
- [183] B. Sarma, A. Dalal, and D. N. Basu. Interfacial dynamics of viscous droplets impacting a superhydrophobic candle soot surface: Overview and comparison. *Phys. Fluids*, 34(1):012121, 2022.
- [184] Y. Tai, Y. Zhao, X. Guo, L. Li, S. Wang, and Z. Xia. Research on the contact time of a bouncing microdroplet with lattice boltzmann method. *Phys. Fluids*, 33(4):042011, 2021.

- [185] F. Chevy, A. Chepelianskii, D. Quéré, and E. Raphaël. Liquid hertz contact: Softness of weakly deformed drops on non-wetting substrates. *Europhys. Lett.*, 100(5):54002, 2012.
- [186] V. Sanjay. Supplemental movies repository: When does a drop stop bouncing? [YouTube](#) (Last accessed: April 4, 2022), 2022.
- [187] D. A. Weiss and A. L. Yarin. Single drop impact onto liquid films: neck distortion, jetting, tiny bubble entrainment, and crown formation. *J. Fluid Mech.*, 385:229–254, 1999.
- [188] A. M. Worthington. *A study of splashes*. London: Longman, Green and Co, 1908.
- [189] R. H. Davis, J. A. Schonberg, and J. M. Rallison. The lubrication force between two viscous drops. *Phys. Fluids A*, 1(1):77–81, 1989.
- [190] S. G. Yiantsios and R. H. Davis. On the buoyancy-driven motion of a drop towards a rigid surface or a deformable interface. *J. Fluid Mech.*, 217:547–573, 1990.
- [191] S. G. Yiantsios and R. H. Davis. Close approach and deformation of two viscous drops due to gravity and van der waals forces. *J. Colloid Interface Sci.*, 144(2):412–433, 1991.
- [192] F. T. Smith, L. Li, and G. X. Wu. Air cushioning with a lubrication/inviscid balance. *J. Fluid Mech.*, 482:291–318, 2003.
- [193] J. de Ruiter, R. Lagraauw, D. van den Ende, and F. Mugele. Wettability-independent bouncing on flat surfaces mediated by thin air films. *Nat. Phys.*, 11(1):48–53, 2015.
- [194] K.-L. Pan and C. K. Law. Dynamics of droplet–film collision. *J. Fluid Mech.*, 587:1–22, 2007.
- [195] C. Hao, J. Li, Y. Liu, X. Zhou, Y. Liu, R. Liu, L. Che, W. Zhou, D. Sun, and L. Li. Superhydrophobic-like tunable droplet bouncing on slippery liquid interfaces. *Nat. Commun.*, 6(1):1–7, 2015.
- [196] X. Tang, A. Saha, C. K. Law, and C. Sun. Bouncing-to-merging transition in drop impact on liquid film: Role of liquid viscosity. *Langmuir*, 34(8):2654–2662, 2018.

- [197] F. Rodriguez and R. Mesler. Some drops don't splash. *J. Colloid Interface Sci.*, 106(2):347–352, 1985.
- [198] I. S. Klyuzhin, F. Ienna, B. Roeder, A. Wexler, and G. H. Pollack. Persisting water droplets on water surfaces. *J. Phys. Chem. B*, 114(44):14020–14027, 2010.
- [199] Z. Wu, J. Hao, J. Lu, L. Xu, G. Hu, and J. M. Floryan. Small droplet bouncing on a deep pool. *Phys. Fluids*, 32(1):012107, 2020.
- [200] Y. Couder, E. Fort, C. H. Gautier, and A. Boudaoud. From bouncing to floating: Noncoalescence of drops on a fluid bath. *Phys. Rev. Lett.*, 94(17):177801, 2005.
- [201] Y. Couder, S. Protiere, E. Fort, and A. Boudaoud. Walking and orbiting droplets. *Nature*, 437(7056):208–208, 2005.
- [202] T. Gilet and J. W. M. Bush. The fluid trampoline: droplets bouncing on a soap film. *J. Fluid Mech.*, 625:167–203, 2009.
- [203] G. E. Charles and S. G. Mason. The coalescence of liquid drops with flat liquid/liquid interfaces. *J. Colloid Interface Sci.*, 15(3):236–267, 1960.
- [204] M. V. Chubynsky, K. I. Belousov, D. A. Lockerby, and J. E. Sprittles. Bouncing off the walls: The influence of gas-kinetic and van der waals effects in drop impact. *Phys. Rev. Lett.*, 124:084501, 2020.
- [205] L. Zhang, T. Soori, A. Rokoni, A. Kaminski, and Y. Sun. Thin film instability driven dimple mode of air film failure during drop impact on smooth surfaces. *Phys. Rev. Fluids*, 6(4):044002, 2021.
- [206] S. T. Thoroddsen, T. G. Etoh, and K. Takehara. Air entrapment under an impacting drop. *J. Fluid Mech.*, 478:125–134, 2003.
- [207] E. Q. Li, I. U. Vakarelski, and S. T. Thoroddsen. Probing the nanoscale: the first contact of an impacting drop. *J. Fluid Mech.*, 785:R2, 2015.
- [208] H. Y. Lo, Y. Liu, and L. Xu. Mechanism of contact between a droplet and an atomically smooth substrate. *Phys. Rev. X*, 7(2):021036, 2017.
- [209] T. Gilet and J. W. M. Bush. Droplets bouncing on a wet, inclined surface. *Phys. Fluids*, 24(12):122103, 2012.

- [210] M. Pack, H. Hu, D. Kim, Z. Zheng, H. A. Stone, and Y. Sun. Failure mechanisms of air entrainment in drop impact on lubricated surfaces. *Soft Matter*, 13(12):2402–2409, 2017.
- [211] S. Lakshman, W. Tewes, K. Harth, J. H. Snoeijer, and D. Lohse. Deformation and relaxation of viscous thin films under bouncing drops. *J. Fluid Mech.*, 920, 2021.
- [212] A. Prosperetti. Viscous effects on perturbed spherical flows. *Q. Appl. Math.*, 34(4):339–352, 1977.
- [213] K. Okumura, F. Chevy, D. Richard, D. Quéré, and C. Clanet. Water spring: A model for bouncing drops. *Europhys. Lett.*, 62(2):237, 2003.
- [214] T. M. Schutzius, S. Jung, T. Maitra, G. Graeber, M. Köhme, and D. Poulikakos. Spontaneous droplet trampolining on rigid superhydrophobic surfaces. *Nature*, 527(7576):82–85, 2015.
- [215] P. Chantelot, M. Coux, C. Clanet, and D. Quéré. Drop trampoline. *Europhys. Lett.*, 124(2):24003, 2018.
- [216] D. Terwagne, F. Ludewig, N. Vandewalle, and S. Dorbolo. The role of the droplet deformations in the bouncing droplet dynamics. *Phys. Fluids*, 25(12):122101, 2013.
- [217] O. W. Jayaratne and B. J. Mason. The coalescence and bouncing of water drops at an air/water interface. *Proc. R. Soc. London, Ser. A*, 280(1383):545–565, 1964.
- [218] P. K. Sharma and H. N. Dixit. Regimes of wettability-dependent and wettability-independent bouncing of a drop on a solid surface. *J. Fluid Mech.*, 908, 2021.
- [219] F. Reizman. Optical thickness measurement of thin transparent films on silicon. *J. Appl. Phys.*, 36(12):3804–3807, 1965.
- [220] M. C. Naru. *Numerical Simulation of a Water/Oil Emulsion in a Multi-scale/Multiphysics context*. PhD thesis, EDsorbonne University, 2021.
- [221] V. Sanjay. Code repository: Drop impact on viscous liquid films. [GitHub](#) (Last accessed: April 1, 2022), 2022.

- [222] C. Josserand, P. Ray, and S. Zaleski. Droplet impact on a thin liquid film: anatomy of the splash. *J. Fluid Mech.*, 802:775–805, 2016.
- [223] Y. Ling, D. Fuster, S. Zaleski, and G. Tryggvason. Spray formation in a quasiplanar gas-liquid mixing layer at moderate density ratios: a numerical closeup. *Phys. Fluids*, 2(1):014005, 2017.
- [224] J. Zhang, M.-J. Ni, and J. Magnaudet. Three-dimensional dynamics of a pair of deformable bubbles rising initially in line. part 1. moderately inertial regimes. *J. Fluid Mech.*, 920:A16, 2021.
- [225] L. G. Leal. *Advanced transport phenomena: fluid mechanics and convective transport processes*, volume 7. Cambridge University Press, 2007.
- [226] C. A. Galeano-Rios, P. A. Milewski, and J.-M. Vanden-Broeck. Non-wetting impact of a sphere onto a bath and its application to bouncing droplets. *J. Fluid Mech.*, 826:97–127, 2017.
- [227] V. Sanjay, P. Chantelot, and D. Lohse. When does a drop stop bouncing? *In preparation*, 2022.
- [228] X. Tang, A. Saha, C.K. Law, and C. Sun. Nonmonotonic response of drop impacting on liquid film: mechanism and scaling. *Soft Matter*, 12(20):4521–4529, 2016.
- [229] V. Sanjay. Supplemental movies repository: Drop impact on viscous liquid films. [YouTube](#) (Last accessed: April 4, 2022), 2022.
- [230] N. Wadhwa, P. Vlachos, and S. Jung. Noncoalescence in the oblique collision of fluid jets. *Phys. Rev. Lett.*, 110(12), 2013.
- [231] H. P. Kavehpour. Coalescence of drops. *Annu. Rev. Fluid Mech.*, 47:245–268, 2015.
- [232] G. Finotello, R. F. Kooiman, J. T. Padding, K. A. Buist, A. Jongsma, F. Innings, and J. A. M. Kuipers. The dynamics of milk droplet–droplet collisions. *Exp. Fluids*, 59(1):1–19, 2018.
- [233] A. Latka, A. M. P Boelens, S. R. Nagel, and J. J. de Pablo. Drop splashing is independent of substrate wetting. *Phys. Fluids*, 30(2):22105, 2018.

- [234] S. Adera, R. Raj, R. Enright, and E. N. Wang. Non-wetting droplets on hot superhydrophilic surfaces. *Nat. Commun.*, 4(1):1–7, 2013.
- [235] J. T. Pham, M. Paven, S. Wooh, T. Kajiya, H.-J. Butt, and D. Vollmer. Spontaneous jumping, bouncing and trampolining of hydrogel drops on a heated plate. *Nat. Commun.*, 8(1):1–9, 2017.
- [236] C. Tang, P. Zhang, and C. K. Law. Bouncing, coalescence, and separation in head-on collision of unequal-size droplets. *Phys. Fluids*, 24(2):22101, 2012.
- [237] T. C. Sykes, A. A. Castrejón-Pita, J. R. Castrejón-Pita, D. Harbottle, Z. Khatir, H. M. Thompson, and M. C. T. Wilson. Surface jets and internal mixing during the coalescence of impacting and sessile droplets. *Phys. Rev. Fluids*, 5(2):023602, 2020.
- [238] V. Bergeron, D. Bonn, J. Y. Martin, and L. Vovelle. Controlling droplet deposition with polymer additives. *Nature*, 405(6788):772–775, 2000.
- [239] C. Sturgess, C. J. Tuck, I. A. Ashcroft, and R. D. Wildman. 3d reactive inkjet printing of polydimethylsiloxane. *J. Mater. Chem. C*, 5(37):9733–9745, 2017.
- [240] M. A. Skylar-Scott, J. Mueller, C.W. Visser, and J. A. Lewis. Vox-elated soft matter via multimaterial multinozzle 3D printing. *Nature*, 575(7782):330–335, 2019.
- [241] J. Lv, Y. Song, L. Jiang, and J. Wang. Bio-inspired strategies for anti-icing. *ACS nano*, 8(4):3152–3169, 2014.
- [242] M. M. Farhangi, P. J. Graham, N. R. Choudhury, and A. Dolatabadi. Induced detachment of coalescing droplets on superhydrophobic surfaces. *Langmuir*, 28(2):1290–1303, 2012.
- [243] M. Damak and K. Varanasi. Expansion and retraction dynamics in drop-on-drop impacts on nonwetting surfaces. *Phys. Rev. Fluids*, 3(9), 2018.
- [244] F. Liu, G. Ghigliotti, J. J. Feng, and C. H. Chen. Numerical simulations of self-propelled jumping upon drop coalescence on non-wetting surfaces. *J. Fluid Mech.*, 752:39–65, 2014.

- [245] P. J. Graham, M. M. Farhangi, and A. Dolatabadi. Dynamics of droplet coalescence in response to increasing hydrophobicity. *Phys. Fluids*, 24(11), 2012.
- [246] J. R. Castrejón-Pita, K. J. Kubiak, A. A. Castrejón-Pita, M. C.T. Wilson, and I. M. Hutchings. Mixing and internal dynamics of droplets impacting and coalescing on a solid surface. *Phys. Rev. E*, 88(2), 2013.
- [247] H. Tavana, N. Petong, A. Hennig, K. Grundke, and A. W. Neumann. Contact angles and coating film thickness. *J. Adhes.*, 81(1):29–39, 2005.
- [248] S. Pan, R. Guo, M. Björnalm, J. J. Richardson, L. Li, C. Peng, N. Bertleff-Zieschang, W. Xu, J. Jiang, and F. Caruso. Coatings superrepellent to ultralow surface tension liquids. *Nat. Mater.*, 17(11):1040–1047, 2018.
- [249] P. Papadopoulos, D. Vollmer, and H.-J. Butt. Long-term repellency of liquids by superoleophobic surfaces. *Phys. Rev. Lett.*, 117(4), 2016.
- [250] H.-J. Butt, C. Semprebon, P. Papadopoulos, D. Vollmer, M. Brinkmann, and M. Ciccotti. Design principles for superamphiphobic surfaces. *Soft Matter*, 9(2):418–428, 2013.
- [251] X. Deng, F. Schellenberger, P. Papadopoulos, D. Vollmer, and H.-J. Butt. Liquid drops impacting superamphiphobic coatings. *Langmuir*, 29(25):7847–7856, 2013.
- [252] L. Moevius, Y. Liu, Z. Wang, and J. M. Yeomans. Pancake bouncing: Simulations and theory and experimental verification. *Langmuir*, 30(43):13021–13032, 2014.
- [253] X. Deng, L. Mammen, H.-J. Butt, and D. Vollmer. Candle soot as a template for a transparent robust superamphiphobic coating. *Science*, 335(6064):67–70, 2012.
- [254] M. Andrew, J. M. Yeomans, and D. O. Pushkin. A solvable model of axisymmetric and non-axisymmetric droplet bouncing. *Soft Matter*, 13(5):985–994, 2017.
- [255] F. Schellenberger, N. Encinas, D. Vollmer, and H.-J. Butt. How water advances on superhydrophobic surfaces. *Phys. Rev. Lett.*, 116(9), 2016.
- [256] D. Quéré. Fakir droplets. *Nat. Mater.*, 1(1):14–15, 2002.

- [257] A. I. ElSherbini and A. M. Jacobi. Retention forces and contact angles for critical liquid drops on non-horizontal surfaces. *J. Colloid Interface Sci.*, 299(2):841–849, 2006.
- [258] V. Sanjay. Code repository: Lifting a sessile drop. GitHub (Last accessed: April 4, 2022), 2020.
- [259] V. Sanjay. Supplemental movies repository: Lifting a sessile drop. YouTube (Last accessed: April 4, 2022), 2020.
- [260] C. Clanet. Waterbells and liquid sheets. *Annu. Rev. Fluid Mech.*, 39: 469–496, 2007.
- [261] G. I. Taylor. The dynamics of thin-sheets of fluid. I. water bells. *Proc. R. Soc. London, Ser. A*, 253(1274):289–295, 1959.
- [262] G. I. Taylor and D. H. Michael. On making holes in a sheet of fluid. *J. Fluid Mech.*, 58(4):625–639, 1973.
- [263] L. Bourouiba. The fluid dynamics of disease transmission. *Annu. Rev. Fluid Mech.*, 53:473–508, 2021.
- [264] C. Summerhayes. Deep water—the gulf oil disaster and the future of offshore drilling. *Underw. Technol.*, 30(2):113–115, 2011.
- [265] G. Sünderhauf, H. Raszillier, and F. Durst. The retraction of the edge of a planar liquid sheet. *Phys. Fluids*, 14:198–208, 2002.
- [266] W. E. Ranz. Some experiments on the dynamics of liquid films. *J. Appl. Phys.*, 30:1950–1955, 1959.
- [267] A. B. Pandit and J. F. Davidson. Hydrodynamics of the rupture of thin liquid films. *J. Fluid Mech.*, 212:11–24, 1990.
- [268] J. B. Keller. Breaking of liquid films and threads. *Phys. Fluids*, 26: 3451–3453, 1983.
- [269] G. Debrégeas, P. Martin, and F. Brochard-Wyart. Viscous bursting of suspended films. *Phys. Rev. Lett.*, 75:3886–3889, 1995.
- [270] G. Debrégeas, P.-G. de Gennes, and F. Brochard-Wyart. The life and death of “bare” viscous bubbles. *Sci. (80-.)*, 279:1704–1707, 1998.

- [271] M. P. Brenner and D. Gueyffier. On the bursting of viscous films. *Phys. Fluids*, 11:737–739, 1999.
- [272] K. Dalnoki-Veress, B. G. Nickel, C. Roth, and J. R. Dutcher. Hole formation and growth in freely standing polystyrene films. *Phys. Rev. E*, 59:2153–2156, 1999.
- [273] D. Tammaro, R. Pasquino, M. M. Villone, G. D’ Avino, V. Ferraro, E. Di Maio, A. Langella, N. Grizzuti, and P. L. Maffettone. Elasticity in bubble rupture. *Langmuir*, 34:5646–5654, 2018.
- [274] M. M. Villone, M. A. Hulsen, and P. L. Maffettone. Numerical simulations of viscoelastic film stretching and relaxation. *J. Non-Newtonian Fluid Mech.*, 266:118–126, 2019.
- [275] P. M. Kamat, C. R. Anthony, and O. A. Basaran. Bubble coalescence in low-viscosity power-law fluids. *J. Fluid Mech.*, 902:A8, 2020.
- [276] U. Sen, C. Datt, T. Segers, H. Wijshoff, J. H. Snoeijer, M. Versluis, and D. Lohse. The retraction of jetted slender viscoelastic liquid filaments. *J. Fluid Mech.*, 929:A25, 2021.
- [277] C. Redon, F. Brochard-Wyart, and F. Rondelez. Dynamics of dewetting. *Phys. Rev. Lett.*, 66:715–718, 1991.
- [278] F. Brochard-Wyart, P. Martin, and C. Redon. Liquid/liquid dewetting. *Langmuir*, 9:3682–3690, 1993.
- [279] K. R. Shull and T. E. Karis. Dewetting dynamics for large equilibrium contact angles. *Langmuir*, 10:334–339, 1994.
- [280] C. Andrieu, C. Sykes, and F. Brochard. Dynamics of fast dewetting on model solid substrates. *J. Adhes.*, 58:15–24, 1996.
- [281] P. Lambooy, K. C. Phelan, O. Haugg, and G. Krausch. Dewetting at the liquid-liquid interface. *Phys. Rev. Lett.*, 76:1110–1113, 1996.
- [282] H. Haidara, L. Vonna, and J. Schultz. Instability and dewetting of confined thin liquid films in nonmiscible external bulk fluids (water and aqueous surfactant solutions): experiments versus theoretical predictions. *Langmuir*, 14:3425–3434, 1998.

- [283] A. Buguin, L. Vovelle, and F. Brochard-Wyart. Shocks in inertial dewetting. *Phys. Rev. Lett.*, 83:1183–1186, 1999.
- [284] N. Péron, F. Brochard-Wyart, and H. Duval. Dewetting of low-viscosity films at solid/liquid interfaces. *Langmuir*, 28:15844–15852, 2012.
- [285] D. Peschka, S. Bommer, S. Jachalski, R. Seemann, and B. Wagner. Impact of energy dissipation on interface shapes and on rates for dewetting from liquid substrates. *Sci. Rep.*, 8:13295, 2018.
- [286] C. Lv, C. Clanet, and D. Quéré. Retraction of large liquid strips. *J. Fluid Mech.*, 778:R6, 2015.
- [287] T. Trittel, T. John, K. Tsuji, and R. Stannarius. Rim instability of bursting thin smectic films. *Phys. Fluids*, 25:52106, 2013.
- [288] P. C. Petit, M. Le Merrer, and A.-L. Biance. Holes and cracks in rigid foam films. *J. Fluid Mech.*, 774:R3, 2015.
- [289] C. Vernay, L. Ramos, and C. Liguore. Bursting of dilute emulsion-based liquid sheets driven by a Marangoni effect. *Phys. Rev. Lett.*, 115:198302, 2015.
- [290] K. J. Mysels and B. R. Vijayendran. Film bursting. V. The effect of various atmospheres and the anomaly of Newton Black films. *J. Phys. Chem.*, 77:1692–1694, 1973.
- [291] J.-F. Joanny and P. G. de Gennes. Bursting of a soap film in a viscous environment. *Physica A*, 147A:238–255, 1987.
- [292] É. Reyssat and D. Quéré. Bursting of a fluid film in a viscous environment. *Eur. Lett.*, 76:236–242, 2006.
- [293] Z. Jian, P. Deng, and M.-J. Thoraval. Air sheet contraction. *J. Fluid Mech.*, 899:A7, 2020.
- [294] P. Martin, A. Buguin, and F. Brochard-Wyart. Bursting of a liquid film on a liquid substrate. *Eur. Lett.*, 28:421–426, 1994.
- [295] H. A. Stone and L. G. Leal. Relaxation and breakup of an initially extended drop in an otherwise quiescent fluid. *J. Fluid Mech.*, 198:399–427, 1989.

- [296] Z. Jian, M. A. Channa, A. Kherbeche, H. Chizari, S. T. Thoroddson, and M.-J. Thoraval. To split or not to split: dynamics of an air disk formed under a drop impacting on a pool. *Phys. Rev. Lett.*, 124(18):184501, 2020.
- [297] C. R. Anthony, M. T. Harris, and O. A. Basaran. Initial regime of drop coalescence. *Phys. Rev. Fluids*, 5(3):33608, 2020.
- [298] J. D. Paulsen, J. C. Burton, S. R. Nagel, S. Appathurai, M. T. Harris, and O. A. Basaran. The inexorable resistance of inertia determines the initial regime of drop coalescence. *Proc. Natl. Acad. Sci. U.S.A.*, 109:6857–6861, 2012.
- [299] J. D. Paulsen. Approach and coalescence of liquid drops in air. *Phys. Rev. E*, 88(6):63010, 2013.
- [300] J. Feng, M. Roché, D. Vigolo, L. N. Arnaudov, S. D. Stoyanov, T. D. Gurkov, G. G. Tsutsumanova, and H. A. Stone. Nanoemulsions obtained via bubble-bursting at a compound interface. *Nat. Phys.*, 10(8):606–612, 2014.
- [301] J. Feng, M. Muradoglu, H. Kim, J. T. Ault, and H. A. Stone. Dynamics of a bubble bouncing at a liquid/liquid/gas interface. *J. Fluid Mech.*, 807:324–352, 2016.
- [302] F. Peters and D. Arabali. Interfacial tension between oil and water measured with a modified contour method. *Colloids Surf. A Physicochem. Eng. Asp.*, 426:1–5, 2013.
- [303] D. Vaynblat, J. R. Lister, and T. P. Witelski. Rupture of thin viscous films by van der Waals forces: evolution and self-similarity. *Phys. Fluids*, 13:1130–1140, 2001.
- [304] J. Schindelin, I. Aganda-Carreras, and E. Frise. Fiji: an open-source platform for biological image analysis. *Nat. Meth.*, 9:676–682, 2012.
- [305] G. Oldenziel, R. Delfos, and J. Westerweel. Measurements of liquid film thickness for a droplet at a two-fluid interface. *Phys. Fluids*, 24:22106, 2012.
- [306] H. de Maleprade, C. Clanet, and D. Quéré. Spreading of bubbles after contacting the lower side of an aerophilic slide immersed in water. *Phys. Rev. Lett.*, 117(9):094501, 2016.

- [307] Y. Li, C. Diddens, T. Segers, H. Wijshoff, M. Versluis, and D. Lohse. Evaporating droplets on oil-wetted surfaces: suppression of the coffee-stain effect. *Proc. Natl. Acad. Sci. U.S.A.*, 117:16756–16763, 2020.
- [308] H. Aryafar and H. P. Kavehpour. Hydrodynamic instabilities of viscous coalescing droplets. *Phys. Rev. E*, 78:37302, 2008.
- [309] I. Cohen and S. R. Nagel. Scaling the selective withdrawal transition through a tube suspended above the fluid surface. *Phys. Rev. Lett.*, 88:74501, 2002.
- [310] S. du Pont and J. Eggers. Sink flow deforms the interface between a viscous liquid and air into a tip singularity. *Phys. Rev. Lett.*, 96:34501, 2006.
- [311] S. du Pont and J. Eggers. Fluid interfaces with very sharp tips in viscous flows. *Proc. Natl. Acad. Sci. U.S.A.*, 117:32238–32243, 2020.
- [312] J. M. Montanero and A. M. Gañán-Calvo. Dripping, jetting and tip streaming. *Rep. Prog. Phys.*, 83:97001, 2020.
- [313] Y.-H. Tseng and A. Prosperetti. Local interfacial stability near a zero vorticity point. *J. Fluid Mech.*, 776:5–36, 2015.
- [314] A. Eri and K. Okumura. Bursting of a thin film in a confined geometry: rimless and constant-velocity dewetting. *Phys. Rev. E*, 82(3):030601, 2010.
- [315] V. Sanjay. Code repository: Taylor-Culick retractions. [GitHub](#) (Last accessed: February 1, 2022), 2021.
- [316] V. Sanjay, U. Jain, M. Jalaal, D. van der Meer, and D. Lohse. Droplet encapsulation. In *APS Div. Fluid Dyn. Meet. Abstr.*, pages B22–001, 2019.
- [317] V. Sanjay. Basilisk sandbox: Three-Phase. [Basilisk](#) (Last accessed: February 1, 2022), 2021.
- [318] Z. Mou, Z. Zheng, Z. Jian, C. Antonini, C. Josserand, and M.-J. Thoraval. Singular jets in compound drop impact. *arXiv Preprint. arXiv:2112.05284*, 2021.

- [319] J. Berthier and K. A. Brakke. *The physics of microdroplets*. John Wiley & Sons, 2012.
- [320] D. Bonn, J. Eggers, J. Indekeu, J. Meunier, and E. Rolley. Wetting and spreading. *Rev. Mod. Phys.*, 81(2):739, 2009.
- [321] M.-J. Thoraval and S. T. Thoroddsen. Contraction of an air disk caught between two different liquids. *Phys. Rev. E*, 88:061001(R), 2013.
- [322] S. Afkhami, J. Buongiorno, A. Guion, S. Popinet, Y. Saade, R. Scardovelli, and S. Zaleski. Transition in a numerical model of contact line dynamics and forced dewetting. *J. Comput. Phys.*, 374:1061–1093, 2018.
- [323] C. Cuttle, A. B. Thompson, D. Pihler-Puzović, and A. Juel. The engulfment of aqueous droplets on perfectly wetting oil layers. *J. Fluid Mech.*, 915:A66, 2021.
- [324] H. Lhuissier and E. Villermaux. Soap films burst like flapping flags. *Phys. Rev. Lett.*, 103:54501, 2009.
- [325] J. G. E. M. Fraaije and A. M. Cazabat. Dynamics of spreading on a liquid substrate. *J. Colloid Interface Sci.*, 133:452–460, 1989.
- [326] M. Reddy, M. Manivannan, M. G. Basavaraj, and S. P. Thampi. Statics and dynamics of drops spreading on a liquid-liquid interface. *Phys. Rev. Fluids*, 5:104006, 2020.
- [327] H. Lamb. *Hydrodynamics*. Cambridge University Press, sixth edition, 1975.
- [328] J. Happel and H. Brenner. *Low Reynolds number hydrodynamics: with special applications to particulate media*, volume 1. Springer Science & Business Media, 2012.
- [329] P.-G. de Gennes. Wetting: statics and dynamics. *Rev. Mod. Phys.*, 57:827–863, 1985.
- [330] A. Marchand, T. S. Chan, J. H. Snoeijer, and B. Andreotti. Air entrainment by contact lines of a solid plate plunged into a viscous fluid. *Phys. Rev. Lett.*, 108:204501, 2012.
- [331] J. H. Snoeijer and B. Andreotti. Moving contact lines: scales, regimes, and dynamical transitions. *Annu. Rev. Fluid Mech.*, 45:269–292, 2013.

- [332] L. Doubliez. The drainage and rupture of a non-foaming liquid film formed upon bubble impact with a free surface. *Int. J. Multiphase Flow*, 17:783–803, 1991.
- [333] S. T. Thoroddsen, M.-J. Thoraval, K. Takehara, and T. G. Etoh. Microbubble morphologies following drop impacts onto a pool surface. *J. Fluid Mech.*, 708:469–479, 2012.
- [334] T. Bohr and B. Scheichl. Surface tension and energy conservation in a moving fluid. *Phys. Rev. Fluids*, 6(5):L052001, 2021.
- [335] D. P. Hoult. Oil spreading on the sea. *Annu. Rev. Fluid Mech.*, 4(1):341–368, 1972.
- [336] L. Gordillo, G. Agbaglah, L. Duchemin, and C. Josserand. Asymptotic behavior of a retracting two-dimensional fluid sheet. *Phys. Fluids*, 23(12):122101, 2011.
- [337] V. Sanjay. Supplemental movies: Taylor-Culick retractions. YouTube (Last accessed: April 4, 2022), 2022.
- [338] G. Liger-Belair, G. Polidori, and P. Jeandet. Recent advances in the science of champagne bubbles. *Chem. Soc. Rev.*, 37(11):2490–2511, 2008.
- [339] S. Poulain and L. Bourouiba. Biosurfactants change the thinning of contaminated bubbles at bacteria-laden water interfaces. *Phys. Rev. Lett.*, 121(20):204502, 2018.
- [340] F. MacIntyre. Flow patterns in breaking bubbles. *J. Geophys. Res.*, 77(27):5211–5228, 1972.
- [341] D. Singh and A. K. Das. Numerical investigation of the collapse of a static bubble at the free surface in the presence of neighbors. *Phys. Rev. Fluids*, 4(2):23602, 2019.
- [342] H. M. Gonnermann and M. Manga. The fluid mechanics inside a volcano. *Annu. Rev. Fluid Mech.*, 39:321–356, 2007.
- [343] Y. Toba. Drop production by bursting of air bubbles on the sea surface (II) theoretical study on the shape of floating bubbles. *J. Ocean. Soc. Jpn.*, 15(3):121–130, 1959.

- [344] H. M. Princen. Shape of a fluid drop at a liquid-liquid interface. *J. Colloid Sci.*, 18(2):178–195, 1963.
- [345] E. Ghabache and T. Séon. Size of the top jet drop produced by bubble bursting. *Phys. Rev. Fluids*, 1(5):51901, 2016.
- [346] P. L. L. Walls, L. Henaux, and J. C. Bird. Jet drops from bursting bubbles: How gravity and viscosity couple to inhibit droplet production. *Phys. Rev. E*, 92(2):21002, 2015.
- [347] J. M. Boulton-Stone and J. R. Blake. Gas bubbles bursting at a free surface. *J. Fluid Mech.*, 254:437–466, 1993.
- [348] M. S. Longuet-Higgins and H. Oguz. Critical microjets in collapsing cavities. *J. Fluid Mech.*, 290:183–201, 1995.
- [349] S. Popinet. Gerris: a tree-based adaptive solver for the incompressible Euler equations in complex geometries. *J. Comput. Phys.*, 190(2):572–600, 2003.
- [350] N. Dubash and I. Frigaard. Conditions for static bubbles in viscoplastic fluids. *Phys. Fluids*, 16(12):4319–4330, 2004.
- [351] B. Sun, S. Pan, J. Zhang, X. Zhao, Y. Zhao, and Z. Wang. A dynamic model for predicting the geometry of bubble entrapped in yield stress fluid. *Chem. Eng. J.*, 391:123569, 2020.
- [352] M. de Corato, B. Saint-Michel, G. Makrigiorgos, Y. Dimakopoulos, J. Tsamopoulos, and V. Garbin. Oscillations of small bubbles and medium yielding in elastoviscoplastic fluids. *Phys. Rev. Fluids*, 4(7):73301, 2019.
- [353] D. Sikorski, H. Tabuteau, and J. R. de Bruyn. Motion and shape of bubbles rising through a yield-stress fluid. *J. Non-Newton. Fluid Mech.*, 159(1-3):10–16, 2009.
- [354] M. K. Tripathi, K. C. Sahu, G. Karapetsas, and O. K. Matar. Bubble rise dynamics in a viscoplastic material. *J. Non-Newton. Fluid Mech.*, 222:217–226, 2015.
- [355] W. F. Lopez, M. F. Naccache, and P. R. de Souza Mendes. Rising bubbles in yield stress materials. *J. Rheol.*, 62(1):209–219, 2018.

- [356] J. P. Singh and M. M. Denn. Interacting two-dimensional bubbles and droplets in a yield-stress fluid. *Phys. Fluids*, 20(4):40901, 2008.
- [357] Y. Dimakopoulos, M. Pavlidis, and J. Tsamopoulos. Steady bubble rise in Herschel–Bulkley fluids and comparison of predictions via the augmented Lagrangian method with those via the Papanastasiou model. *J. Non-Newton. Fluid Mech.*, 200:34–51, 2013.
- [358] J. Tsamopoulos, Y. Dimakopoulos, N. Chatzidai, G. Karapetsas, and M. Pavlidis. Steady bubble rise and deformation in Newtonian and viscoplastic fluids and conditions for bubble entrapment. *J. Fluid Mech.*, 601:123–164, 2008.
- [359] N. Mougins, A. Magnin, and J.-M. Piau. The significant influence of internal stresses on the dynamics of bubbles in a yield stress fluid. *J. Non-Newton. Fluid Mech.*, 171:42–55, 2012.
- [360] M. Jalaal and N. J. Balmforth. Long bubbles in tubes filled with viscoplastic fluid. *J. Non-Newton. Fluid Mech.*, 238:100–106, 2016.
- [361] B. Laborie, F. Rouyer, D. E. Angelescu, and E. Lorenceau. Yield-stress fluid deposition in circular channels. *J. Fluid Mech.*, 818(2):838–851, 2017.
- [362] P. Zamankhan, S. Takayama, and J. B. Grotberg. Steady displacement of long gas bubbles in channels and tubes filled by a bingham fluid. *Phys. Rev. Fluids*, 3(1):13302, 2018.
- [363] M. Deserno. Notes on differential geometry. https://www.cmu.edu/biolphys/deserno/pdf/diff_geom.pdf (Last accessed: March 31, 2021), 2004.
- [364] J. Magnaudet and M. J. Mercier. Particles, drops, and bubbles moving across sharp interfaces and stratified layers. *Annu. Rev. Fluid Mech.*, 52:61–91, 2020.
- [365] Al Pourzahedi, E. Chaparian, A. Roustaei, and I. A. Frigaard. Flow onset for a single bubble in a yield-stress fluid. *J. Fluid Mech.*, 933:A21, 2022.
- [366] M. Jalaal, M. K. Schaarsberg, C.-W. Visser, and D. Lohse. Laser-induced forward transfer of viscoplastic fluids. *J. Fluid Mech.*, 880:497–513, 2019.

- [367] S. Gekle, J. M. Gordillo, D. van der Meer, and D. Lohse. High-speed jet formation after solid object impact. *Phys. Rev. Lett.*, 102(3):34502, 2009.
- [368] S. Krishnan, E. J. Hopfinger, and B. A. Puthenveettil. On the scaling of jetting from bubble collapse at a liquid surface. *J. Fluid Mech.*, 822:791–812, 2017.
- [369] J. S. Lee, B. M. Weon, S. J. Park, J. H. Je, K. Fezzaa, and W.-K. Lee. Size limits the formation of liquid jets during bubble bursting. *Nat. Commun.*, 2(1):1–7, 2011.
- [370] B. M. Rauzan, A. Z. Nelson, S. E. Lehman, R. H. Ewoldt, and R. G. Nuzzo. Particle-free emulsions for 3d printing elastomers. *Adv. Funct. Mater.*, 28(21):1707032, 2018.
- [371] A. Z. Nelson, K. S. Schweizer, B. M. Rauzan, R. G. Nuzzo, J. Vermant, and R. H. Ewoldt. Designing and transforming yield-stress fluids. *Curr. Opin. Solid State Mater. Sci.*, 23(5):100758, 2019.
- [372] M. Jalaal, B. Stoeber, and N. J. Balmforth. Spreading of viscoplastic droplets. *J. Fluid Mech.*, 914:A21, 2021.
- [373] V. Sanjay. Code repository: Bursting bubble in a viscoplastic medium. [GitHub](#) (Last accessed: March 31, 2021), 2020.
- [374] I. A. Frigaard and C. Nouar. On the usage of viscosity regularisation methods for visco-plastic fluid flow computation. *J. Non-Newton. Fluid Mech.*, 127(1):1–26, 2005.
- [375] V. Sanjay. Supplemental movies repository: Bursting bubble in a viscoplastic medium. [YouTube](#) (Last accessed: April 4, 2022), 2020.
- [376] D. Lohse and X. Zhang. Physicochemical hydrodynamics of droplets out of equilibrium. *Nat. Rev. Phys.*, 2(8):426–443, 2020.

Summary

This thesis investigates several free-surface phenomena to illustrate the role of viscous stresses. In part I (chapters 1–4), we study the impact of spherical liquid drops on non-wetting substrates, while in part II (chapters 5–6), we focus on capillary-driven retraction of films and bursting of free-surface bubbles.

In **chapter 1**, we study water drops impacting non-wetting substrates and find that not only is the inertial shock at impact associated with a distinct peak in the temporal evolution of the normal force, but so is the jump-off, which was hitherto unknown. Furthermore, the inertial pressure force sets the magnitude of both these peaks in the normal reaction force. Surprisingly, some low-velocity impacts can lead to a remarkably high second peak in the normal force, which can even be three times larger than the first. This enhancement can be attributed to the collapse of an air cavity inside the liquid drop leading to singular Worthington jets. Our results thus give a fundamental understanding of the drop impact dynamics on a non-wetting surface and the forces associated with it. Such insight is crucial to developing countermeasures to the failure of superhydrophobicity in technological applications (for example, by avoiding the regime with high impact forces).

In **chapter 2**, we delineate the bouncing to the non-bouncing transition of drops falling on a non-wetting substrate. Throughout the drop impact process, viscous dissipation enervates internal momentum. A drop will cease bouncing and stay on the substrate if its upward momentum (driven by capillarity and resisted by viscous stresses) after the drop impact, spreading, and retraction process is insufficient to overcome gravity. Indeed, gravity and viscosity conspire to inhibit drop bouncing off non-wetting substrates. We further observe that close to this transition, the rebound process is independent of the impact parameters. This observation disentangles the later stages of the rebound from the initial impact dynamics. These results are helpful in applications where drop bouncing must be suppressed, for example, inkjet printing, cooling ap-

plications, pesticides application, and criminal forensics.

In **chapter 3**, we investigate drops bouncing off viscous liquid films that mimic atomically smooth substrates. The repellent behavior of such substrates requires the presence of an air layer trapped between the impacting drop and the liquid film. Drops impacting on viscous liquid films show two distinct bouncing regimes: (i) the substrate-independent and (ii) substrate-dependent bouncing. In the former, the impact dynamics are not affected by the presence of the viscous film owing to its high viscosity or negligible thickness. However, in the latter, both the drop and film properties influence the rebound dynamics and govern the bouncing to non-bouncing transition. On the other hand, within the substrate-independent limit, repellency is suppressed once the drop viscosity exceeds a critical value as on superamphiphobic substrates discussed in chapter 2.

In **chapter 4**, we find that in the presence of a non-wetting substrate, the drop-on-drop impact results in five rebound scenarios, four of which do not involve coalescence. The impacting drop lifts a lazy sessile one in two of the four rebound scenarios. If sufficient energy is transferred between the drops, both drops can take off the substrate, while in some cases, the impacting drop kicks the sessile drop off the substrate but itself cannot bounce. Furthermore, one-to-one comparisons between the experimentally and numerically determined drop boundaries and center of mass mechanical energies illustrate the power of the direct numerical simulations for quantitatively predicting the dynamics of drop-on-drop impact. Insights from chapters 3 and 4 are essential because, for most industrial applications, such as inkjet printing or additive manufacturing, droplets are deposited on a pre-existing layer of another drop or film. Hence, the relative precision of the drop deposition and its shape evolution may decide the success or failure of these devices.

Note that although we do direct numerical simulations of the several drop impact scenarios in chapters 1–4, we do so using the continuum equations. Consequently, our numerical method is inadequate to predict whether or not a drop will coalesce with another drop or the substrate. We take this information from the experiments. Indeed the coalescence or non-coalescence of interfaces depends on several multi-physics aspects, including surface asperities and van der Waals forces. Prediction of such coalescence (or rupture) behaviors is beyond the scope of the present thesis. Still, one can couple a consistent molecular dynamics technique (like gas kinetic theory) with the continuum-based volume of fluid method to bridge this lacuna in our model in the future.

In **chapter 5**, we show that even when the surrounding medium inter-

acts with the Taylor-Culick retraction of a film, the film still retracts with a constant velocity, provided that it is long enough to avoid finite film size and internal viscous effects. However, both the inertia and viscosity of the surroundings influence the magnitude of this constant velocity. Even when the surroundings have negligible viscosity, they still influence the retraction process through inertial (added mass-like) effects. On the other hand, for highly viscous surroundings, viscous dissipation dictates the retraction velocity scale. The exact nature of this variation depends on the geometry of the canonical configuration in question. For example, for retracting sheets submerged in a viscous oil, the retraction velocity scales with the visco-capillary velocity (i.e., the capillary number is a constant). However, the capillary number shows a power-law behavior for sheets retracting at an oil-air interface with the dimensionless viscosity (Ohnesorge number) of the surrounding viscous medium.

To investigate Taylor-Culick retractions at a liquid-gas free-surface in chapter 5, we develop a precursor film-based three-fluid volume of fluid method that captures the experimentally-observed scaling behavior very well. In a broader perspective, one can use this method to elucidate several spreading phenomena, both at small and large scales, such as, drop-film interactions in the inkjet printing process and late time spreading during oil spillage, respectively. However, this numerical assumption is applicable only when it is thermodynamically favorable for one of the fluids to spread over the other fluids it comes in contact with, i.e., it has a positive spreading coefficient. Indeed, extending this method to generalized three-phase contact line motions is expected to yield interesting results. The current three-fluid model can also handle different surface tension forces for the three interfaces and can be used as a base model to incorporate multi-physical aspects, such as Marangoni flows and multicomponent systems.

In chapter 6, we reveal that the influence of viscoplasticity on the capillary-driven bursting of a bubble at a liquid-gas free-surface is twofold: (i) it manifests as an increase in effective viscosity to attenuate the capillary waves that control the bursting process, and (ii) the plasticity of the medium resists any attempts to deform its free-surface. Immediately after bursting, the large capillary stresses localized at the intersection of the bubble cavity and the free-surface result in a train of capillary waves that travel down the bubble cavity. In liquids with low yield stresses, these waves still follow the same behavior as their Newtonian counterpart. Subsequently, the cavity collapse leads to a Worthington jet that might break into droplets owing to the Rayleigh-Plateau instability. However, the capillary waves and the Worthington jet vanish for

liquids with a large yield stress. Furthermore, yield-stress fluids can sustain deformations. Consequently, even after waiting a long time, the cavity never returns to its zero surface energy configuration (a flat free-surface). For high yield-stress liquids, the plasticity of the medium can even overcome the capillary waves that try to yield the free surface, thus freezing a zoo of final crater shapes.

Samenvatting[◦]

In dit proefschrift hebben wij verschillende verschijnselementen aan het vrije oppervlak onderzocht om de rol van viskeuze spanningen te illustreren. Deel I (hoofdstukken 1–4) bestudeerde de impact van sferische vloeistofdruppels op niet-natte substraten. Deel II (hoofdstukken 5–6) concentreerde zich op capillair-gedreven terugtrekking van films en het barsten van vrije-oppervlakte bellen.

In **hoofdstuk 1** bestuderen we waterdruppels die inslaan op niet-natte substraten. We vinden dat zowel de impact als de take-off gepaard gaan met een toename van de impactkracht op het substraat. De traagheidsdrukkkracht bepaalt de grootte van deze beide pieken in de normale reactiekracht. Maar verrassend genoeg kunnen zelfs botsingen bij lage snelheid leiden tot een opmerkelijk hoge tweede piek in de normaalkracht, die zelfs groter kan zijn (bijna driemaal) dan de eerste. Deze verbetering kan worden toegeschreven aan de ineenstorting van een luchtholte binnenin de vloeistofdruppel, wat leidt tot enkelvoudige Worthington-stralen. Onze resultaten geven dus een fundamenteel inzicht in de dynamica van de druppelinslag op een niet-bevochtigd oppervlak en de krachten die ermee gepaard gaan. Zulk inzicht is van cruciaal belang om tegenmaatregelen te ontwikkelen tegen het falen van superhydrofobiciteit in technologische toepassingen (bijvoorbeeld door het vermijden van het regime met hoge impactkrachten).

In **hoofdstuk 2** we bepalen de overgang van stuiterende naar niet-stuiterende druppels die op een niet-nat substraat vallen. Tijdens het druppel impact proces verstoort de viskeuze dissipatie het interne momentum. Een druppel zal ophouden met stuiteren en op het substraat blijven liggen als zijn opwaartse momentum (aangedreven door capillariteit en tegengewerkt door viskeuze spanningen) na het proces van druppelinslag, verspreiding en terugtrekking onvoldoende is om de zwaartekracht te overwinnen. Zwaartek-

[◦]I would like to thank Sander Huisman, Maaike Rump, and Carola Seyfert for proofreading the Dutch summary.

racht en viscositeit werken dus samen om te voorkomen dat druppels van een niet-nat substraat stuiteren. Wij stellen verder vast dat dicht bij deze overgang het terugslagproces onafhankelijk is van de inslagparameters. Deze waarneming ontkoppelt de latere fasen van de terugslag van de initiële dynamica van de inslag. Deze resultaten zijn nuttig in toepassingen waar het terugkaatsen van een druppel moet worden onderdrukt, bijvoorbeeld bij inkjet-druk, koeltoepassingen, de toepassing van pesticiden en criminale forensische wetenschap.

In hoofdstuk 3 onderzoeken we druppels die weerkaatsen op viskeuze vloeistoffilms die atomair gladde substraten nabootsen. Het afstotend gedrag van dergelijke substraten vereist de aanwezigheid van een luchtlaag opgesloten tussen de stotende druppel en de vloeibare film. Druppels die inslaan op viskeuze vloeistof films vertonen twee verschillende stuiteren regimes, namelijk het substraat-onafhankelijke en het substraat-afhankelijke stuiteren. In het eerste regime wordt de botsingsdynamiek niet beïnvloed door de aanwezigheid van de viskeuze film, als gevolg van zijn hoge viscositeit of verwaarloosbare dikheid. In het laatste echter beïnvloeden zowel de eigenschappen van de druppel als die van de film de terugstuitdynamiek. Binnen de substraat-onafhankelijke grens wordt de afstoting onderdrukt zodra de druppelviscositeit een kritische waarde overschrijdt, zoals bij superamphiphobische substraten die in hoofdstuk 2. Het substraat-afhankelijke regime laat ook een grens toe voor druppels met lage viscositeit, waarin alleen de eigenschappen van de film de remming van afstoting bepalen.

In hoofdstuk 4 hebben wij ontdekt dat in aanwezigheid van een niet-bevochtigend substraat, de druppel-op-druppel botsing vijf terugslagscenario's oplevert, waarvan er vier geen coalescentie inhouden. De botsende druppel tilt in twee van de vier terugspringscenario's een luie sessiele op. Als er voldoende energie tussen de druppels wordt overgedragen, kunnen beide druppels van het substraat kunnen nemen, terwijl in sommige gevallen de botsende druppel de sessiele druppel van het substraat schopt, maar zelf niet kan stuiteren. Bovendien illustreert een één-op-eén vergelijking tussen de experimenteel en numeriek bepaalde druppelgrenzen en de mechanische energieën van het massamiddelpunt de kracht van de directe numerieke simulaties voor het kwantitatief voorspellen van de dynamica van druppel-op-druppel inslag. Inzichten uit de hoofdstukken 3 en 4 zijn belangrijk omdat voor de meeste industriële toepassingen, zoals inkjet printing of additive manufacturing, druppels worden afgezet op een reeds bestaande laag van een andere druppel of film. Vandaar dat de relatieve precisie van de druppelafzetting en zijn vormevolutie het suc-

ces of het falen van deze toestellen kunnen bepalen.

Merk op dat, hoewel wij directe numerieke simulaties doen van de verschillende scenario's van druppelinslagen in de hoofdstukken 1–4, wij dat doen met behulp van de continuümvergelijkingen. Bijgevolg is onze numerieke methode ontoereikend om te voorspellen of een druppel al dan niet met een andere druppel of met het substraat zal samensmelten. Wij halen deze informatie uit de experimenten. Het al of niet samensmelten van grensvlakken hangt namelijk af van verschillende multifysische aspecten, waaronder oppervlakteasperiteiten en vanderwaalskrachten. Voorspelling van zulke coalescentie (of breuk) gedragingen valt buiten het bereik van dit schrift, maar men kan een consistente moleculaire dynamica techniek (zoals de gaskinetische theorie) koppelen aan de continuüm-gebaseerde vloeistofvolume methode om deze lacune in ons model in de toekomst te overbruggen.

In hoofdstuk 5 vinden wij dat zelfs wanneer het omringende medium interacteert met de Taylor-Culick terugtrekking van een film, de film nog steeds met een constante snelheid terugtrekt, op voorwaarde dat de film lang genoeg is om eindige filmgrootte en inwendige viskeuze effecten te vermijden. Zowel de traagheid als de viscositeit van de omgeving beïnvloeden echter de grootte van deze constante snelheid. Voor de veralgemeende Taylor-Culick terugtrekkingen geldt dat zelfs wanneer de omringende delen een verwaarloosbare viscositeit hebben, zij toch het terugtrekproces beïnvloeden door inertiële (toegevoegde massa achtige) effecten. Voor een zeer viskeuze omgeving daarentegen dicteert de viskeuze dissipatie de schaal van de terugtreksnelheid. De precieze aard van deze variatie hangt af van de geometrie van de canonische configuratie in kwestie. Bijvoorbeeld, voor terugtrekkende vellen ondergedompeld in een viskeuze olie, schaalt de terugtreksnelheid met de visco-capillaire snelheid (d.w.z., het capillair getal is een constante). Voor vellen die zich terugtrekken aan een olie-lucht grensvlak vertoont het capillair getal echter een power-law gedrag met de dimensieloze viscositeit (Ohnesorge getal) van het omringende viskeuze medium.

Om de Taylor-Culick terugtrekkingen aan een vloeistof-gas vrij-oppervlak te onderzoeken in hoofdstuk 5, ontwikkelen we een precursor film-gebaseerde drie-vloeistof vloeistofvolume methode die het experimenteel waargenomen schalingsgedrag zeer goed weergeeft. In een breder perspectief kan men deze methode gebruiken om verschillende verspreidingsfenomenen op te helderen, zowel op kleine als op grote schaal, zoals respectievelijk druppel-film interacties in het inkjet drukproces en laattijdige verspreiding tijdens olielekage. Deze numerieke aanname is echter alleen van toepassing wanneer het

thermodynamisch gunstig is voor een van de vloeistoffen om zich te verspreiden over de andere vloeistoffen waarmee het in contact komt, d.w.z. dat het een positieve verspreidingscoëfficiënt heeft. Uitbreiding van deze methode tot veralgemeende driefasige contactlijnbewegingen zal naar verwachting interessante resultaten opleveren. Het huidige drie-fasen model kan ook omgaan met verschillende oppervlaktespanningskrachten voor de drie grensvlakken en kan worden gebruikt als basismodel om multi-fysische aspecten te incorporeren, zoals Marangoni stromingen en multicomponent systemen.

In **hoofdstuk 6**, hebben wij aangetoond dat de invloed van viscoplasticitet op het capillair-gedreven barsten van een luchtbol aan een vloeistof-gas vrije-oppervlak tweevoudig is: (i) het manifesteert zich als een verhoging van de effectieve viscositeit om de capillaire golven te dempen die het barstproces regelen, en (ii) de plasticiteit van het medium verzet zich tegen alle pogingen om het vrije-oppervlak te vervormen. Onmiddellijk na het barsten leiden de grote capillaire spanningen, gelokaliseerd op het snijpunt van de belholte en het vrije-oppervlak, tot een trein van capillaire golven die langs de belholte naar beneden beweegt. In vloeistoffen met lage vloeispanningen volgen deze golven nog steeds hetzelfde gedrag als hun Newtoniaanse tegenhanger. Vervolgens leidt het instorten van de holte tot een Worthington straal die in druppels kan breken ten gevolge van de Rayleigh-Plateau instabiliteit. Voor vloeistoffen met een grote vloeispanning echter verdwijnen de capillaire golven en de Worthington jet. Opbrengstdruk vloeistoffen kunnen vervormingen volhouden. Bijgevolg keert de holte, zelfs na lang wachten, nooit terug naar de nulconfiguratie van de oppervlakte-energie (een vlak vrij-oppervlak). Voor vloeistoffen met hoge vloeispanning kan de plasticiteit van het medium zelfs de capillaire golven overwinnen die het vrije-oppervlak trachten op te leveren, en zo een zoo van uiteindelijke kratervormen bevriezen.

Acknowledgments

First of all, I want to thank **you**, the reader, for picking up this thesis. Thank you for reading through all the chapters, or if you are anything like me, thank you for coming straight to the acknowledgment section. Whenever I find a Ph.D. thesis, this section is my first stop. The journey of any doctoral candidate is long with all its ups and downs, which often (hopefully) culminates in a collection of chapters. Every journey is unique, and one can understand the person on this journey by knowing who they acknowledge after completing such a taxing yet inciting endeavor. My Ph.D. journey at the Physics of Fluids (PoF) group, like all others, has been made possible by the support of many people. I want to spend the next few pages sharing my gratitude towards them.

Detlef, thank you so much for giving me this opportunity to work with you and all the independence to pursue the wide variety of intellectually stimulating problems in this thesis. We first got in touch via email and Skype (in the old pre-pandemic, non-zoom days). I received a one-line reply to my long request seeking a research position at PoF, which I now know to be your efficient style, as these one-line emails have become a part of my daily life. I cannot express in words how much I have enjoyed working with you over the past four years. Someone once told me that working with you is like working with Albert Einstein but in fluid dynamics. After four incredible years, I can attest to this fact. I particularly enjoy our meetings when they do not have an end time. I get to hear your thoughts and learn about the rich history of fluid dynamics, which are equally inspiring. I am often amazed by your energy. For example, I remember once, while we recorded lectures for the Advanced Fluid Dynamics course, we spent almost eight hours in your office. My job was simply to hit record and listen in as you taught the modules on turbulence, boundary layers, and instabilities. It was incredibly one of the most informative sessions of my life. Even after eight hours, you were still as

energetic as when we started. Indeed, that day I witnessed the perfect example of what happens when one does what they love. In your words, the only essential thing in one's life is the brain and the passion for science; everything else is just background noise. **Detlef**, for all the hours that you spent with me working out the Physics, thanks a lot. I want to continue this quest in the world of fluid dynamics by asking relevant questions, as you so often told me, and answer them to the best of my abilities. I am looking forward to working ever so closely with you in the future. I have a lot yet to learn from you, and I am sure we will have many long sessions filled with intellectually stimulating discussions in the future.

Mazi, the transition at the beginning of anyone's Ph.D. journey is often overwhelming and confusing. Thank you for helping me through this phase. Working on chapter six of this thesis, I learned a lot about fluid dynamics and non-Newtonian flows. Furthermore, you have always lent an ear whenever I felt stuck in the past four years. The long scientific discussions and the ideas you passed on have been invaluable to me. But, of course, your influence on this thesis is not restricted to just being the go-to person for quenching Scientific curiosity. You have also acted as the perfect Yoda on this Ph.D. journey, both academically and otherwise. Thank you so much for inspiring me all through the process. I look forward to working together on many ideas and projects.

I have been fortunate to be always surrounded by some of the most incredible mentors, **Detlef**, **Mazi**, **Stéphane Z.**, **Andrea**, **John S.**, **Jean-Philippe**, **Mickaël**, and **Arup**. The privilege often reminds me of these words taken from a letter Newton wrote to Robert Hooke, "If I have seen further, it is by standing on the shoulders of giants." I am indebted to all of you for encouraging and showing me the way. **Stéphane Z.**, thank you for teaching me all I know about the volume of fluid method. Given that this method forms the backbone of my entire Ph.D. thesis, it is safe to say that this thesis would not exist without the GIAN course on two-phase flow at the Indian Institute of Technology Roorkee. You are always eager to discuss science whenever we meet during conferences or during your visits to PoF. These discussions have benefited me tremendously throughout my career. **Andrea**, your enthusiasm, passion, and search for new fluid dynamics problems have motivated me. The long sessions with you always leave me full of thoughts and ideas. **Arup**, I would also like to thank you for introducing me to the fascinating world of fluid dynamics. The journey that started in your office about eight years ago has now reached this stage, with hopefully more to come.

Here, I would like to take the opportunity to thank my **committee members**. Thanks a lot for agreeing to be a part of my graduation committee and for spending so much of your precious time reading this thesis. I look forward to interacting with you all on the day of the defense and in the future.

Next, I want to thank my paranymphs, **UJ** and **Udo**. First of all, thanks for agreeing to accompany me on the stage as I defend this Ph.D. thesis and for dressing up formally for the occasion. I know how much both of you share my discomfort in adhering to formal attire. **Udo**, your passion for perfection is a force to reckon with. Thanks for always being critical of my work and providing honest feedback. We had a great time working on the Taylor-Culick retractions, which formed the largest chapter of this thesis. I hope we will continue our collaboration and the long walks that consistently contributed to pushing these collaborations. I hope we will tackle many more interesting fluid dynamics problems in the future. **UJ**, I have found a great friend in you. We have spent many weekends in our offices discussing all things related to fluid dynamics and life. **Yanshen, Peter**, you, and I made the weekend warriors at PoF. We also had a wonderful and insightful time in Copenhagen. I have also always enjoyed our long walks. By the way, **UJ**, we have known each other since my first visit to PoF when we went out for dinner following my interview with **Detlef** where he offered me this doctoral position. Little did I know that we share a common friend, who, as it turns out, is one of my closest allies in life. Thank you, **Sonali** for always being available at a phone call's notice and for all the help you have provided throughout these years.

Pierre, we have shared an office for almost three years. We have interacted on several open projects and ideas throughout this time and often had heated but spirited discussions about our works. Collaborating with you on chapters 2 and 3 of this thesis has been excellent. I have thoroughly enjoyed our brainstorming sessions. In one of them, we also came up with the title of this thesis. In fact, the first part of this work on drop impact processes draws motivation from these discussions and your thesis. The latter has also contributed to improving my understanding of the French language. I also want to thank you for always lending an ear to my, at times, crazy ideas.

Next, I would like to thank all my collaborators and coauthors, **Claas-Willem, Olinka, Doris, Jon, Bin, Cunjing, Srinath, and Pallav**. I have learned a lot from all of you and am looking forward to several stimulating collaborations in the future.

Next, I want to thank the entire group at PoF, my professional family. The Wednesday seminars are a tour de force. We get to share ideas, listen

to fluid dynamics leaders from across the globe, and most importantly, enjoy stimulating discussions. Being a part of this group is a privilege I have enjoyed as a young researcher. I want to thank **Joanita** for her superhuman organizational skills. You show an ideal combination of speed and precision. Thank you for always having a solution to any and all of my problems.

Of course, the group is only as good as the people in it. At PoF, I interacted with amazing fluid dynamicists. Where else would one find a fluid dynamics rock star like **Leen** whose contributions to fluid dynamics research and several lives are both incredible and humbling.

Devaraj, thank you for agreeing to be the chairperson of my committee and for all the positiveness during our interactions. Your knowledge of all matters, Physics or otherwise, is terrific. I got a first-hand experience during the pop quiz at Landal Village. It was a pleasure to be a part of the team centurions and compete alongside **Javier** and **Loréne**. Indeed, it was a lovely group outing. I really enjoyed the place, the science, and most of all, the company in the bungalow #100. Thanks a lot.

Jacco, thank you for the insightful conversations regarding free-surface flows. We have run into each other several times at Starbucks, and I am often intrigued by how easy it is to talk to you about everything, irrespective of the complexity. I remember the one conversation we had regarding the origin of viscosity and the no-slip boundary condition in continuum mechanics. It was, in a word, inspiring. I would also like to thank **Alvaro**, **Richard**, **Corinna**, **Dominik**, **Tim**, **Michel**, **Marjolein**, and **Christian** for always asking just the right questions during group meetings, seminars, or even at dinner tables.

Sander, thank you for all the chocolates that helped maintain my blood sugar level over the years. I could always rely on your (not-so) secret stash whenever I needed something. Also, thank you for giving me a chance to teach some of the Advanced Fluid Mechanics modules. The best way to learn something is to teach it, and I thank you for allowing me to gauge and sharpen my knowledge through these lectures. Lastly, thank you for proofreading the Dutch summary despite your busy schedule and for your help with making the PoF-Basilisk logo, along with all the illustrator tricks you have shown me over the years. I look forward to spending more time with you and, finally, learning Mathematica.

Diana, we went on several long walks together through the woods, despite being scared of the caterpillars. We also had so much fun in the pre-pandemic (almost prophetic) Pandemic games. Thank you for all the fun we had together. Also, thank you for all the relatable stories from Columbia; oops, I

meant Colombia, captain correct America.

Youssef, we share several commonalities. We started our respective doctoral works at a gap of a few months, share the same office, and perhaps most importantly, specialize in Basilisk. Thank you for always providing a bouncing board for new and old Basilisk ideas and tricks. Now, coincidentally, we are also getting married within a few months of each other. I wish you an amazing married life.

Maaike, thank you for all the fun and scientific discussions we have had over the years. Thank you for always listening in with so much attention and being ever so polite. I wish you the best for your bike trip across a few continents.

Carola, I always look forward to our coffee breaks. Thank you for all the discussions and advice you have given me throughout the years. And also, thanks a lot for allowing me to ‘steal’ some of your thesis template ideas.

Jessica, I have always enjoyed your company. Thank you so much for all the fun and, at times, serious conversations we have had over the years.

Varghese, **Shantanu**, and **Vamsi**: you formed the previous generation of doctoral candidates who graduated immediately before I joined PoF. You all were also deeply involved in my hiring interviews. Thank you for sharing your experiences and showing me what a wonderful place PoF is. There are still many PoF colleagues and friends who I would like to thank for making the last four years a delight and a blast, **CS**, **Yibo**, **Timothy**, **Robert**, **Anupam**, **Youan**, **Morgan**, **Chris**, **Farzan**, **Ambre**, **Alex**, **Martin E.**, **Vanshu**, and **Anja**. Thank you, **Minkush** for being so kind and caring for everyone. **Lijun** and **Yogesh**, thank you for the several dinners we have had together and never kicking **Udo** or me out even if we self-invited ourselves. I also enjoyed our cricket games together with **Srinidhi**.

My old and current office-mates: **Rodrigo**, **Dennis B.**, **Mazi**, **Martin**, **Marvin**, **Pierre**, and **Youssef**. Thanks for always maintaining such a great environment at **ME 246B**. **Dennis B.**, your passion for open-source programming is unparalleled. I have always enjoyed out long discussions on this topic.

My office neighbors, the gang in **ME 24/7**: **Jelle**, **Pieter**, **Srinidhi**, and **UJ**, thank you for always providing a place to cool off and swap stories.

Next, I would like to thank the fantastic technicians and the support team at PoF. **Dennis vG.**, thank you for maintaining order at PoF. **Bas** and **Thomas** for helping me with all the tech support and acquiring gadgets. **Gert-Wim** and **Martin B.**, even though I did not participate in any exper-

imental work during my Ph.D., it was always a delight to talk to both of you whenever we met.

During my Ph.D., I had the privilege to engage with several motivated students, **Laurence**, **Coen**, **Mihir**, **Pim**, **Steven**, **Thijmen**, **Tom**, **Toon**, and **Twan**, just to name a few. I thank you all for working with me and wish you all the best for your subsequent undertakings.

Stéphane P., you have developed and maintained one of the largest free-software programs in our community. I started my research career with Gerris and then moved to Basilisk C. I want to thank you and the entire Basilisk community for providing a well-documented partial differential equation solver. Learning the code and implementing new modules are both very easy, thanks to your efforts.

I would be amiss if I did not mention all the love and support I have received from **my family members**, including my parents, sister, and in-laws. Your willingness to support me through higher studies is commendable. In a society where graduating from college and seeking a job represent the norm, I am lucky to be associated with a family encouraging higher education. Words cannot acknowledge the support I have received from all of you. Of course, my extended family includes my fantastic close friends, **Akash** and **Akanksha**; thank you for always being there whenever I needed you.

Vatsalya, thank you for providing a sanctuary whenever I needed one and for proofreading parts of this thesis despite all the technical jargon. We have been friends since high school, and we (almost) share our first names but have pursued very different and arguably complementary career paths. My love for Physics and yours for music benefited us during high-school exams. But, I have only you to thank for introducing me to my favorite human being and now, my wife.

Anjali, there is nothing I can say that you do not know already. We have known each other since high school. A Physics question on Kirchhoff's circuit laws brought us together, and you have been with me ever since. You have seen me both at my best and worst. Thank you for always believing in me, even when I did not. You bring a smile to my face, irrespective of the situation. This journey would have been difficult without your constant presence in my life. My warm hugs and a big thank you to you. Thank you so much for always being there. I dedicate this thesis to you, my lovely wife and the one constant in my life.

About the author



These are the last two pages of my Ph.D. thesis where I am supposed to write about myself. Before doing so, I must admit that it is a herculean task, but I will try my best to share my story with you.

I was born on February 5th, 1996, in Laheriasarai, a small town in Bihar, India. As a kid, my first love was reading stories, which soon became a love for history. If I were not a fluid dynamicist today, I would probably have been a historian. The only problem was that I could only read stories about others and not write one of my own, which is another of my passions. Apart from reading, I also love collecting books. Ever since childhood, I have maintained a healthy collection of books, both antique and modern.

Thanks to one of these books, I stumbled into the fascinating world of Physics. I remember getting puzzled by a question that seemed like a paradox at the time. I still remember the question. *To pull a cart, a horse applies a force on it. However, Newton's third law dictates that the cart applies an equal and opposite force on the horse. If we take the horse and the cart as a system, the net force on this system is zero. Then, how does a horse pull a cart?* It took me an entire sleepless night to come up with an answer, ending in a midnight call to my secondary school Physics teacher.

The satisfaction of coming up with the correct answer set me up on this journey which led me to do a bachelors in Mechanical Engineering from the Indian Institute of Technology Roorkee, during which I worked as an under-

graduate researcher with Prof. A. K. Das in the two-phase flow lab. I also did an internship with Prof. M. Bourgoin, Prof. J-P. Matas, and Prof. J. J. Jerome. This internship introduced me to the rich European research culture and the fluid dynamics community. The style of asking questions and exploring the fundamental fluid dynamics of everyday flows appealed to me. Subsequently, I decided to switch my bachelor's program to an integrated dual degree. I finished my master's thesis with Prof. Das. These works led me to pursue a doctoral work with Prof. D. Lohse in the Physics of Fluids group, where I have spent the last four years working on this Ph.D. thesis.

But the story is not over yet. In the future, I want to continue this quest in the world of fluid dynamics by asking relevant questions and answering them to the best of my abilities. I also want to read more books and contribute to spreading the beautiful world of fluid dynamics to everyone. One day, I would also like to run a marathon, thanks to my recently acquired love for running.